

Analytical and Experimental Study of Gas Flow Regime in the Matrix and
Fractures of Shale Gas Reservoirs

by
Alireza Ashrafi Moghadam

A thesis submitted in partial fulfillment of the requirements for the degree of

Doctor of Philosophy
in
Geotechnical Engineering

Department of Civil and Environmental Engineering
University of Alberta

© Alireza Ashrafi Moghadam, 2016

Abstract

One of the most significant differences between conventional and unconventional gas resources is the ultra-low matrix permeability of unconventional gas reservoirs such as shale, coal and tight gas. Matrix permeability of shales is an elusive but important parameter in characterizing shale gas reservoirs. It is believed that the long-term performance of shale wells is controlled by matrix permeability. Permeability is typically measured using steady-state flow tests or the more timely transient methods such as pulse-decay. Due to the low permeability nature of shale rocks, a slip or transition flow regime is observed to be dominant at the pore scale and as a result, permeability changes with pore pressure. Traditionally, permeability is measured at various mean pore pressures and the data is used to extract the Klinkenberg or absolute permeability. However, the assumptions behind the Klinkenberg's equation do not apply to the nanoscale pore networks in shales and other tight rocks. Additionally, various methods of permeability measurement can lead to significantly different results at similar test conditions.

In this thesis, a fundamental analytical study was conducted to understand the dominant flow regimes under laboratory and reservoir conditions, which is important for modelling gas flow and predicting gas production. Based on the findings, an analytical model is developed capable of modelling gas flow in low permeability reservoirs while retaining the simplicity of Klinkenberg's original formulation. The theory suggests, that the gas permeability is in essence a function of the pore radius open to gas flow, but further enhanced by the slippage of gas molecules at the pore wall. The slippage factor is also a function of available pore

radius to flow, increasing as the pores diminish in size. These findings imply that any parameter that changes the effective pore radius in the porous media (water saturation, adsorption, effective stress, etc.) alters the absolute permeability and the slip factor. This alteration in gas permeability can be quantified using the approach proposed and verified in this work. Extensive laboratory testing has been conducted to measure gas permeability in tight rocks at various conditions. The lab tests are uniquely designed to capture the influence of pressure, effective stress, temperature, gas type, and flow rate. The influence of gas flow rate on permeability has never been investigated before in this class of materials. This phenomenon casts a shadow of doubt around the common non-steady-state permeability measurement methods. A more complete picture of the gas flow regime as a function of pore pressure and velocity is introduced.

The outcomes of this research focus on designing more representative gas permeability tests, proposing accurate methods of analyzing lab results, and finally to be able to convert the lab results to the in-situ values to model gas flow in the reservoir. This work lays the foundation to revisit the basic definition of gas permeability, in order to set up new standards (concerning testing pressure, rate, and stress state) to obtain meaningful and comparable permeability measurements.

Preface

The laboratory setup described in chapter 5 was originally designed by Dr. Nathan Deisman. I was responsible for the modifications done to the setup for this work. The analytical work in chapters 3 and 4, and the data analysis in chapter 6, are my original work, as well as the literature review in chapter 2.

Chapter 3 and part of chapter 6 of this thesis have been published as “Moghadam, A.A. and Chalaturnyk, R. 2016. Analytical and Experimental Investigations of Gas-Flow Regimes in Shales Considering the Influence of Mean Effective Stress. SPE Journal 21(02), 557-572”. Chapter 4 has been published as “Moghadam, A.A., Chalaturnyk, R., 2014. Expansion of the Klinkenberg’s slippage equation to low permeability porous media. International Journal of Coal Geology 123, 2-9”. For both publications, I was responsible for the laboratory experiments, data collection and analysis, and manuscript composition. Dr. Rick Chalaturnyk was the supervisory author and was involved in concept formation and manuscript composition.

Acknowledgements

I would like to express my gratitude to my supervisor, Dr. Rick Chalaturnyk, for his continuous support throughout my PhD. During this time, he taught me to be an ethical scientist, a professional, and a good speaker, among other priceless life skills. I am forever indebted to him.

Support from the GeoRef laboratory staff, Gilbert Wong and Keivan Khaleghi, is gratefully acknowledged. I would like to thank Nathan Deisman, for the valuable guidance on designing the experimental setup, Noga Vaisblat for the great discussions, and Nora Hehemann for her editorial assistance. The efforts made by my supervisory committee, Dr. Derek Martin and Dr. Nicholas Harris, are gratefully appreciated. I owe many thanks to Hope Walls for her administrative support and providing a boost of morale whenever needed.

At last, I should send my regards to the City of Edmonton and all its wonderful inhabitants. Edmonton became my new home from the very beginning of my PhD program and provided everything I needed to flourish. I hope to be able to provide the same support back to the community.

Table of Contents

Abstract.....	ii
Preface.....	iv
Acknowledgements.....	v
List of Tables	ix
List of Figures.....	x
Chapter 1: Introduction.....	1
Motivation.....	1
Gas and Liquid Permeability	2
Research Focus	4
Structure of the Thesis	4
Literature Review.....	4
Flow Regime Analysis.....	4
Analytical Model	5
Laboratory Experiments.....	5
Model Verification and Discussions.....	6
Appendices.....	7
References.....	7
Chapter 2: Literature Review.....	9
Gas Flow Regime and Permeability	11
Knudsen Number	12
Darcy Flow Regime	14
Inertial Flow.....	14
Slip Flow Regime	16
Transition Flow Regime	18
Free-molecule Flow Regime.....	19
Influence of Geomechanics on Apparent Permeability	19
References.....	21
Chapter 3: Analysis of Gas Flow Regime in Porous Media.....	29
Range of Permeability and Pressure in shale reservoirs	29
Analytical investigation of flow regime	31

Pore Radius Calculations	36
Conclusions.....	37
References.....	38
Chapter 4: Expansion of the Klinkenberg’s Slippage Equation to Low Permeability Porous Media.....	41
Introduction.....	42
Theory.....	43
Results and Discussions.....	49
Conclusion	58
Nomenclature.....	59
References.....	60
Chapter 5: Laboratory Investigation of Shale and Siltstone Permeability.....	63
Introduction.....	64
Permeability Models	64
Permeability Measurement Techniques.....	65
Laboratory Experiments.....	68
Sample Description.....	68
Laboratory Setup.....	70
Methodology.....	72
Calculations.....	78
Summary.....	79
References.....	80
Chapter 6: Analytical and Experimental Investigations of Gas Flow Regimes in Shales Considering the Influence of Mean Effective Stress.....	83
Analytical Model	85
Model Verification.....	85
Rate Dependency of Permeability	96
Flow Regime Transition	107
Rate-Dependent Model.....	111
Gas Type and Temperature.....	114
Water Permeability	118

Influence of Geomechanics.....	120
Mean Effective Stress	122
Depletion Scenario.....	128
Failure	131
Creep.....	137
Influence of Water Saturation.....	138
Verification	140
Relative Permeability to Gas	142
Summary of the Analysis.....	145
Potential Sources of Error.....	148
Experimental Error.....	148
Samples.....	148
Adsorption.....	149
Pore Plugging by Residual Water or Gas	150
Effective Stress Coefficient for Permeability	150
Conclusions.....	153
Nomenclature.....	155
References.....	156
Chapter 7: Conclusions and Recommendations	165
Future Work	171
References.....	172
Appendix A: Derivation of Eq. 17	187
Appendix B: Experimental Results.....	189
Appendix C: Derivation of Eq. 52	199

List of Tables

Table 1: Summary of shale permeability reported in the literature	30
Table 2: Comparison of the results of Eq. 33 and Klinkenberg's equation to the liquid permeability data	53
Table 3: Values of constants in Eq. 33 for various data sets	55
Table 4: Summary of samples used in the steady-state gas permeability experiments	69
Table 5: Minerology of the Montney samples (mass %).	69
Table 6: The steps of the experimental investigation for each sample.	77
Table 7: Steady-state gas permeability results for the Clearwater sample.	86
Table 8: Summary of the experimental results from this work and the literature.	94
Table 9: Summary of the parameters used in Eq. 44 to match the experimental results	114
Table 10: Summary of the water permeability measurements.....	119
Table 11: Parameters for Eq. 45 Calculated from the experimental results.	123
Table 12: Summary of the input parameters for the dried sample Alum#2 in Ghanizadeh et al. (2014) tests.....	140
Table 13: Summary of the parameters that should be m required to fully characterize gas permeability.....	146
Table 14: Summary of the recommendations to measure gas permeability in the lab.....	170
Table 15: Results of the gas permeability measurements in this work.....	189

List of Figures

Fig. 1: Typical gas production plots from several shale plays in the United States (Baihly et al., 2015).	2
Fig. 2: Gas production history and projections for different regions. Top left: Natural gas production in the United States. Top right: Natural gas production in Canada. Bottom left: Natural gas production in Europe. Bottom right: Natural gas production in China. Gas volume are demonstrated in Tcf (Trillion Cubic Foot) unless mentioned otherwise (Annual Energy Outlook 2013; Canada’s Energy Future 2013; World’s Energy Outlook 2013).	10
Fig. 3: Flow regime characterization based on Knudsen number. Gas permeability enhancement (permeability of gas divided by the absolute or liquid permeability) is the highest at the free-molecule flow regime. It then decreases in the transition and slip flow regime until the enhancement disappears at Darcy flow regime. ...	13
Fig. 4: Knudsen number with respect to permeability and pressure.	31
Fig. 5: Flow Regime map for methane at 60 and 120 Celsius.	33
Fig. 6: Flow regime map for methane at 60 Celsius.	34
Fig. 7: Flow regime map for helium at 60 Celsius.	35
Fig. 8: Comparison of the pore radius estimates using three well-known correlations with the results of Mercury injection tests.	37
Fig. 9: Illustration of the velocity boundary conditions in a capillary tube in this work, Klinkenberg’s work, and no slip boundary.	44
Fig. 10: Permeability versus inverse of pressure for Core Samples M and L, from the original Klinkenberg paper.	50
Fig. 11: Non-linearity of Klinkenberg plot in data published by Rushing et al. (2004), Sample 2-33.	51
Fig. 12: Application of the new equation in experimental data by Li et al. (2009) and Dong et al. (2012).	52
Fig. 13: Comparison of the accuracy of the Klinkenberg equation and Eq. 33.	54
Fig. 14: Relationship between the constants “a” and “b” in Eq. 33.	54
Fig. 15: The dependency of “a” (Plot on the right) and “b” (Plot on the left) to permeability. Validation of Eq. 40 and Eq. 41.	56

Fig. 16: Variation of permeability with pore pressure for the samples used in this study.....	67
Fig. 17: Montney 10D sample. Porous stones are placed at the top and the bottom of the sample to ensure linear flow. Pictures of other samples are available upon request, though they look very similar to the Montney 10D sample.	70
Fig. 18: Schematics of the laboratory setup. Gas flows through a Quizix pump into the bottom of the sample and exits at the top. The gas is then collected in the accumulator which keeps the downstream pressure constant.	71
Fig. 19: On the right: An image of the whole setup. Gas cylinders, ISCO pumps and the temperature-controlled oven are displayed. On the left: An image of the inside of the temperature-controlled oven. The cell, the ram, accumulators, and the Quizix pump are displayed.	72
Fig. 20: Flow rate and mean pressure steps for permeability tests. Time axis is not to scale. Sufficient time was allowed between each step for the pressures to equilibrate. Tests at lower rates took longer than higher rates. Each gas permeability test took 1 to 8 hours to equilibrate depending on the sample and rate.....	74
Fig. 21: An example of the pressure response for two consecutive rate steps. After equilibrium in the first step, the rate is increased to 0.6 ml/min from 0.4 ml/min. Downstream pressure is set to a lower number in the accumulator to keep the mean pressure constant within an acceptable range.	75
Fig. 22: Verification of Eq. 33 using laboratory results for the Clearwater sample.	87
Fig. 23: Comparison of the accuracy of liquid permeability estimation between Eq. 33 and Klinkenberg from experimental data (data provided in Table 8).	88
Fig. 24: The realistic deviation of the Klinkenberg's equation from apparent permeability data.....	89
Fig. 25: Typical lab tests at low pressure leads to overestimation of absolute permeability using Klinkenberg's equation.	90
Fig. 26: Experimental values of "a" versus permeability (data provided in Table 8).	91

Fig. 27: Experimental values of “ b ” versus permeability (data provided in Table 8).	91
Fig. 28: Plot of “ a ” versus “ b ”, with theoretical relationship plotted in solid line (data provided in Table 8).	93
Fig. 29: Addition of best-fit line to describe relationship between “ a ” and “ b ” (data provided in Table 8).	93
Fig. 30: Gas permeability measurements for the Clearwater sample versus mass flow rate. The results are plotted at each mean pressure or Knudsen number.	97
Fig. 31: Gas permeability measurements for the Montney 10D sample versus mass flow rate. The results are plotted at each mean pressure or Knudsen number.	97
Fig. 32: Gas permeability measurements for the Montney 17O sample versus mass flow rate. The results are plotted at each mean pressure or Knudsen number.	98
Fig. 33: Gas permeability measurements for the Montney 8H sample versus mass flow rate. The results are plotted at each mean pressure or Knudsen number.	98
Fig. 34: Gas permeability measurements after failure for the Clearwater sample versus mass flow rate.	99
Fig. 35: Gas permeability measurements after failure for the Montney 10D sample versus mass flow rate.	100
Fig. 36: Gas permeability measurements after failure for the Montney 17O sample versus mass flow rate.	100
Fig. 37: Gas permeability measurements after failure for the Montney 8H sample versus mass flow rate.	101
Fig. 38: Change in permeability with respect to velocity or pressure gradient after Kutilek (1972) and Basak (1977) with modifications.	102
Fig. 39: Change in permeability with respect to gas pressure.	103
Fig. 40: Permeability surface with respect to velocity and Knudsen number. Mean effective stress moves the surface up (decrease in effective stress) or down (increase in effective stress).	105
Fig. 41: An overview of the governing gas flow regimes in porous media.	107

Fig. 42: A plot of the apparent permeability versus mass rate for all the samples, in the intact and failed states. The horizontal axis is linear. The transition between the pre-laminar and laminar regimes can be observed in the experimental results, as anticipated from Fig. 38 and Fig. 40.	109
Fig. 43: A plot of the apparent permeability versus mass rate for all the samples, in the intact and failed states. The horizontal axis is logarithmic. The transition between the pre-laminar and laminar regimes can be observed in the experimental results, as anticipated from Fig. 38 and Fig. 40.	110
Fig. 44: Prediction of the rate dependent apparent permeability using Eq. 44 for the Clearwater sample.	112
Fig. 45: Prediction of the rate dependent apparent permeability using Eq. 44 for the Montney 10D sample.	112
Fig. 46: Prediction of the rate dependent apparent permeability using Eq. 44 for the Montney 17O sample.	113
Fig. 47: Prediction of the rate dependent apparent permeability using Eq. 44 for the Montney 8H sample.	113
Fig. 48: Nitrogen and methane permeability versus mass flow rate for the Montney 10D sample. One of the nitrogen tests sets have been done at 45 C. Temperature increases the Knudsen number therefore should increase the permeability. However, permeability is observed to be smaller than predicted comparing the Knudsen values.	116
Fig. 49: Methane and nitrogen permeability for the Montney 17O sample. Nitrogen permeability values are comparable to methane permeability, considering the Knudsen number.	117
Fig. 50: Methane permeability at 25 and 45 C and different pressures for the Montney 8H sample. Temperature seems to dampen the apparent permeability.	117
Fig. 51: Continuous water permeability measurements during shearing for the Montney 8H sample. Permeability slightly decreases as the sample contracts (according to volumetric strain) and then increases significantly as dilation occurs.	120

Fig. 52: Experimental results for change in water permeability with respect to mean effective stress. Left axis shows water permeability values for Montney 10D and 17O samples. Right axis shows water permeability values for Montney 8H sample. 121

Fig. 53: Experimental results for change in water permeability with respect to mean effective stress for the samples after failure. Left axis shows water permeability values for Montney 10D. Right axis shows water permeability values for Montney 8H sample. 122

Fig. 54: Permeability multiplier (ratio of apparent permeability to initial water permeability) with respect to reservoir pressure. Dotted curve shows evolution of permeability multiplier considering only slip flow and ignoring influence of effective stress..... 125

Fig. 55: sensitivity of the permeability multiplier to α for the case with $k_{wi}=5$ nd. 126

Fig. 56: Experimental results of apparent permeability versus reciprocal of pressure at mean effective stresses of 10 MPa and 20 MPa on the Montney 17O sample. Lines present predictions obtained based on Eq. 47. Note that the data points must be selected from tests at similar mass rate. Generally, in order to analyze the change of permeability with mean pressure (i.e. the slippage effect) all the tests must be conducted at the same mass rate..... 128

Fig. 57: Depletion scenario for the Montney 10D sample. Total stress is held at 26 MPa. At each stage pressure is reduced while maintaining a constant total stress. 130

Fig. 58: Depletion scenario for the Montney 8H sample. Total stress is held at 26 MPa. At each stage pressure is reduced while maintaining a constant total stress. 130

Fig. 59: Depletion scenario for the Montney 17O sample. Total stress is held at 26 MPa. At each stage pressure is reduced while maintaining a constant total stress. 131

Fig. 60: Depletion scenario for the Clearwater sample. Total stress is held at 10 MPa. At each stage pressure is reduced while maintaining a constant total stress.	131
Fig. 61: Gas permeability versus mass flow rate for the Clearwater sample. Both sets of tests presented in the figure are conducted at 5MPa mean pressure. One set represents isotropic stress conditions and the other, axial stress is 1.5 times more than the confining stress. Both results show similar behavior for permeability; it increases with rate but reaches a plateau. The case with the deviatoric stress shows higher permeability which suggests some failure has happened in the sample.	132
Fig. 62: Apparent permeability increase with respect to the absolute permeability at several pore pressures. The permeability enhancement due to slippage decreases as absolute permeability increases. This is apparent from the data approaching the solid line at high permeability values.....	133
Fig. 63: Apparent permeability increase with respect to the absolute permeability at 8 MPa for the Montney 8H. The dashed line shows the apparent permeability increase if the permeability dependency of “a” and “b” is neglected.....	134
Fig. 64: Measured apparent permeability versus mass rate, before and after failure for the Montney 10D sample.	135
Fig. 65: Measured apparent permeability versus mass rate, before and after failure for the Montney 17O sample.	136
Fig. 66: Measured apparent permeability versus mass rate, before and after failure for the Montney 8H sample. Gas permeability after failure is higher than the intact condition. However, rate dependency of permeability is still observed.	137
Fig. 67: Permeability results versus rate considering the influence of creep. Apparent permeability for the Clearwater sample is measured once immediately after applying the deviatoric stress, and again after one week. No significant permeability change is observed, within the range of the experimental error.	138
Fig. 68: An illustration of the ideal capillary tube with (on the right) and without (on the left) water saturation. The effective pore radius to flow is smaller in presence of water.	139

Fig. 69: Prediction of permeability under wet conditions from the dry values. The proposed method shows a good match with the experimental permeability results of the wet sample.	141
Fig. 70: Gas relative permeability curves for Montney 8H sample at different pressures. The curves are generated using Eq. 54.	143
Fig. 71: Gas relative permeability curves for Montney 17O sample at different pressures. The curves are generated using Eq. 54.	143
Fig. 72: A flow chart summarizing the method proposed in this work to convert gas permeability measurements in the lab on dry samples, to gas permeability under in-situ conditions.....	147
Fig. 73: On the left, the variation of absolute permeability with pore pressure at a constant confining stress is presented. On the right, the variation of absolute permeability with stress at a constant pore pressure is shown. The data presented is for Montney and Marcellus shale samples by Heller et al., (2014), corrected for slippage. The two slopes on the left and right, for Montney and Marcellus shale is equal which leads to $\chi=1$	152
Fig. 74: An element of flow with the applicable forces in a capillary tube.	188

Chapter 1: Introduction

Shale gas and oil reservoirs have become a significant contributor to the overall hydrocarbon production in North America. The development of these reservoirs has nearly doubled the United States oil production, leading to the low oil and gas price environment today. The cost of production from shale plays are some of the highest in the world, as these reservoirs are poorly understood. Significant research is dedicated to various aspects of shale gas development such as horizontal drilling, hydraulic fracturing, sweet spot recognition, and shale matrix properties.

This dissertation investigates the matrix permeability of low-permeability porous media, including shales, both analytically and experimentally. The goal is to propose a more accurate model to predict gas flow, and to analyze laboratory tests with higher precision. The present work attempts to commence the fundamental discussions necessary to improve the permeability measurement standards, in order to obtain more comparable, and representative permeability results.

Motivation

The production from a shale gas well typically consists of three stages. Fig. 1 demonstrates the typical gas production plot for several shale gas plays in the United States. At the first stage, production rises rapidly as the fractures generated by hydraulic fracturing are depleted of the fracturing fluid. After reaching the peak, gas rate declines rapidly at the second stage usually within six to twelve months. This is typically attributed to fracture (and matrix adjacent to the fracture face) depletion and closure (Kalantari-Dahaghi and Mohaghegh, 2011). Finally, the gas

rate reaches a relatively constant plateau and will likely produce at that rate for a long period of time.

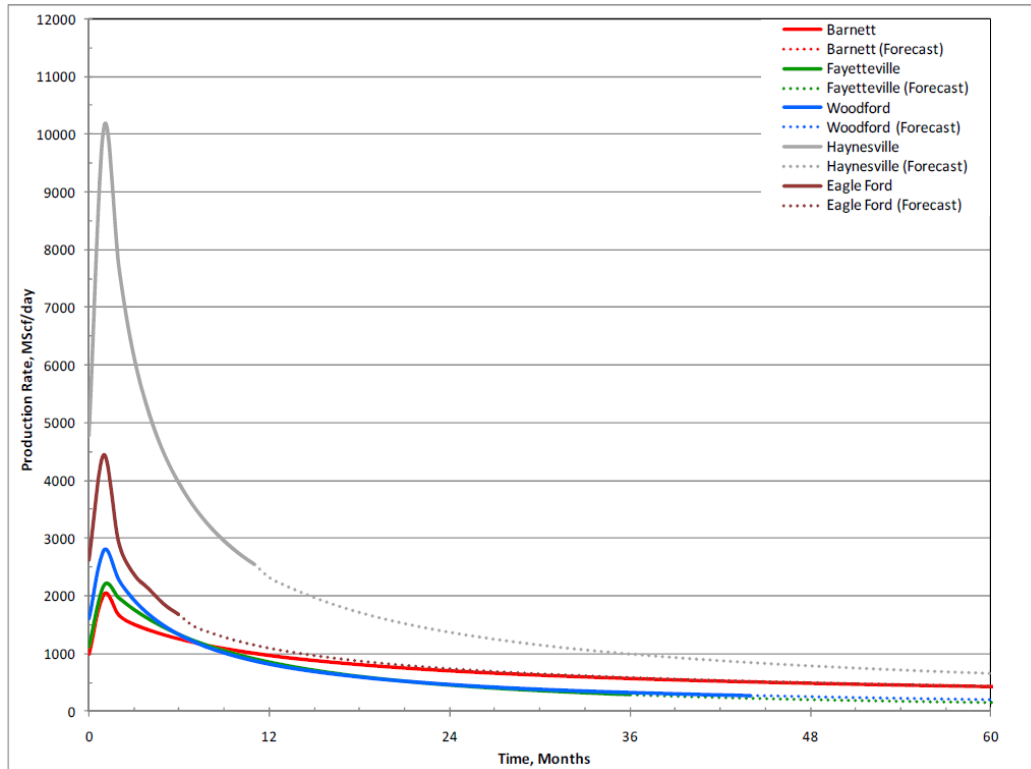


Fig. 1: Typical gas production plots from several shale plays in the United States (Baihly et al., 2015).

During stage three in the gas production plot, the matrix feeds gas into the fracture network. Therefore, the long term production from the shale gas wells is controlled by matrix permeability (Bustin and Bustin, 2012; Chalmers et al., 2012; Swami and Settari, 2012; Amann-Hildenbrand, 2012).

Gas and Liquid Permeability

Permeability is traditionally defined using the Darcy equation. Darcy equation is valid for a liquid flowing through a homogenous porous media, under laminar and isothermal flow conditions (Craft, 1991). Under these circumstances the permeability of the porous medium is taken to be a constant value. However,

laboratory measurements of gas permeability consistently show that gas permeability is a strong function of the mean pressure of the experiment. The permeability measured by gas is always higher than the liquid permeability of a porous media, under similar experimental conditions (Tanikawa and Shimamoto, 2009). The higher gas permeability has been attributed to the slippage phenomenon, where the gas molecules have a non-zero velocity at the pore walls that leads to an acceleration of flow due to less drag (Klinkenberg, 1941).

Considering the slippage, Klinkenberg (1941) addressed the pressure dependency of gas permeability for various gases and rock types in his iconic paper. According to his work, gas permeability has a linear relationship with the reciprocal of mean pressure. He successfully verified the relationship with several lab tests. His work has shown to be in excellent agreement with the lab measurements, on conventional reservoir rocks (Jones and Owens, 1980).

One of the most significant differences between the conventional and unconventional (tight reservoirs, shale, coal, etc.) gas reservoirs is the ultra-low matrix permeability. While the permeability of the conventional sandstone or limestone reservoirs are typically above 1 md, the shale matrix permeability is in the range of nano-darcy (nd). Due to the extremely low permeability nature of shale and tight rocks, the gas permeability exhibits a more complicated behavior. The Klinkenberg's equation does not apply to this class of materials.

The pressure dependency of gas permeability of the ultra-low permeability rocks is not well understood. In addition to pressure, other factors such as gas rate, effective stress, testing techniques, etc. also influence the permeability of low permeability rocks. A better understanding of gas permeability and additional experimental work is required to be able to design more accurate tests, analyze the tests with better precision, and to be able to predict the gas flow under the reservoir conditions.

Research Focus

The objective of this research is first to investigate the dominant flow regimes in the shale matrix throughout the life of a shale gas reservoir and under laboratory conditions. This includes studying the effect of mean pressure (Knudsen number) and flow rate (Reynolds number) on the flow. Second, proposing an analytical model that captures the physics of the dominant flow regime while maintaining simplicity. The new model is capable of modelling gas flow at reservoir condition, as well as analyzing lab results accurately. Third, the influence of parameters such as mean effective stress, and shear failure, flow rate, water saturation, temperature, and gas type, on the flow regime and on the proposed model's parameters will be investigated experimentally, and theoretically. The outcomes of this research focus on designing more representative gas permeability tests, proposing accurate methods of analyzing lab results, and finally to be able to convert the lab results to the in-situ values to model gas flow under reservoir conditions.

Structure of the Thesis

The research objectives will be fulfilled using a variety of analytical, numerical and experimental methods. The structure of the dissertation is outlined below.

Literature Review

Chapter 2 includes a literature review on different flow regimes encountered in gas flow. The prevalent theories to describe flow in each flow regime are reviewed. Several investigations into the influence of geomechanics on apparent permeability are summarized.

Flow Regime Analysis

Chapter 3 describes an analytical investigation, in order to find dominant flow regimes in low permeability porous media such as Shale gas. The analysis is done

by relating Knudsen number to tangible reservoir parameters, i.e. pressure and permeability. A discussion on the consequences of the findings is provided. This chapter has been published as part of a peer-reviewed journal article.

Analytical Model

In chapter 4, a new analytical model is proposed based on refining the erroneous Klinkenberg's assumptions and proposing a more accurate yet simple model to predict apparent permeability and pressure in the dominant flow regime. The derivation of the new model, assumptions, and limitations are outlined. A version of this chapter is published as a peer-reviewed journal article.

Laboratory Experiments

Chapter 5 includes the details of the laboratory experiments conducted in this work. Steady-state gas flow experiments are conducted at various mean pressures and rates on four shale/siltstone samples. Initially, the mean effective stress is fixed and the goal is to find the gas apparent permeability at different mean pressures in order to verify the model proposed in chapter 4. The tests are then conducted at several rates to investigate the rate dependency of permeability. In these tests the mean pressure and mean effective stress are held constant while pressure gradient across the core is changed. While the mean pressure and mean effective stress are constant, the Knudsen number is fixed, and change in pressure gradient will change Reynolds number (or flow rate). Apparent permeability is measured at fixed Knudsen numbers and different Reynolds numbers. These tests are designed to investigate the effect of Reynolds number (rate) as well as Knudsen number on the flow regime and apparent permeability in order to get a full picture of gas permeability in the reservoir. Approximately 225 permeability tests are conducted on one shale sample from Clearwater formation in Alberta and three siltstone samples from Montney formation. After the gas tests are completed the samples are saturated with water and liquid permeability is measured. Some of the lab tests are repeated at two

different mean effective stresses in order to study the influence of geomechanics on the flow model's parameters and the gas flow regime.

Laboratory experiments are continued by shearing the samples. After failure is reached, steady-state gas flow experiments are conducted on the failed sample the same manner as in the intact samples. The goal of these tests is to study the flow regime and the apparent permeability behavior with respect to Knudsen number and Reynolds number in fractures. Additionally, the pore pressure in sheared sample is lowered step by step while keeping stresses constant. At each step gas flow tests are conducted. This is to simulate the production phase of Shale gas reservoirs after hydraulic fracturing operation. Information on the samples, the laboratory setup, and test designs are provided in chapter 5. This chapter has been published as part of a peer-reviewed journal article.

Model Verification and Discussions

Chapter 6 provides a comprehensive discussion on the results of the tests outlined in chapter 5. The model proposed in chapter 4 is verified using the experimental results. The model parameters are evaluated for the present samples and other datasets in the literature. The laboratory results on the rate dependency of permeability are analyzed. The results indicate that apparent permeability increases with mass rate until it reaches a constant value. This phenomenon casts a shadow of doubt around the common non-steady-state permeability measurement methods and has never been discussed in shale gas reservoirs.

In addition to the rate dependency of permeability, the influence of several other parameters such as mean effective stress, temperature, gas type, and water saturation is investigated. A work flow is presented to capture the influence of several parameters such as mean effective stress, rate and water saturation on the apparent permeability, considering the flow regime. Using the proposed methodology, the permeability measurements on dry samples under lab conditions can be converted to the permeability of the in-situ rock under the reservoir effective

stress and water saturation. Additionally, the new approach enhances the analysis of permeability tests to calculate important parameters such as the effective stress coefficient for permeability (similar to Biot coefficient), and relative permeability values. Based on the results of this work, recommendations are made on designing more representative gas permeability lab tests. This chapter has been published as part of a peer-reviewed journal article.

Appendices

Appendix A and Appendix C outline the derivation of Eq. 17 and Eq. 52, respectively. A summary of the experimental data is provided in Appendix B.

References

Amann-Hildenbrand, A., Ghanizadeh, A., Krooss, B.M., 2012. Transport Properties of Unconventional Gas Systems. *Marine and Petroleum Geology* 31, 90-99.

Baihly, J.D., Malpani, R., Altman, R., Lindsay, G., and Clayton, R., 2015. Shale Gas Production Decline Trend Comparison Over Time and Basins—Revisited. Paper SPE 135555 presented at the SPE Unconventional Resources Technology Conference, San Antonio, Texas, USA, 20-22 July.

Bustin, A.M.M., Bustin, R.M., 2012. Importance of Rock Properties on the Producibility of Gas Shales. *International Journal of Coal Geology*, 103, 132-147.

Chalmers, G.R.L., Ross, D.J.K., Bustin, R.M., 2012. Geological controls on matrix permeability of Devonian Gas Shales in the Horn River and Liard basins, northeastern British Columbia, Canada. *International Journal of Coal Geology* 103, 120-131.

Craft, B.C, Hawkins, M., Terry, R.E. 1991. *Applied Petroleum Reservoir Engineering*. Second edition, Prentice Hall, Inc.

Jones, F.O., Owens, W.W., 1980. A Laboratory Study of Low Permeability Gas Sands. *Journal of Petroleum Technology* 32, 1631-1640.

Kalantari-Dahaghi, A., Mohaghegh, S.D., 2011. Numerical Simulations and Multiple Realizations for Sensitivity Study of Shale Gas Reservoir. Paper SPE 141058 presented at the 2011 SPE Productions and Operations Symposium, Oklahoma City, Oklahoma, USA, 27-29 March.

Klinkenberg, L.J 1941. The permeability of porous media to liquids and gases. *API Drilling and Production Practice*, 200-213.

Kundt, A., Warburg, E., 1875. *Poggendorfs Ann. Physik* 155, 337 and 525.

Swami, V., Settari, A., 2012. A pore scale gas flow model for shale gas reservoir. Paper SPE 155756-MS presented at 2012 SPE Americas Unconventional Resources Conference, Pittsburgh, Pennsylvania, USA, 5-7 June.

Tanikawa W., Shimamoto, T., 2009. Comparison of Klinkenberg-Corrected Gas Permeability and Water Permeability in Sedimentary Rocks. *International journal of Rock Mechanics & Mining Sciences* 46, 229-238.

Chapter 2: Literature Review

Unconventional hydrocarbon reservoirs have become a major contributor to the world's energy supplies. Shale gas reservoirs comprise 30% of the current gas production in the United States with over 40,000 producing wells over 20 states (Rivard et al., 2013). Production is expected to increase up to 50% by 2040 (Annual Energy Outlook 2013). The recoverable reserves of gas and oil from shales have been estimated to be large enough to free the United States from oil and gas imports and almost replace all coal-generated electricity (Soeder, 2013). Currently, Canada only produces 5% of its natural gas from Shale gas reservoirs. This is estimated to increase to 28% by 2035. Canada has an estimated 222 Tcf of natural gas in Shale gas reservoirs. Horn River basin in northeast British Columbia is the most developed Shale gas reserve in Canada and has an estimated 78 Tcf of natural gas as of 2012 (Canada's Energy Future 2013). Utica Shale and Horton Bluff are two known Shale plays in eastern Canada that are in early stages of assessment. Besides North America, Pilots and extensive studies have started in United Kingdom, Germany, Poland, China, Argentina, etc. Fig. 2 illustrates natural gas production history and projections for the United States, Canada, Europe and China.

Typically, the gas bearing unconventional reserves such as Shale gas, tight gas and Coalbed Methane have very low matrix permeability. Primary production with such permeability is not economical. This has made hydraulic fracturing and horizontal drilling a necessary part of the industry which paved the way to economical production from unconventional reservoirs.

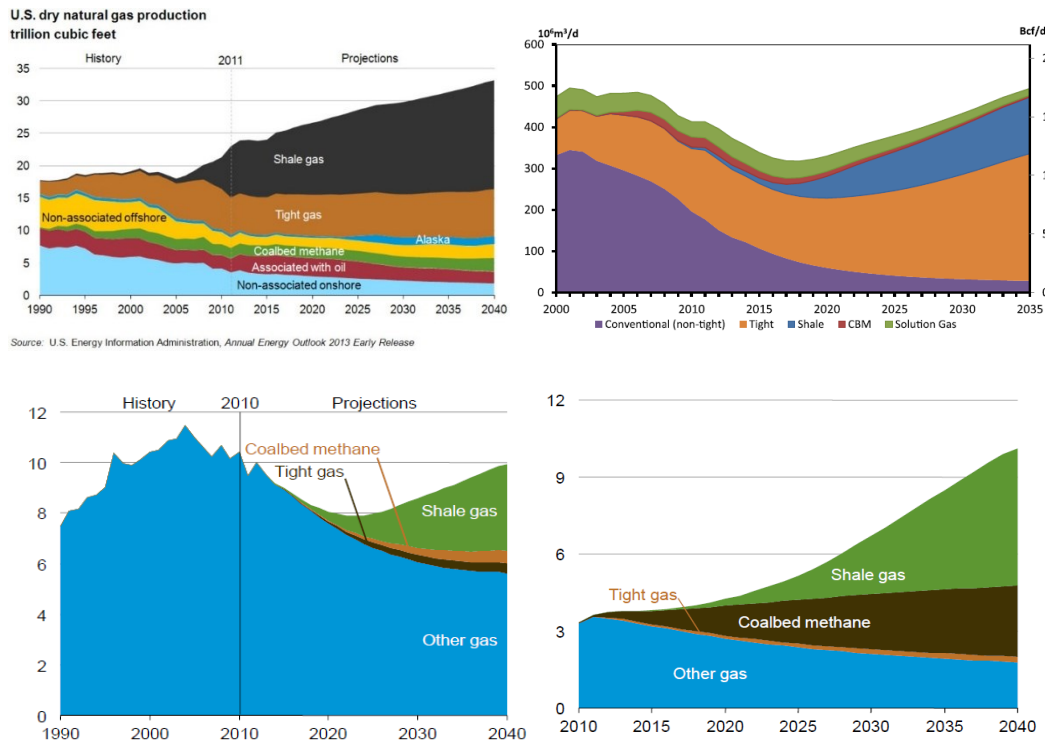


Fig. 2: Gas production history and projections for different regions. Top left: Natural gas production in the United States. Top right: Natural gas production in Canada. Bottom left: Natural gas production in Europe. Bottom right: Natural gas production in China. Gas volume are demonstrated in Tcf (Trillion Cubic Foot) unless mentioned otherwise (Annual Energy Outlook 2013; Canada's Energy Future 2013; World's Energy Outlook 2013).

The goal of hydraulic fracturing is to create fractures that act as a conduit for gas to flow into the wellbore. This translates to a higher contact area with the gas bearing rock. The contact area is further increased by drilling long horizontal wells. The production response to hydraulic fracturing is an initial rise in flow rate followed by a rapid decline until it reaches a relatively constant production rate. A successful hydraulic fracturing operation creates a large fracture area as far as possible into the reservoir maximizing the stimulated reservoir volume (SRV). However, it is the matrix permeability that dominates the long term production and recovery in the reservoir (Bustin and Bustin, 2012; Chalmers et al., 2012; Swami and Settari, 2012; Amann-Hildenbrand, 2012).

Gas Flow Regime and Permeability

Accurate measurement of permeability is necessary in order to model reservoir production and estimate recoveries. Matrix permeability measurements are typically done in the lab. Under the extremely low permeability condition for unconventional gas reservoirs the permeability measurements are done using gas as the flowing fluid. However, analysis of gas permeability measurements requires extra care for effects such as slippage (Ghanizadeh et al., 2014). The measured values of gas permeability are typically higher than the liquid permeability for the same rock. This enhancement of gas permeability over liquid permeability is attributed to the slippage effect (or flow regime effect), which changes with the gas pressure. Therefore, in order to have a representative permeability value for a rock, liquid or absolute permeability values are more suitable. The absolute permeability values are then converted to gas permeability at various pressures using appropriate models. Generally, the lower the absolute permeability and lower the pressure, the higher the permeability enhancement due to flow regime becomes (Ziarani and Aguilera, 2012). In addition to the state-of-the-art equipment necessary to measure the permeability of the cores, selecting the correct mathematical model to describe the flow behaviour is essential. Numerous articles have been published on gas flow models in low permeability porous media in recent years (Javadpour et al., 2007; Darabi et al., 2012; Cipolla et al., 2010; Freeman et al., 2011; Cui et al., 2009; Roy et al., 2003; Civan, 2010; Beskok and Karniadakis, 1999; Moghadam and Chalaturnyk, 2014). The first step in selecting the best model for gas flow is to recognize the flow regime. Flow regime in gas is known to be a function of rarefaction of gas molecules. Closer the gas molecules together (high density) compared to the pore size, flow is continuum. As pressure is decreased, the gas molecules will be further away or rarefied, and the flow approaches non-continuum flow or molecular behaviour. In continuum flow the gas can be looked at as a bulk continuous stream where macroscopic properties are solved while ignoring molecular interactions. In molecular approach the molecules are far apart and have

little to no effect on one another (Rahmanian et al., 2013). Computational techniques and models for the continuum and molecular approach are very different which makes the flow regime an important factor.

Knudsen Number

Knudsen number is a dimensionless number named after Danish physicist Martin Knudsen (1871-1949) which is a measure of rarefaction of gas molecules and therefore used to distinguish flow regimes in gas flow. Knudsen number is defined as the ratio of mean free path of the gas molecules (a measure of distance between molecules) over the size of the pore which is illustrated in Eq. 1.

$$kn = \frac{\lambda}{r_{pores}} \quad \text{Eq. 1}$$

λ is the mean free path of the gas and r_{pores} represents the average pore radius. Mean free path is calculated according to Eq. 2 (Loeb, 1934).

$$\lambda = \frac{k_B T}{\sqrt{2} \pi \delta^2 P} \quad \text{Eq. 2}$$

Where k_B is the Boltzmann constant (1.381×10^{-23} J/K), P is pressure, δ is the diameter of the gas molecules and T represents the fluid temperature.

A challenging task to find Knudsen numbers is to have a representative value for pore radius. Average pore dimensions are seldom measured in porous media. However, Permeability and porosity are generally taken to be a representation of the pore dimensions. There are several correlations relating permeability and porosity of the porous media to average pore radius (Ziarani and Aguilera, 2012; Heid et al., 1950; Kolodzie, 1980; Aguilera, 2002). Here in order to calculate Knudsen number we adopted the correlation proposed by Kolodzie (1980) as shown by Eq. 3.

$$r_{pores} = 5.395 \times 10^{-6} \left(\frac{k^{0.588}}{(100\phi)^{0.864}} \right) \quad \text{Eq. 3}$$

r_{pores} is the average pore radius in meters, k is the routine air permeability in mDarcy and ϕ is porosity. Eq. 3 is based on experimental data from several formations with various lithologies throughout the United States. According to Eq. 1, Eq. 2, and Eq. 3 under isotherm conditions, the Knudsen number changes with pressure and permeability (and to a lesser extent porosity). A high Knudsen value indicates that the distance between gas molecules is comparable to the pore dimension resulting in a rarefied gas.

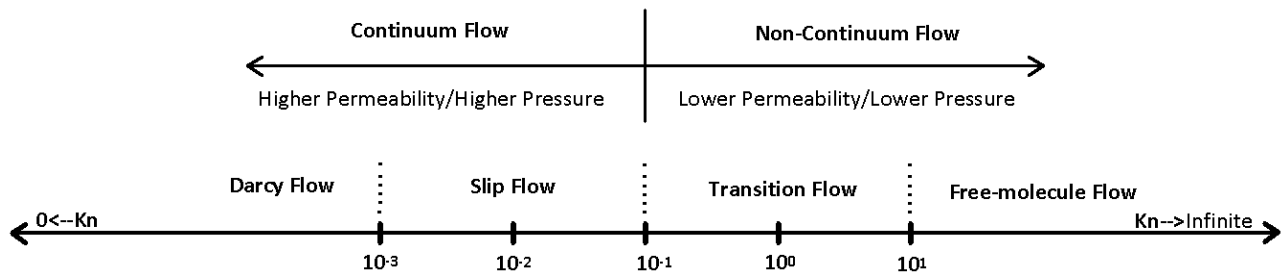


Fig. 3: Flow regime characterization based on Knudsen number. Gas permeability enhancement (permeability of gas divided by the absolute or liquid permeability) is the highest at the free-molecule flow regime. It then decreases in the transition and slip flow regime until the enhancement disappears at Darcy flow regime.

Gas flow regime is characterized according to the Knudsen number magnitude as illustrated in Fig. 3. Lower Knudsen numbers represent a formation with higher permeability or higher pore pressure and high Knudsen number values indicate a tight formation or a low pressure condition. Gas permeability enhancement (permeability of gas divided by the absolute or liquid permeability) is the highest at the free-molecule flow regime. It then decreases in the transition and slip flow regime until the enhancement disappears at the Darcy flow regime (Darabi et al., 2012; Ziarani and Aguilera, 2012). A description of each flow regime is presented in the following.

Darcy Flow Regime

Darcy flow regime sometimes referred to as laminar or viscous flow regime is dominant at Knudsen values below 0.001. This is the most typical flow regime in porous media dominant in almost all conventional reservoirs. Darcy equation (Eq. 4) is the most well known model, governing flow of gases and liquids under laminar flow regime. The equation is derived from the classic Navier-Stokes equation by using an averaging method (Whitaker, 1986). The model only applies to continuum flow regime with no inertial effects.

$$-\frac{\partial p}{\partial x} = \frac{\mu}{k} v \quad \text{Eq. 4}$$

The applicability of this equation has been proven over a wide range of conditions (Craft, 1991). In Eq. 4, it is an acceptable assumption that permeability is a constant rock property.

Inertial Flow

As the gas velocity increases the assumption of fully laminar flow is jeopardized. Inertial forces become significant and flow deviates from Darcy equation. This flow regime is commonly referred to as inertial flow. Forchheimer (1901) proposed a quadratic equation to describe this flow regime, indicated in Eq. 5.

$$-\frac{\partial p}{\partial x} = \frac{\mu}{k} v + \beta \rho v^2 \quad \text{Eq. 5}$$

β is the non-Darcy coefficient. The right hand side of the Forchheimer equation (Eq. 5) has two terms. The left term represents viscous flow, as in the Darcy equation. The right term represents the deviation from viscous flow, which leads to a greater pressure drop with the same flow rate. Several authors have studied the non-Darcy coefficient. Recent studies relate non-Darcy flow to inertial forces, explaining the extra pressure drop with the loss of energy due to the continuous compression and expansion of the gas as it moves through the pores with different diameters (Friedel and Voigt, 2006). This energy loss presents itself as the extra pressure drop term in the Forchheimer equation. Since there is a square of velocity term in the second term

it shows that this inertial effect is significant at high velocities. Several correlations are proposed relating the non-Darcy coefficient to rock properties such as permeability, porosity, tortuosity, etc (Belhaj et al., 2003; Li et al., 2002). Comparing these correlations it is evident that the most important factor in all of them is permeability. Therefore the velocity of gas and permeability of the medium are the determining factors of applicability of non-Darcy flow.

There have been debates about the empirical or analytical nature of Forchheimer's equation (Huang and Ayoub, 2008; Ruth and Ma, 1992). Recently, Barree and Conway (2004) have pointed out the shortcomings of the Forchheimer equation and proposed a new equation to account for inertial flow. Their work was further confirmed by Lai et al. (2012). If the velocity increases further, the inertial flow will turn into fully turbulent flow. The quadratic part of the Forchheimer's equation has been proposed to be suitable to describe fully turbulent flow (Ezeudembah and Dranchuk, 1982). There are discrepancies around the transition from Darcy to inertial flow among researchers (Seguin et al., 1998a; Seguin et al., 1998b; Comiti et al., 2000). The transition from Darcy to non-Darcy is described by a critical Reynolds number above which the inertial and turbulent effects emerge. Difficulty arises in definition of Reynolds number for a porous medium. There are several definitions of Reynolds number used in the literature (Seguin et al., 1998a). Zeng and Grigg (2006) proposed a new Reynolds number using Forchheimer's inertial parameter multiplied by permeability as a length scale of the porous media. The simplest form of the Reynolds number equation is adopted in this work presented as Eq. 6.

$$Re = \frac{\rho v d_p}{\mu} \quad \text{Eq. 6}$$

In Eq. 6, ρ is the gas density, v is the mean velocity in a pore, d_p is the average pore diameter and μ is the gas viscosity. While Darcy flow is most common in fluid flow through conventional porous media, inertial flow usually occurs in fractures or near high flow rate gas wells.

Slip Flow Regime

Slip flow regime occurs when Knudsen number is in range of 0.001-0.1. At this range the dimensions of the pores are comparable to mean free path of the molecules but still a few orders of magnitude larger. Continuum flow is still dominant but the classic assumption of zero velocity at the pore walls start to fail. Molecules will have a non-zero velocity at the pore walls which is called slip velocity. This phenomenon, called the slippage effect (or sometimes referred to as Klinkenberg effect), causes gas molecules to accelerate, as there is less drag, or no stationary layer to slow them. This acceleration shows itself as an apparent increase in system permeability. A higher Knudsen number (up to 0.1) leads to a more significant slip effect or a larger permeability enhancement. In a specific formation or core with a certain permeability, pressure changes the Knudsen number. Lower pressure leads to higher Knudsen number and hence higher apparent permeability. This results in a change in apparent gas permeability with mean pressure which is confirmed through a plethora of lab experiments in the literature. In terms of flow models, typically conventional continuum flow models (i.e. Darcy equation) are used with some modifications in order to take the permeability enhancement into account. Klinkenberg (1941) presented the following correction on the gas permeability:

$$K_a = K_0 \left(1 + \frac{b}{\bar{P}} \right), \quad \text{Eq. 7}$$

where K_a is the apparent gas permeability, K_0 is the absolute permeability (liquid permeability), \bar{P} is the average pressure, and b is the slope of the straight line of the plot of K_a versus the reciprocal of the average pressure. Parameter b depends on the fluid and the rock structure and is calculated using a correlation or measured in the lab. In order to calculate pressure or rate considering slip flow, apparent permeability in Eq. 7 simply replaces the permeability in Darcy equation (Eq. 4). Another use of Eq. 7 is to find the correct permeability of the porous media in gas permeability tests. The permeability obtained using gas as flowing fluid is apparent

permeability and higher than the absolute (liquid) permeability. Apparent permeability will change with mean pressure and according to Eq. 7 it follows a straight line. The intercept of the straight line of the plot of apparent permeability with the reciprocal of mean pressure is taken to be the absolute permeability (Wu et al., 1998; Klinkenberg, 1941)

At typical reservoir pressures in conventional reservoirs, the apparent permeability is very close to the absolute permeability, and the slippage effect is negligible. On the other hand, laboratory flow experiments are usually done at lower pressures than those present in typical gas reservoirs, and the slippage effect is significant and needs to be considered. Li et al. (2009) showed that the presence of a backpressure in the flow system reduces the Klinkenberg effect, and proposed a correlation for the minimum backpressure required to avoid the slippage effect. According to their results for reservoirs with permeability in the order of one millidarcy, the typical backpressures in the gas wells are sufficient to negate the slippage effect. As permeability in tight gas and shale gas reservoirs is lower than one millidarcy, slippage effects may need to be considered in calculations, even at the reservoir scale.

Several correlations based on lab experiments have been proposed for b in Eq. 7 (Heid et al., 1950; Jones and Owens, 1980; Sampath and Keighin, 1982, Florence et al., 2007; Tanikawa and Shimamoto, 2009). b is generally taken to be a function of absolute permeability (and in some cases porosity) and to a lesser extent the type of gas. Throughout the literature there is evidence of deviations from Eq. 7 (Noman, et al., 1990; Dong et al., 2012; Sampath and Keighin, 1982; Jones and Owens, 1980; Klinkenberg, 1941; Li et al., 2009; Rushing et al., 2004; Fathi et al., 2012; Macini et al., 2011; Wu et al., 1988) with most reporting a deviation from the Klinkenberg straight-line plot, especially in low-permeability cores. Jones and Owens (1980) conducted a series of experiments on low-permeability gas sands. While they got reasonable straight lines in Klinkenberg plots, they noticed an overestimation of absolute permeability of up to 25%. Fathi et al. (2012) ran Lattice-Boltzmann based simulations of gas dynamics, illustrated a deviation from the straight line, and

proposed an empirical quadratic equation to match their results. Li et al. (2009) also observed a deviation from the linear Klinkenberg correlation for low-permeability cores, and concluded that the correlation overestimates the absolute permeability of low-permeability reservoirs. Similar results are observed in the data published by Rushing et al. (2004) and Tanikawa and Shimamoto (2009).

Klinkenberg (1941) anticipated deviations from the straight line due to the assumption of constant velocity gradient in his work. According to his work the value of b is not a constant and should increase with pressure. However, in his experiments the permeability was high enough for the assumption to hold. Jones and Owens (1980) acknowledged that the deviations are due to the departure from Warburg's (1875) model caused by the constant velocity gradient assumption. Li et al. (2009) discussed that the deviations emerge since unlike Klinkenberg's assumption, the mean free path is not strictly inversely proportional to pressure.

Transition Flow Regime

Transition flow regime occurs when Knudsen number is in the range of 0.1-10. This flow regime is a transition between continuum and non-continuum flow regimes. Fundamentally, both continuum slip flow and diffusion flow occur at the same time and both need to be considered. The higher the Knudsen number the more dominant diffusion will get. Several approaches have been proposed in order to model flow in this regime. Darcy model with Knudsen correction have shown questionable results (Ziarani and Aguilera, 2012). Models have been proposed combining Knudsen diffusion and Darcy flow with slip correction (Javadpour, 2009; Rahmanian et al., 2013; Darabi et al., 2012; Sakhaee-Pour and Bryant, 2012; Civan, 2010). Another approach has been proposed implementing shear stress laws in Navier-Stokes equations along with higher order boundary conditions for velocity to predict results of the Monte Carlo simulations (Karniadakis et al., 2005). While these models can capture some of the physics governing flow in transition regime it comes at a price of large number of parameters and higher computing cost.

Free-molecule Flow Regime

Free-molecule flow regime occurs at high Knudsen numbers (above 10). This condition is relevant to very low pressure conditions (such as ambient pressure). At this condition the flow is non-continuum with molecules having minimum interaction to neighbouring molecules and continuum flow equations fully break down. Typically the flow is thought to follow Knudsen diffusion equation which relates mass flux to density gradient of gas molecules. Other approaches such as Molecular Dynamics (MD) and Lattice-Boltzmann method (LBM) have been gaining attention recently (Fathi et al., 2012; Gad-el-Hak, 1999). However, these methods have not yet found practical application in large scale flow modelling (Mao and Sinnot, 2001).

It is therefore clear that the dominant gas flow regime must be determined in order to analyze gas permeability lab results and simulate gas flow in reservoir condition. The flow regime governs the physics of flow and indicates the applicable model to be used in the analyses. Generally, the influence of flow regime acts as an enhancement of apparent permeability compared to that of liquid or Darcy permeability. This work aims to create a guideline to determine the governing flow regime under laboratory and reservoir conditions.

Influence of Geomechanics on Apparent Permeability

Several phenomena influence shale reservoir matrix permeability. As discussed, flow regime (slip flow) can increase apparent permeability by a few orders of magnitude. However, stress on rock is also a determinant of permeability magnitude. Typically, permeability is related to an effective stress parameter. Terzaghi first introduced the concept of effective stress in 1925. Since then, numerous publications have shown permeability of porous media to be a function of mean effective stress (Warpinski and Tuefel, 1992; Heller et al., 2014; Ghanizadeh et al., 2014; Bernabe, 1987; Berryman, 1992; Zoback and Byerlee,

1975; Kwon et al., 2001). Eq. 8 shows the most basic definition of mean effective stress (assuming isotropic stress).

$$\sigma_{\text{eff}} = \sigma_c - P \quad \text{Eq. 8}$$

In its simplest form, effective stress is the difference between confining stress on rock and fluid pressure in pores. According to the effective stress principle, rock properties such as permeability, porosity, and volumetric strain are functions of the effective stress on the rock, regardless of confining stress and pore pressure values. However, it has been observed that some rocks are less sensitive to pore pressure than to stress changes. Eq. 9 more completely represents effective stress for this class of materials.

$$\sigma_{\text{eff}} = \sigma_c - \chi P \quad \text{Eq. 9}$$

The value of χ (commonly called “Biot’s coefficient” in poroelasticity) is generally less than or equal to unity for conventional reservoir rocks such as sandstones and carbonates. At $\chi = 1$, Eq. 9 is equivalent to Eq. 8. Kwon et al., (2001) measured the χ values for Wilcox shale and observed that χ is approximately equal to one. Heller et al. (2014) investigated the magnitude of χ on shale samples from Barnett, Eagle Ford, Marcellus, and Montney. They obtained values for χ in the range of 0.15 to 0.85. The measurements by Heller et al. (2014) were made using helium as the flowing fluid. Permeability was measured at high pressures and slip flow effects were neglected in calculating χ . Kwon et al. (2001), on the other hand, used water to measure χ values. For the purpose of calculating mean effective stress in this work, the present study takes χ to be equal to unity, relying on the findings by Kwon et al. (2001).

The range of Knudsen numbers in the reservoir or laboratory environment dictates the relevant flow regime and flow model. The Knudsen number depends on pressure and permeability. Therefore, any changes in reservoir pressure and permeability can induce a change in gas flow regime. As mean effective stress increases, permeability of the porous medium decreases. Therefore, a change in mean effective stress can change Knudsen number which, in turn, can trigger a flow

regime change. Mean effective stress also influences fracture permeability, resulting in a change in Knudsen number. Additionally, changes in effective stress can impose shear stresses that may generate shear fractures, increasing the permeability (e.g. in hydraulic fracturing operations). This permeability change induces a change in Knudsen number and flow regime. No previous research was found on the direct effect of geomechanics on gas flow regime. There are two classes of studies on shale permeability change in the literature. First, there are the studies that focus on measuring gas permeability with respect to mean effective stress without or with little consideration for flow regime (Bustin et al., 2008; Ghanizadeh et al., 2014; Kwon et al., 2001; Reyes and Osisanya, 2002). Second, there is the considerable work that has been done on the change of apparent permeability with pore pressure as mentioned previously (Javadpour, 2009; Rahmanian et al., 2013; Darabi et al., 2012; Klinkenberg, 1941). Permeability changes with both pore pressure and mean effective stress. Mean effective stress can also change the flow regime and the related slip flow parameters. The interrelated influence of flow regime and mean effective stress on permeability is investigated in this work.

References

Aguilera, R., 2002. Incorporating capillary pressure, pore throat aperture radii, height above free water table and Winland r_{35} values on Pickett plots. AAPG Bulletin 86, 605–624.

Amann-Hildenbrand, A., Ghanizadeh, A., Krooss, B.M., 2012. Transport Properties of Unconventional Gas Systems. Marine and Petroleum Geology 31, 90-99.

Barree, R.D., Conway, M.W., 2004. Beyond Beta Factors: A Complete Model for Darcy, Forchheimer, and Trans-Forchheimer Flow in Porous Media. Paper SPE 89325 presented at the SPE Annual Technical Conference and Exhibition, Houston, 26-29 September.

Belhaj, H.A., Agha, K.R., Nouri, A.M., Butt, S.D. and Islam, M.R., 2003. Numerical and Experimental Modeling of Non-Darcy Flow in Porous Media. Paper SPE 81037 presented at the SPE Latin American and Caribbean Petroleum Engineering Conference, Port-of-Spain, Trinidad and Tobago, 27-30 April.

Bernabe, Y., 1987. The Effective Pressure Law for Permeability During Pore Pressure and Confining Pressure Cycling of Several Crystalline Rocks. *Journal of Geophysical Research* 92, 649-657.

Berryman, J.G., 1992. Effective Stress for Transport Properties of Inhomogeneous Porous Rock. *Journal of Geophysical Research* 97, 17409-17424.

Beskok, A., Karniadakis, G.E., 1999. A model for flows in channels, pipes, and ducts at micro and nano scales. *Nanoscale and Microscale Thermophysical Engineering* 3, 43–77.

Bustin, A.M.M., Bustin, R.M., 2012. Importance of Rock Properties on the Producibility of Gas Shales. *International Journal of Coal Geology*, 103, 132-147.

Bustin, R.M., Bustin, A.M.M., Cui, A., Ross, D., and Pathi, V.M., 2008. Impact of shale properties on pore structure and storage characteristics. Paper SPE 119892-MS presented at the SPE Shale Gas Production Conference, Fort Worth, Texas, USA.

Chalmers, G.R.L., Ross, D.J.K., Bustin, R.M., 2012. Geological controls on matrix permeability of Devonian Gas Shales in the Horn River and Liard basins, northeastern British Columbia, Canada. *International Journal of Coal Geology* 103, 120-131.

Cipolla, C. L., Lolon, E. P., Erdle, J. C., Rubin, B., 2010. Reservoir Modeling in Shale-Gas Reservoirs. *SPE Reservoir Evaluation & Engineering* 13 (04), 638-653.

Civan, F., 2010. Effective correlation of apparent gas permeability in tight porous media. *Transport in Porous Media* 82, 375–384.

Comiti, J., Sabiri, N.E., Montillet, A., 2000. Experimental characterization of flow regimes in various porous media — III: limit of Darcy's or creeping flow regime for Newtonian and purely viscous non-Newtonian fluids. *Chemical Engineering Science* 55(15), 3057-3061.

Craft, B.C, Hawkins, M., Terry, R.E. 1991. *Applied Petroleum Reservoir Engineering*. Second edition, Prentice Hall, Inc.

Cui, X., Bustin, A.M., and Bustin, R., 2009. Measurements of Gas Permeability and Diffusivity of Low-permeability Reservoir Rocks: Different Approaches and Their Applications. *Geofluids* 9, 208-223.

Darabi, H., Etehad, A., Javadpour, F., Sepehrnoori, K., 2012. Gas Flow in Ultra-Tight Shale Strata. *Journal of Fluid Mechanics* 710, 641-658.

Dong, M., Li, Z., Li, S., Yao, J., 2012. Permeabilities of Tight Reservoir Cores Determined for Gaseous and Liquid CO₂ and C₂H₆ Using Minimum Backpressure Method. *Journal of natural Gas Science and Engineering* 5, 1-5.

Ezeudembah, A.S. and Dranchuk, P.M., 1982. Flow Mechanism of Forchheimer's Cubic Equation in High-Velocity Radial Gas Flow Through Porous Media. Paper SPE 10979 presented at the SPE Annual Technical Conference and Exhibition, NewOrleans, 26-29 September.

Fathi, E., Tinni, A., Akkutlu, Y., 2012. Correction to Klinkenberg Slip Theory for Gas Flow in Nano-capillaries. *International Journal of Coal geology* 103, 51-59.

Florence, F.A., Rushing, J.A., Newsham, K.E., Blasingame, T.A., 2007. Improved permeability prediction relations for low permeability sands. Paper SPE 107954 presented at the 2007 SPE Rocky Mountain Oil and Gas Technology Symposium, Denver, Apr 16–18.

Forchheimer, P. 1901. Wasserbewegung durch Boden. *Zeitz ver Deutch Ing.*, 45, 1781-1788.

- Freeman, C.M., Moridis, G.J., Blasingame, T.A., 2011. A Numerical Study of Microscale Flow Behavior in Tight Gas and Shale Gas Reservoir Systems. *Transport in Porous Media* 90(1) 253-268.
- Friedel, T., Voigt, H.D., 2006. Investigation of non-Darcy flow in tight-gas reservoirs with fractured wells. *Journal of Petroleum Science and Engineering* 54(3-4), 112-128.
- Gad-el-Hak, M., 1999. The Fluid Mechanics of Microdevices-The Freeman Scholar Lecture. *Journal of Fluids Engineering* 121, 5-33.
- Ghanizadeh, A., Gasparik, M., Amann-Hildenbrand, A., Gensterblum, Y., Krooss, B.M., 2014. Experimental study of fluid transport processes in the matrix system of the European organic-rich shales: I. Scandinavian Alum Shale. *Marine and Petroleum Geology* 51, 79-99.
- Heid, J.G., McMahon, J.J., Nielsen, R.F., Yuster, S.T., 1950. Study of the Permeability of Rocks to Homogenous Fluids. *API Drilling & Production Practice*, New York 230–246.
- Heller, R., Vermynen, J., Zoback, M., 2014. Experimental Investigation of Matrix Permeability of Gas Shales. *AAPG Bulletin* 98 (5), 975-995.
- Huang, H., Ayoub, J. A., 2008. Applicability of the Forchheimer Equation for Non-Darcy Flow in Porous Media. *SPE Journal* 13(01), 112-122.
- International Energy Agency, 2013. *World's Energy Outlook 2013*. November 213.
- Javadpour, F., 2009. Nanopores and Apparent Permeability of Gas Flow in Mudrocks (Shales and Siltstone). *Journal of Canadian Petroleum Technology* 48, 16-21.
- Javadpour, F., Fisher, D., Unsworth, M., 2007. Nanoscale Gas Flow in Shale Gas Sediments. *Journal of Canadian Petroleum Technology* 46.

Jones, F.O., Owens, W.W., 1980. A Laboratory Study of Low Permeability Gas Sands. *Journal of Petroleum Technology* 32, 1631-1640.

Karniadakis, G., Beskok, A., Aluru, N., 2005. *Microflows and Nanoflows: Fundamentals and Simulation*, Vol. 29. New York: Interdisciplinary Applied Mathematics, Springer.

Klinkenberg, L.J 1941. The permeability of porous media to liquids and gases. *API Drilling and Production Practice*, 200-213.

Kolodzie, J.S., 1980. Analysis of pore throat size and use of the Waxman–Smits equation to determine OOIP in Spindle field, Colorado. Paper SPE 9382-MS presented at SPE 55th Annual Technical Conference and Exhibition, Dallas, Sep 21–24.

Kundt, A., Warburg, E., 1875. *Poggendorfs Ann. Physik* 155, 337 and 525.

Kwon, O., Kronenberg, A.K., Gangi, A.F., 2001. Permeability of Wilcox Shale and its Effective Pressure Law. *Journal of Geophysical Research* 106 (B9), 19339-19353.

Lai, B., Miskimins, J. L., Wu, Y.-S., 2012. Non-Darcy Porous-Media Flow According to the Barree and Conway Model: Laboratory and Numerical-Modeling Studies. *SPE Journal* 17(01), 70-79.

Li, D., 2002. Analytical Study of the Wafer Non-Darcy Flow Experiments. Paper SPE 76778 presented at the SPE Western Regional/AAPG Pacific Section Joint Meeting, Anchorage, Alaska, 20-22 May.

Li, S., Dong, M., Li, Z., 2009. Measurement and Revised Interpretation of Gas Flow Behaviour in Tight Reservoir Cores. *Journal of Petroleum Science and Engineering* 65, 81-88.

Loeb, L.B. 1934. *The Kinetic Theory of Gases*. Second edition, McGraw-Hill Co., Inc.

- Macini, P., Mesini, E., Viola, R., 2011. Laboratory measurements of non-Darcy flow coefficients in natural and artificial unconsolidated porous media. *Journal of Petroleum Science and Engineering* 77 (3-4), 365-374.
- Mao, Z., Sinnott, S.B., 2001. Separation of organic molecular mixtures in carbon nanotubes and bundles: Molecular dynamic simulations. *Journal of Physical Chemistry* 105, 6916-6924.
- Moghadam, A.A., Chalaturnyk, R., 2014. Expansion of the Klinkenberg's slippage equation to low permeability porous media. *International Journal of Coal Geology* 123, 2-9.
- National Energy Board, 2013. Canada's Energy Future 2013. November 2013.
- Noman, R. and Kalam, M.Z. 1990. Transition from Laminar to Non-Darcy Flow of Gases in Porous Media. In *Advances in Core Evaluation: Accuracy and Precision in Reserves Estimation*. Edited by P.F. Worthington, 447-482.
- Rahmanian, M., Aguilera, R., & Kantzas, A., 2013. A New Unified Diffusion--Viscous-Flow Model Based on Pore-Level Studies of Tight Gas Formations. *SPE Journal* 18(01), 38-49.
- Reyes, L., Osisanya, S.O., 2002. Empirical Correlation of Effective Stress Dependant Shale Rock Properties. *Journal of Canadian Petroleum Technology* 41(12).
- Rivard, C., Lavoie, D., Lefebvre, R., Sejourne, S., Lamontagne, C., Duchesne, M., 2014. An overview of Canadian shale gas production and environmental concerns. *International Journal of Coal Geology* 126, 64-76.
- Roy, S., Raju, R., Chuang, H.F., Cruden, B.A., Meyyappan, M., 2003. Modeling gas flow through microchannels and nanopores. *Journal of Applied Physics* 93, 4870-4879.

Rushing, J.A, Newsham, K.E., Lasswell, P.M., Cox, J.C. and Blasingame, T.A. 2004. Klinkenberg-Corrected Permeability Measurements in Tight Gas Sands: Steady-State Versus Unsteady-State Techniques. Paper SPE 89867 presented at the 2004 SPE Annual Technical Conference and Exhibition, Houston, Texas, 26-29 September.

Ruth, D., Ma, H., 1992. On the derivation of the Forchheimer equation by means of the averaging theorem. *Transport in Porous Media* 7(3), 255-264.

Sakhaee-Pour, A., Bryant, S., 2012. Gas Permeability of Shale. *SPE Reservoir Evaluation & Engineering* 15(04) 401-409.

Sampath, K., Keighin, C.W., 1982. Factors Affecting Gas Slippage in Tight Sandstones of Cretaceous Age in the Uinta Basin. *Journal of Petroleum Technology* 34, 2715-2720.

Seguin, D., Montillet, A., and Comiti, J., 1998a. Experimental characterisation of flow regimes in various porous media—I: limit of laminar flow regime. *Chemical Engineering Science* 53(21), 3751-3761.

Seguin, D., Montillet, A., Comiti, J., and Huet, F., 1998b. Experimental characterisation of flow regimes in various porous media—II: Transition to turbulent regime. *Chemical Engineering Science* 53(22), 3897-3909.

Soeder, D., 2013. Groundwater protection during shale gas development. Abstract, Americana, Salon international des technologies environnementales, 19-21 mars 2013, Montreal, Quebec, Canada.

Swami, V., Settari, A., 2012. A pore scale gas flow model for shale gas reservoir. Paper SPE 155756-MS presented at 2012 SPE Americas Unconventional Resources Conference, Pittsburgh, Pennsylvania, USA, 5-7 June.

Tanikawa W., Shimamoto, T., 2009. Comparison of Klinkenberg-Corrected Gas Permeability and Water Permeability in Sedimentary Rocks. *International journal of Rock Mechanics & Mining Sciences* 46, 229-238.

Terzaghi, K., 1925. Principles of Soil Mechanics. Engineering News Record 95, 987-996.

U.S. Energy Information and Administration, 2013. Annual Energy Outlook 2013 with projections to 2040. April 2013.

Warpinski, N.R., and Teufel, L.W., 1992. Determination of the Effective-Stress Law for Permeability and Deformation in Low-Permeability Rocks. SPE Formation Evaluation 7, 123-131.

Whitaker, S., 1986. Flow in porous media I: A theoretical derivation of Darcy's law. Transport in Porous Media 1, 3–35.

Wu, Y.S., Pruess, K., Persoff, P., 1998. Gas flow in porous media with Klinkenberg effects. Transport in Porous Media 32, 117–137.

Zeng, Z., Grigg, R., 2006. A criterion for non-Darcy flow in porous media. Transport in Porous Media 63(01), 57-69.

Ziarani, A.S., Aguilera, R., 2012. Knudsen's permeability correction for tight porous media. Transport in Porous Media 91(1), 239-260.

Zoback, M.D., and Bayerlee, J.D., 1975. Permeability and Effective Stress. AAPG Bulletin 59, 154-158.

Chapter 3: Analysis of Gas Flow

Regime in Porous Media¹

In this chapter, an analytical study is conducted on the dominant gas flow regimes under typical shale gas reservoir conditions. Knudsen number is evaluated with respect to reservoir parameters and flow regime maps are produced with respect to gas pressure and matrix permeability.

Range of Permeability and Pressure in shale reservoirs

Sigal and Qin (2008) reported that permeability values for Barnett shale vary between 10 and 600 nanodarcy (nd). Similar measurements by Heller and Zoback (2013) showed values between 60 and 160 nd, while the presence of carbonate streaks in samples increased permeability to microdarcy range. Heller and Zoback (2013) also measured the permeability of Eagle Ford shale samples to be in the range of 5 to 40 nd. Kang et al. (2011) measured permeability values in the range of 10 to 100 nd for Barnett. Mullen (2010) reported a permeability range of 1 to 800 nd for Eagle Ford Shale. Ross and Bustin (2008) described the permeability of several Canadian shales to be in the microdarcy range. Measurements of Montney shale samples have also indicated permeabilities in the microdarcy range (Heller and Zoback, 2013). Permeability in the Horn River Basin

¹ A version of this chapter has been published at the SPE Journal: Moghadam, A. A. and Chalaturnyk, R. 2016. Analytical and Experimental Investigations of Gas-Flow Regimes in Shales Considering the Influence of Mean Effective Stress. SPE Journal 21(02), 557-572. <http://dx.doi.org/10.2118/178429-PA>.

in British Columbia ranges between 100 and 300 nd (British Columbia Ministry of Energy and Mines, 2005). Well logs and cutting analysis of the Duvernay Formation indicates a permeability of 394 nd (Dunn et al., 2012). Table 1 summarizes some of the permeability measurements reported in the literature for various formations. Overall, the literature shows great variability of permeability at reservoir scale. Based on permeability measurements provided in the literature over major North American shale plays, matrix permeability seems to vary between 1 nanodarcy and 10 microdarcy. Meanwhile, the initial pressure for shale gas reservoirs typically varies between 15 and 35 MPa, largely depending on the depth of the formation (Ross and Bustin, 2008).

Table 1: Summary of shale permeability reported in the literature

Authors	Formation	Permeability range (nD)
Sigal and Qin (2008)	Barnett	10 - 600
Heller and Zoback (2013)	Barnett	60 - 160
Heller and Zoback (2013)	Eagle Ford	5 - 40
Kang et al. (2011)	Barnett	10 - 100
Mullen (2010)	Eagle Ford	1 - 800
Heller and Zoback (2013)	Montney	Microdarcy
Ross and Bustin (2008)	-	Microdarcy
British Columbia Ministry of Energy and Mines (2005)	Horn River	100 - 300
Dunn et al., 2012	Duvernay	394
Cui et al. (2013)	Montney	20 – 20,000
Clarkson et al. (2012)	Montney	130 – 30,000
Ghanizadeh et al. (2015)	Duvernay	22 – 1,700

Analytical investigation of flow regime

In order to create a flow regime map readily applicable to reservoir conditions, evaluations of the Knudsen number were carried out with respect to reservoir parameters. Eq. 1 defines the Knudsen number, and Eq. 2 defines mean free path. Eq. 3 proposed by Kolodzie (1980) relates pore radius to permeability and porosity. While there are several similar correlations, Eq. 3 is based on a large database of experimental data and its predictions reasonably match expectations. The Knudsen number can be calculated with respect to reservoir parameters (pressure and permeability) by combining Eq. 1, Eq. 2, and Eq. 3. Fig. 4 illustrates values of the Knudsen number versus pressure and permeability as a 3D graph assuming methane at 60 degrees Celsius. It must be noted that formation permeability in Fig. 4 is measured by a routine air permeability test and is therefore higher than the absolute or liquid permeability of the formation.

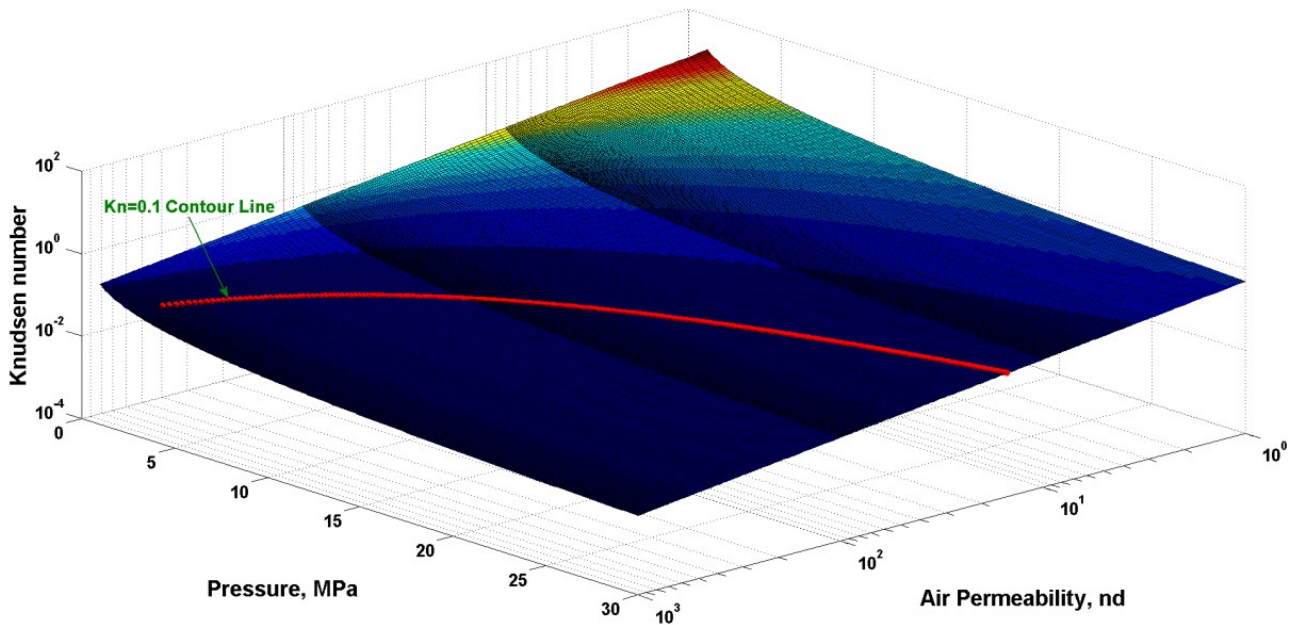


Fig. 4: Knudsen number with respect to permeability and pressure.

According to Fig. 4, Knudsen number values are generally very low, except in conditions of ultra-low permeability and very low pressure. In order for the flow regime to be in the continuum region, the Knudsen number needs to be below 0.1 (Rahmanian et al., 2013). Considering the limit of 0.1 for the Knudsen number, a

horizontal plane is passed through the 3D graph in Fig. 4 at the value of 0.1, and the curve where the two surfaces cross shows a relationship between pressure and permeability over which the transition of flow regime occurs. Fig. 5 shows the relationship between permeability and pressure, where the transition between continuum and non-continuum flow occurs. The region above the curve in Fig. 5 represents the continuum flow region where the Knudsen number is below 0.1. The region below the curve represents the conditions for non-continuum flow where the Knudsen number is above 0.1. The plots in Fig. 5 are for methane at 60 and 120 degrees Celsius. According to Fig. 5, temperature does not move the curve significantly; therefore temperature has minimal influence on flow regime transition. Considering the permeability of the majority of shale gas reservoirs varies between 1 nanodarcy and 10 microdarcy, and pressures range from 35 MPa in the beginning to as low as 10 MPa at abandonment, an area can be drawn representing flow conditions for the majority of shale gas plays throughout the life of the reservoir.

The shaded area in Fig. 5 represents the typical flow conditions of shale gas reservoirs. Fig. 5 indicates that for a reservoir with average air permeability higher than 30 nd the gas flow regime most likely lies in the continuum region throughout the life of the reservoir. It should be noted that in Fig. 5, permeability is in log scale.

Repeating this procedure by passing a horizontal plane through the 3D graph in Fig. 4 at Knudsen numbers 0.001 and 10 can generate the full flow regime map with respect to permeability and pressure. Fig. 6 illustrates the full flow regime map for methane at 60 degrees Celsius. All flow regimes are specified in the plot, and the permeability and pressure of the reservoir can be used to determine the dominant flow regime. Considering the typical permeability and pressure range of shale gas reservoirs in initial and abandonment conditions, most cases will lie in the slip flow regime and some in the early transition flow regime. Additionally, Fig. 6 demonstrates that within the permeability range of Shale rocks slip flow is dominant even at very high reservoir pressures. Permeability measurements in the

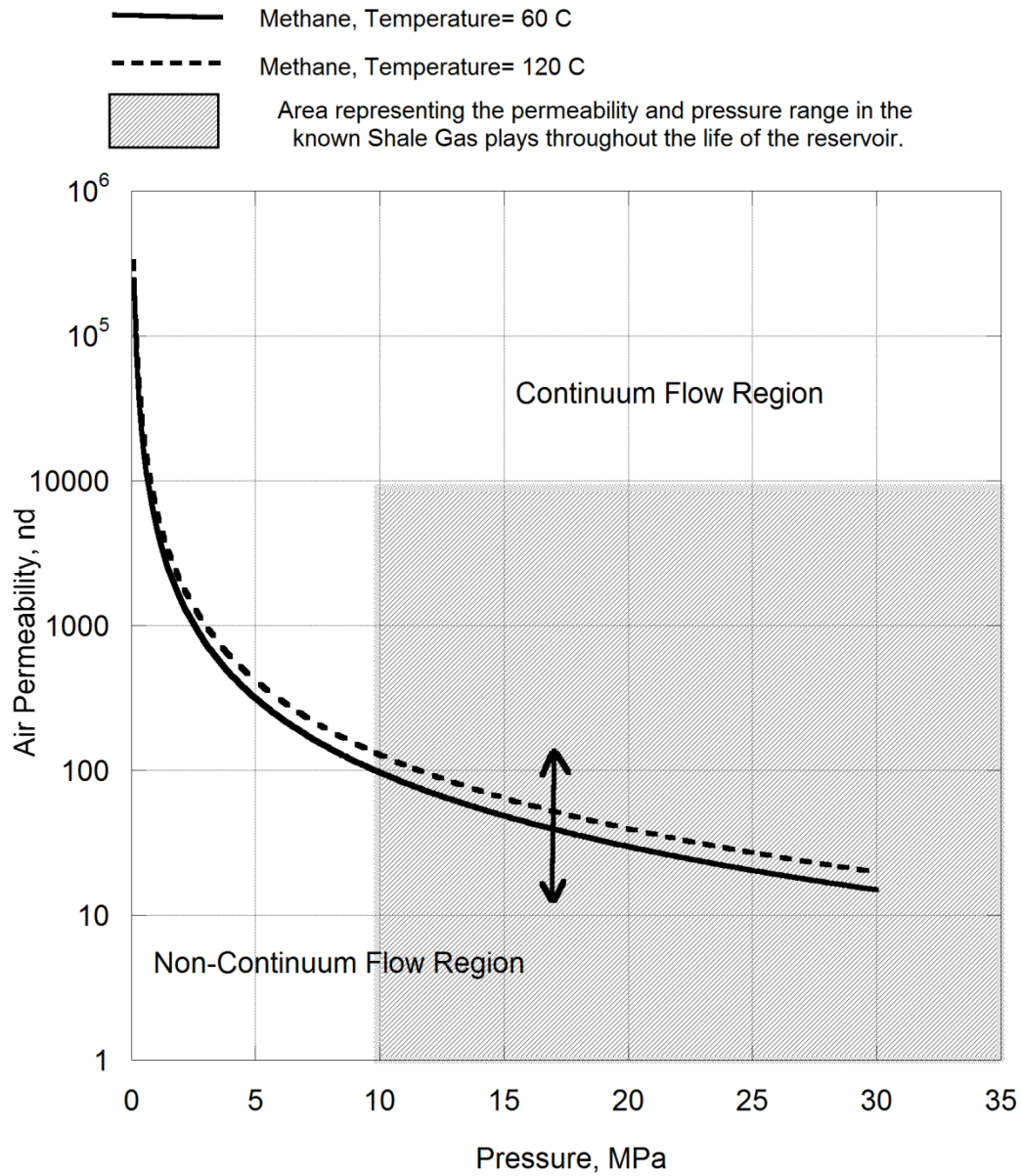


Fig. 5: Flow Regime map for methane at 60 and 120 Celsius.

lab are commonly conducted using nitrogen, carbon dioxide, and helium as the flowing fluid. Therefore, it is useful to generate flow regime maps for these gases in order to recognize the flow regime under experimental conditions. Nitrogen and carbon dioxide have a molecular diameter comparable to that of methane (Halpern and Glendening, 1996), thus the flow regime map for nitrogen and carbon dioxide are very similar (within the same order of magnitude) to the flow regime map of

methane. Fig. 6 could then be used to analyze the flow regime for nitrogen and carbon dioxide under experimental conditions. Helium has a lower diameter compared to methane and consequently, the flow regime map is significantly different. Fig. 7 illustrates the flow regime map for helium which can be used to analyze the helium flow regime for permeability measurement tests. Fig. 7 indicates that, for helium, slip flow regime is dominant even at relatively high permeability (as high as 1 md).

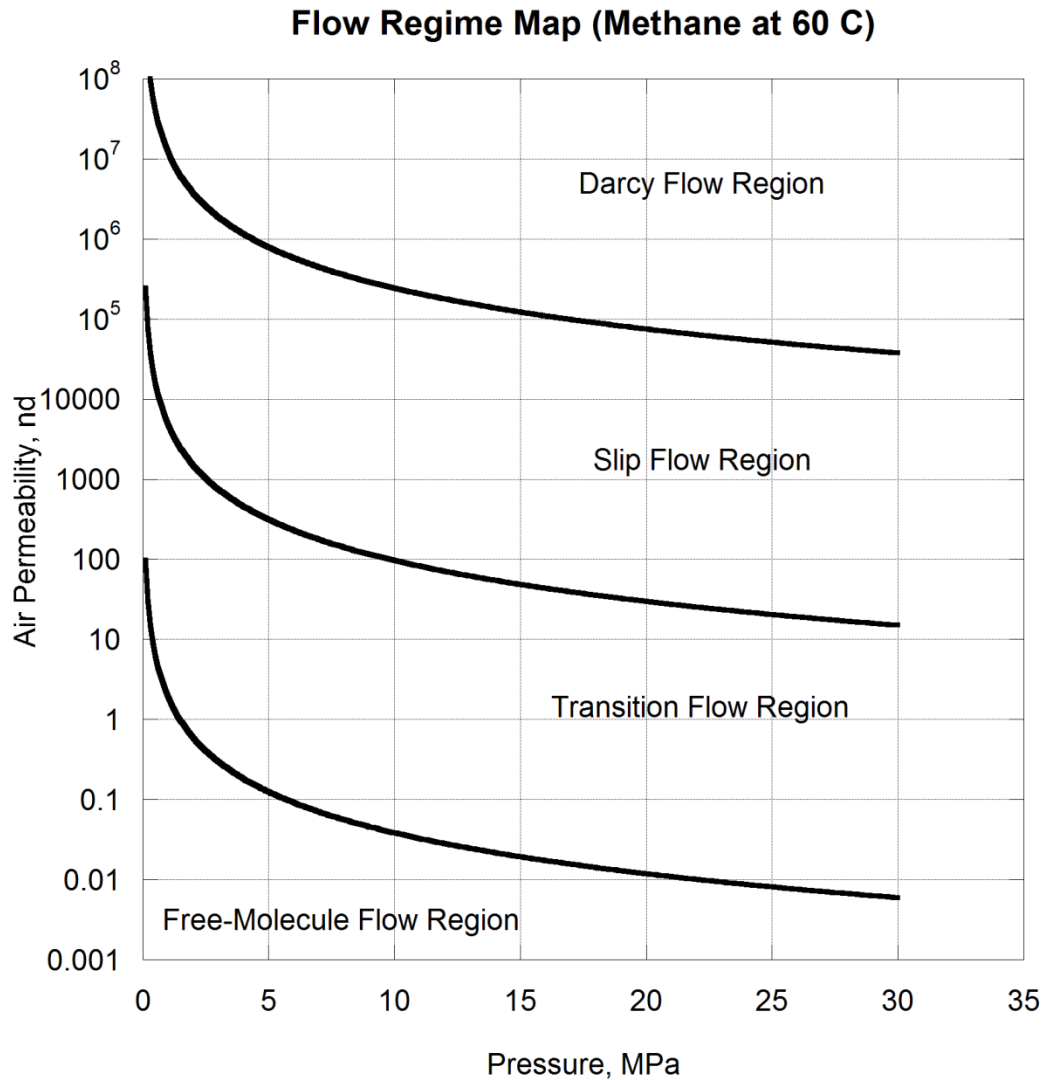


Fig. 6: Flow regime map for methane at 60 Celsius.

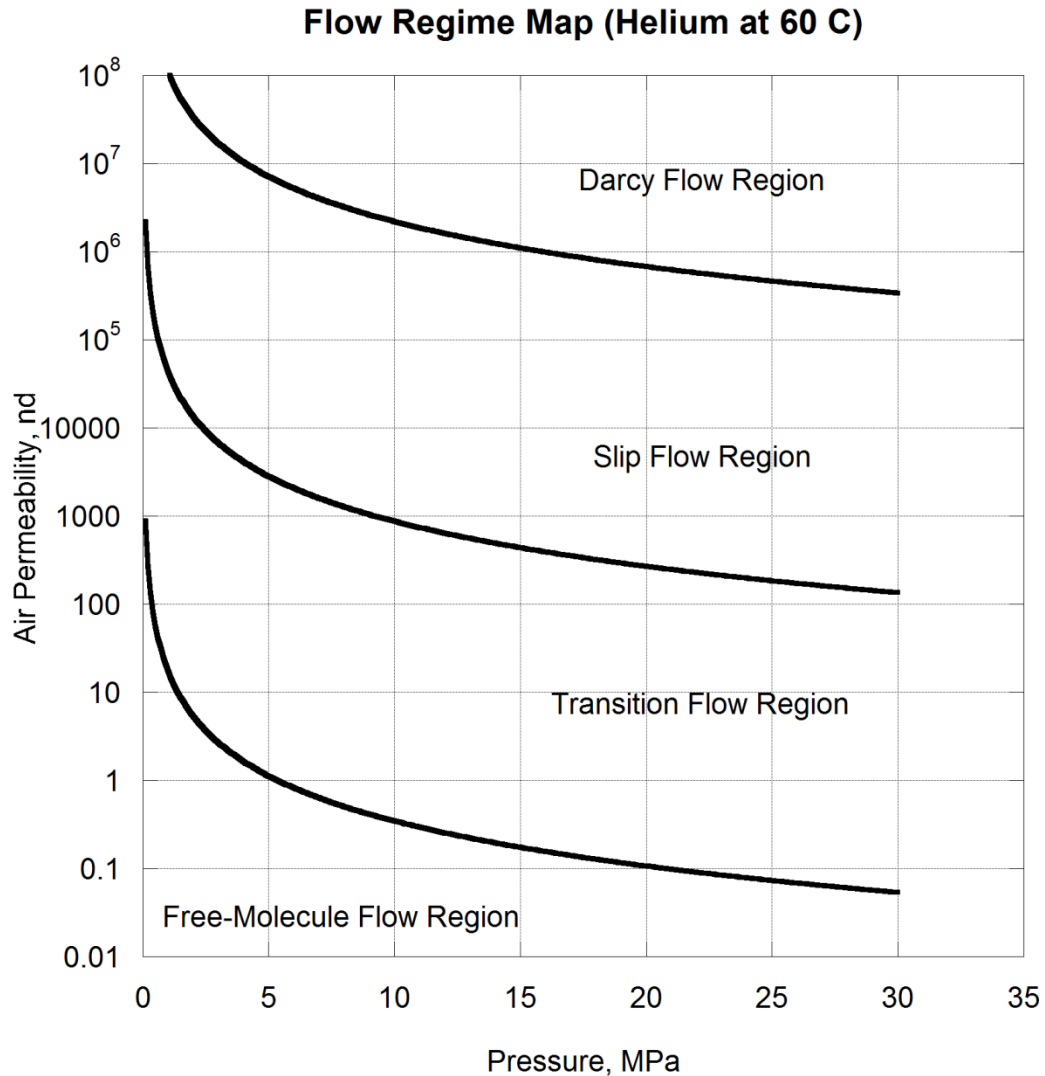


Fig. 7: Flow regime map for helium at 60 Celsius.

According to the flow regime map for helium (Fig. 7), permeability measurements in the lab are most likely conducted under the transition flow regime, or the free-molecule regime. Therefore, complicated models that take into account Knudsen diffusion (Javadpour, 2009; Ziarani and Aguilera, 2012; Rahmanian et al., 2013) should be used to analyze the results of the lab tests using helium. It should be noted that for low-permeability porous media, helium permeability measurements can never be in the darcy flow regime and therefore, the measured permeability is always the apparent permeability. This implies that in order to analyze the influence

of parameters such as effective stress (for example in calculation of the Biot coefficient from permeability values), water saturation, adsorption layer, etc., on permeability, the results need to be first corrected for the influence of flow regime. More details regarding the methodology to correct the permeability values are provided in chapter 6.

Pore Radius Calculations

Measures of permeability in Fig. 4, Fig. 5, Fig. 6, and Fig. 7 originate from Eq. 3, which appeared in an unpublished work by H. D. Winland (Amoco Production Company). Kolodzie (1980) refined and published the correlation. According to Pittman (1992), the permeability in Eq. 3 is uncorrected air permeability. However, there is no mention of the confining stress of the experiments. Consequently, it is assumed that the permeability in Fig. 4, Fig. 5, Fig. 6, and Fig. 7 is measured from a routine air permeability test uncorrected for slip effects and at low confining stress. The permeability that should be used in the figures is higher than the absolute or liquid permeability of the formations. To illustrate this, if the water permeability of a formation is measured at 10 nd and the air permeability at 100 nd, the air permeability should be used in Fig. 6 to determine the flow regime. Location of the flow regime boundaries in Fig. 5, Fig. 6, and Fig. 7 depend on the pore radius estimations. Using correlations other than Eq. 3 to calculate Knudsen number values, will slightly shift the boundaries. Therefore, the flow regime predictions close to the boundaries come with a degree of uncertainty. An extensive database of pore radius and permeability measurements is required for shales in order to improve the accuracy of the predictions.

In addition to the correlation published by Kolodzie (1980), there are a number of theoretical and experimental based correlations available. Two well-known correlations are proposed by Heid et al., (1950), and Aguilera (2002) presented in Eq. 10 and Eq. 11, respectively.

$$r_{\text{pore}} = 88.5 \sqrt{\frac{k}{\phi}} \quad \text{Eq. 10}$$

$$r_{\text{pore}} = 2665 \left(\frac{k}{100\phi} \right)^{0.45} \quad \text{Eq. 11}$$

In Eq. 10 and Eq. 11, r_{pore} is the average pore radius in nm, k is permeability in md and ϕ is porosity in fraction. Mercury injection tests were conducted by a commercial lab on three Montney samples to estimate the average pore radius. Steady-state permeability of the samples to air were also measured and the results are compared to the pore radius estimations using Eq. 3, Eq. 10, and Eq. 11. Fig. 8 presents the comparison of the Mercury injection tests and the three aforementioned correlations. According to Fig. 8, the Eq. 3 published by Kolodzie (1980) matches the experimental data better than the other two correlations.

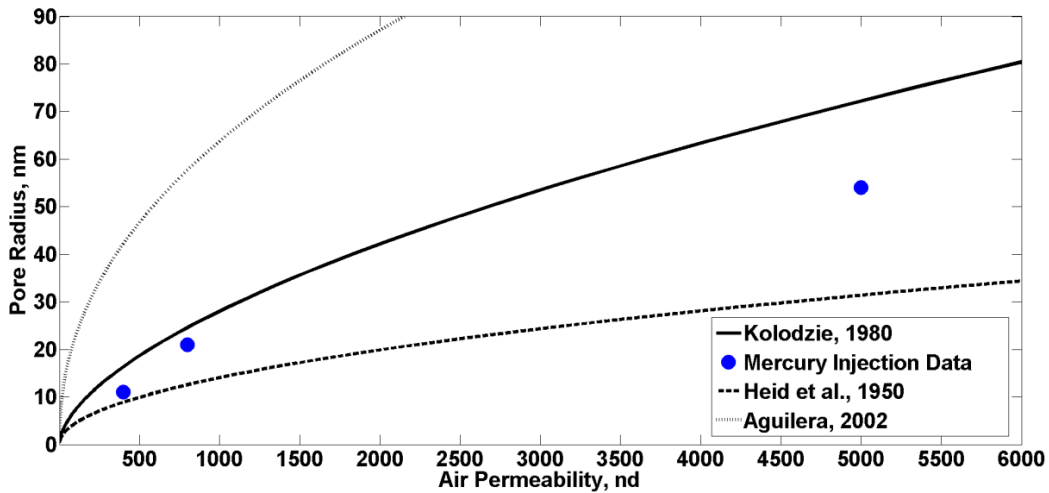


Fig. 8: Comparison of the pore radius estimates using three well-known correlations with the results of Mercury injection tests.

Conclusions

Theoretical investigations are conducted into the gas flow regimes under shale gas reservoir, and laboratory conditions. Flow regime maps were created for methane and helium indicating the dominant flow regime at a given pressure and permeability. These maps could be useful to assess the gas flow regime under reservoir and laboratory conditions, and to indicate the appropriate flow model. Additionally, the flow regime maps show that under typical shale gas reservoir

conditions, slip flow occurs at pressures as high as 30 MPa. Therefore, slippage must be accounted for even in high-pressure experiments or reservoir flow modelling. Under typical conditions, most shale gas reservoirs lie in the slip flow regime or early transition flow regime. This indicates that for most practical purposes, diffusion may not be a major driving force in gas flow through shale gas reservoirs.

Permeability measurements using helium on the other hand, are under transition, or free-molecule flow regime conditions. This leads to extra enhancement of helium permeability in the lab tests. Permeability measurements using helium must be corrected for the influence of flow regime regardless of the pressure of the lab tests. Due to the high Knudsen values for helium, more complicated flow models that consider Knudsen diffusion should be used to analyze the lab results.

References

Aguilera, R., 2002. Incorporating capillary pressure, pore throat aperture radii, height above free water table and Winland r_{35} values on Pickett plots. AAPG Bulletin 86, 605–624.

BC Ministry of Energy and Mines, 2012. Summary of shale gas activities in Northeast British Columbia 2011. Geoscience and Strategic Initiatives Branch, Oil and Gas Division. Oil and Gas report 2012-1, 19 p.

Clarkson, C.R., Jensen, J.L., Pedersen, P.K., Freeman, M., 2012. Innovative Methods for Flow Unit and Pore Structure Analysis in a Tight Siltstone and Shale Gas Reservoir. AAPG Bulletin 96(2), 355-374.

Cui, A., Wust, R., Nassichuk, B., Glover, K., Brezovski, R., Twemlow, C., 2013. A Nearly Complete Characterization of Permeability to Hydrocarbon Gas and Liquid for Unconventional Reservoirs: A Challenge to Conventional Thinking. Paper SPE 168730 presented at the 2013 SPE Unconventional Resources Technology Conference, Denver, USA.

- Darabi, H., Ettehad, A., Javadpour, F., Sepehrnoori, K., 2012. Gas Flow in Ultra-Tight Shale Strata. *Journal of Fluid Mechanics* 710, 641-658.
- Dunn, L., Schmidt, G., Hammermaster, K., Brown, M., Bernard, R., Wen, E., Befus, R., Gardiner, S., 2012. The Duvernay Formation (Devonian): sedimentology and reservoir characterization of a shale gas/liquids play in Alberta, Canada. Canadian Society of Petroleum Geologists, Annual Convention, Calgary.
- Ghanizadeh, A., Bhowmik, S., Haeri-Ardakani, O., Sanei, H., Clarkson, C.R., 2015. A Comparison of Shale Permeability Coefficients Derived Using Multiple Non-steady-state Measurement Techniques: Examples from the Duvernay Formation, Alberta (Canada). *Fuel* 140, 371-387.
- Halpern, A.M., Glendening, E.D., 1996. Estimating Molecular Collision Diameter Using Computational Methods. *Journal of Molecular Structure* 365, 9-12.
- Heid, J.G., McMahon, J.J., Nielsen, R.F., Yuster, S.T., 1950. Study of the Permeability of Rocks to Homogenous Fluids. *API Drilling & Production Practice*, New York 230–246.
- Heller, R., Vermynen, J., Zoback, M., 2014. Experimental Investigation of Matrix Permeability of Gas Shales. *AAPG Bulletin* 98 (5), 975-995.
- Heller, R., Zoback, M., 2013. Laboratory Measurements of Matrix Permeability and Slippage Enhanced Permeability in Gas Shales. Paper SPE 168856-MS presented at Unconventional Resources Technology Conference, Denver, Colorado, USA, August 12-14.
- Javadpour, F., 2009. Nanopores and Apparent Permeability of Gas Flow in Mudrocks (Shales and Siltstone). *Journal of Canadian Petroleum Technology* 48, 16-21.
- Kang, S. M., Fathi, E., Ambrose, R. J., Akkutlu, I. Y., Sigal, R. F., 2011. Carbon Dioxide Storage Capacity of Organic-Rich Shales. *SPE Journal* 16(04), 842-855.

Kolodzie, J.S., 1980. Analysis of pore throat size and use of the Waxman–Smits equation to determine OOIP in Spindle field, Colorado. Paper SPE 9382-MS presented at SPE 55th Annual Technical Conference and Exhibition, Dallas, Sep 21–24.

Moghadam, A. A. and Chalaturnyk, R. 2016. Analytical and Experimental Investigations of Gas-Flow Regimes in Shales Considering the Influence of Mean Effective Stress. SPE Journal 21(02), 557-572. <http://dx.doi.org/10.2118/178429-PA>.

Mullen, J., 2010. Petrophysical Characterization of the Eagle Ford Shale in South Texas. Paper SPE 138145-MS presented at Canadian Unconventional Resources and International Petroleum Conference, Calgary, Alberta, Canada, 19-21 October.

Pittman, E.D., 1992. Relationship of porosity and permeability to various parameters derived from mercury injection-capillary pressure curves for sandstone. AAPG Bulletin. 76, 191-198.

Rahmanian, M., Aguilera, R., & Kantzas, A., 2013. A New Unified Diffusion--Viscous-Flow Model Based on Pore-Level Studies of Tight Gas Formations. SPE Journal 18(01), 38-49.

Ross, D.J.K., Bustin, R.M., 2008. Characterizing the Shale Gas Resource Potential of Devonian-Mississippian Strata in the Western Canada Sedimentary Basin: Application of an integrated Formation Evaluation. The American Association of Petroleum Geologists Bulletin 92(No. 1), 87-125.

Sigal, R.F. and Qin, B. 2008. Examination of the Importance of Self Diffusion in the Transportation of Gas in Shale Gas Reservoirs. Petrophysics 49 (3).

Ziarani, A.S., Aguilera, R., 2012. Knudsen's permeability correction for tight porous media. Transport in Porous Media 91(1), 239-260.

Chapter 4: Expansion of the Klinkenberg's Slippage Equation to Low Permeability Porous Media²

Gas is commonly used in measuring the permeability of low-permeability media such as coals and shales. It is well established that gas permeability depends on the pressure of the experiment, and generally yields higher values than when liquids are used. While Klinkenberg (1941) proposed a rather accurate equation to account for the slip effect, recent studies on low-permeability media have shown deviations from it. These deviations are more significant in low-permeability media.

This chapter presents a new analytical approach to predicting and explaining the gas slip effect. It proposes a new equation based on Klinkenberg's theoretical work and findings of Kundt and Warburg (1875), which expands the applicability of Klinkenberg's slip theory to low-permeability porous media while keeping the simplicity of the original equation. The proposed equation is validated by the experimental results of different authors. This chapter further discusses the new equation's constants and the range of applicability of the theory. The new equation successfully predicts the deviations from Klinkenberg's equation in low-permeability media and reasonably matches the experimental results.

² A version of this chapter has been published at the International Journal of Coal Geology: Moghadam, A.A., Chalaturnyk, R., 2014. Expansion of the Klinkenberg's slippage equation to low permeability porous media. International Journal of Coal Geology 123, 2-9.

Introduction

A common characteristic of these reservoirs (coal beds, shale gas, tight sands, etc.) is a low to ultra-low permeability matrix. Gas flow in low-permeability formations differs from that in medium-to-high permeability matrices, and its description requires a different set of physical laws. The approach to studying the production and simulation of these low-permeability reservoirs can revolve around describing the drilling technologies required (horizontal drilling, hydraulic fracturing, etc.), describing the fracture system (dual porosity, dual permeability, Multiple Interacting Continua, etc.), explaining possible desorption or adsorption of gas in the matrix (Langmuir isotherms, etc.) and studying the flow mechanism of gas and the governing flow equations. This last approach is the one adopted in this paper.

Numerous investigations have been done on gas flow in porous media, and recent interest in unconventional gas reservoirs has led to studies focused on gas flow in low-permeability media. These have shown behavioural differences between gases and liquids (Muskat, 1982; Noman et al., 1990), which are usually attributed to the differences in molecular structure and intermolecular forces. This work uses analytical, empirical, and experimental studies to analyze the unique behaviour of gas in low-permeability media.

The flow of fluids in porous media is usually described by Darcy equation (Eq. 4). In Darcy equation, it is an acceptable assumption that permeability is a rock property. However, it was discovered that for gases in a low-pressure range, permeability could vary with gas pressure. The apparent permeability of gases is larger than the absolute permeability of the rock. This phenomenon is attributed to the slip of gas molecules on the surface of capillaries (Jones and Owens, 1980; Klinkenberg, 1941).

Slippage is usually only noticeable in the laboratory. Gas molecules constantly collide with each other and with pore walls. There is a layer of stationary molecules on the walls of a large conduit (Bird et al., 1960). On the other hand, there is an average distance between the gas molecules called the mean free path (Loeb, 1934).

This distance (technically, the displacement by the molecule between two collisions) is dependent on temperature, pressure, and the type of gas (i.e., the size and polar characteristics of its molecules). As pores shrink and permeability falls, there are pore throats with a hydraulic diameter comparable to the mean free path of the gas. This could cause a non-zero velocity (slip velocity) at the surface of the capillaries. This phenomenon, called the slippage effect, causes gas molecules to accelerate, as there is less drag, or no stationary layer to slow them. This acceleration shows itself as an apparent increase in system permeability.

The next section of the chapter discusses the development of a new equation for slippage effect using an approach similar to that of Klinkenberg, which explains the deviations from the linear Klinkenberg correlation and addresses the problem of overestimation of permeability in low-permeability porous media. This new equation provides enhanced accuracy in the interpretation of the experimental data on permeability, and provides a basis for improved reservoir simulation models.

Theory

To analyze the slippage effect, an approach was adopted which is similar to that used by Klinkenberg to describe slip flow in a capillary tube. Kundt and Warburg (1875) established that the average velocity of gas in the vicinity of the wall of a capillary tube is not zero and has a finite value. Klinkenberg assumed a constant velocity gradient perpendicular to the wall. Kundt and Warburg (1875) showed that the assumption of a constant velocity gradient does not hold. The velocity gradient changes with the distance from the wall and is greater in the vicinity of the wall than at a large distance from the wall. Fig. 9 provides a visual description of the velocity boundary condition in a capillary tube. The non-linear boundary condition in this work, the linear boundary in Klinkenberg's work, and no slip boundary condition are depicted in Fig. 9.

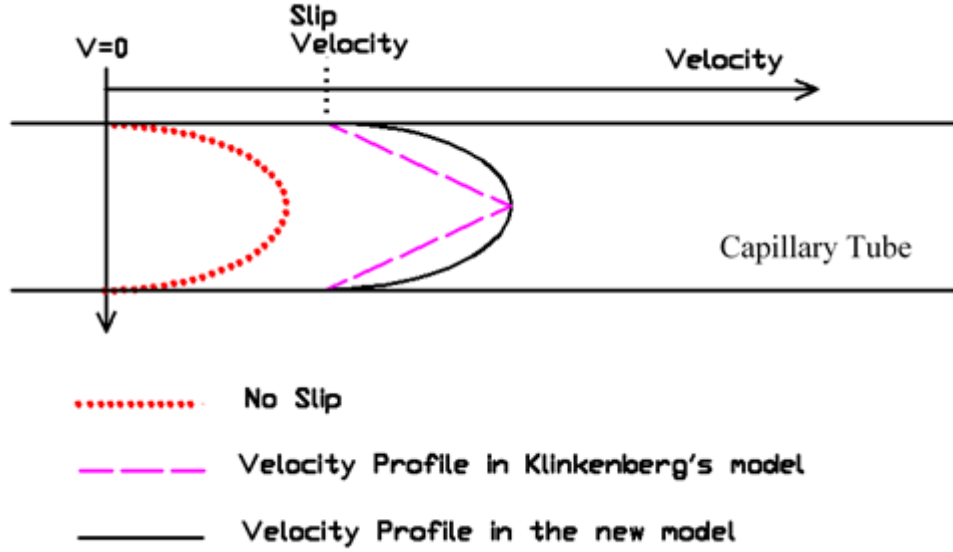


Fig. 9: Illustration of the velocity boundary conditions in a capillary tube in this work, Klinkenberg's work, and no slip boundary.

In order to relieve the constant velocity gradient assumption, we can assume velocity v_0 in the direction of flow at the tube wall, and a variable velocity gradient perpendicular to the wall, the velocity at distance ε from the wall can be computed using a Taylor series approximation to the second order for the velocity around the wall region:

$$v_\varepsilon = v_0 + \varepsilon \frac{\partial v}{\partial \varepsilon}(0) + \frac{\varepsilon^2}{2} \frac{\partial^2 v}{\partial \varepsilon^2}(0) \quad \text{Eq. 12}$$

where, $\varepsilon=0$ is the coordinate at the wall surface. Since gas molecules are constantly colliding with each other, the average distance of the last collision of the molecules depends on λ (the mean free path of the gas molecules). Using a proportionality factor, this can be translated into the distance of the last collision from the wall. Assuming the proportionality factor, c , such that the distance between the last collision and the wall would be $c\lambda$, the velocity equation at distance $c\lambda$ is:

$$v_{c\lambda} = v_0 + c\lambda \frac{\partial v}{\partial \varepsilon}(0) + \frac{(c\lambda)^2}{2} \frac{\partial^2 v}{\partial \varepsilon^2}(0) \quad \text{Eq. 13}$$

Considering a thin layer of gas in the immediate vicinity of the wall with a thickness of less than λ , it can be assumed that there are practically no collisions between the gas molecules. In this thin layer at a given time, half of the molecules have a velocity component towards the wall and the other half have a velocity component in the opposite direction. Those moving towards the wall have had their last collision somewhere away from the wall in the flowing mass, and therefore have a velocity component in the direction of the gas flow. After the collision with the wall, part or all of this average velocity in the direction of the flow will be lost. Assuming that the collision with the wall is entirely inelastic, and the molecules colliding with it lose their average velocity in the direction of the flow, then the average velocity of all the molecules near the wall in the considered layer would be half of those moving towards the wall.

$$v_0 = \frac{1}{2} v_{c\lambda} \quad \text{Eq. 14}$$

Fathi et al., (2012) conducted lattice Boltzmann simulations of gas dynamics in a nano-scale capillary tube. Their results show that the inelastic collision of molecules with the pore wall is a suitable assumption for gas flow. The multiplier in Eq. 14 is equal to 0.5 for the fully inelastic collision assumption, and will equal to 1 for the fully elastic collision. Therefore, any departure from the fully inelastic assumption will only increase the multiplier from 0.5 closer to 1. This will change a constant in the final derivation. However, the final constants of the slippage equation will be measured using lab results. Therefore, the potential error in the fully inelastic collision assumption, does not translate to errors in the final results.

Replacing Eq. 13 in Eq. 14,

$$v_0 = 1/2 \left(v_0 + c\lambda \frac{\partial v}{\partial \varepsilon}(0) + \frac{(c\lambda)^2}{2} \frac{\partial^2 v}{\partial \varepsilon^2}(0) \right) \quad \text{Eq. 15}$$

Therefore,

$$v_0 = c\lambda \frac{\partial v}{\partial \varepsilon}(0) + \frac{(c\lambda)^2}{2} \frac{\partial^2 v}{\partial \varepsilon^2}(0) \quad \text{Eq. 16}$$

Considering the velocity in a larger scale in a straight capillary tube, the equations accounting for drag and pressure difference on an element of flow and integrating accordingly in a capillary with radius r_0 , the following is derived:

$$v = \frac{1}{4\mu} \frac{dP}{dx} r^2 + A \ln(r) + B \quad \text{Eq. 17}$$

where r is the radial coordinate, x is the coordinate along the length of the capillary, P is the pressure, and μ is the gas viscosity. The derivation of Eq. 17 is presented in Appendix A.

Since the velocity in the center of the capillary is finite, $A=0$. Using Eq. 16 as a boundary condition (ε and r have opposite directions):

$$v_0 = c\lambda \frac{\partial v}{\partial \varepsilon}(0) + \frac{(c\lambda)^2}{2} \frac{\partial^2 v}{\partial \varepsilon^2}(0) = -c\lambda \frac{\partial v}{\partial r}(r_0) + \frac{(c\lambda)^2}{2} \frac{\partial^2 v}{\partial r^2}(r_0) \quad \text{Eq. 18}$$

Substituting Eq. 18 in Eq. 17:

$$B = -c\lambda \frac{\partial v}{\partial r}(r_0) + \frac{(c\lambda)^2}{2} \frac{\partial^2 v}{\partial r^2}(r_0) - \frac{1}{4\mu} \frac{dP}{dx} r_0^2 \quad \text{Eq. 19}$$

According to Eq. 17:

$$\frac{\partial v}{\partial r}(r_0) = \frac{1}{2\mu} \frac{dP}{dx} r_0 \quad \text{Eq. 20}$$

$$\frac{\partial^2 v}{\partial r^2}(r_0) = \frac{1}{2\mu} \frac{dP}{dx} \quad \text{Eq. 21}$$

Substituting Eq. 19, Eq. 20, and Eq. 21 in Eq. 17 yields:

$$v = \frac{-1}{4\mu} \frac{dP}{dx} (r_0^2 - r^2 + 2c\lambda r_0 - (c\lambda)^2) \quad \text{Eq. 22}$$

For flow rate, the velocity in Eq. 22 is multiplied by the area of a shell between two cylinders of radius r and $r + dr$ and integrated with respect to r :

$$Q = \frac{-\pi r_0^4}{8\mu} \frac{dP}{dx} \left(1 + \frac{4c\lambda}{r_0} - \frac{2(c\lambda)^2}{r_0^2} \right) \quad \text{Eq. 23}$$

The ideal gas law states that:

$$Q = \frac{\dot{n}RT}{P} \quad \text{Eq. 24}$$

According to the kinetic theory of gases (Loeb, 1934), the mean free path of the gas is dependent on the reciprocal of pressure. Therefore:

$$c\lambda = m/P \quad \text{Eq. 25}$$

$$m = c\mu \sqrt{\frac{\pi RT}{2M}} \quad \text{Eq. 26}$$

Substituting Eq. 24 and Eq. 25 into Eq. 23:

$$\dot{n}RTdx = \frac{-\pi r_0^4}{8\mu} \left(PdP + \frac{4m}{r_0} dP - \frac{2m^2}{r_0^2} \frac{dP}{P} \right) \quad \text{Eq. 27}$$

Eq. 27 can be integrated over the length of the capillary and substituted back into Q in Eq. 24 using the ideal gas law and an arithmetic average pressure:

$$Q = \frac{\dot{n}RT}{\bar{P}} = \frac{\pi r_0^4}{8\mu l} \left(1 + \frac{4m}{r_0 \bar{P}} - \frac{2m^2 \ln(P_1) - \ln(P_2)}{r_0^2 \bar{P} (P_1 - P_2)} \right) (P_1 - P_2) \quad \text{Eq. 28}$$

where \bar{P} is the average pressure along the capillary. The Poiseuille equation for the flow in a capillary (Eq. 29), and the Darcy equation (Eq. 30) are:

$$Q = \frac{\pi r_0^4}{8\mu l} (P_1 - P_2) \quad \text{Eq. 29}$$

$$Q = \frac{K}{\mu l} (P_1 - P_2) \quad \text{Eq. 30}$$

In the case of a liquid, “K” in Eq. 30 is equivalent to K_{liquid} or K_{absolute} which compared to Eq. 29 is equivalent to $\frac{\pi r_0^4}{8}$. In the case of a gas as the flowing fluid, replacing $\frac{\pi r_0^4}{8}$ in Eq. 28 by K_{absolute} we obtain:

$$K_{\text{apparent}} = K_{\text{absolute}} \left(1 + \frac{4m}{r_0 \bar{P}} - \frac{2m^2 \ln(P_1) - \ln(P_2)}{r_0^2 \bar{P} (P_1 - P_2)} \right) \quad \text{Eq. 31}$$

Replacing the natural logarithm term in Eq. 31 with its Taylor’s series approximation around the value of \bar{P} obtains the following simple relationship:

$$\frac{\ln(P_1) - \ln(P_2)}{P_1 - P_2} \cong \frac{2}{\bar{P}} \quad \text{Eq. 32}$$

Substituting Eq. 32 in Eq. 31 and replacing constants by “a” and “b”:

$$K_{\text{apparent}} = K_{\text{absolute}} \left(1 + \frac{b}{\bar{P}} - \frac{a}{\bar{P}^2} \right) \quad \text{Eq. 33}$$

Eq. 33 clearly shows a quadratic dependency between apparent gas permeability and mean pressure. The constants, “a” and “b”, are dependent on the fluid properties and pore geometry, and both are positive. The constant “b” is similar to the Klinkenberg constant, and if the value of “a” is zero, then the linear Klinkenberg equation is recovered. Comparing Eq. 31, Eq. 32, and Eq. 33, the following relationships are obtained:

$$b = \frac{4m}{r_0} \quad \text{Eq. 34}$$

$$a = \frac{4m^2}{r_0^2} \quad \text{Eq. 35}$$

$$a = \frac{b^2}{4} \quad \text{Eq. 36}$$

According to Eq. 35, “a” is inversely related to the square of pore radius. In high-permeability media, the pore radius is large. Therefore, the value of “a” is close to zero, making the Klinkenberg equation sufficiently accurate. In this case “b” in Eq. 33 will be equal to Klinkenberg constant. Only at small values of r_0 (i.e., low-permeability medium) does “a” become considerably large and the curvature in the plot of apparent permeability versus mean pressure becomes noticeable.

It is interesting to note that using higher order Taylor series for the boundary condition in Eq. 12 will not change Eq. 33 in any way since according to Eq. 17, when solving for boundary conditions the higher derivatives of velocity will be zero. This means that the second derivative expansion is the maximum non-trivial value. This indicates that the “a” here has a theoretical significance and is not part of an infinite series.

In Klinkenberg’s work, the factor “b” originated from the assumption of non-zero velocity at the wall. Therefore, “b” is simply a representation of the non-zero velocity (slippage) at the wall. If the velocity at the wall is effectively zero, then “b” will disappear as it is the case for liquid flow. The parameter “a”, on the other hand, is introduced when a non-linear velocity profile is assumed in the pores. Therefore, “a” is the slip effect with a non-constant velocity distribution. “a” in Eq. 33 could be a representation of a dynamic or secondary slippage factor.

We can rewrite Eq. 33 as:

$$K_{\text{apparent}} = K_{\text{absolute}} \left(1 + \frac{1}{\bar{p}} \left(b - \frac{a}{\bar{p}} \right) \right) \quad \text{Eq. 37}$$

Comparing Eq. 37 with the Klinkenberg’s equation (Eq. 7), we obtain:

$$b_{\text{Klinkenberg}} = b - \frac{a}{\bar{p}} \quad \text{Eq. 38}$$

According to Eq. 33, the curvature is always negative. Klinkenberg mentions in his paper that the value of “b” rises as the pressure increases (and the inverse of pressure decreases). This observation is captured in Eq. 38 which is a result of Eq. 33. This leads to the conclusion that the Klinkenberg plot is a curve with a negative curvature. This is also in accordance with the experimental data presented in the literature. Negative curvature leads to the lower values of absolute permeability estimated by Eq. 33, which solves the problem of overestimation when using the Klinkenberg equation (Jones et al., 1980; Li et al., 2009; Rushing et al., 2004; Fathi et al., 2012).

Results and Discussions

Klinkenberg conducted gas flow experiments on several cores and glass filters. He plotted the permeability against the inverse of the average fluid pressure to validate his equation. His results showed a reasonably straight line, of which the intercept was the intrinsic permeability. The permeability of all the samples was in the order of millidarcies. Revisiting Klinkenberg’s experimental results, Fig. 10 shows the plot for Core Sample M and Core Sample L from his paper.

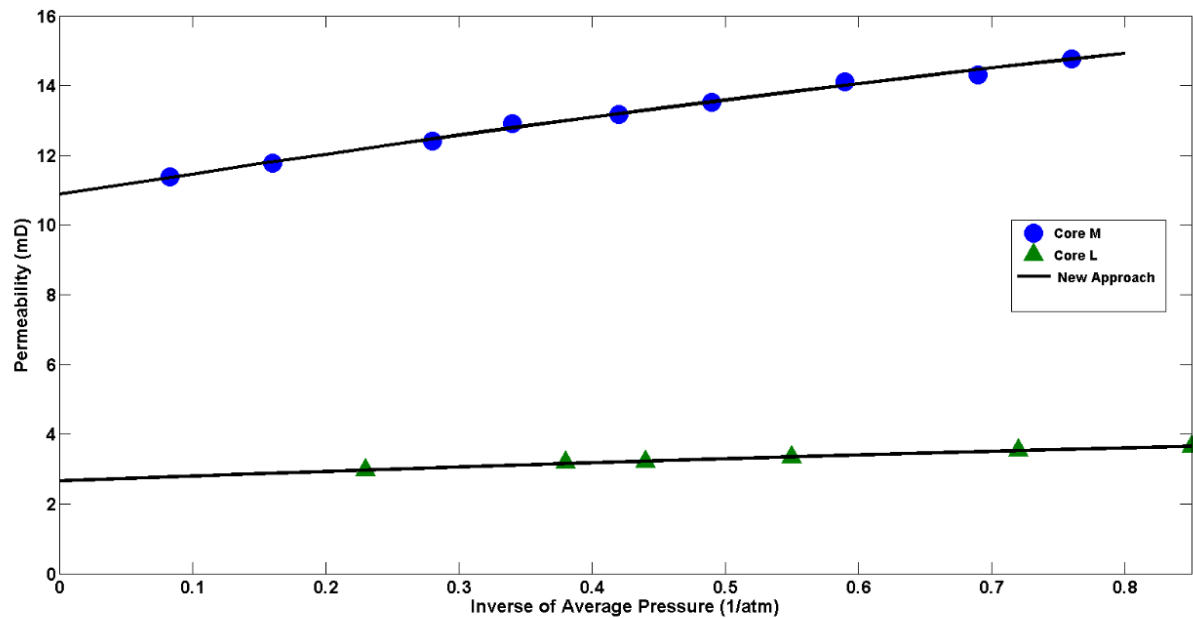


Fig. 10: Permeability versus inverse of pressure for Core Samples M and L, from the original Klinkenberg paper.

By fitting the data in Fig. 10 to Eq. 33, the permeability for Core Samples M and L is calculated to be 10.88 and 2.66 md, respectively. Klinkenberg's corrected values for Cores M and L are 11.1 and 2.75 md. The new approach gives a lower value for the intrinsic permeability than does Klinkenberg's original correlation. However, for this set of data this difference is not large. As mentioned, in the case of high permeability in the order of millidarcies, this difference is negligible and the original Klinkenberg correlation is sufficiently accurate. This is because according to Eq. 35, in the case of relatively larger average pore radii (higher permeability), the curvature of the plot (related to "a") becomes negligible. In the case of low-permeability media, the curvature becomes large, and significant difference is observed in the results of the new approach and Klinkenberg's original equation. Such difference is illustrated in experimental data by Rushing et al. (2004), plotted in Fig. 11. The permeability is a thousand times smaller than that of Klinkenberg's samples, and as expected, the curvature of the plot is significant. The intrinsic

permeability using the straight line method is 36% greater than the permeability using the new equation.

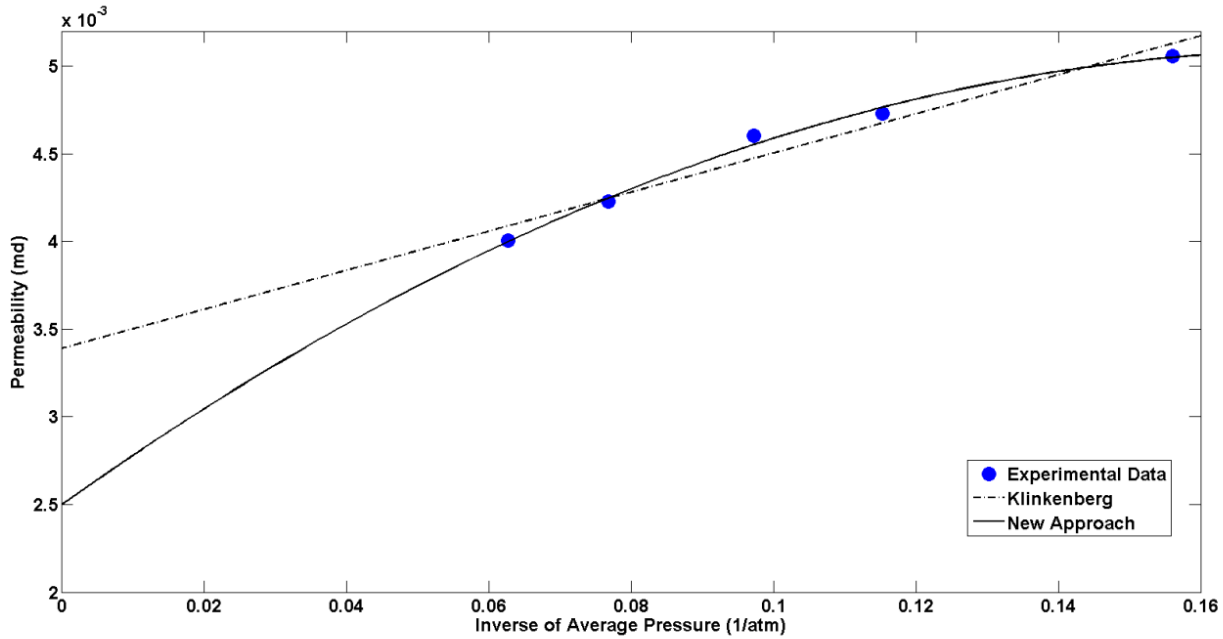


Fig. 11: Non-linearity of Klinkenberg plot in data published by Rushing et al. (2004), Sample 2-33.

Fig. 12 presents experimental data published by Li et al., (2009) (Sample S3) and Dong et al., (2012) (Sample C1). The permeabilities in both samples are low enough to show significant curvature as apparent from the plot. The liquid permeability was measured experimentally by the authors for both samples and was equal to 0.028 md for Sample S3 and 0.020 md for Sample C1. Using the original Klinkenberg method, the intrinsic permeability is calculated to be 0.034 and 0.032 for Samples S3 and C1, respectively. There is clear overestimation in the straight-line method. Using the new quadratic equation (Eq. 33), the intrinsic permeability is calculated to be 0.0281 md and 0.0212 md for the Samples S3 and C1, respectively. It is clear that the new approach relieves the problem of overestimation and is more accurate in calculating the intrinsic (liquid) permeability. Table 2 summarizes the permeability values obtained by utilizing the new approach and the straight-line method for different experimental results in the

literature. All the liquid permeability values are obtained using water as the flowing fluid except the Klinkenberg's experiments which have been done using Isooctane.

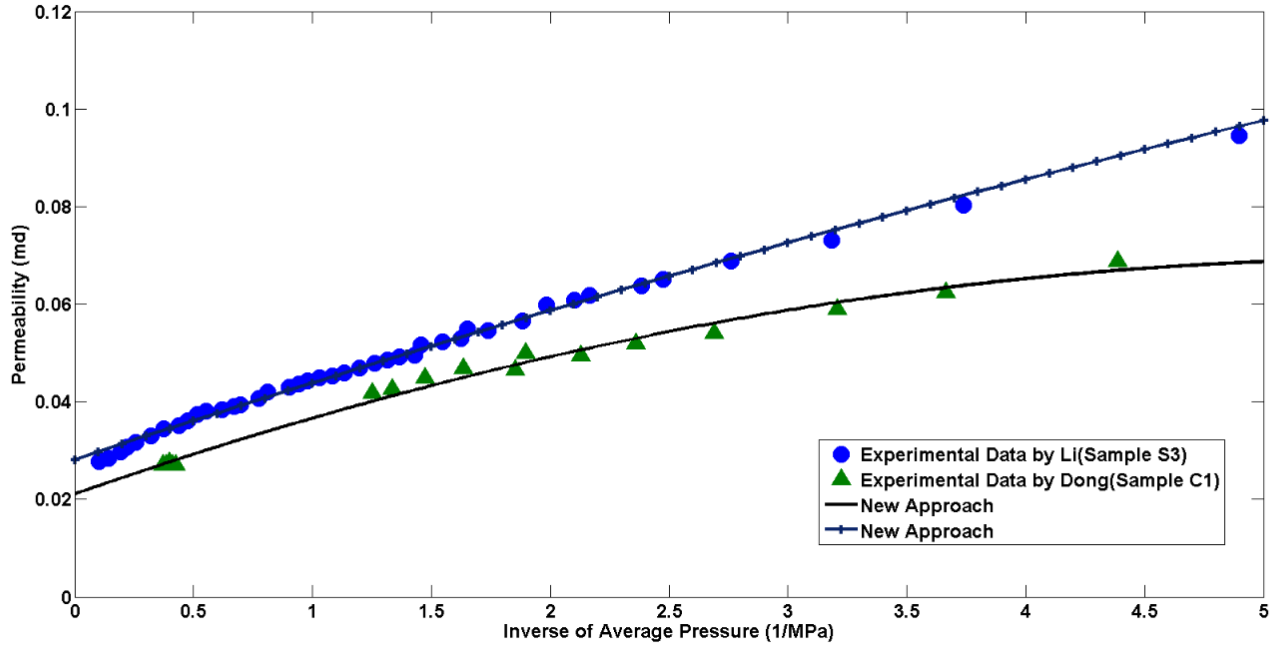


Fig. 12: Application of the new equation in experimental data by Li et al. (2009) and Dong et al. (2012).

Fig. 13 presents further comparison of the estimated permeability values using Eq. 33 and Klinkenberg's equation (Eq. 7). The permeability values are normalized by dividing by the liquid permeability values. The farther normalized permeability is from unity, the less accurate the calculation. Fig. 13 plots normalized permeability against liquid permeability from the experimental data. The dashed line represents unity. According to the graph, the values obtained using Eq. 33 are much closer to unity than are those estimated using Klinkenberg's equation. The liquid permeability for data numbers 6 and 7 in Table 2 are an order of magnitude lower than the gas permeability and therefore are not considered in the analysis in Fig. 13. The reason could be, sensitivity of sample to water (data numbers 6 and 7 are the same sample at different effective stresses) or irreversible reduction in permeability due to increasing and decreasing effective stress in their experiments (The effective stress changes from 10MPa to 160MPa and back for four cycles

before measuring the liquid permeability). Explaining such phenomena is not in the scope of this work.

Table 2: Comparison of the results of Eq. 33 and Klinkenberg's equation to the liquid permeability data

	Author	Sample	Klinkenberg 's Permeability (md)	Permeability Using Eq. 33 (md)	Liquid Permeability (md)
1	Klinkenberg (1941)	Core M	11.1	10.88	10.45
2	Klinkenberg (1941)	Core L	2.75	2.66	2.55
3	Li et al., (2009)	S3	0.034	0.0281	0.028
4	Dong et al., (2012)	C1	0.032	0.0215	0.02
5	Dong et al., (2012)	C2	0.043	0.0326	0.03
6	Tanikawa et al., (2009)	IVA418-60 MPa	1.02	0.91	0.122
7	Tanikawa et al., (2009)	IVA418-80 MPa	0.95	0.75	0.117
8	Tanikawa et al., (2009)	IVA419-60 MPa	10.42	4.02	3.66
9	Tanikawa et al., (2009).	IVA419- 100 MPa	9.82	3.52	3.23

The values of the constants “a” and “b” can be calculated by fitting the experimental data to Eq. 33. Table 3 summarizes the calculated values of “a” and “b” for the experimental data considered here. As expected from Eq. 34 and Eq. 35, the values of “a” and “b” increase as permeability decreases. The relationship between “a” and “b” is investigated to further validate the theory behind Eq. 33. According to the theory, the values of “a” and “b” should follow Eq. 36. Fig. 14 plots the values of “a” versus those of “b” from Table 3. The solid line represents the expected relationship in Eq. 36. Although some scatter is observed at larger values of “b”, a fairly satisfying match is still obtained between the calculated

values of “a” and “b” using the experimental data and the theory. However, a larger data set will be more helpful to further investigate this relationship.

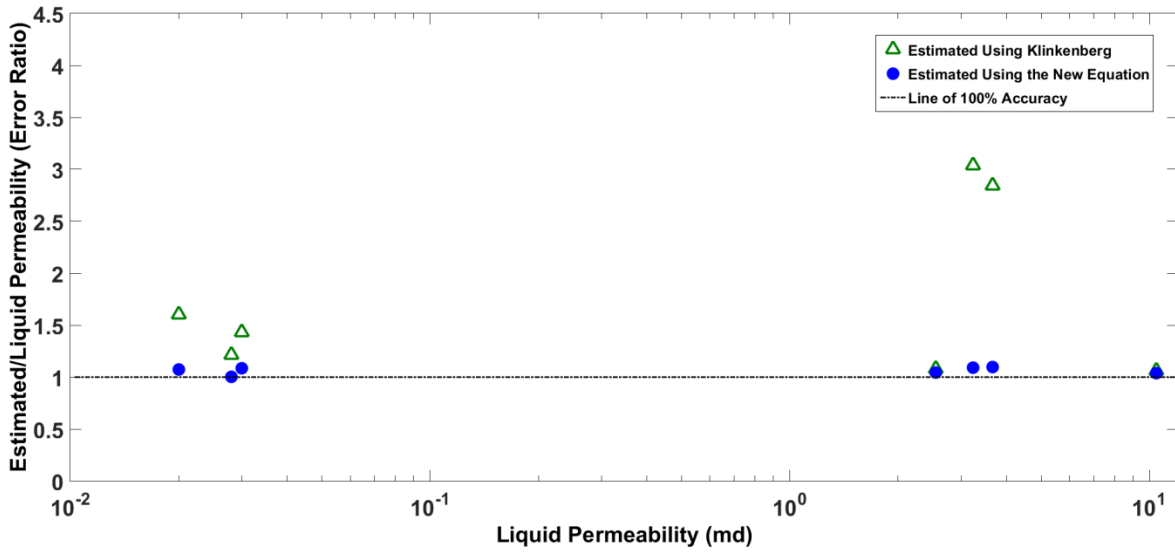


Fig. 13: Comparison of the accuracy of the Klinkenberg equation and Eq. 33.

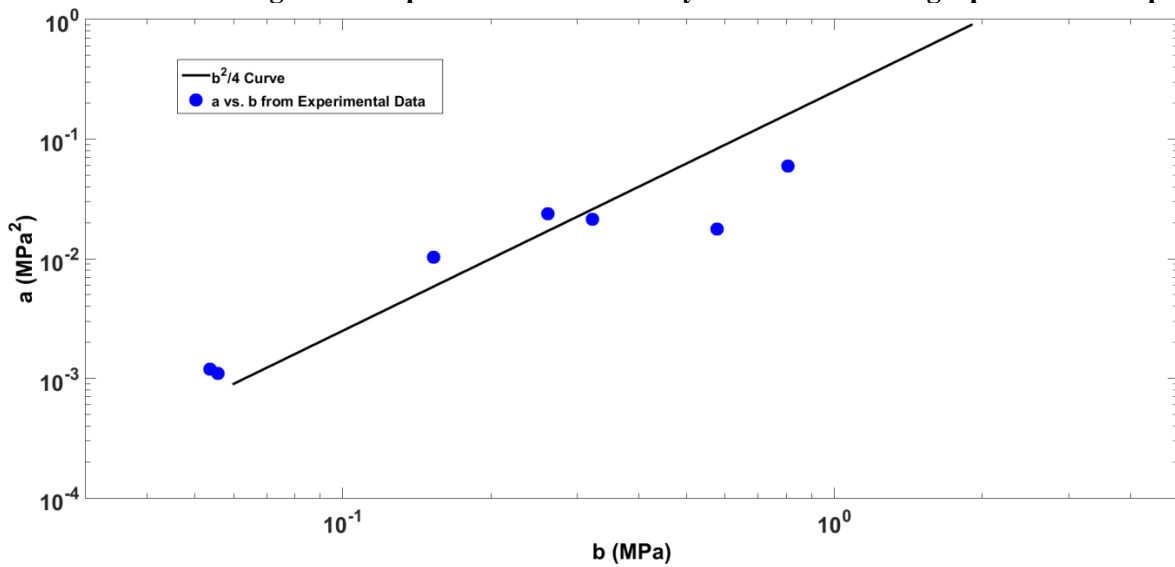


Fig. 14: Relationship between the constants “a” and “b” in Eq. 33.

Table 3: Values of constants in Eq. 33 for various data sets

	Author	Sample	Lithology/Fluid	a (MPa ²)	b (MPa)
1	Klinkenberg (1941)	Core M	Nitrogen/Not Specified	0.00110	0.0557
2	Klinkenberg (1941)	Core L	Carbon Dioxide/Not Specified	0.00119	0.0537
3	Li et al., (2009)	S3	Nitrogen/Dolomite(Slightly Shaly)	0.0178	0.577
4	Dong et al., (2012)	C1	Ethane/Dolomite	0.0598	0.805
5	Dong et al., (2012)	C2	Ethane/Dolomite	0.0215	0.322
6	Tanikawa et al., (2009)	IVA418-60 MPa	Nitrogen/Sandstone	0.0103	0.153
7	Tanikawa et al., (2009)	IVA418-80 MPa	Nitrogen/Sandstone	0.0239	0.261
8	Tanikawa et al., (2009)	IVA419-60 MPa	Nitrogen/Sandstone	0.142	1.736
9	Tanikawa et al., (2009).	IVA419- 100 MPa	Nitrogen/Sandstone	0.159	1.883

As mentioned, the values of “a” and “b” should increase as the permeability decreases. This is backed by the experimental results presented in Table 3. Eq. 34 and Eq. 35 can be used to find a direct relationship between a and b and permeability. Heid et al., (1950) proposed an equation relating the pore throat radius to porosity and permeability of a porous medium:

$$r_{\text{pores}} = 8.85 \times 10^{-8} \sqrt{\frac{k}{\phi}} \quad \text{Eq. 39}$$

Substituting Eq. 39 into Eq. 34 and Eq. 35 and merging all of the constants results in the following equations:

$$b = \frac{\beta}{\sqrt{k}} \quad \text{Eq. 40}$$

$$a = \frac{\alpha}{k} \quad \text{Eq. 41}$$

where α and β are constants related to the porosity of the medium, temperature, and the type of gas. Eq. 40 and Eq. 41 present a theoretical relationship between the values of “a” and “b” and permeability. The validity of the proposed equations is investigated in Fig. 15.

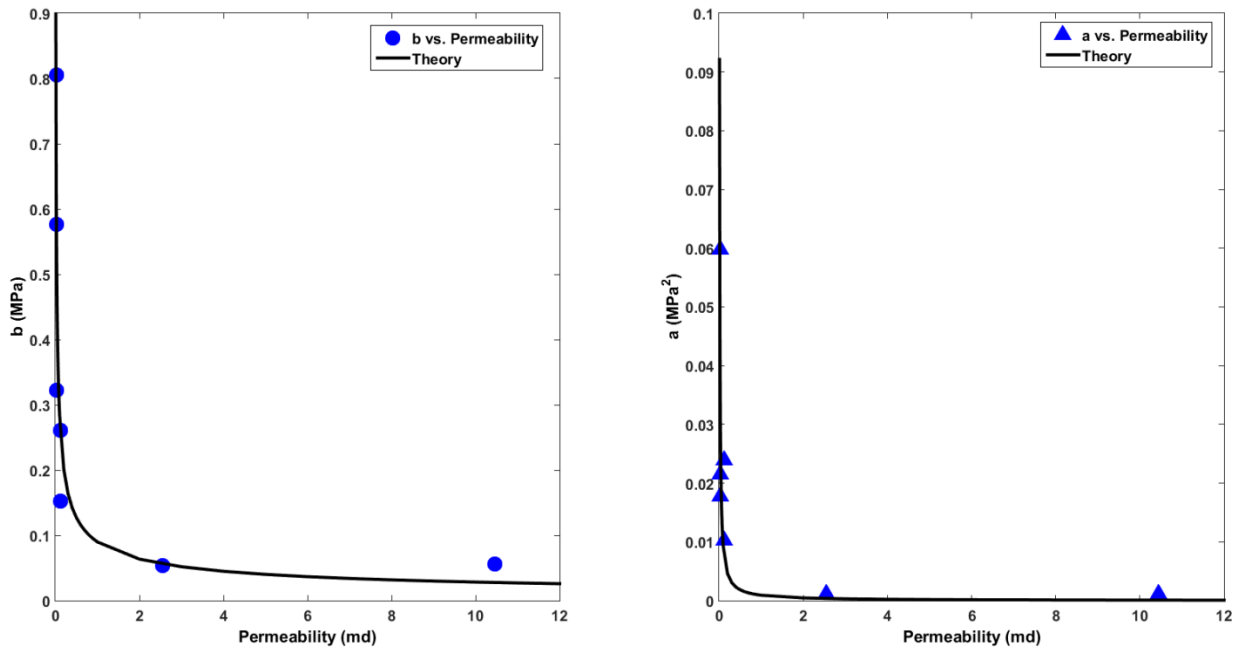


Fig. 15: The dependency of “a” (Plot on the right) and “b” (Plot on the left) to permeability. Validation of Eq. 40 and Eq. 41.

According to Fig. 15, rather accurate matches are obtained between Eq. 40 and Eq. 41 and the experimental data. This agreement leads to the validation of the slip theory from which Eq. 33, Eq. 36, Eq. 40, and Eq. 41 arise. According to Fig. 15, the values of “a” and “b” drop significantly, as permeability increases. This drop is more significant for the values of “a”. From the right hand side plot in Fig. 15, it is observed that the value of “a” is negligible at permeabilities higher than 1 md. Based on the results presented above, it is recommended to use Eq. 33 to consider

the deviation in the Klinkenberg theory. If the quadratic nature of Eq. 33 poses numerical difficulties, then as a rule of thumb for permeabilities above 1 md the value of a can be ignored and Klinkenberg's original equation can provide sufficient accuracy. According to Fig. 15, a has a significant value for permeabilities below 1 md. Therefore, large errors can occur by neglecting " a " for below 1 md.

The fundamental assumption throughout this work is continuum flow. At very large Knudsen numbers ($Kn > 0.1$) where the flow is dominated by molecular flow and diffusion, the continuum flow assumption breaks down. In such conditions Eq. 17 and Darcy equation are not suitable to describe the flow and Eq. 33 does not apply. Theories on molecular dynamics and diffusion are more suitable for that type of flow (Darabi et al., 2012). The applicability of this work is where the continuum flow assumption is valid and slip flow is dominant which is the case where Knudsen number is smaller than 0.1. The results of the gas flow regime analysis in chapter 3 illustrate that the majority of low permeability reservoirs lie under the slip or early transition flow regime. This supports the assumption of continuum flow for derivation of Eq. 33. The applicability of the new model is further investigated in chapter 6.

Production from unconventional gas reservoirs usually involves complex mechanisms. Flow in natural and induced fractures, flow through the matrix, desorption, etc., all contribute to the production of gas. Typically, an initial hike in the gas rate is observed, which is attributed to gas production from the fracture network. After the peak rate, the production declines until it reaches a certain plateau (Kalantari-Dahaghi and Mohaghegh, 2011). Assuming the matrix permeability is lower than the fracture permeability, the short term production from such reservoirs depends mainly on the fracture properties while the long term production is also dominated by matrix properties (Bustin and Bustin, 2012; Amann-Hildenbrand, 2012). According to simulations, overestimating the matrix permeability in unconventional gas reservoirs will lead to overestimation of the initial production rate and more importantly an overestimation of the long term

production (Bustin et al., 2008). Matrix permeability of less than 1 md is common in unconventional gas plays such as tight sand, shale gas (Ross and Bustin, 2008) and coal bed methane (CBM) reservoirs. Using the original Klinkenberg equation for such reservoirs can lead to overestimation of permeability that creates overestimations in the long-term production analysis and financial planning. These overestimations can be significantly reduced by using the equation proposed in this work.

Conclusion

Klinkenberg's equation has been used for decades to take the slippage effect into account. The equation has proven to be applicable over a wide range of problems. Recently, the inability of Klinkenberg's equation to describe the slippage effect accurately for the low permeability media has been detected and investigated in the literature. By using the findings of Kundt and Warburg, this work proposes a new theoretical equation similar to that of Klinkenberg to describe the slippage effect. The new equation accurately predicts the intrinsic permeability from gas flow data. Its accuracy is significantly higher than that of Klinkenberg's equation in low-permeability porous media, while it converges to Klinkenberg's at higher permeabilities.

The new equation shows a quadratic relationship between apparent permeability and the reciprocal of pressure. Validation is done using the experimental data available in the literature. The relationships between the constants and permeability are discussed. The theory is further validated by comparing the experimental calculations of the constants to the values predicted theoretically. The new equation solves the problem of overestimation of intrinsic permeability in Klinkenberg's equation and gives more accurate values. It is suggested that the proposed equation be used to analyze unconventional gas reservoirs where permeabilities are commonly less than 1 md.

Nomenclature

A, B = constants of integration, L.t-1, m.sec-1

a, b = gas slippage factor, m.L-1.t-2, atm

c = proportionality factor

k = rock permeability, L2, md

K_a = apparent permeability, L2, md

K_0 = absolute permeability, L2, md

kn = Knudsen number, dimensionless

l = length, L, m

m = coefficient

M = molecular weight, m.n-1, gr.mol-1

n = coefficient

\dot{n} = gas molar rate, n.t-1, mol.sec-1

p = fluid pressure, m.L-1.t-2, kPa [atm, Psia]

\bar{P} = average pressure, m.L-1.t-2, kPa [atm, Psia]

Q = Flow rate, L3.t-1, cm3.sec-1

R = universal gas constant, mL2.t-2.T-1, j.mol-1.k-1

T = temperature, T, K

v = fluid velocity, L.t-1, m.sec-1

μ = fluid viscosity, m.L-1.t-1, cp

ρ = fluid density, m.L-3, Kg.m-3

λ = mean free path of gas molecules, L, m

ϕ = porosity, dimensionless

α, β = Coefficients

References

- Amann-Hildenbrand, A., Ghanizadeh, A., Krooss, B.M., 2012. Transport Properties of Unconventional Gas Systems. *Marine and Petroleum Geology* 31, 90-99.
- Bird, R. B., Stewart, W. E., Lightfoot, E. N., 1960. *Transport Phenomena*. John Wiley and Sons, Inc.
- Bustin, A.M.M., Bustin, R.M., Cui, X., 2008. Importance of Fabric on the Production of Gas Shales. Paper SPE 114167 presented at the 2008 SPE Unconventional Reservoirs Conference, Keystone, Colorado, USA, 10-12 February.
- Bustin, A.M.M., Bustin, R.M., 2012. Importance of Rock Properties on the Producibility of Gas Shales. *International Journal of Coal Geology*, 103, 132-147.
- Darabi, H., Ettehad, A., Javadpour, F., Sepehrnoori, K., 2012. Gas Flow in Ultra-Tight Shale Strata. *Journal of Fluid Mechanics* 710, 641-658.
- Dong, M., Li, Z., Li, S., Yao, J., 2012. Permeabilities of Tight Reservoir Cores Determined for Gaseous and Liquid CO₂ and C₂H₆ Using Minimum Backpressure Method. *Journal of natural Gas Science and Engineering* 5, 1-5.
- Fathi, E., Tinni, A., Akkutlu, Y., 2012. Correction to Klinkenberg Slip Theory for Gas Flow in Nano-capillaries. *International Journal of Coal geology* 103, 51-59.
- Heid, J.G., McMahon, J.J., Nielsen, R.F., Yuster, S.T., 1950. Study of the Permeability of Rocks to Homogenous Fluids. *API Drilling & Production Practice*, New York 230–246.
- Jones, F.O., Owens, W.W., 1980. A Laboratory Study of Low Permeability Gas Sands. *Journal of Petroleum Technology* 32, 1631-1640.
- Kalantari-Dahaghi, A., Mohaghegh, S.D., 2011. Numerical Simulations and Multiple Realizations for Sensitivity Study of Shale Gas Reservoir. Paper SPE

141058 presented at the 2011 SPE Productions and Operations Symposium, Oklahoma City, Oklahoma, USA, 27-29 March.

Klinkenberg, L.J 1941. The permeability of porous media to liquids and gases. API Drilling and Production Practice, 200-213.

Kundt, A., Warburg, E., 1875. Poggendorfs Ann. Physik 155, 337 and 525.

Li, S., Dong, M., Li, Z., 2009. Measurement and Revised Interpretation of Gas Flow Behaviour in Tight Reservoir Cores. Journal of Petroleum Science and Engineering 65, 81-88.

Loeb, L.B. 1934. The Kinetic Theory of Gases. Second edition, McGraw-Hill Co., Inc.

Muskat, M. 1982. The Flow of Homogeneous Fluids through Porous Media. International Human Resources Development Corporation, Boston.

Noman, R. and Kalam, M.Z. 1990. Transition from Laminar to Non-Darcy Flow of Gases in Porous Media. In Advances in Core Evaluation: Accuracy and Precision in Reserves Estimation. edited by P.F. Worthington, 447-482.

Ross, D.J.K., Bustin, R.M., 2008. Characterizing the Shale Gas Resource Potential of Devonian-Mississippian Strata in the Western Canada Sedimentary Basin: Application of an integrated Formation Evaluation. The American Association of Petroleum Geologists Bulletin 92 (No. 1), 87-125.

Rushing, J.A, Newsham, K.E., Lasswell, P.M., Cox, J.C. and Blasingame, T.A. 2004. Klinkenberg-Corrected Permeability Measurements in Tight Gas Sands: Steady-State Versus Unsteady-State Techniques. Paper SPE 89867 presented at the 2004 SPE Annual Technical Conference and Exhibition, Houston, Texas, 26-29 September.

Tanikawa W., Shimamoto, T., 2009. Comparison of Klinkenberg-Corrected Gas Permeability and Water Permeability in Sedimentary Rocks. *International journal of Rock Mechanics & Mining Sciences* 46, 229-238.

Chapter 5: Laboratory Investigation of Shale and Siltstone Permeability³

Matrix permeability of shales is an important parameter in characterizing shale gas reservoirs. Permeability is typically measured using steady-state flow tests or the more timely transient methods such as pulse-decay. Due to the low permeability nature of shale rocks, slip flow regime is observed to be dominant in pore scale. As a result, permeability changes with pore pressure. Traditionally, permeability is measured at various mean pore pressures and the data is used to extract the Klinkenberg or absolute permeability. However, it has been shown recently that Klinkenberg permeability significantly overestimates the absolute (liquid) permeability of shale rocks. Additionally, several studies have shown different methods of permeability measurement can lead to significantly different results at similar pressures. In this chapter, steady-state laboratory gas flow experiments have been conducted on four shale samples using methane and nitrogen as flowing fluid. At each stage, mean pressure and mean effective stress is held constant and permeability is measured at various gas flow rates. Mean pressure is then raised and the tests are repeated at the next stage. The tests are designed to study the influence of mean pressure as well as flow rate on gas permeability. Subsequently, the samples are sheared in a triaxial cell and similar permeability tests are repeated

³ A version of this chapter has been presented at the SPE/CSUR Unconventional Resources Conference held in Calgary, Alberta, Canada, 20–22 October 2015. Additionally, part of this chapter is under review, at the time of writing this dissertation, to be published at the Journal of Natural Gas Science and Engineering. A section of this chapter is already published at SPE Journal: Moghadam, A. A. and Chalaturnyk, R. 2016. Analytical and Experimental Investigations of Gas-Flow Regimes in Shales Considering the Influence of Mean Effective Stress. SPE Journal 21(02), 557-572. <http://dx.doi.org/10.2118/178429-PA>.

to compare the permeability behavior before and after shearing. Finally, the samples are saturated with water to measure water permeability in order to analyze the gas permeability observations using theory. The results of the laboratory tests are discussed in chapter 6. The results of the laboratory measurements are presented in Appendix B.

Introduction

Permeability is one of the most important parameters that control production. Permeability is defined for a rock according to a steady state flow of fluids (liquid) through a porous media and is a measure of fluid conductivity. This parameter has been measured using laboratory testing, logs, correlations, etc. for conventional reservoirs. However, permeability measurement in ultra-low permeability shale rocks is challenging and does not follow similar physics to conventional rocks. Gas permeability in low permeability porous media is not a constant value and changes with pore pressure. This pressure dependence has been observed by numerous researchers. Klinkenberg (1941) proposed an equation to estimate the permeability of the porous medium from gas permeability measurements. However, the dependence of permeability to pressure for shales is far more complex and Klinkenberg's correlation gives erroneous results (Moghadam and Chalaturnyk, 2016; Ziarani and Aguilera, 2012).

Permeability Models

Significant research has been conducted on shale permeability. Theoretical and analytical investigations into shale permeability have been done by several authors (Moghadam and Chalaturnyk, 2014; Sakhaee-Pour, and Bryant, 2012; Javadpour et al., 2007; Ziarani and Aguilera, 2012; Roy et al., 2003). Moghadam and Chalaturnyk (2014) proposed an expansion to Klinkenberg's equation for slip flow by changing the zero velocity gradient assumption in Klinkenberg's original work (details presented in chapter 4). The proposed equation is expected to predict gas

permeability in shales flowing under slip and early transition flow regime. Laboratory results are used to match the equation and provide a range for parameters. Ziarani and Aguilera (2012) investigated a second-order Knudsen correlation to calculate gas permeability and concluded that Klinkenberg's correlation underestimates the permeability enhancement due to slip flow. Darabi et al., (2012) proposed an apparent permeability function (APF) assuming Knudsen diffusion and slip flow are the dominant flow regimes in shale pores. Rahmanian et al., (2013) assumed that flow in shales is composed of a viscous flow and a free molecular flow component. Singh et al., (2014) proposed an equation for apparent permeability based on Darcy and Knudsen flow. The proposed equations for apparent permeability tend to come with a myriad of parameters (typically empirical) that should be evaluated using laboratory experiments. Difficulties arise when some parameters cannot be directly measured in the lab. Additionally, relating the apparent permeability to Knudsen number requires pore size measurements which are not common and change with test conditions, such as mean effective stress. Ideally, apparent permeability should be related to more tangible parameters such as pore pressure and liquid permeability.

Permeability Measurement Techniques

In addition to the extensive theoretical studies, several experimental investigations of shale permeability has been conducted (Moghadam and Chalaturnyk, 2015; Heller and Zoback, 2013; Bustin et al., 2008; Ghanizadeh et al., 2013; Ghanizadeh et al., 2014; Heller et al., 2014). There are a few experimental techniques to measure the permeability of a core. Steady-state, pulse-decay, profile permeability, and crushed rock permeability are some of the most popular methods. There is no consistency between these methods and each could yield a different value for permeability sometimes orders of magnitude different (Ghanizadeh et al., 2015; Rushing et al., 2004; Sinha et al., 2012; Clarkson et al., 2012). Typically, profile permeability returns a higher permeability value at the same test conditions compared to pulse-decay method and both methods measure higher permeability

values than crushed rock permeability (Ghanizadeh et al., 2015). Crushed rock and profile permeability measurements are conducted on samples with no confining stress. Effective stress has a dominant effect on the permeability of rocks (Heller et al., 2014; Moghadam and Chalaturnyk, 2016) therefore the permeability measured at no confining stress is not a representation of reservoir condition. Pulse-decay method is a transient technique that creates a pressure pulse across the core. Permeability is then derived indirectly from the pressure decay with time typically using the solution proposed by Brace et al., (1968). The tests can be done at various pore pressures and confining stresses in a timely manner. Deriving permeability from transient pressure response needs further assumptions and parameters that add a layer of uncertainty when dealing with shale rocks. The physics of flow are not well understood in shales and therefore the number of assumptions should be minimized. Additionally, in pulse-decay method the pressure across the sample changes with time. This causes the flow rate through the sample to change and therefore the potential rate dependency of permeability is not captured.

Steady-state permeability measurements are done by flowing gas through the core at a constant rate or constant differential pressure. When the equilibrium is reached the pressure difference across the sample and flow rate is used to calculate the apparent permeability using the Darcy equation. Fundamentally, permeability is defined for steady-state flow through porous media. Therefore, the results of this method come directly from definition and no assumption on flow regime is needed. Tests can be done at various mean pore pressures, confining stresses, and flow rates. Using steady-state method to measure shale permeability takes a longer time compared to other testing techniques and therefore is not popular. In this work however, we have used the steady-state method due to the higher flexibility in testing conditions and more fundamentally accurate results.

Apparent permeability measured in the lab has a strong relationship with mean pore pressure, due to the slip flow regime. As pore pressure increases apparent permeability decreases, due to a reduction in slippage effect. Moghadam and Chalaturnyk (2016) proposed a flow regime map (presented in chapter 3) that

outlines the gas flow regime versus permeability and pore pressure. Fig. 6 shows the flow regime map for methane at 60 degrees Celsius. Their results according to Fig. 6 show that for the shale rocks the flow regime lies under the slip flow regime or early transition flow regime regardless of the pore pressure. Therefore, for low permeability shale rocks the apparent permeability is very sensitive to pore pressure. Fig. 16 illustrates the range of permeability values measured for four shale/siltstone samples in this study. The permeability changes more than one order of magnitude depending on the pore pressure of the test. Pore pressure in experiments presented in Fig. 16 changes from 2 to 8 MPa.

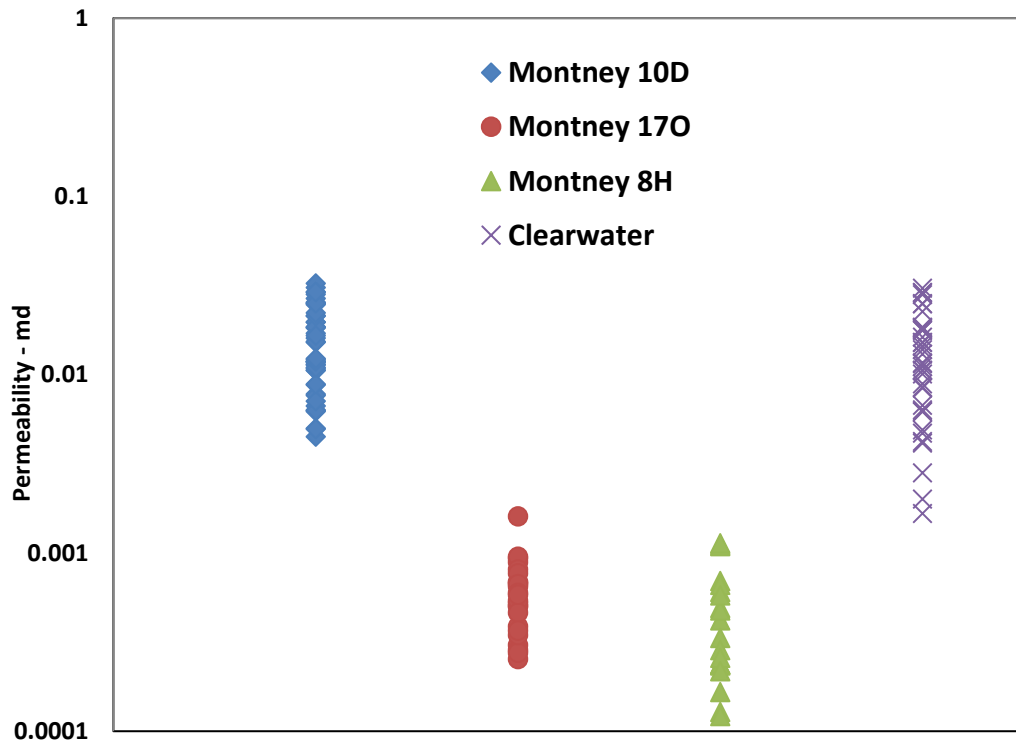


Fig. 16: Variation of permeability with pore pressure for the samples used in this study.

In this work, an experimental study is conducted to investigate permeability of shales. Steady-state permeability measurement technique is used for all the tests. The influence of mean pore pressure, gas flow rate, temperature, and mean effective

stress on apparent permeability is investigated. Measurements are repeated on failed samples to study the influence of fractures on apparent gas permeability.

Laboratory Experiments

Sample Description

Steady-state gas permeability tests were conducted on four dry shale/siltstone samples, one from the Clearwater Formation in Alberta, Canada, and three from the Montney formation in British Columbia, Canada. Nitrogen was used as the flowing fluid for the Clearwater sample, and methane for the Montney samples, all at room temperature (25°C). Table 4 shows a summary of sample dimensions and experimental conditions. The size of the Montney samples was chosen to be relatively small (1.2 cm in length) in order to save time when running steady-state permeability tests. Fig. 17 shows an image of the Montney 10D sample. Table 5 presents the mineralogy of the Montney samples. The Montney 10D and 8H samples are mainly comprised of silicates (quartz) while the Montney 17O sample has significant amounts of carbonates (dolomite). All samples had relatively low clay content (8-16%). Clearwater formation is a caprock shale and does not contain organic matter. The organic content of the Montney samples are below 2% also presented in Table 5. The porosity of the samples is measured using Mercury injection method through a commercial lab. Samples were cored from bigger specimens and ground to ensure that top and bottom surfaces were parallel. The Clearwater sample was cored perpendicular to the bedding and the Montney samples were drilled parallel to the bedding planes. While all samples were largely intact, hairline cracks were noticed on their surfaces. None of these seemed to go through the samples.

Table 4: Summary of samples used in the steady-state gas permeability experiments.

Sample	Height (cm)	Diameter (in.)	Porosity (%)	Fluid Type	Eff. Stress (MPa)	Pore Pressure Range (MPa)
Clearwater	4.0	2.5	20	Nitrogen	3.5	0.4-5.0
Montney 10D	1.2	1.5	4.4	Methane	20.0	2.0-8.0
Montney 17O	1.2	1.5	2.1	Methane	10.0, 20.0	2.0-8.0
Montney 8H	1.2	1.5	2.8	Methane	10.0, 20.0	2.0-8.0

Table 5: Mineralogy of the Montney samples (mass %).

Sample	Quartz	Clays	Carbonates	Feldspar + Plagioclase + Muscovite	Other	TOC (%)
Montney 10D	37.78	13.35	24.58	20.00	4.29	1.19
Montney 17O	18.67	8.36	65.92	5.04	2.01	0.56
Montney 8H	35.62	16.92	18.71	25.04	3.71	1.94



Fig. 17: Montney 10D sample. Porous stones are placed at the top and the bottom of the sample to ensure linear flow. Pictures of other samples are available upon request, though they look very similar to the Montney 10D sample.

Laboratory Setup

The samples are placed in a triaxial cell with a Viton membrane separating them from the confining fluid. The confining fluid (Silicon oil) exerts isotropic stress on the samples. A ram sits at the top of the sample to apply axial stress. Confining and axial stress are controlled using two ISCO pumps with hydraulic oil as the pressurized fluid. Porous stones similar in thickness to the samples are placed at the top and bottom of the samples to minimize end effects. Given the high permeability of the porous stones (in the order of Darcies) compared to the samples, the influence of porous stone permeability is ignored in the data analysis. The bottom of the sample is connected to a Quizix Q-5000 pump for upstream pressure. Gas is supplied to the Quizix pump from a high pressure gas cylinder. The top of the sample is connected to an accumulator. The accumulator is used to maintain downstream pressure and to collect the gas passing through the sample. The

pressure at the accumulator is controlled using an ISCO pump. The entire setup is built inside a temperature-controlled oven to ensure isothermal condition. Pressure is recorded at the upstream and downstream of the sample using Honeywell FP2000 pressure transducers with an accuracy of $\pm 0.1\%$. Temperature of the gas and confining fluid is measured using thermocouples. The gas rate is measured using the Quizix pump at the upstream capable of measuring flow rate as low as 100 nL/min with an accuracy of $\pm 0.1\%$. The flow rate measured at the upstream is matched with the rate measured by ISCO pump at the downstream to ensure no leakage exists. The measurements are recorded in 30-second increments using an in-house data logging program based on LABVIEW. Fig. 18, and Fig. 19 present the schematics of the laboratory setup and a picture of the setup, respectively.

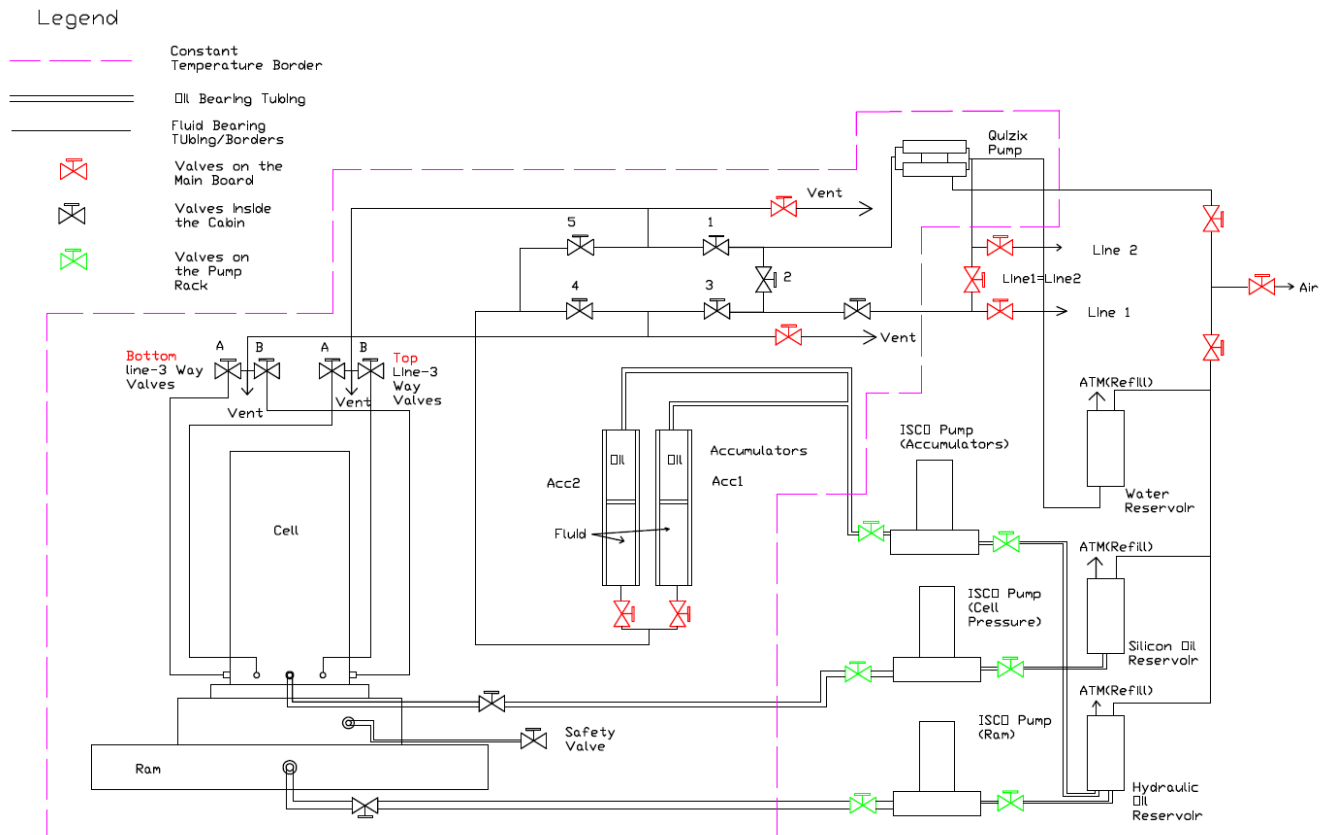


Fig. 18: Schematics of the laboratory setup. Gas flows through a Quizix pump into the bottom of the sample and exits at the top. The gas is then collected in the accumulator which keeps the downstream pressure constant.



Fig. 19: On the right: An image of the whole setup. Gas cylinders, ISCO pumps and the temperature-controlled oven are displayed. On the left: An image of the inside of the temperature-controlled oven. The cell, the ram, accumulators, and the Quizix pump are displayed.

Methodology

After the samples are prepared, they are placed in the triaxial cell. The Clearwater sample is saturated with nitrogen, and the Montney samples with methane. Nitrogen or methane first flows through the sample to extract most of the air in the pores and in the system. Afterwards, the downstream is closed and pore pressure is raised. The samples are consolidated (pre-stressed) at the predetermined mean effective stress level and saturated over 24 hours or until the gas pressure is constant, whichever takes longer. During the tests, the mean effective stress (confining stress minus pore pressure) is kept constant within 1%. For all the tests, gas flows into the bottom of each sample and exits at the top. The upstream gas rate is controlled via the Quizix Q-5000 pump, and gas is collected downstream in the accumulator. The gas tests are done at a constant flow rate (as measured by the Quizix pump), and

pressures at the top and bottom are recorded with high-precision pressure transducers. As neither of the samples contain significant organic material, the effect of adsorption on permeability is ignored. One out of ten experiment runs are repeated to ensure repeatability of the tests. The apparent permeability of the repeated tests is observed to be within the range of the experimental error (5-30% depending on the testing condition).

After the consolidation and saturation phases, downstream pressure is set to a constant value in the accumulator and the Quizix pump injects gas through the bottom of the sample at a constant rate. Gas pressure upstream and downstream of the samples was monitored until equilibrium was reached. Subsequently, the gas flow rate is increased in the Quizix pump while the downstream pressure is slightly decreased. Gas flows until pressure equilibrium is reached. Then the flow rate is raised once more. The purpose of this methodology is to measure gas permeability at a constant mean pressure and effective stress while changing the rate. At each mean pressure, the tests are done at several different flow rates. The mean pressure is then raised to a higher value at the same time the confining stress is raised accordingly to keep the mean effective stress constant. Similar tests are repeated at the new mean pressure. The tests are done at mean pressures of approximately 2, 4, 6 and 8 MPa. Mean effective stress is kept constant for all mean pressure levels. Fig. 20 shows an example of the rate and mean pressure steps at which the tests are conducted. It should be noted that the flow rate of gas depends on the pressure. The flow rates in Fig. 20 are measured at the specific mean pressure the test is conducted. For the purpose of the calculations, the flow rates are converted to mass rate. An example of the pressure response for two consecutive rate steps is presented in Fig. 21. After the equilibrium in the first step is reached, the rate is raised. This will cause the upstream pressure to increase accordingly. However, in order to keep the mean pressure reasonably constant the downstream pressure in the accumulator is reduced.

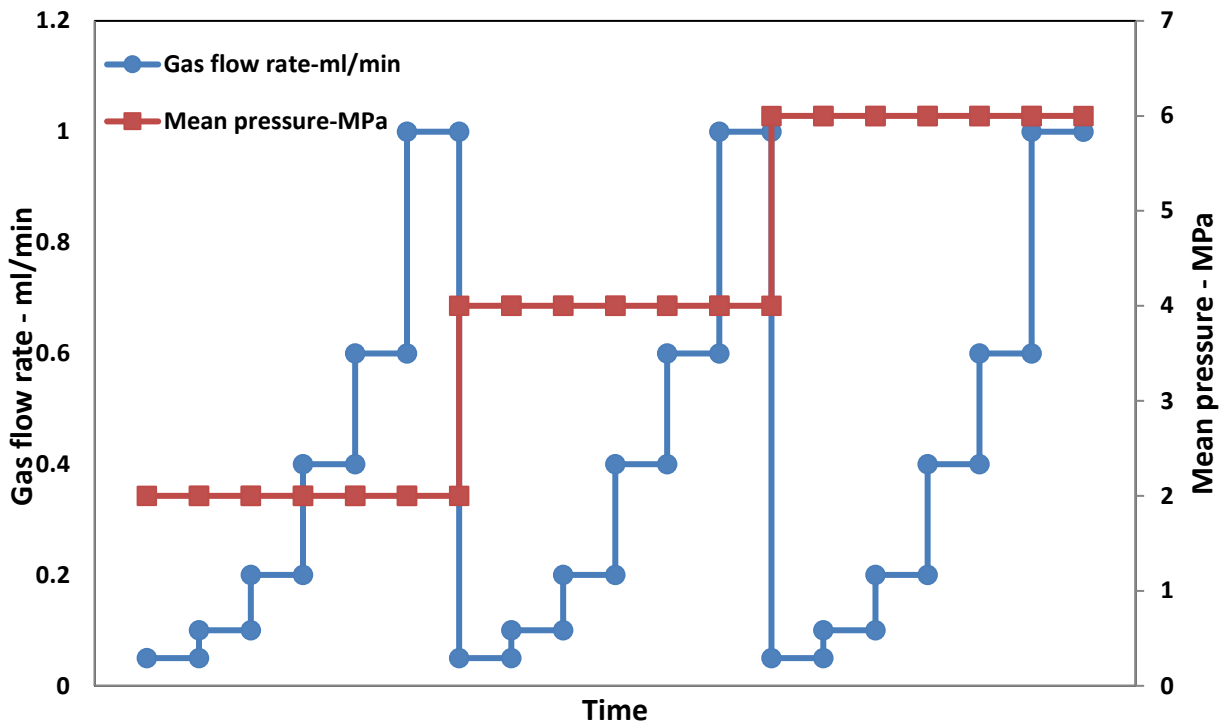


Fig. 20: Flow rate and mean pressure steps for permeability tests. Time axis is not to scale. Sufficient time was allowed between each step for the pressures to equilibrate. Tests at lower rates took longer than higher rates. Each gas permeability test took 1 to 8 hours to equilibrate depending on the sample and rate.

To save time, at the start of each test, upstream pressure is raised higher than the downstream pressure in order to reach equilibrium faster. Each steady state gas test takes 1 to 8 hours depending on the sample, and flow rate. Tests at lower rates take longer to reach equilibrium compared to higher rates. In order to avoid creating an unbalanced effective stress at the two ends of the samples and possible non-darcy flow behavior at high pressure gradients, the pressure difference across all samples is kept at less than 5% of the mean effective stress. After the gas permeability tests, each sample goes through different experiments designed to investigate various phenomena, outlined in the following.

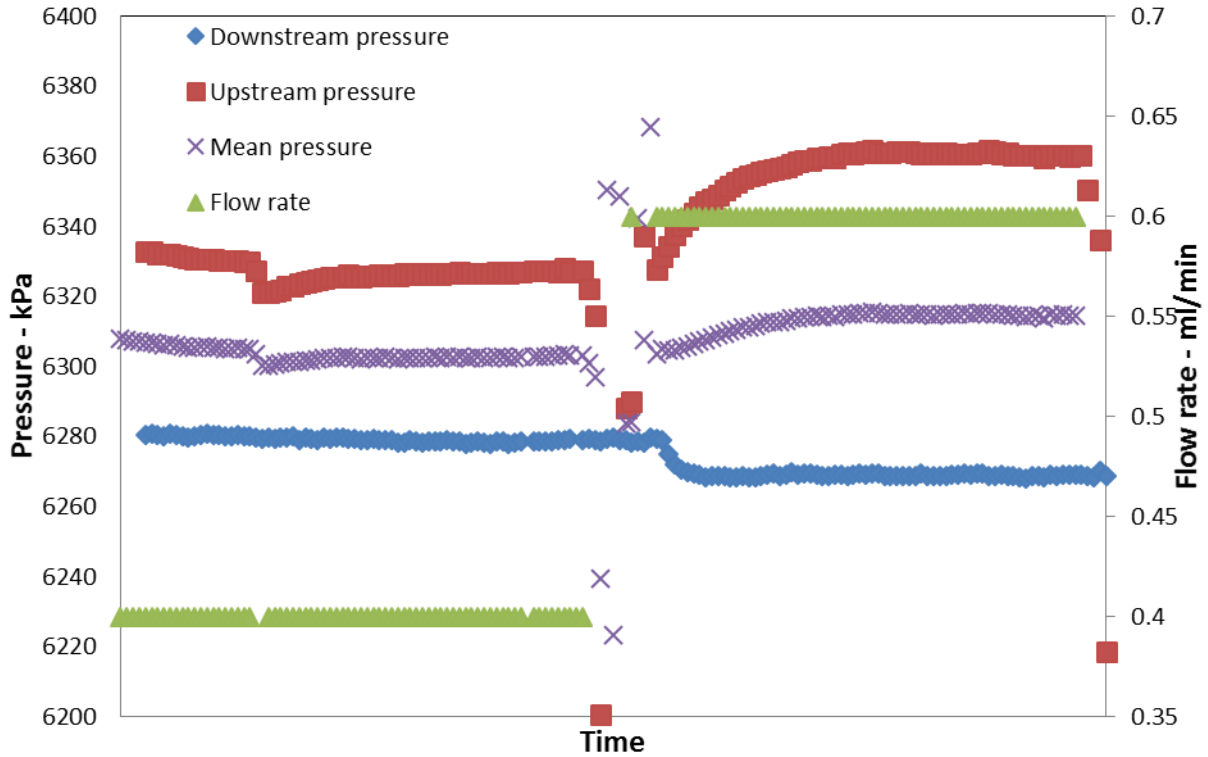


Fig. 21: An example of the pressure response for two consecutive rate steps. After equilibrium in the first step, the rate is increased to 0.6 ml/min from 0.4 ml/min. Downstream pressure is set to a lower number in the accumulator to keep the mean pressure constant within an acceptable range.

Axial stress is raised on the Clearwater sample to create a deviatoric stress condition. The gas tests are then repeated in the manner depicted in Fig. 20 at various rates and constant mean pressure. The goal is to observe the behavior of permeability under a deviatoric stress condition as opposed to an isotropic stress condition.

The Montney 10D sample is saturated with nitrogen, and gas permeability tests are conducted to compare nitrogen permeability to that of methane. The tests are once again done at various rates and constant mean pressure. In order to saturate the sample with nitrogen, first the sample is isolated from the system and nitrogen flows through all the lines. Then the valves to the sample are opened to the system and nitrogen flows through the sample for 3 hours, while the downstream is open

to atmosphere. This process is done at a low gas pressure in order to ensure the remaining methane in the sample has low concentration. The nitrogen pressure is raised and the sample sits for 24 hours or until the pressure stays constant, whichever takes longer. During the saturation process the mean effective stress is kept constant. For one of the test sets for the Montney 10D sample, temperature is raised to 45 C in order to observe the effect of temperature on apparent permeability.

For the Montney 17O sample, the mean effective stress is reduced from 20 MPa to 10 MPa and gas permeability tests are conducted at several mean pressures and constant rate.

After all the gas permeability tests are over, the gas is vented. The accumulator valve is closed to ensure a minimal volume of gas in the system. Afterwards, the system (flow lines and sample) is saturated with water at 5 MPa for 72 hours while maintaining the effective stress constant. It is presumed that all the remaining gas in the sample would dissolve in water at 5 MPa. Water permeability tests have been carried out on each sample at different mean effective stresses. Each test with water takes approximately one week to equilibrate. In our experience, it is easier to run steady-state gas permeability tests at a constant rate, and steady-state water permeability tests at a constant differential pressure. The rate sensitivity of water permeability was not investigated due to the long stabilization period.

Next stage, the ram is lowered slowly to increase the axial stress on all the samples. As axial stress increases at a constant confining stress, the sample fails. The pore pressure valves during the shearing stage are left open to simulate drained conditions. After the failure, water permeability is measured once again.

Subsequently, the system is drained and again saturated with gas. Gas is allowed to flow through the sample for 6 hours to push the water out of the sample. At this stage, there are cracks in the sample that enhance the permeability. Gas permeability measurements are repeated as explained previously and presented in Fig. 20. The mean pressure levels are raised from 2 to 6 or 8 MPa while keeping

the mean effective stress constant. After reaching the highest mean pressure intended, then confining stress is kept constant and pore pressure is dropped. This is intended to simulate a reservoir depletion scenario. As the mean pressure is dropped, at certain levels (typically 4 and 2 MPa) gas permeability tests are repeated at various rates. Table 6 summarizes the experimental investigations conducted on each sample.

Table 6: The steps of the experimental investigation for each sample.

Steps	Clearwater	Montney 10D	Montney 17O	Montney 8H
1	Gas permeability tests using nitrogen at various mean pressures and flow rates	Gas permeability tests using methane at various mean pressures and flow rates	Gas permeability tests using methane at various mean pressures and flow rates	Gas permeability tests using methane at various mean pressures and flow rates
2	Exerting a deviatoric stress on the sample and running gas permeability tests at various mean pressures and flow rates	Saturated with nitrogen. Gas permeability tests conducted at various flow rates at 25 and 45 C	Mean effective stress is decreased to 10 MPA and the tests from the last step are repeated	Gas permeability tests conducted at one mean pressure and various flow rates at 45 C
3	Water permeability is measured	Water permeability is measured	Water permeability is measured	Water permeability is measured
4	Sample is sheared	Sample is sheared and water permeability is measured again	Sample is sheared and water permeability is measured again	Sample is sheared and water permeability is measured again
Steps	Clearwater	Montney 10D	Montney 17O	Montney 8H

5	Gas permeability tests are repeated for the post failure condition	Gas permeability tests are repeated for the post failure condition	Gas permeability tests are repeated for the post failure condition	Gas permeability tests are repeated for the post failure condition
6	A depletion scenario is simulated by decreasing pore pressure while maintaining a constant confining stress. Gas permeability is measured.	A depletion scenario is simulated by decreasing pore pressure while maintaining a constant confining stress. Gas permeability is measured.	A depletion scenario is simulated by decreasing pore pressure while maintaining a constant confining stress. Gas permeability is measured.	A depletion scenario is simulated by decreasing pore pressure while maintaining a constant confining stress. Gas permeability is measured.

Calculations

Eq. 42 shows the apparent permeability calculated using the Darcy equation modified for gases.

$$k_{app} = \frac{2\bar{\mu}\bar{z}\dot{m}RTL}{AM(P_{up}^2 - P_{Down}^2)} \quad \text{Eq. 42}$$

k_{app} is apparent permeability and $\bar{\mu}$ is gas viscosity calculated at the average gas pressure using the correlation proposed by Kestin and Liedenfrost (1959) for nitrogen and the correlation proposed by Lee et al. (1966) for methane. \bar{z} is the gas compressibility factor measured at average pressure using the Peng-Robinson equation of state (Peng and Robinson, 1976). R is the gas constant, T is temperature, L and A are the length and cross-sectional area of the sample, respectively, M is the molecular weight of the gas, and P_{up} and P_{Down} are the pressures upstream and

downstream of the sample, respectively. \dot{m} is the mass flow rate of gas through the sample and is calculated using Eq. 43, which is a form of real gas law.

$$\dot{m} = \frac{P_{up}QM}{zRT} \quad \text{Eq. 43}$$

Q is the flow rate measured upstream using the Quizix pump. After the flow reaches equilibrium, upstream and downstream pressures are recorded along with flow rate, and Eq. 42 and Eq. 43 are used to calculate apparent permeability.

The Knudsen number is a dimensionless number used as a measure of rarefaction of gas molecules, and to distinguish flow regimes in gas flow. The Knudsen number is defined as the ratio of mean free path of gas molecules (a measure of distance between molecules) to pore size (Eq. 1). The values of Knudsen number is reported with the lab results where appropriate. The mean free path is calculated using Eq. 2 at the test temperature and mean pressure. Determining a representative pore radius is a challenging part of calculating Knudsen numbers. The pore radius value in Eq. 1 is taken from the mercury injection results. It must be noted however, that the tests were conducted at a high mean effective stress (20 MPa for the Montney samples). Therefore, the pore radius of the samples under the test conditions should be smaller than the values obtained from the mercury injection tests. This leads to an underestimation of the calculated Knudsen values. As the underestimation exists equally for all the tests, it is still meaningful to make a comparison of the reported Knudsen number values. Analyzing the Knudsen numbers of the tests indicate an agreement with the theories of gas flow regime and is helpful in analyzing the data.

The mean effective stress for all the tests is calculated using Eq. 9. In this work, χ is assumed to be equal to 1. A discussion on the value of χ is provided in chapter 6.

Summary

In this chapter, extensive steady-state gas and water permeability tests have been conducted on four shale/siltstone samples, using methane or nitrogen. Sample preparation, description of the laboratory setup, testing methodology for each

sample, and apparent permeability calculations are explained. The experiments are designed in order to verify the analytical equation proposed to model gas apparent permeability, in chapter 4. Additionally, the influence of flow rate, pore pressure, mean effective stress, and temperature on apparent permeability of gas is investigated. The results of the permeability measurements are presented in Appendix B.

References

Brace, W.F., Walsh, J.B., and Frangos, W.T., 1968. Permeability of granite under high pressure. *Journal of Geophysical Research* 73, 2225-2236.

Bustin, R.M., Bustin, A.M.M., Cui, A., Ross, D., and Pathi, V.M., 2008. Impact of shale properties on pore structure and storage characteristics. Paper SPE 119892-MS presented at the SPE Shale Gas Production Conference, Fort Worth, Texas, USA.

Clarkson, C.R., Jensen, J.L., Pedersen, P.K., Freeman, M., 2012. Innovative Methods for Flow Unit and Pore Structure Analysis in a Tight Siltstone and Shale Gas Reservoir. *AAPG Bulletin* 96(2), 355-374.

Darabi, H., Ettehad, A., Javadpour, F., Sepehrnoori, K., 2012. Gas Flow in Ultra-Tight Shale Strata. *Journal of Fluid Mechanics* 710, 641-658.

Ghanizadeh, A., Amann-Hildenbrand, A., Gasparik, M., Gensterblum, Y., Krooss, B.M., Littke, R., 2013. Experimental study of fluid transport processes in the matrix system of the European organic-rich shales: II. Posidonia Shale (Lower Toarcian, northern Germany). *International Journal of Coal Geology* 123, 20-33.

Ghanizadeh, A., Bhowmik, S., Haeri-Ardakani, O., Sanei, H., Clarkson, C.R., 2015. A Comparison of Shale Permeability Coefficients Derived Using Multiple Non-steady-state Measurement Techniques: Examples from the Duvernay Formation, Alberta (Canada). *Fuel* 140, 371-387.

Ghanizadeh, A., Gasparik, M., Amann-Hildenbrand, A., Gensterblum, Y., Krooss, B.M., 2014. Experimental study of fluid transport processes in the matrix system of the European organic-rich shales: I. Scandinavian Alum Shale. *Marine and Petroleum Geology* 51, 79-99.

Heller, R., Vermilyen, J., Zoback, M., 2014. Experimental Investigation of Matrix Permeability of Gas Shales. *AAPG Bulletin* 98 (5), 975-995.

Heller, R., Zoback, M., 2013. Laboratory Measurements of Matrix Permeability and Slippage Enhanced Permeability in Gas Shales. Paper SPE 168856-MS presented at Unconventional Resources Technology Conference, Denver, Colorado, USA, August 12-14.

Javadpour, F., Fisher, D., Unsworth, M., 2007. Nanoscale Gas Flow in Shale Gas Sediments. *Journal of Canadian Petroleum Technology* 46.

Kestin, J., and Leidenfrost, W., 1959. An Absolute Determination of Viscosity of Eleven Gases over a Range of Pressures. *Physica* 25 (7-12), 1033-1062.

Klinkenberg, L.J 1941. The permeability of porous media to liquids and gases. *API Drilling and Production Practice*, 200-213.

Lee, A. L., Gonzalez, M. H., Eakin, B. E., 1966. The Viscosity of Natural Gases. *Journal of Petroleum Technology* 18(08), 997-1000.

Moghadam, A.A., Chalaturnyk, R., 2014. Expansion of the Klinkenberg's slippage equation to low permeability porous media. *International Journal of Coal Geology* 123, 2-9.

Moghadam, A.A., Chalaturnyk, R., 2015. Laboratory Investigation of Shale Permeability. Paper SPE 175919 presented at the the SPE/CSUR Unconventional Resources Conference held in Calgary, Alberta, Canada, 20–22 October 2015.

Moghadam, A. A. and Chalaturnyk, R. 2016. Analytical and Experimental Investigations of Gas-Flow Regimes in Shales Considering the Influence of Mean

Effective Stress. SPE Journal 21(02), 557-572. <http://dx.doi.org/10.2118/178429-PA>.

Peng, D.Y., and Robinson, D.B., 1976. A New Two-Constant Equation of State. Industrial and Engineering Chemistry: Fundamentals 15, 59-64.

Rahmanian, M., Aguilera, R., & Kantzas, A., 2013. A New Unified Diffusion--Viscous-Flow Model Based on Pore-Level Studies of Tight Gas Formations. SPE Journal 18(01), 38-49.

Roy, S., Raju, R., Chuang, H.F., Cruden, B.A., Meyyappan, M., 2003. Modeling gas flow through microchannels and nanopores. Journal of Applied Physics 93, 4870–4879.

Rushing, J.A, Newsham, K.E., Lasswell, P.M., Cox, J.C. and Blasingame, T.A. 2004. Klinkenberg-Corrected Permeability Measurements in Tight Gas Sands: Steady-State versus Unsteady-State Techniques. Paper SPE 89867 presented at the 2004 SPE Annual Technical Conference and Exhibition, Houston, Texas, 26-29 September.

Sakhaee-Pour, A., Bryant, S., 2012. Gas Permeability of Shale. SPE Reservoir Evaluation & Engineering 15(04) 401-409.

Singh, H., Javadpour, F., Ettehadtavakkol, and A., Darabi, H., 2014. Nonempirical apparent permeability of shale. SPE Reservoir Evaluation & Engineering 17(03), 414-424.

Sinha, S., Braun, E. M., Passey, Q. R., Leonardi, S. A., Wood, A. C., Zirkle, T., Kudva, R. A. 2012. Advances in Measurement Standards and Flow Properties Measurements for Tight Rocks such as Shales. Paper SPE 152257 presented at the 2012 SPE/EAGE European Unconventional Resources Conference and Exhibition, Vienna, Austria, 20-22 March.

Ziarani, A.S., Aguilera, R., 2012. Knudsen's permeability correction for tight porous media. Transport in Porous Media 91(1), 239-260.

Chapter 6: Analytical and Experimental Investigations of Gas Flow Regimes in Shales Considering the Influence of Mean Effective Stress⁴

Flow conditions determine the flow regimes governing gas flow in porous media. Slip flow regime commonly occurs in laboratory gas permeability measurements of conventional reservoir rocks, and the physics of that must be considered when finding the absolute permeability of a sample. Accurate permeability estimates are paramount for production forecasts, financial planning, and recovery estimation. The results from chapter 3 indicate that slip flow is present in low-permeability rocks both in the laboratory environment and reservoir conditions. Gas flow through the matrix lies under the slip flow regime for the majority of low-permeability reservoir production scenarios, and accurate prediction of pressure and production rate requires a good understanding of the flow regime. Chapter 4

⁴ A version of this chapter has been presented at the Geoconvention 2015 held by the Canadian Society of Petroleum geologists (CSPG), Calgary, Alberta. Additionally, part of this chapter is under review, at the time of writing this dissertation, to be published at the Journal of Natural Gas Science and Engineering. A section of this chapter is already published at SPE Journal: Moghadam, A. A. and Chalaturnyk, R. 2016. Analytical and Experimental Investigations of Gas-Flow Regimes in Shales Considering the Influence of Mean Effective Stress. SPE Journal 21(02), 557-572. <http://dx.doi.org/10.2118/178429-PA>.

presents a new equation to describe gas flow under reservoir and lab conditions, suitable for low permeability porous media. Chapter 5 outlines the details of the laboratory experiments conducted to first verify the new equation in chapter 4 and second, to investigate the influence of effective stress, temperature, gas rate, and gas type on apparent permeability. In this chapter, the results of steady-state gas permeability experiments are presented. The analytical model proposed in chapter 4 is used to match the experimental results which could explain the order of magnitude difference between the gas and liquid permeability in shales. Experimental results are combined with further tests available in the literature to inform a discussion of the model's parameters. The results improve the accuracy of gas flow modelling and of absolute permeability estimates from lab tests. Similar tests done at various mean effective stresses investigate the influence of mean effective stress on flow regime and apparent permeability. The results indicate that flow regime is a function of mean effective stress, and that the apparent permeability of shale rocks is a function of both flow regime and mean effective stress.

The permeability tests are conducted at various gas flow rates. The results indicate strong rate sensitivity in shale permeability measurements. Measured shale permeability is observed to rise as flow rate increases and reaches a constant value at higher rates. Permeability of the sheared samples shows a similar trend although with higher permeability values. This phenomenon casts a shadow of doubt around the common non-steady-state permeability measurement methods and has never been discussed previously with respect to shale gas reservoirs. The basic definition of gas permeability needs to be revisited in order to set up new standards (concerning testing pressure, rate, and stress state) in order to obtain meaningful and comparable permeability measurements.

Analytical Model

Fig. 5 illustrates that the majority of shale gas reservoirs lie within the continuum flow regime throughout their production life. According to Fig. 6, slip flow is the dominant regime for the majority of conditions in shale gas plays. Therefore the analytical model to describe flow in shale should be based on continuum conditions while honouring slip flow. A new equation is proposed in chapter 4 (Eq. 33) to describe slip flow in a capillary tube. The proposed equation is an expansion of Klinkenberg's work on low-permeability porous media that eliminates the constant velocity gradient assumption at the pores walls. The aim of the new model is to ameliorate the issue of overestimation of absolute permeability by Klinkenberg's equation while keeping its simplicity. Eq. 33 illustrates a quadratic dependency for permeability versus pressure, as opposed to the linear relationship in Klinkenberg's equation.

Parameters "a" and "b" in Eq. 33 are functions of fluid properties, temperature, and pore radius, and both are positive. According to Eq. 41, "a" is inversely related to absolute permeability. At sufficiently high permeabilities, parameter a is close to zero, making the Klinkenberg equation adequately accurate. In that case, "b" in Eq. 33 is equal to Klinkenberg's constant. Only for a low-permeability medium in the range of micro-nano darcy does "a" become considerably large and the curvature in the plot of apparent permeability versus mean pressure noticeable. K_{abs} is the absolute or liquid permeability of the rock. In this work, absolute and liquid permeability are defined similarly.

Model Verification

Table 7 presents the results of the steady-state gas permeability tests for the Clearwater sample. The water permeability of the sample was measured to be 0.001 md. As expected, the values of gas permeability were measured to be generally higher than water, and to decrease with average pressure. Fig. 22 plots apparent permeability measured in the tests against the reciprocal of pressure. The data is

fitted with both Klinkenberg's equation and Eq. 33. According to Fig. 22, using Klinkenberg's equation to analyze the results will overestimate permeability, while Eq. 33 estimates an absolute permeability close to that of water. It must be noted that due to the quadratic nature of Eq. 33 it could show a maximum at very low pressures (or high values of reciprocal of pressure). This is due to the fact that at very low pressures in shale rocks, the continuum flow assumption completely breaks down and therefore Eq. 33 will not be applicable.

Table 7: Steady-state gas permeability results for the Clearwater sample.

P_{upstream}	$P_{\text{downstream}}$	Flow Rate	Average Pressure	Mean Effective Stress	K_{app}
kPa	kPa	ml/min	kPa	kPa	md
457.7	431.6	0.075	444.7	1963.6	0.0120
556.5	529.9	0.075	547.3	1954.5	0.0110
759.7	727.3	0.075	743.6	1958.9	0.0091
865.3	835.8	0.075	850.5	1960.8	0.0099
948.7	918.5	0.075	933.6	1977.1	0.0096
1059.0	1022.8	0.075	1040.9	1974.0	0.0081
1278.6	1235.2	0.075	1256.8	1967.1	0.0067
5130.5	5094.9	0.075	5112.7	1963.2	0.0028

Table 8 presents the experimental data from this work and from 15 different permeability tests in literature. The data is taken from tests on samples of a variety of types and permeabilities. For each sample, the parameters in Eq. 33 are calculated from a set of permeability measurements at different pressures. The

absolute permeability is estimated and presented using Eq. 33 and Klinkenberg's correlation. The liquid permeability of each sample is reported where available.

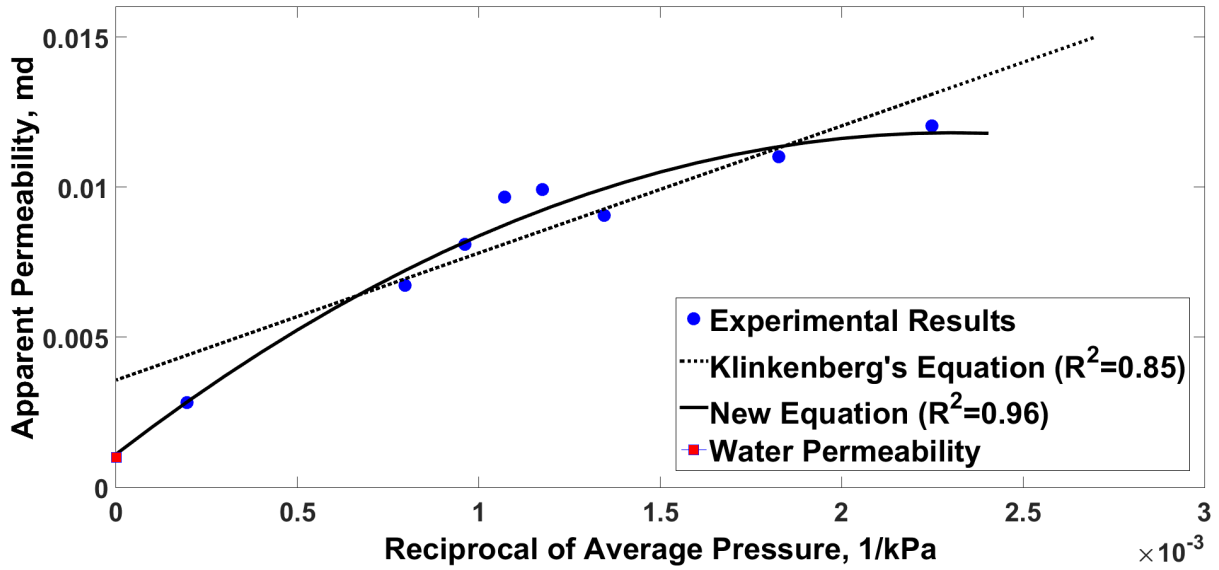


Fig. 22: Verification of Eq. 33 using laboratory results for the Clearwater sample.

Water permeability for the Montney 10D, 17O, and 8H samples was measured to be 5 nd, 1.5 nd, and 87 nd respectively. As expected from Eq. 40 and Eq. 41, the values for parameters “a” and “b” are significantly higher for the Montney 10D, and 17O samples than for samples with higher permeability. Slippage effect is more pronounced in low permeability porous media as indicated by high values of the slip parameters, “a” and “b”. High values for “a” and “b” explain the significant difference between the gas permeability and water permeability of such samples. Gas permeability measurements for ultra-low-permeability rocks have shown results orders of magnitude higher than those of water (Ghanizadeh et al., 2014, Tanikawa and Shimamoto, 2009). In such results reported in the literature, gas permeability is only corrected using the classic Klinkenberg correlation. The introduction of parameter “a” in Eq. 33 could explain the considerable difference between Klinkenberg-corrected gas permeability and water permeability. According to Table 8, this difference was also observed in all the Montney samples in the present experiments. However, taking parameter “a” into consideration,

reasonably accurate estimates of water permeability could be achieved. For this class of materials, significant error up to a few orders of magnitude is observed when using Klinkenberg’s correlation to estimate absolute (liquid) permeability. Fig. 23 compares the accuracy of Klinkenberg-corrected permeability to that of Eq. 33 with respect to liquid permeability. The solid line in Fig. 23 represents the measured liquid permeability for the 22 datasets considered. According to Fig. 23 the Klinkenberg-corrected gas permeability results in errors up to a few orders of magnitude when attempting to estimate the liquid permeability of ultra-low-permeability samples (i.e. permeability of less than 0.01 md). The error in estimating the liquid permeability using the Klinkenberg’s equation increases as permeability decreases. This could be attributed to the increase in the value of “a” as the permeability decreases. At low permeability the value of “a” increases to an extent that creates a large deviation from the Klinkenberg’s estimation of liquid permeability.

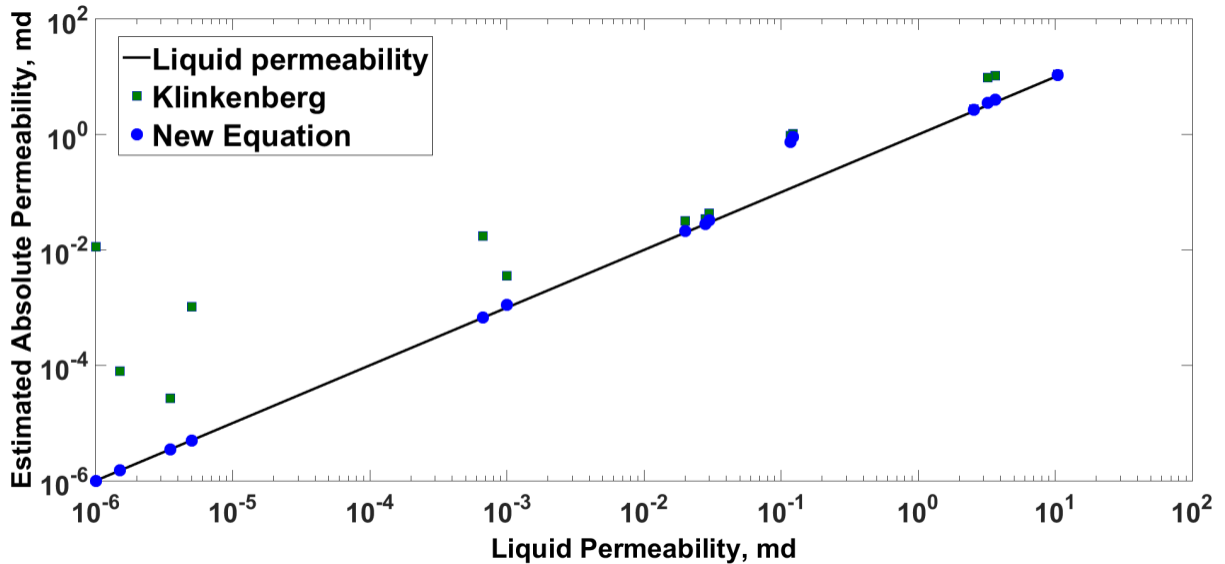


Fig. 23: Comparison of the accuracy of liquid permeability estimation between Eq. 33 and Klinkenberg from experimental data (data provided in Table 8).

From Fig. 22 and Fig. 23 it appears that the deviation from Klinkenberg’s equation occurs at high pressures close to the liquid permeability. However, concluding that Klinkenberg’s equation deviates from reality at high pressures is not entirely accurate. From the discussion in chapter 3 and Fig. 6, at higher pressures it is more

likely to be in the slip flow regime (for moderately permeable rocks). Therefore, Klinkenberg's equation should stand at higher pressures and deviate from the data at lower pressures. Fig. 24 shows an example of the behavior for the new equation and Klinkenberg's prediction. According to Fig. 24, Klinkenberg's straight line assumption should stand if the data is gathered at high enough pressures.

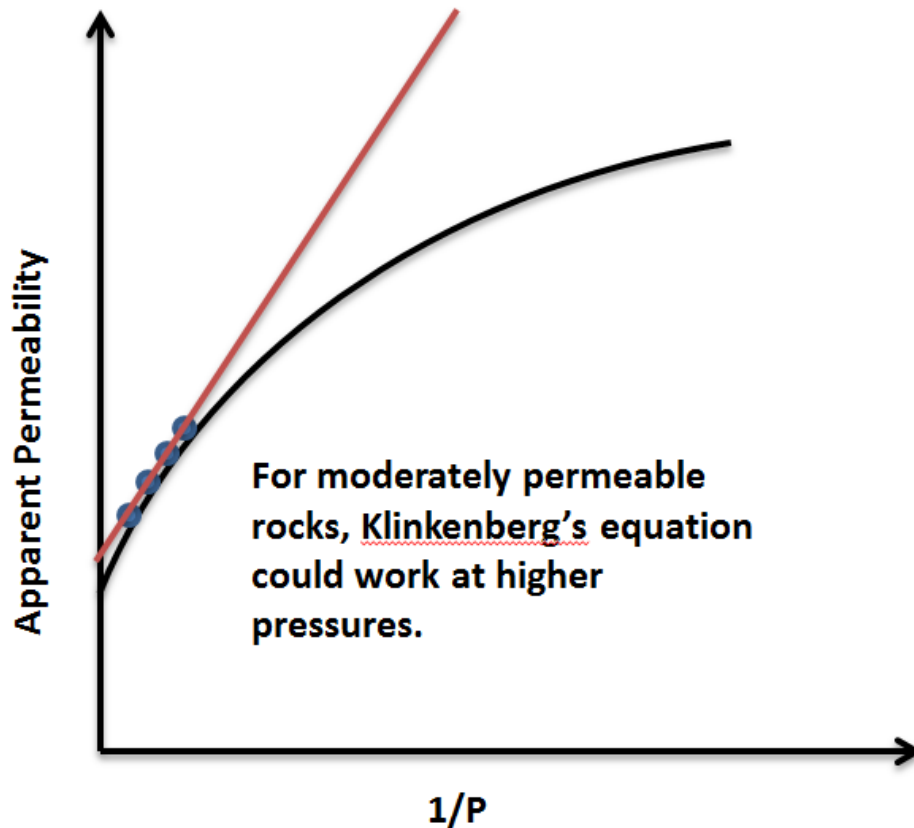


Fig. 24: The realistic deviation of the Klinkenberg's equation from apparent permeability data.
The reason that the Klinkenberg's equation overestimates the permeability is that the laboratory data used to back-calculate absolute permeability is typically measured at lower pressures. Therefore, applying Klinkenberg's equation for that set of data will yield erroneous results when extrapolated to calculate the absolute permeability. Fig. 25 shows an example of the typical data analysis of the low pressure permeability measurements, to explain the deviations from Klinkenberg.

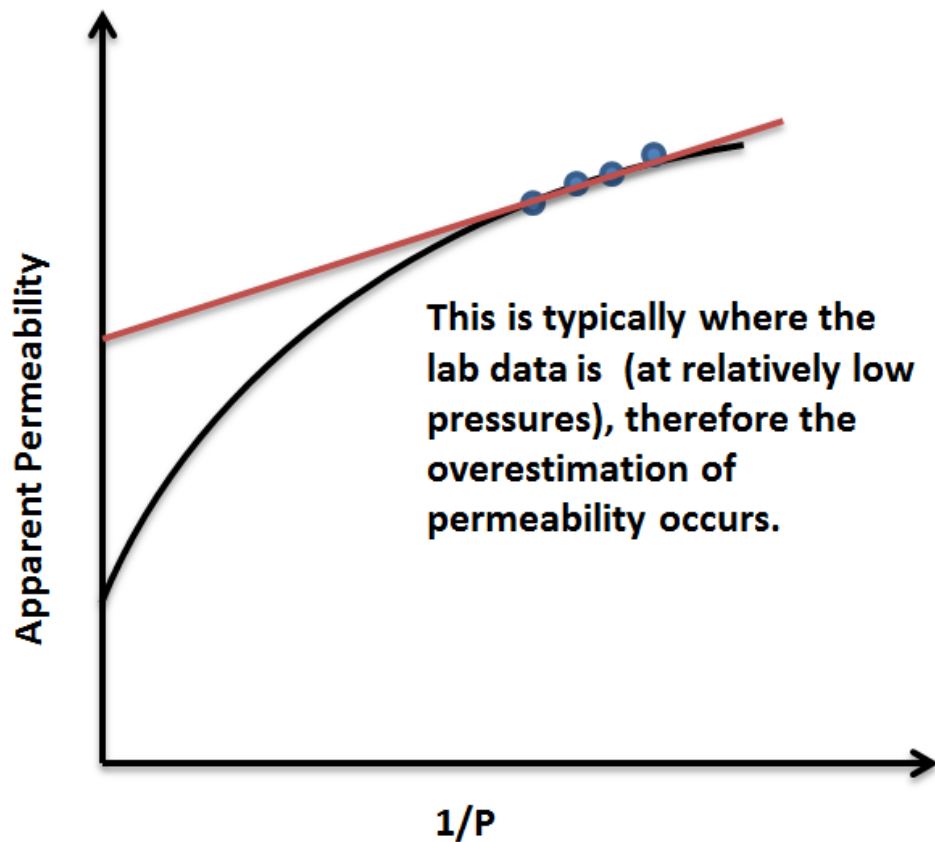


Fig. 25: Typical lab tests at low pressure leads to overestimation of absolute permeability using Klinkenberg's equation.
 Fig. 26 and Fig. 27 show that as expected, according to the experimental results, the values of parameters "a" and "b" increase as permeability decreases. According to Eq. 40 and Eq. 41, the logarithmic plot of "a" and "b" versus permeability should show a linear trend with a slope of 1 and 0.5, respectively. The dashed lines in the Fig. 26 and Fig. 27 have slopes equal to 1 and 0.5 respectively, to create a comparison to theory. The dataset is further divided by the rock types. The results show that for the dataset under study, the values of "a" and "b" change with permeability as suggested by theory, through Eq. 40 and Eq. 41.

As "a" and "b" are also dependent on fluid type, pore geometry, and temperature, all experiments here are not necessarily comparable, but a clear trend is observed. More data is required to reduce the scatter in a and b plots in order to predict reasonable values for these parameters. The data should ideally be measured using

the same gas at the same temperature to be able to eliminate the influence of such parameters. However, the plot of “a” versus “b” shows a clearer relationship and can be used as a benchmark to ensure reasonable accuracy.

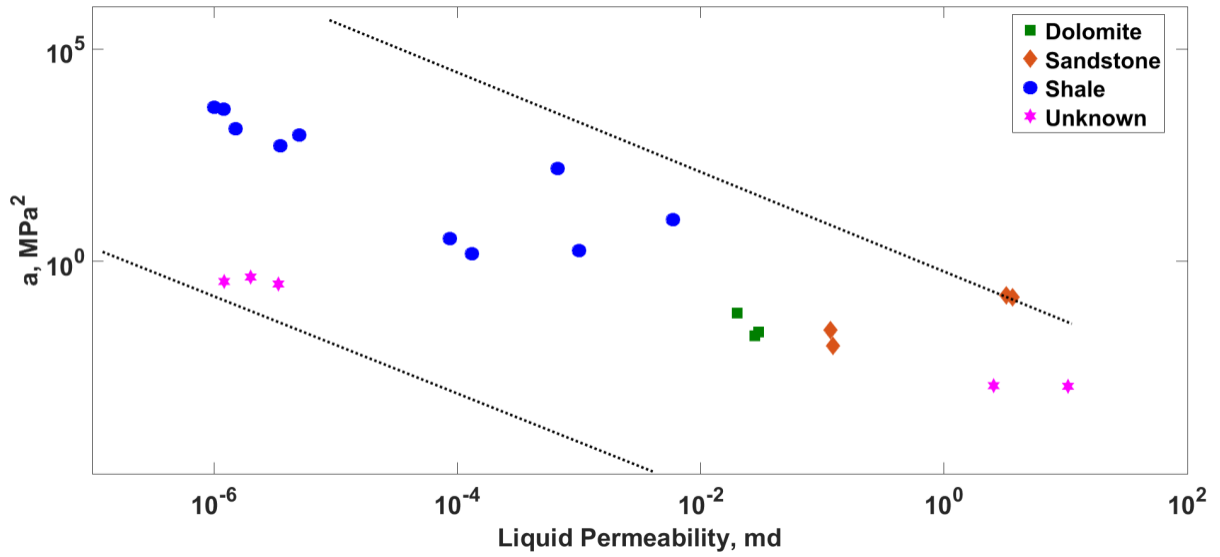


Fig. 26: Experimental values of “a” versus permeability (data provided in Table 8).

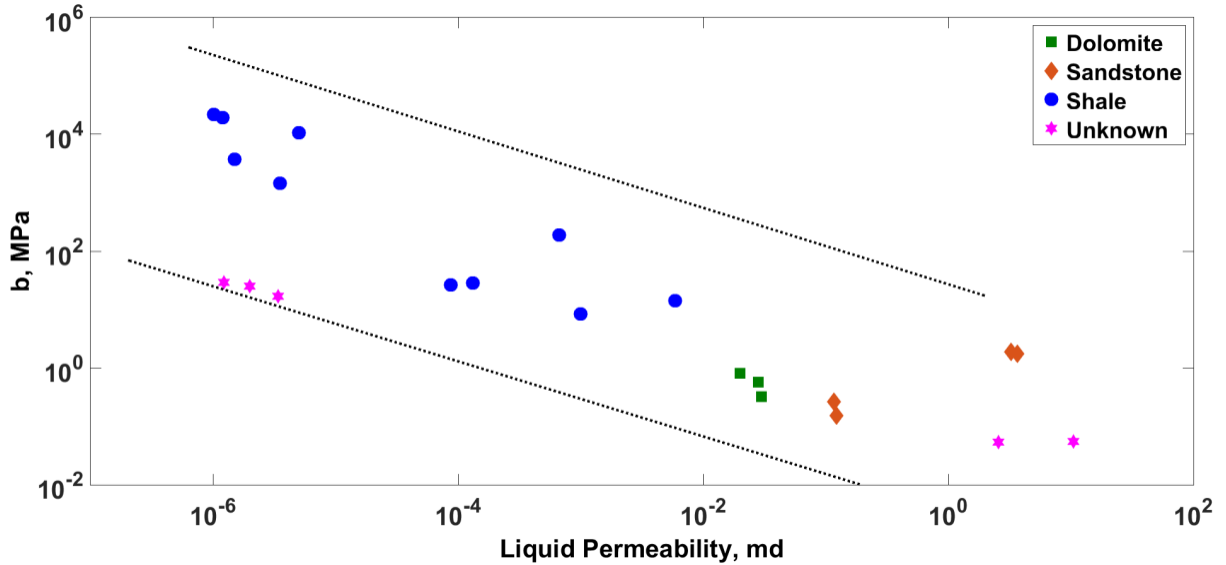


Fig. 27: Experimental values of “b” versus permeability (data provided in Table 8).

According to Eq. 36, the logarithmic plot of “a” versus “b” should show a linear trend. Fig. 28 illustrates the relationship between “a” and “b” from our

experimental data set. The solid line in Fig. 28 shows a purely theoretical relationship as predicted by Eq. 36. The data shows a good match at smaller values of “a” and “b” but deviates from the theoretical line at higher values. The higher values of “a” and “b” represent a lower permeability that approaches the transition flow regime. Hence, from a theoretical perspective, the deviation from theory occurs. However, according to the discussion of the flow regime map in Fig. 5, most shale reservoir cases are in slip flow regime or early stages of transition flow. Adopting the new equation (Eq. 33) in a semi-empirical way can reasonably capture the permeability enhancement due to the early stages of transition flow. The high “a” and “b” values in Fig. 28 are from samples with permeability in the range of 1 to 100 nd, which is the bottom range of permeability for shale gas reservoirs. Fig. 29 shows the same “a” versus “b” plot with a best-fit line. It can be used as a benchmark to ensure the “a” and “b” estimates are reasonable. Due to the quadratic nature of Eq. 33, unlike Klinkenberg’s linear correlation, there is no unique curve that can fit the data. Therefore it is paramount to have high quality data and to use Fig. 26, Fig. 27, and Fig. 29 to ensure that the “a” and “b” estimates are within typical range. In this work we have calculated the “a” and “b” values by matching the results from Eq. 33 to the experimental data using the least square method, while setting a reasonable range (as specified in Fig. 26, Fig. 27) for the parameters.

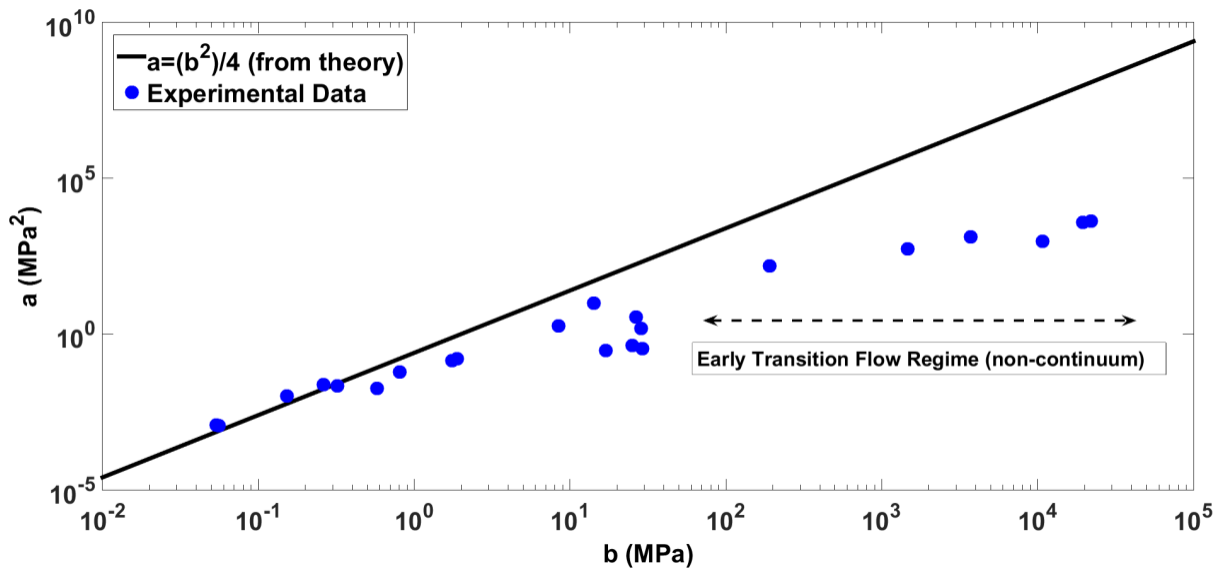


Fig. 28: Plot of “a” versus “b”, with theoretical relationship plotted in solid line (data provided in Table 8).

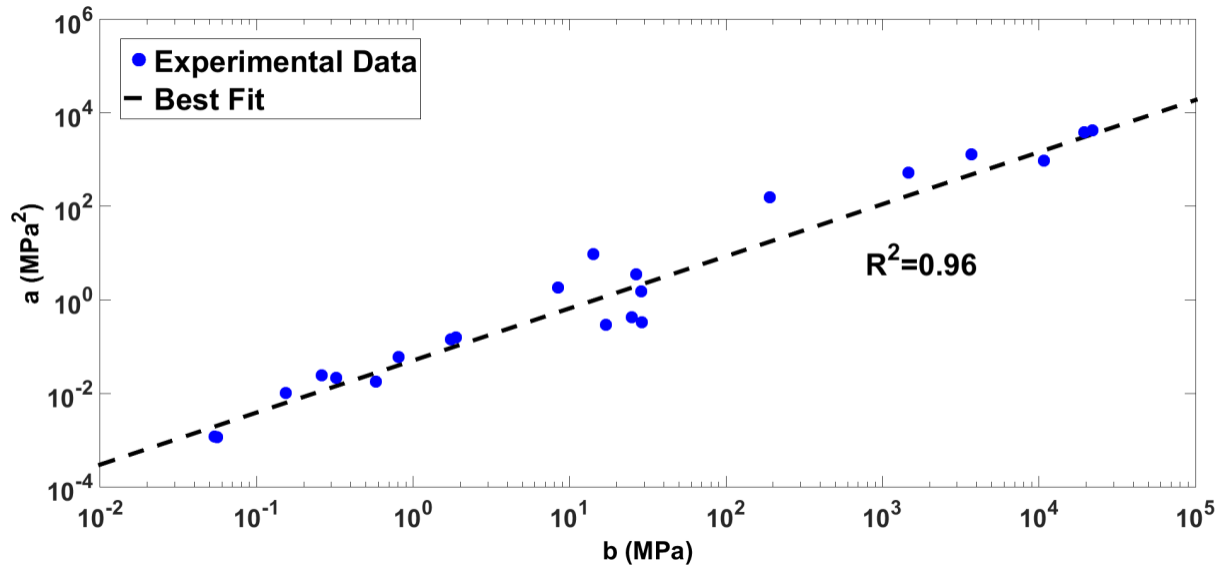


Fig. 29: Addition of best-fit line to describe relationship between “a” and “b” (data provided in Table 8).

Table 8: Summary of the experimental results from this work and the literature.

Author	Sample	Fluid/Lithology	a (MPa ²)	b (MPa)	Klinkenberg 's Perm. (md)	Perm. Using Eq. 33 (md)	Liquid Perm. (md)
Klinkenberg (1941)	Core M	Nitrogen/Not Specified	0.00114	0.0557	11.1	10.88	10.45
Klinkenberg (1941)	Core L	Carbon Dioxide/Not Specified	0.00119	0.0537	2.75	2.66	2.55
Li et al. (2009)	S3	Nitrogen/Dolomite(Slightly Shaly)	0.0178	0.577	0.034	0.0281	0.028
Dong et al. (2012)	C1	Ethane/Dolomite	0.0598	0.805	0.032	0.0215	0.02
Dong et al. (2012)	C2	Ethane/Dolomite	0.0215	0.322	0.043	0.0326	0.03
Tanikawa et al. (2009)	IVA418-60 MPa	Nitrogen/Sandstone	0.0103	0.153	1.02	0.91	0.122
Tanikawa et al. (2009)	IVA418-80 MPa	Nitrogen/Sandstone	0.0239	0.261	0.95	0.75	0.117
Tanikawa et al. (2009)	IVA419-60 MPa	Nitrogen/Sandstone	0.142	1.74	10.42	4.02	3.66
Tanikawa et al. (2009)	IVA419-100 MPa	Nitrogen/Sandstone	0.159	1.88	9.82	3.52	3.23
Ghanizadeh et al. (2014)	HAD-1-II-Dry	Argon/Shale	4186	22020	0.011	1.00E-06	1.01E-06
Ghanizadeh et al. (2014)	HAD-2-II-Dry	Methane/Shale	3895	19542	0.011	1.20E-06	Not Available
Firouzi et al. (2014)	-	Helium/Shale	156	190	0.017	6.70E-04	6.70E-04
Wu et al. (1998)	36	Nitrogen/Not Specified	0.336	29	1.68E-05	1.22E-06	Not Available

Author	Sample	Fluid/Lithology	a (MPa ²)	b (MPa)	Klinkenberg 's Perm. (md)	Perm. Using Eq. 33 (md)	Liquid Perm. (md)
Wu et al. (1998)	9a	Nitrogen/Not Specified	0.421	25	3.19E-05	2.00E-06	Not Available
Wu et al. (1998)	9b	Nitrogen/Not Specified	0.295	17	4.44E-05	3.40E-06	Not Available
This work	Montney (10D)	Methane/Shale	954	10710	0.001047	5.00E-06	5.00E-06
This work	Montney (10D)- failed	Methane/Shale	9.6	14.2	9.60E-03	5.90E-03	5.90E-03
This work	Montney (17O)- 10Mpa	Methane/Shale	532	1466	2.70E-05	3.50E-06	3.50E-06
This work	Montney (17O)- 20Mpa	Methane/Shale	1308	3713	7.90E-05	1.50E-06	1.50E-06
This work	Montney (8H)	Methane/Shale	3.5	26.6	Negative	8.70E-05	8.70E-05
This work	Montney (8H)-failed	Methane/Shale	1.5	28.6	Negative	1.32E-04	1.32E-04
This work	Clearwater	Nitrogen/Shale	1.82	8.42	0.0036	0.0011	0.001

Rate Dependency of Permeability

Steady-state gas permeability tests are conducted on four intact samples at different rates and pressures, and a constant mean effective stress. Fig. 30, Fig. 31, Fig. 32, and Fig. 33 show the measured permeability values versus mass flow rate at each mean pressure stage for the Clearwater, Montney 10D, 17O, and 8H, respectively. The results indicate the permeability to be in the micro darcy range for the Clearwater and the Montney 10D sample and nano darcy range for Montney 17O and Montney 8H samples. Apparent permeability in all the samples increases with rate but seems to reach a plateau at sufficiently higher rates. The increase in permeability with rate is significant in our results. As the mean pressure increases, the apparent permeability decreases due to the slippage effect. The same behavior with rate is observed at higher mean pressures, though the permeability enhancement with rate is more depressed at higher pressures. The Knudsen number values are also reported in Fig. 30 through Fig. 33. According to the results as the Knudsen number decreases (pressure increases) permeability declines, in agreement with the slippage theory. The range of Knudsen values show that for the tests in intact rock the gas flow regime lies under slip regime or, early transition regime at lower pressures. Previous studies on gas flow regime in shales revolve around the Knudsen number and gas flow regimes. While the Knudsen number explains the change in apparent permeability with mean pressure, it does not explain the change in permeability due to rate.

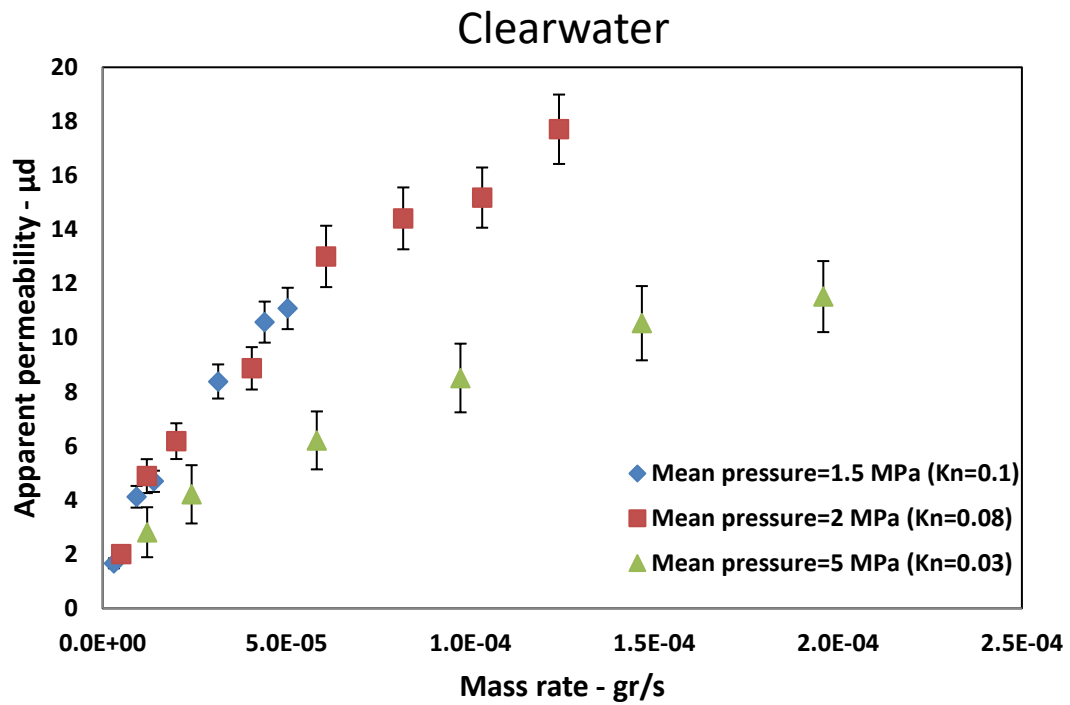


Fig. 30: Gas permeability measurements for the Clearwater sample versus mass flow rate. The results are plotted at each mean pressure or Knudsen number.

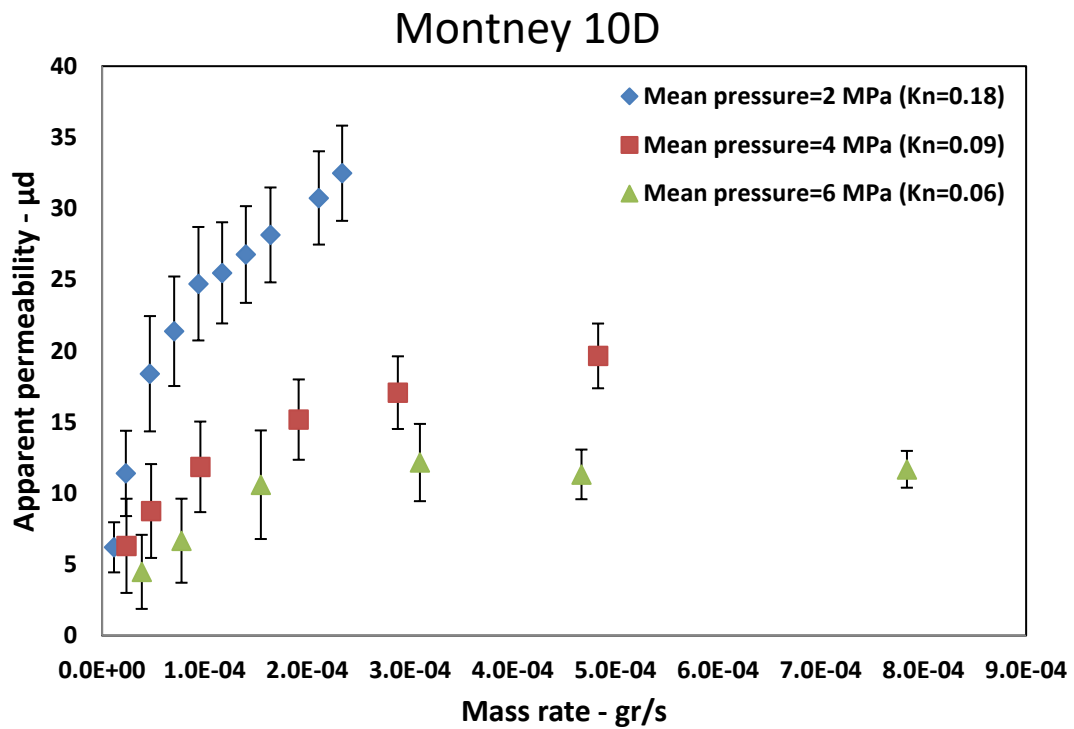


Fig. 31: Gas permeability measurements for the Montney 10D sample versus mass flow rate. The results are plotted at each mean pressure or Knudsen number.

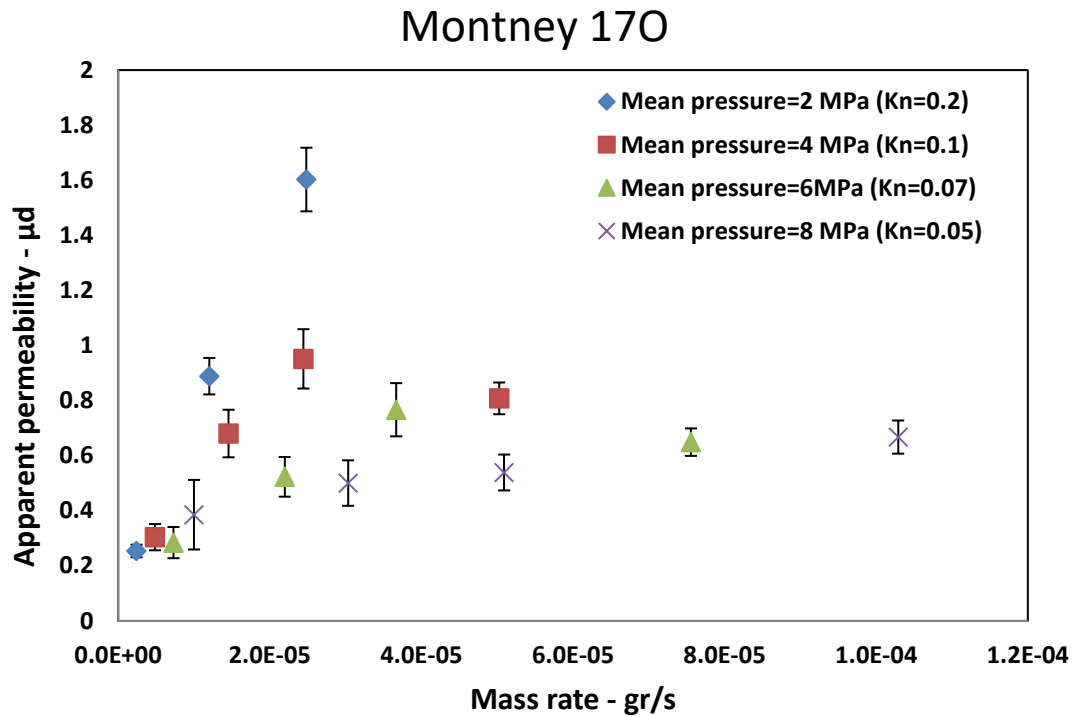


Fig. 32: Gas permeability measurements for the Montney 17O sample versus mass flow rate. The results are plotted at each mean pressure or Knudsen number.

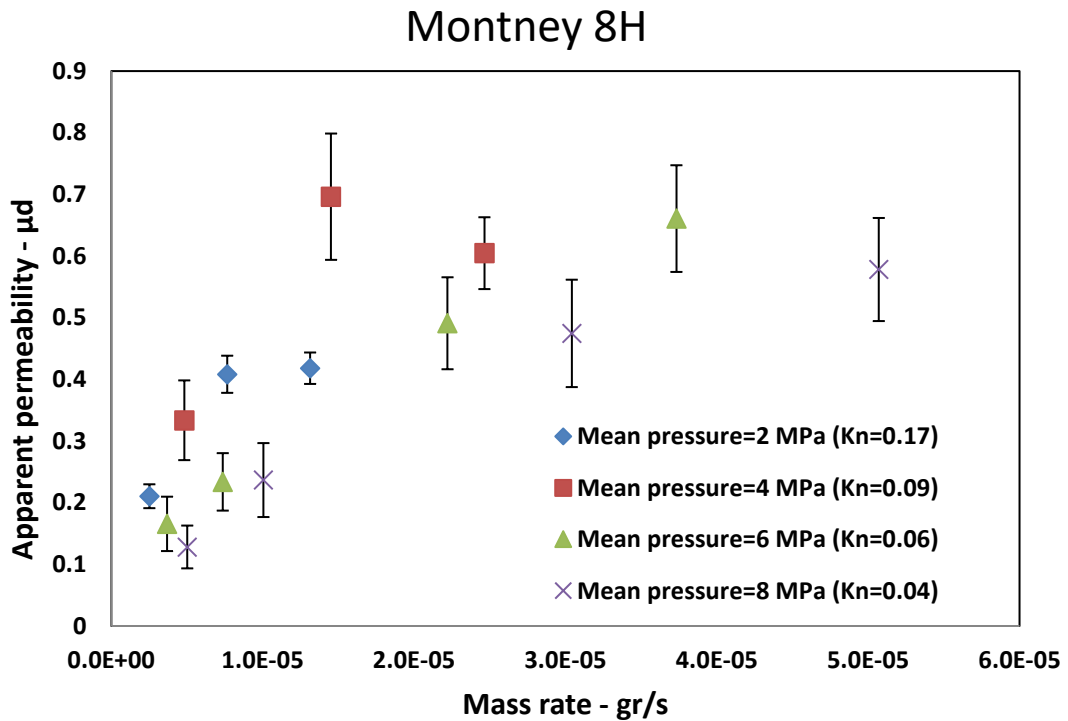


Fig. 33: Gas permeability measurements for the Montney 8H sample versus mass flow rate. The results are plotted at each mean pressure or Knudsen number.

After post-failure water permeability measurements, the samples are again saturated with gas as explained in the methodology section in chapter 5. Gas permeability measurements are repeated on the failed samples similar to intact samples. Mean effective stress is once again held constant at 20 MPa for the Montney samples and permeability is measured at different rates and mean pressures. The failed samples contain micro-fractures that enhance the permeability; however the rate dependency is still observed. Fig. 34, Fig. 35, Fig. 36, and Fig. 37 show the gas permeability results after failure. All samples show higher permeability except Montney 17O, which shows a similar permeability to the pre-failure measurements. This is most likely due to the fact that no significant failure occurred in the Montney 17O sample as there is also no significant increase in its water permeability. The water permeability results are discussed later in this chapter. The observed behavior of permeability with respect to rate in the failed samples is similar to the intact condition; Permeability rises with rate until it reaches a plateau.

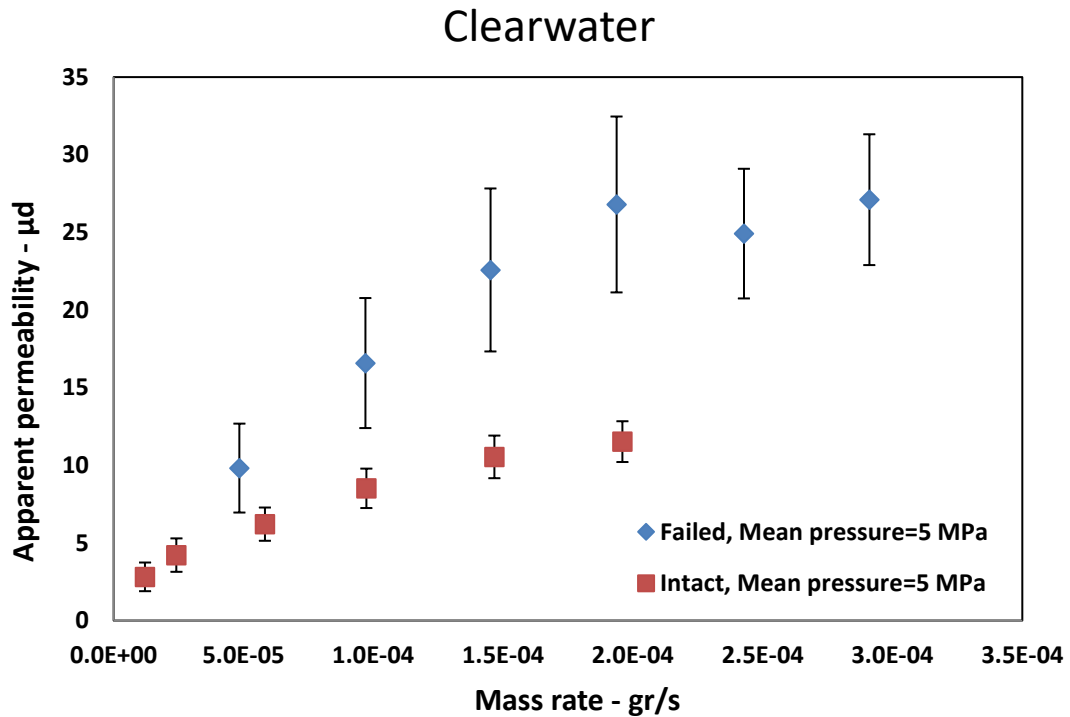


Fig. 34: Gas permeability measurements after failure for the Clearwater sample versus mass flow rate.

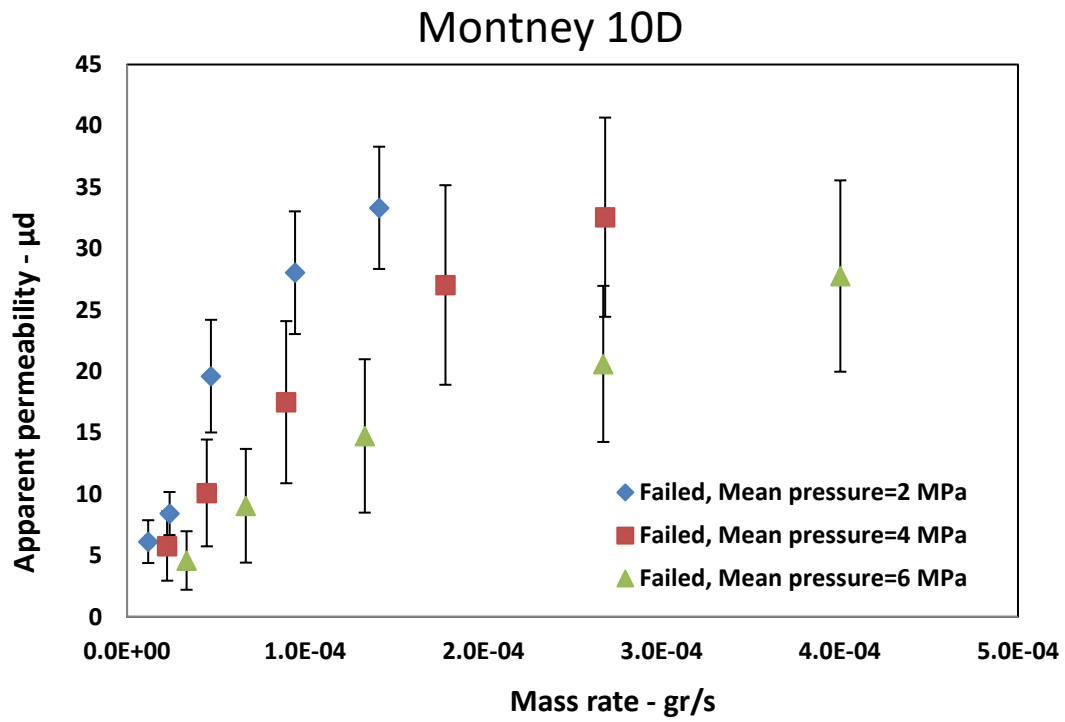


Fig. 35: Gas permeability measurements after failure for the Montney 10D sample versus mass flow rate.

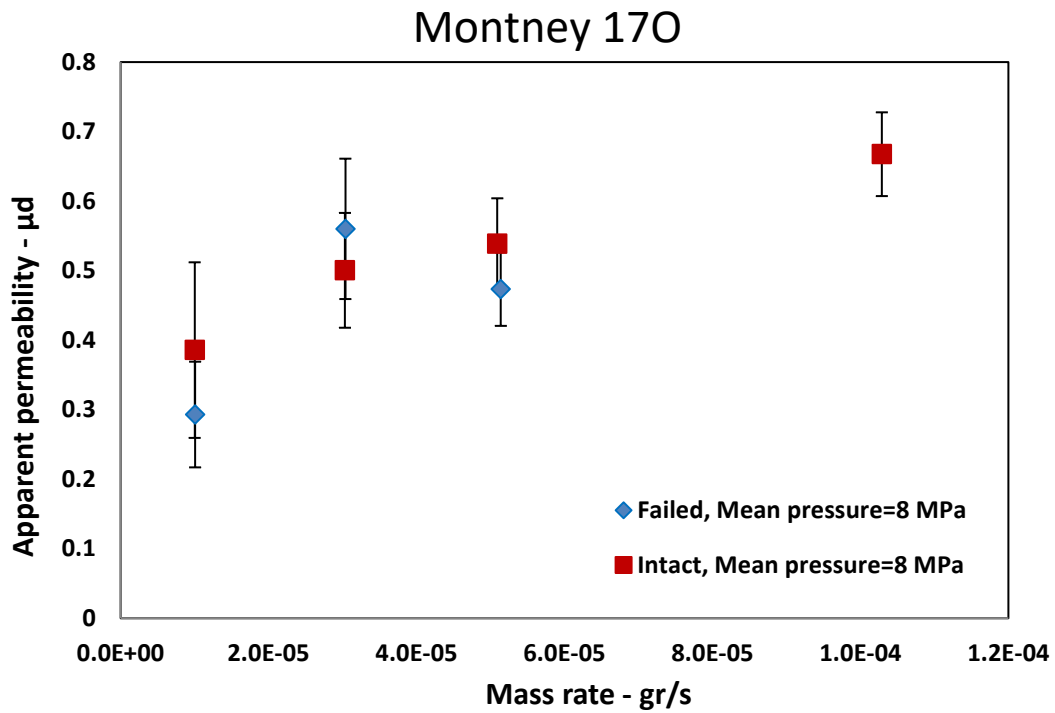


Fig. 36: Gas permeability measurements after failure for the Montney 170 sample versus mass flow rate.

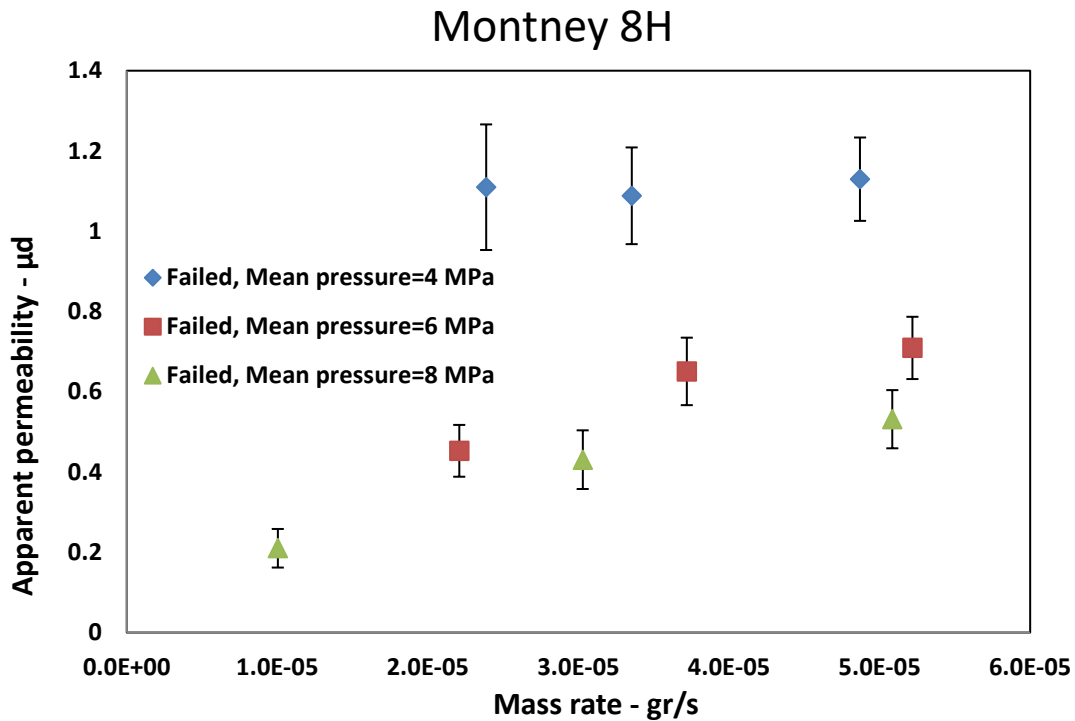


Fig. 37: Gas permeability measurements after failure for the Montney 8H sample versus mass flow rate.

Dependence of permeability to flow rate or velocity has been investigated in oil and gas industry, though typically in a different context than this work. At high velocity, typical of high rate gas wells, inertial forces cause extra pressure drop therefore effectively decrease permeability. There have been numerous publications dedicated to studying this phenomenon (Venkataraman and Rao, 1998; Macini et al., 2011; Huang and Ayoub, 2008; Barree and Conway, 2004). On the other side of the spectrum, low velocity flow also known as pre-darcy or pre-laminar flow has not attracted much attention (Gavin, 2004). The permeability in the pre-darcy zone has been reported to increase with velocity until it reaches a constant value in the laminar or darcy flow regime (Von Engelhardt and Tunn, 1954; Kutilek, 1972; Basak, 1977). Some researchers have also reported the existence of a minimum threshold pressure gradient under which no flow occurs (Dou et al., 2014). The physics behind the pre-darcy flow regime is unclear. Several mechanisms have been proposed to explain the pre-darcy behavior such as capillary pressure effect,

boundary layer effect, interactions between fluid and matrix, and non-newtonian fluid behavior (Dou et al., 2014; Gavin, 2004; Miller and Low, 1963; Swartzendruber, 1962). Due to the very low permeability of shale reservoirs, fluid velocity in the matrix is small, which could result in a dominant pre-laminar (pre-darcy) flow regime. Fig. 38 shows the change in permeability with respect to flow velocity (or pressure gradient) after Basak (1977) and Kutilek (1972) with modifications. The velocity dependent flow regimes are commonly described as pre-darcy (low velocity), darcy, and non-darcy (high velocity) flow. According to Fig. 38, permeability increases with rate or pressure gradient at low velocity until it reaches a constant value which is the beginning of laminar (darcy) flow. At high velocity, permeability decreases due to inertial or turbulent effects. The pre-darcy behavior is observed in all our permeability measurements presented in Fig. 30 through Fig. 33. The range of pressure gradients for our tests is 1 to 20 MPa/m, which is relatively high. Therefore, it is likely that under in-situ conditions pre-laminar (pre-darcy) regime prevails in the matrix and permeability increases with rate or pressure gradient.

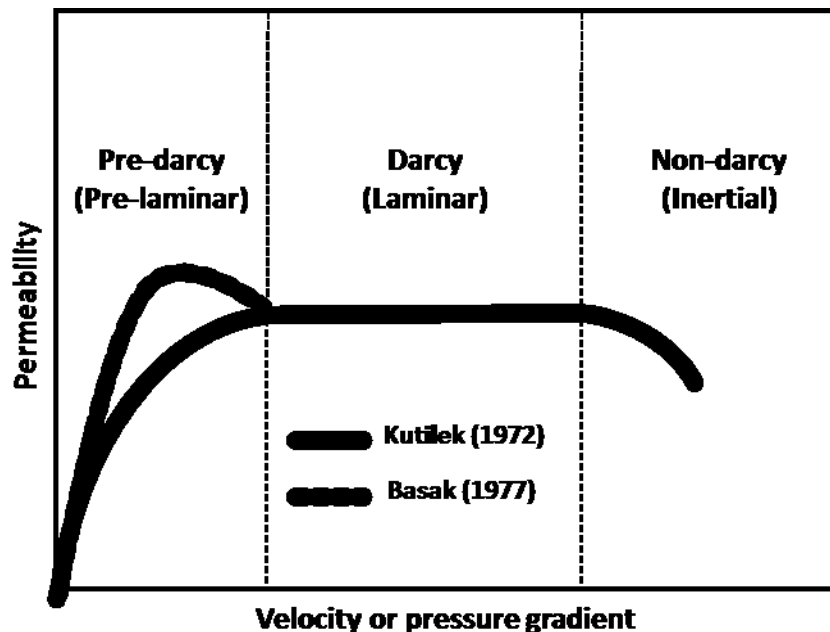


Fig. 38: Change in permeability with respect to velocity or pressure gradient after Kutilek (1972) and Basak (1977) with modifications.

The term “darcy flow” has been used in the literature to describe two different flow regimes. The velocity dependant flow regimes are commonly divided into pre-darcy, darcy, and non-darcy flow regimes, as discussed previously. On the other hand, Knudsen (or pressure) dependent gas flow regimes are described as darcy, slip, transition, and free-molecule flow. The use of the term “darcy flow” for both velocity and pressure dependent flow regimes is incorrect as it does not necessarily refer to the same flow conditions. We suggest using the terms pre-laminar, laminar, and inertial flow, to be more appropriate for the velocity dependent flow regimes. These terms will be used to refer to the velocity dependent flow regime through the rest of this work.

The majority of the work published on the relationship between permeability and velocity is for liquid flow. However, similar behavior is observed for gases in our results and in literature (Meyer and Krause, 1998). On the other hand, gas permeability has been observed in our data and numerous sources in literature to change with mean pore pressure. Traditionally, this is known as slippage effect. Fig. 39 shows the change in permeability with mean pressure and various flow regimes associated with it.

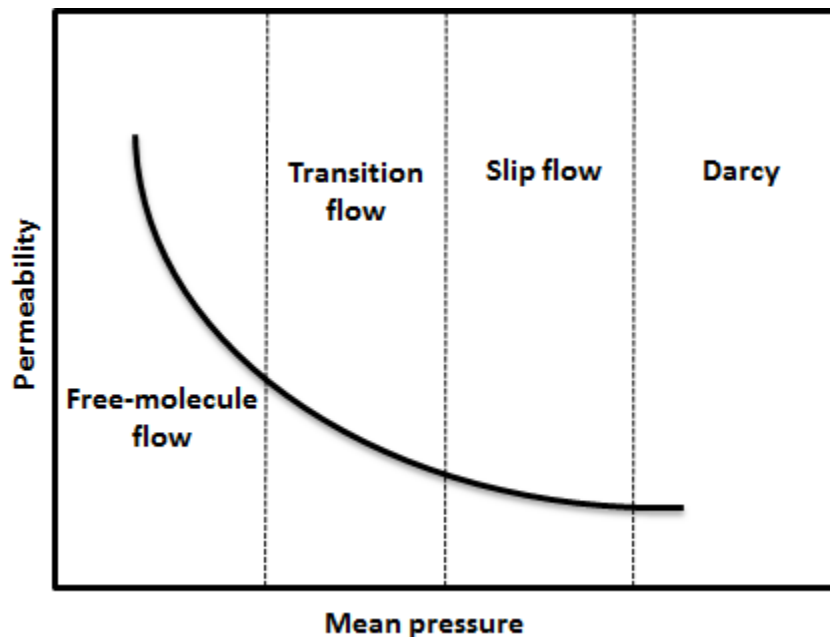


Fig. 39: Change in permeability with respect to gas pressure.

Gas permeability is related to Knudsen number, however in a certain rock at a constant effective stress and constant temperature Knudsen number is in essence a function of pressure. Since pressure is a more tangible parameter, it is used in Fig. 39 instead of Knudsen number. It must be noted that the range of each regime depicted in Fig. 39 is not to scale. Since Knudsen number is also a function of pore radius, for some rocks (e.g. shales) the range for darcy regime is very small if it practically exists at all. For shale and tight rocks slip flow and transition flow regimes are dominant at pressure ranges encountered in the lab and in-situ. Revisiting Fig. 6, at permeability of 1000 nd, flow regime is slip or transition flow at any pore pressure. In all the experimental results in the present study, gas permeability changes with mass rate (which could be related to velocity or pressure gradient). Additionally, Fig. 30 through Fig. 33 show that at a constant rate, permeability decreases with pore pressure. Therefore, gas permeability is both a function of gas velocity (due to pre-laminar flow regime) and mean pressure (due to slippage) at a constant effective stress as illustrated in Fig. 38 and Fig. 39.

A complete picture of gas permeability and flow regime is then obtained by depicting permeability as a surface that changes with Knudsen number (or pore pressure) and velocity (or pressure gradient). Using the permeability behavior in Fig. 38, Fig. 39, and the experimental observations, permeability is depicted as a plane in three dimensions in Fig. 40. An increase in mean effective stress moves the permeability plane downwards and a decrease in mean effective stress moves it upwards. The range of Knudsen dependant flow regimes (darcy, slip, transition, and free-molecule flow regimes) is clearly defined using Knudsen values. However, same is not the case for the range of applicability of velocity dependant flow regimes (pre-laminar, laminar, and inertial). It is not clearly understood at what velocity or Reynolds number the transitions between velocity dependent regimes occur (Seguin et al., 1998a; Seguin et al., 1998b; Comiti et al., 2000). The traditional definition of darcy flow (constant permeability) is then limited to low Knudsen values and moderate velocities i.e., laminar-darcy flow regime under the

terminology used in the work. The entire surface illustrated in Fig. 40 does not apply to all rocks. For example, free-molecule flow regime is never practically reached in high permeability sandstones (due to high pore radius) or inertial flow is not practically achieved in nanometer sized pores of a shale matrix.

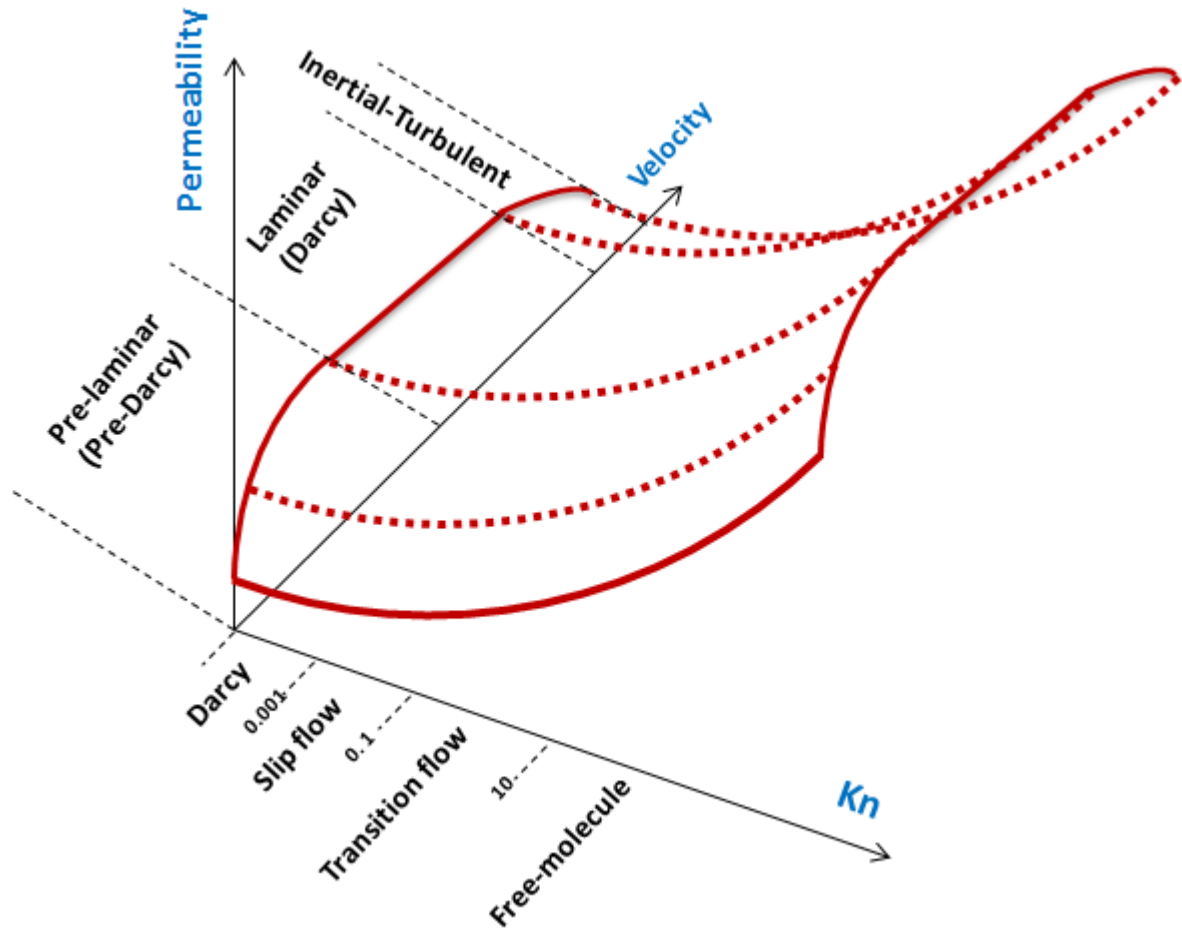


Fig. 40: Permeability surface with respect to velocity and Knudsen number. Mean effective stress moves the surface up (decrease in effective stress) or down (increase in effective stress).

An important consequence of the permeability behavior illustrated in Fig. 40 is the analysis of the lab results. Permeability measurements at different pressures can only be compared if the tests are conducted at similar velocity or mass rates. This could cast a shadow of doubt around gas permeability experiments using techniques that use transient rates. Similarly, to compare permeability measurements at

different rates the tests must be conducted at the same mean pressure. According to Fig. 6 and the behavior observed in the present lab results, the gas permeability in shales is dominantly governed by slip (or transition) flow regime under pre-laminar flow. Fig. 41 shows a plan view of Fig. 40 that illustrates an overview of the governing flow regimes for gas flow in porous media. High rate gas reservoirs have been observed to be governed by inertial-turbulent flow while under darcy regime due to high pore pressure or low Knudsen number for these reservoirs. Based on experimental observations, conventional reservoirs generally lie under pre-laminar-darcy, laminar-darcy, and laminar-slip flow regimes while shale gas and tight reservoirs flow under pre-laminar-slip, laminar-slip, and pre-laminar-transition regimes. More investigations are required to understand the physics of pre-laminar flow, to be able to quantify the permeability change, and understand the regime boundaries. The new description of gas permeability proposed in this work calls for new standardized laboratory testing procedures. Reporting a single number as gas permeability of a core seems to be an unrealistic goal. In order to accurately describe fluid conductivity in a reservoir, we need to construct the relevant portion of the permeability plane depicted in Fig. 40 using experimental results at conditions as close as possible to the in-situ (pressure, velocity, temperature, and stress). Numerical simulations are needed to study the field scale ramifications of this phenomenon. Simple thought experiments can lead to speculations such as higher than expected production by increasing the pressure gradient in the reservoir (could also be effective for liquid production), and possibly a delayed production as it could take time for pressure gradient to build up in the matrix away from fracture faces.

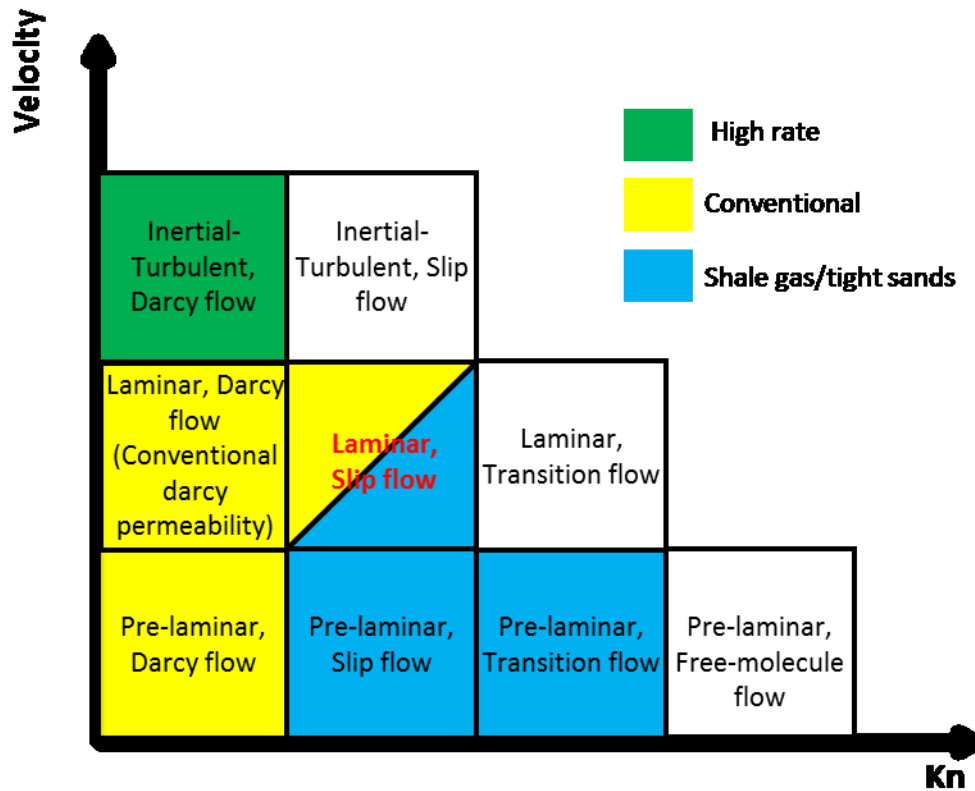


Fig. 41: An overview of the governing gas flow regimes in porous media.

Flow Regime Transition

The physics behind the pre-laminar flow is not well-understood. Several hypotheses have been proposed for the rate dependency of permeability at low velocity, such as capillary pressure effect, boundary layer effect, interactions between fluid and matrix, and non-Newtonian fluid behavior (Dou et al., 2014; Gavin, 2004; Miller and Low, 1963; Swartzendruber, 1962). Understanding the physics behind the rate dependency of permeability is not in the scope of this work. However, an attempt is made to analyze the transition between pre-laminar and laminar flow regime using the experimental results in this work. Fig. 42 presents the results of the apparent permeability versus mass rate for all the samples, in the intact and failed states. The general trend of the data captures the pre-laminar and laminar flow regimes as depicted in Fig. 38 and Fig. 40. The data in Fig. 42 roughly

consists of two groups. One group comprises of the Clearwater and Montney 10D permeability results that are in the range of 10 micro darcy and higher. The second group includes the results for the Montney 17O and 8H with apparent permeability of 1 micro darcy or less. By comparing all the permeability results Fig. 42, it appears that the transition between the pre-laminar and laminar flow regimes occur at a mass rate of approximately 10^{-4} gr/s for the first group (Clearwater and Montney 10D), and a rate of approximately 5×10^{-5} gr/s for the second group (Montney 17O and 8H). Fig. 43 shows the same plot as in Fig. 42 with the mass rate in logarithmic scale. The transition between pre-laminar and laminar flow regimes occur at different rates for samples with different apparent permeabilities. The transition between velocity dependent flow regimes is best represented by the Reynolds number. However, in this work we refrained from using the Reynolds number and used mass rate instead. In order to calculate the Reynolds number, for the materials under study, estimations of pore radius size and gas velocity in pores are required (Eq. 6). Due to this difficulty, mass rate is chosen as a representation of velocity as it is also independent of gas pressure.

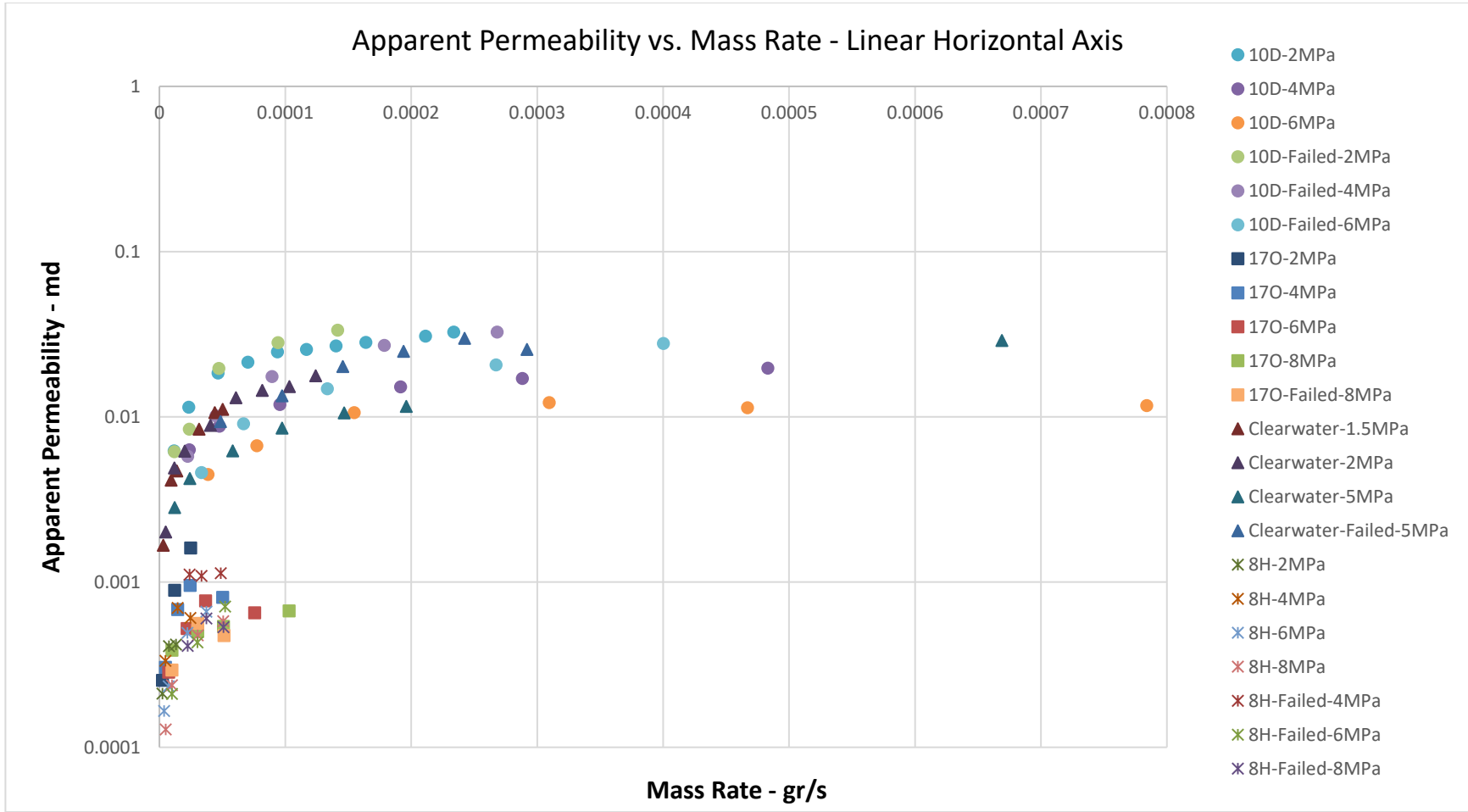


Fig. 42: A plot of the apparent permeability versus mass rate for all the samples, in the intact and failed states. The horizontal axis is linear. The transition between the pre-laminar and laminar regimes can be observed in the experimental results, as anticipated from Fig. 38 and Fig. 40.

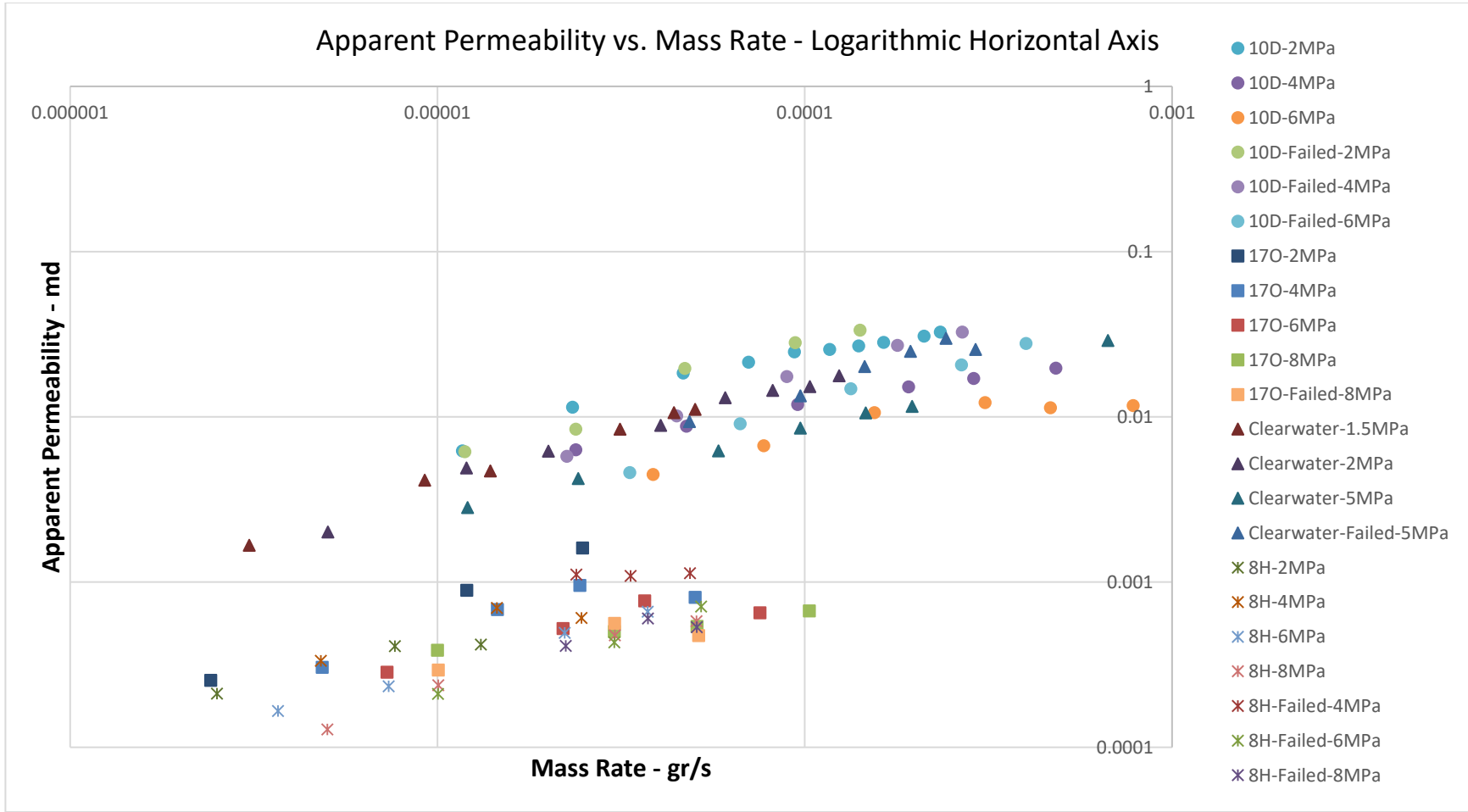


Fig. 43: A plot of the apparent permeability versus mass rate for all the samples, in the intact and failed states. The horizontal axis is logarithmic. The transition between the pre-laminar and laminar regimes can be observed in the experimental results, as anticipated from Fig. 38 and Fig. 40.

Rate-Dependent Model

In order to quantify the change in apparent permeability with rate, we assume that at extremely low rates (or low pressure gradients) the fluid will only flow through the center of the pore, where the friction is the lowest. Therefore, a smaller portion of the pore size is used for flow. As the rate increases, the extra energy helps mobilize the fluid through the rest of the pore diameter until the laminar flow boundary reaches the pore walls. This point coincides with the transition from pre-laminar to laminar flow. If the rate is increased further there will be no noticeable change in permeability, as the entire area of the pore is already in use for flow. The laminar flow regime stands until the rate increases to a point where inertial energy loss emerges. This hypothesis leads to the conclusion that rate in the pre-laminar flow regime changes the effective pore radius to flow, which determines the absolute permeability. Therefore, the absolute permeability increases with rate until the laminar flow regime is reached. Assuming the limit of zero permeability at the rate of zero, and that permeability increases with rate until it reaches the laminar permeability value; we can write the following relationship between absolute permeability and rate:

$$k_{abs} = k_{laminar}(1 - \exp(-\delta\dot{m})), \quad \text{Eq. 44}$$

where $k_{laminar}$ is the absolute or water permeability in the laminar flow regime, \dot{m} is the mass flow rate, and δ is a parameter that determines the transition between pre-laminar and laminar regimes. Replacing Eq. 44 for the absolute or liquid permeability in Eq. 33, we can calculate the apparent permeability with respect to pressure and flow rate. It should be noted that the values of “a” and “b” in Eq. 33 are calculated using k_{abs} values obtained from Eq. 44. “a” and “b” change with k_{abs} according to Fig. 26 and Fig. 27. Therefore, the “a” and “b” values also change with rate. Combining Eq. 44 and Eq. 33, the pre-laminar/laminar section of the permeability surface depicted in Fig. 40 can be characterized. Fig. 44, Fig. 45, Fig. 46, and Fig. 47 show the predictions of the apparent permeability versus rate and pressure using Eq. 44 for the Clearwater, Montney 10D, 17O, and 8H, respectively.

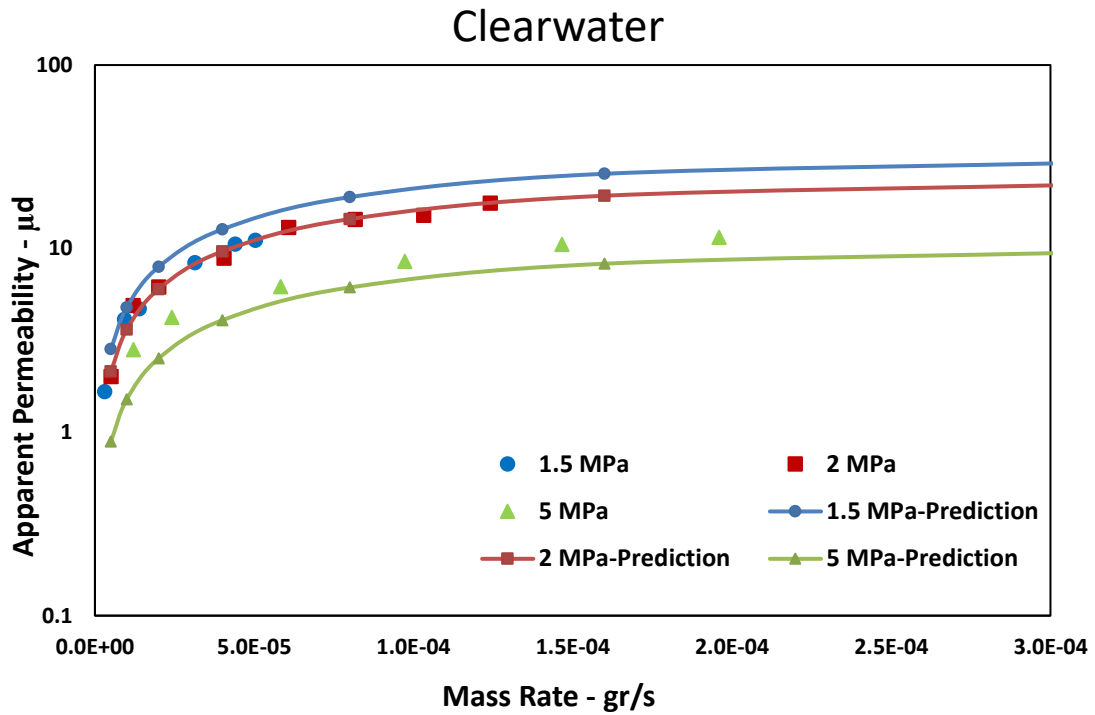


Fig. 44: Prediction of the rate dependent apparent permeability using Eq. 44 for the Clearwater sample.

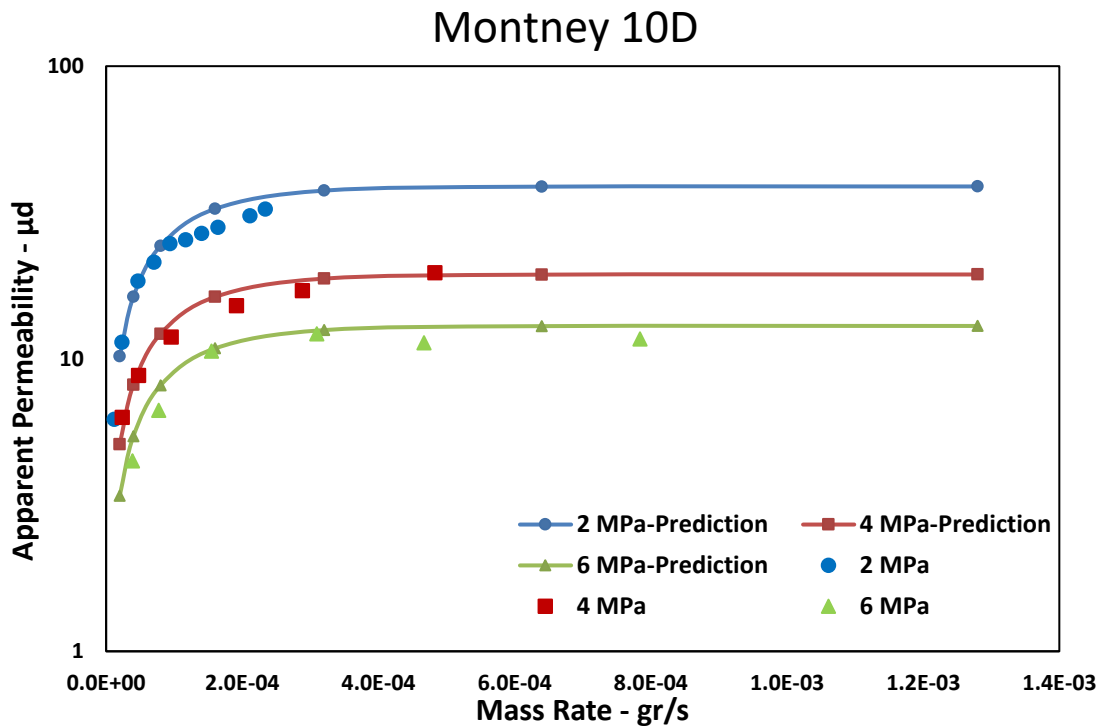


Fig. 45: Prediction of the rate dependent apparent permeability using Eq. 44 for the Montney 10D sample.

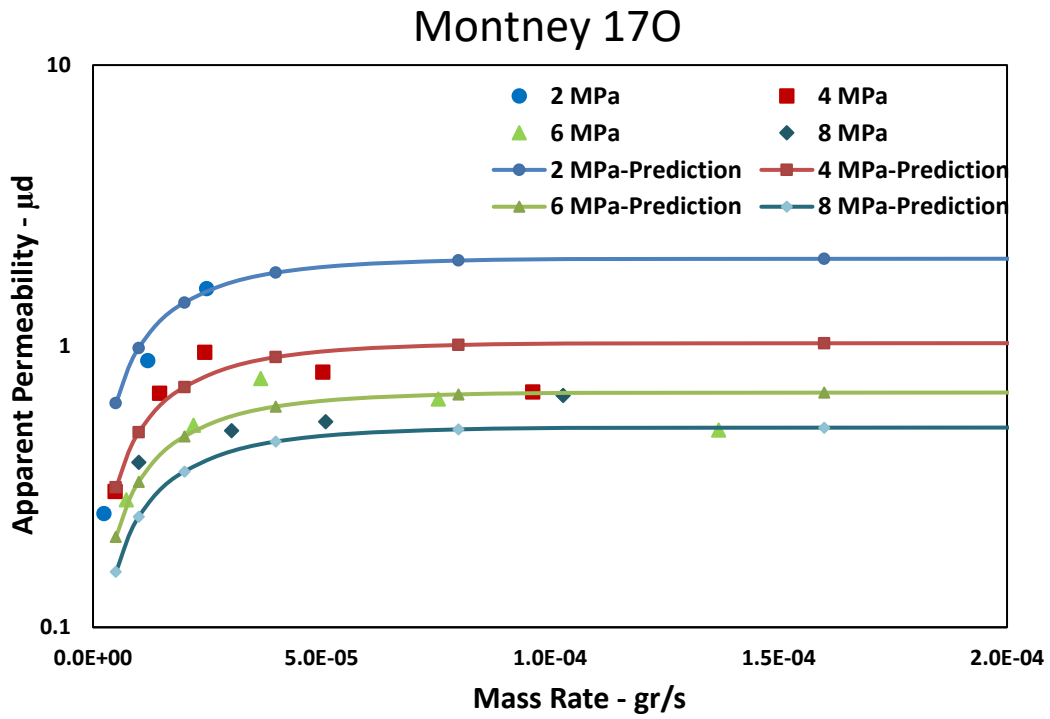


Fig. 46: Prediction of the rate dependent apparent permeability using Eq. 44 for the Montney 17O sample.

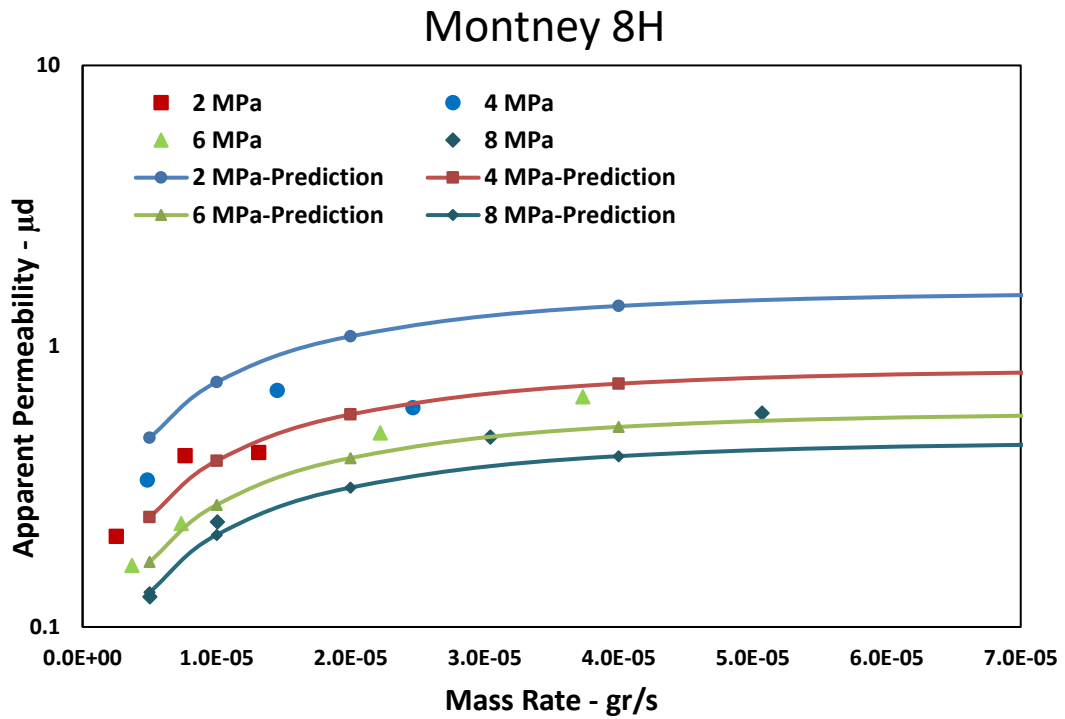


Fig. 47: Prediction of the rate dependent apparent permeability using Eq. 44 for the Montney 8H sample.

Fig. 44, Fig. 45, Fig. 46, and Fig. 47 indicate a good match between the laboratory results and the predictions using Eq. 44. k_{laminar} values are taken to be equal to the water permeability. The right hand side of the Eq. 44 seems to be sufficient to characterize the rate dependency of permeability. δ is the only parameter that needs to be determined. The values of δ are dependent on the rate at which the transition between pre-laminar and laminar flow regimes occur. δ for the Clearwater and Montney 10D samples is taken to be 10^4 (for these samples the transition from pre-laminar to laminar occurs around 10^{-4} gr/s mass rate). For the Montney 17O and 8H samples δ was found to be 5×10^4 (for these samples the transition from pre-laminar to laminar occurs around 5×10^{-5} gr/s mass rate).

Table 9 summarizes the values of parameters used to get the matches in Fig. 44, Fig. 45, Fig. 46, and Fig. 47. k_{laminar} is the absolute or liquid permeability during the laminar flow regime which is mainly a function of the pore radius. Parameters such as water saturation, effective stress, etc. that change the pore radius, influence k_{laminar} . The influence of such parameters on k_{laminar} and apparent permeability are discussed later in this chapter.

Table 9: Summary of the parameters used in Eq. 44 to match the experimental results

Sample	$k_{\text{laminar}}(\text{nd})$	δ (gr/s ⁻¹)
Clearwater	1000	10000
Montney 10D	5	10000
Montney 17O	1.5	50000
Montney 8H	87	50000

Gas Type and Temperature

The Montney 10D sample is saturated with nitrogen, and permeability tests are repeated in order to compare the measurements with methane permeability. Fig. 48

shows the permeability results for methane and nitrogen. All the tests are conducted at a constant mean effective stress. Nitrogen has a slightly higher mean free path compared to methane (at the same pressure and temperature) therefore Knudsen number values for nitrogen tests are slightly higher. This leads to a higher permeability for nitrogen compared to methane that is evident in Fig. 48. The permeability of nitrogen and methane are comparable according to the ratio of their mean free path (or Knudsen number) at the flow condition. This does not apply to helium. It is very common to use helium for permeability measurements to avoid the postulated effect of adsorption on permeability. However, helium permeability is observed to be much larger than methane or nitrogen (Sinha et al., 2013; Ghanizadeh et al., 2014). This cannot be entirely explained by comparing Knudsen numbers of helium and methane. The enhanced permeability of helium is larger than what the current models can predict (Sinha et al., 2013). The small size of the helium molecule could provide access to pathways that methane and nitrogen cannot flow through. These small pathways should not be considered part of the effective permeability as methane is the typical in-situ fluid. Additionally, Fig. 7 shows that helium permeability measurements in the lab are well into the transition or even free-molecule flow regime which leads to a large permeability enhancement. This makes the data analysis of the lab results more difficult. Therefore, estimates of the absolute permeability from helium tests become questionable. With the current understanding, helium permeability data could be a qualitative measurement at best. Fig. 49 shows a similar behavior for methane and nitrogen permeability for the Montney 17O sample.

The rate dependency of permeability is observed for both gases. One of the nitrogen test sets is conducted at 45 C (as opposed to 25 C for the rest of the tests). The results of those tests are also presented in Fig. 48. Looking at the Knudsen number values for the high temperature tests and comparing to the Knudsen values from the tests with methane, temperature seems to dampen the permeability. Similar observation is made on Montney 8H sample presented in Fig. 50. For the case of Montney 8H sample, temperature is raised to 45 C and methane permeability is measured at different rates. The behavior with mean pressure or Knudsen number

is as expected; as pressure increases (Knudsen number decreases) the permeability decreases. Comparing the Knudsen values, the temperature is expected to increase the permeability (by increasing the mean free path and hence the Knudsen number) but the results for both Montney 17O and 8H show a reduction in permeability by temperature. This observation has also been made elsewhere (Sinha et al., 2013). Currently, no method exists to relate the permeability at room temperature to the permeability at reservoir temperature. Therefore, in order to measure the in-situ permeability, experiments need to be done at reservoir temperature. Further work is needed to explain the behavior of shale permeability with temperature.

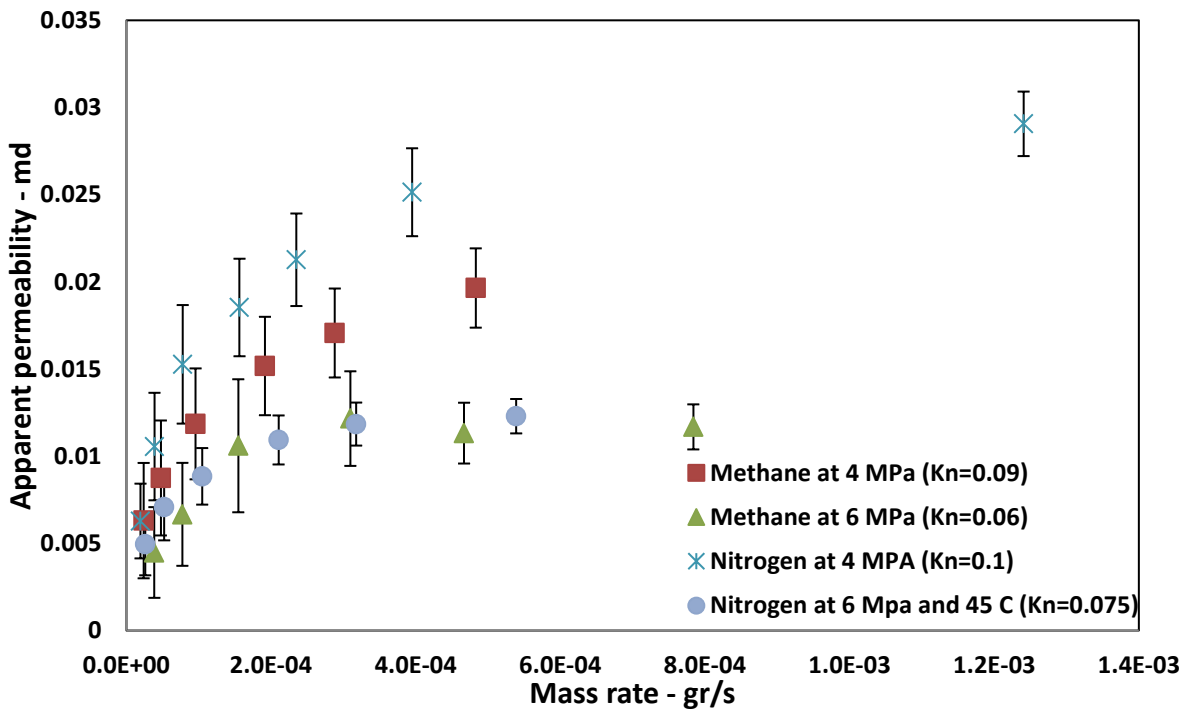


Fig. 48: Nitrogen and methane permeability versus mass flow rate for the Montney 10D sample. One of the nitrogen tests sets have been done at 45 C. Temperature increases the Knudsen number therefore should increase the permeability. However, permeability is observed to be smaller than predicted comparing the Knudsen values.

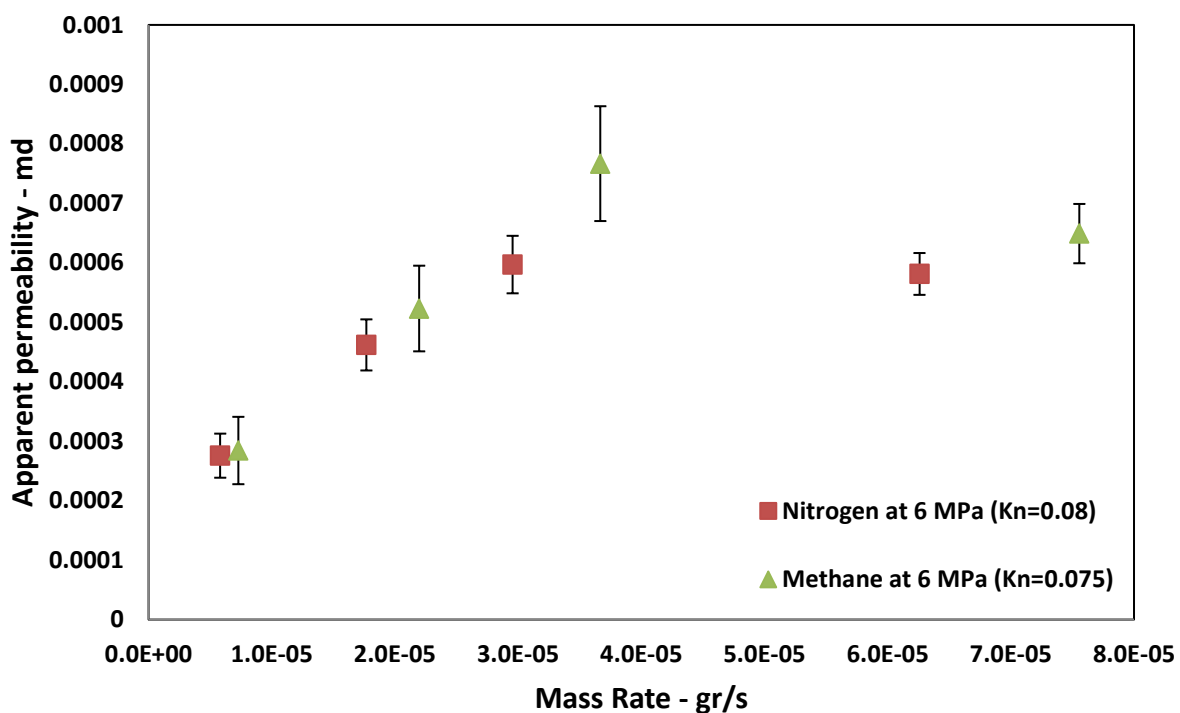


Fig. 49: Methane and nitrogen permeability for the Montney 17O sample. Nitrogen permeability values are comparable to methane permeability, considering the Knudsen number.

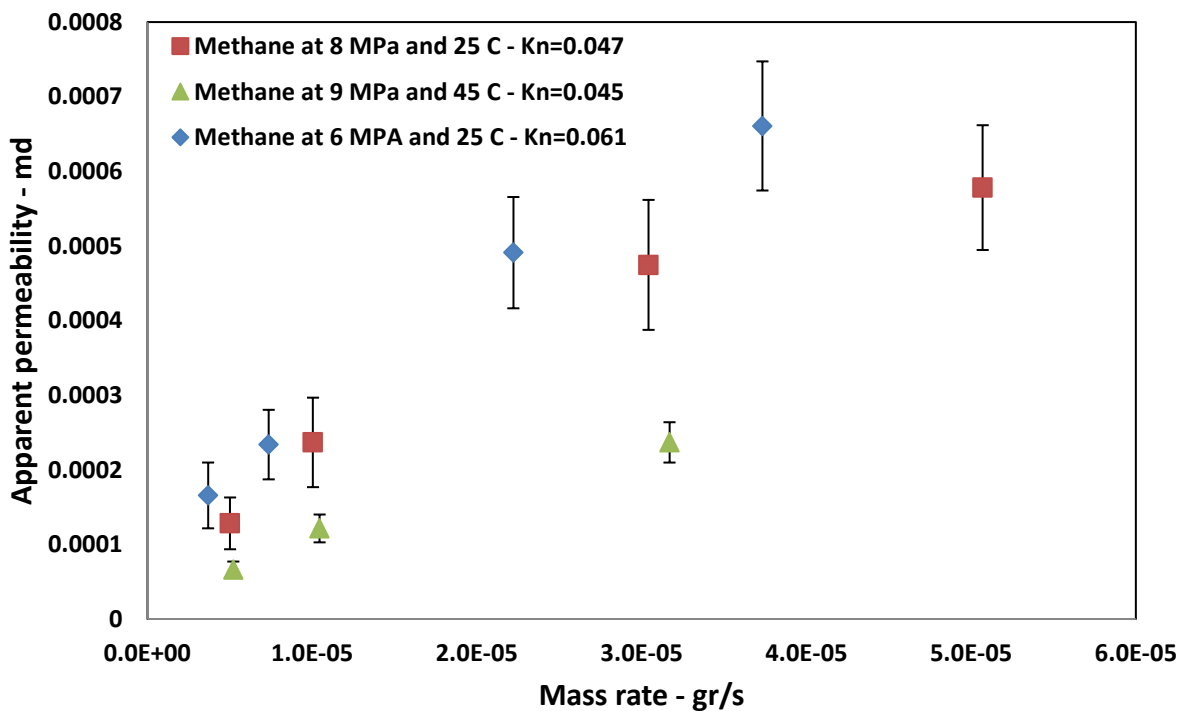


Fig. 50: Methane permeability at 25 and 45 C and different pressures for the Montney 8H sample. Temperature seems to dampen the apparent permeability.

Water Permeability

Water permeability is measured for all the Montney samples before and after shearing at three different mean effective stresses. The permeability of all the intact samples is in the nano darcy range. Each water permeability test on Montney 170 and 10D took approximately one week to stabilize at a pressure differential of 5 MPa. The pressure differential exceeds the recommended value of 10% of the mean effective stress. However, at lower pressure differentials the flow rate was lower than the rate measurement resolution of the available apparatus. Due to the difficulty and the duration of the water tests, rate sensitivity of water permeability was not investigated. Water permeability of the Montney 8H sample is considerably higher and took only 24 hours to stabilize. After the tests on intact samples, the ram increases the axial stress on the sample to create fractures. The length of the samples is too small to make meaningful strength measurements due to scale effects. In order to measure the strength accurately, the height to diameter ratio of the samples should be at least two and a diameter of more than two inches (Brown, 1981; Jackson and Lau, 1990). In the present work the length of the samples are smaller than the diameter and due to the size effects the strength of the sample will be significantly overestimated. Additionally, due to the size effects no strain softening behavior was observed. In order to capture onset of fracture initiation, a differential pressure along the sample is maintained with water. Axial stress is raised slowly until it reaches a stress level at which water flows considerably through the sample. At this deviatoric stress level the sample is assumed to have an open fracture. The stress level is then reverted back to the initial isotropic condition and the water permeability tests are repeated. Setting the stresses back to the original isotropic condition will close most of the fractures created in the samples. However; the fractures retain some of the permeability. Table 10 summarizes the water permeability measurement before and after shearing. The Montney 10D sample shows the most significant enhancement in permeability while the Montney 8H sample shows a more modest increase. Unfortunately, due to the small size of the samples and lack of internal displacement gauges, it is difficult to distinguish

between the extent of fractures created in each sample. Ideally, volumetric strain of the samples should be monitored accurately in order to compare the fracture volume and therefore permeability enhancement. The Montney 17O sample does not show noticeable increase in permeability. There is a possibility that the sample was not sheared significantly, or that the fractures created completely closed and did not retain any permeability. Post-shear gas permeability measurements confirm the lack of permeability enhancement in the Montney 17O sample.

Table 10: Summary of the water permeability measurements.		Pre-shear	Post-shear
Sample	Mean effective stress (MPa)	Permeability (nd)	Permeability (nd)
Montney 10D	10	34	11046
Montney 10D	15	8	7518
Montney 10D	20	5	5913
Montney 17O	10	3.5	7
Montney 17O	15	2.2	12
Montney 17O	20	1.5	2
Montney 8H	10	165	380
Montney 8H	15	111	177
Montney 8H	20	87	132

Higher permeability of the Montney 8H sample enabled us to continuously measure water permeability while shearing. During the shearing process, a constant differential pressure (1.5 MPa) was maintained across the sample using water. Therefore water continuously flows through the sample as the axial stress is increased. The rate at which water flows through the sample is measured every 30 seconds during the shearing process and permeability is calculated for each rate. Fig. 51 shows the permeability evolution during shearing for the Montney 8H sample. The volumetric strain is also provided in Fig. 51. There were no internal

gauges in the cell to measure the volumetric strain and the values reported in Fig. 51 are estimated from the change in the confining oil volume in the triaxial cell. Therefore, the accuracy of the volumetric strain values is questionable. Nonetheless, the estimate is useful for a qualitative analysis. Permeability is observed to decrease slightly as the sample contracts during the early stages of shearing. It then increases significantly as the sample dilates according to the volumetric strain (negative volumetric strain shows dilation). It should be emphasized that permeability values reported in Table 10 are measured after setting the stress condition back to the original isotropic value prior to shearing.

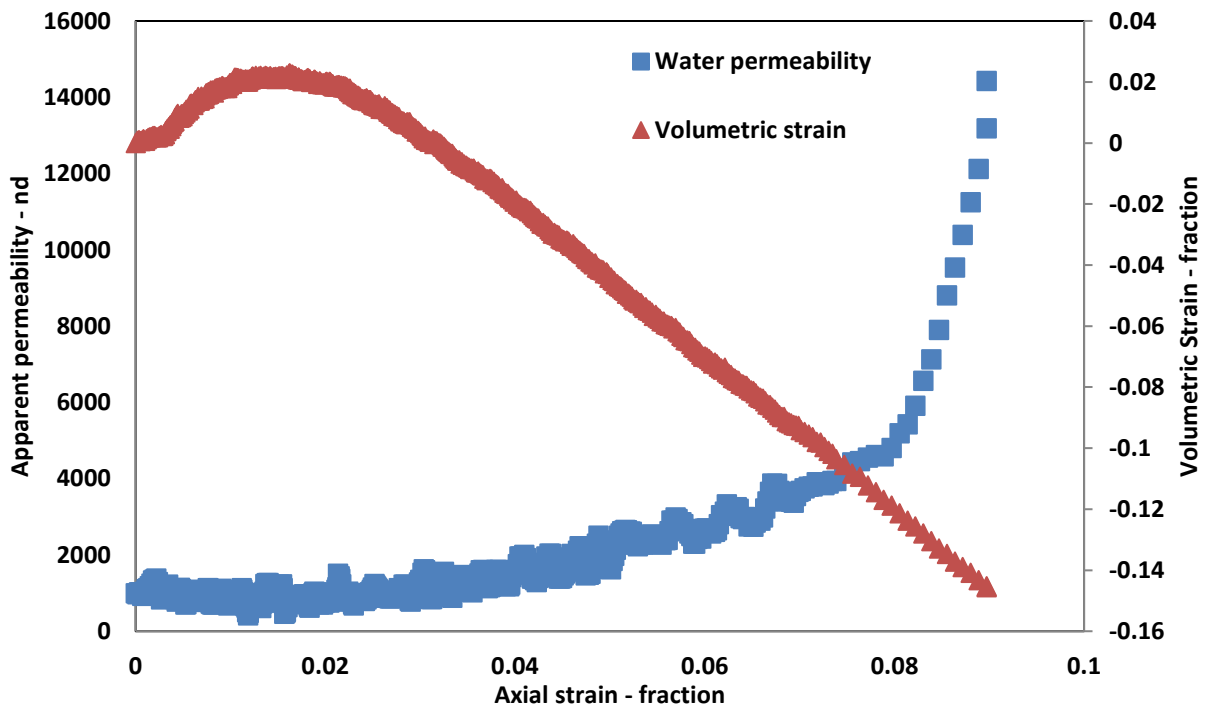


Fig. 51: Continuous water permeability measurements during shearing for the Montney 8H sample. Permeability slightly decreases as the sample contracts (according to volumetric strain) and then increases significantly as dilation occurs.

Influence of Geomechanics

To study the effect of flow regime on permeability, lab experiments need to be done at a constant mean effective stress. However, the influence of mean effective stress

on permeability needs to be addressed in order to study the evolution of permeability in a shale gas reservoir throughout its production life. Fig. 52 shows the water permeability of the Montney samples at various confining stresses. As expected, permeability decreases as mean effective stress increases. In all tests carried out for the present study, the confining stress is isotropic, unless mentioned otherwise. Applying a deviatoric stress on samples could result in different behaviour for permeability. Deviatoric (shear) stress could induce small shear fractures in samples even at stress levels below the peak (Martin and Chandler, 1994; Nicksiar and Martin, 2014). Fractures increase rock permeability and could change the gas flow regime and slip flow parameters.

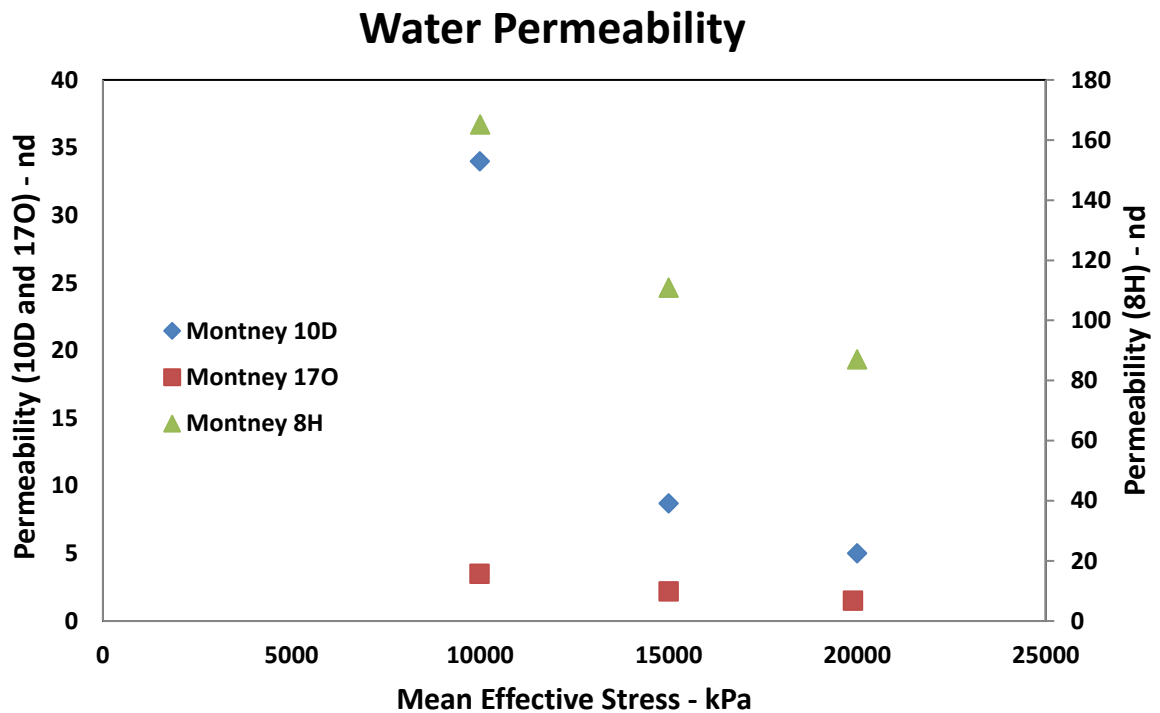


Fig. 52: Experimental results for change in water permeability with respect to mean effective stress. Left axis shows water permeability values for Montney 10D and 17O samples. Right axis shows water permeability values for Montney 8H sample.

Fig. 53 shows the water permeability of the samples after failure at different isotropic effective confining stress values. Water permeability is significantly higher for the failed samples compared to the intact water permeability (Table 10).

Similar to the intact samples, water permeability of the failed samples decreases as the mean effective stress increases. The post-failure permeability of Montney 170 sample was not included as no significant failure had occurred in that sample.

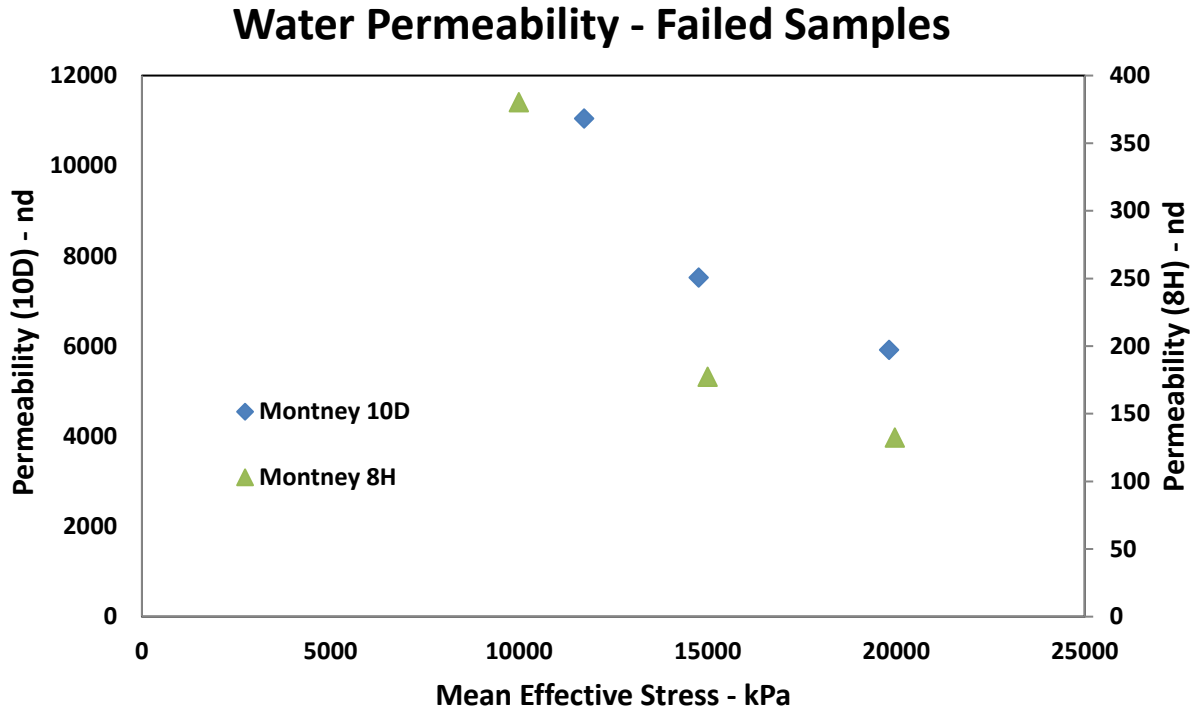


Fig. 53: Experimental results for change in water permeability with respect to mean effective stress for the samples after failure. Left axis shows water permeability values for Montney 10D. Right axis shows water permeability values for Montney 8H sample.

Mean Effective Stress

Permeability is then influenced by slip flow and mean effective stress (ignoring effects such as water saturation and adsorption at this stage). Therefore, the measured apparent permeability is a result of the balance of the geomechanical and flow regime effects. The change in permeability with mean effective stress is typically fitted empirically with an exponential or power law function (Davies and Davies, 2001; Ghabezloo et al., 2009). As mean effective stress increases, the pore radius decreases and therefore permeability is observed to decrease. On the other hand, slip effect enhances the apparent permeability compared to the liquid permeability. At the same time, the slip flow parameters in Eq. 33 are all functions of liquid permeability as observed in Fig. 26 and Fig. 27. Therefore the slip flow

parameters also change with the mean effective stress. A typical reservoir production scenario starts with high pressure and a fixed in-situ stress in the reservoir. Assuming the in-situ stress is isotropic and constant, after production starts, the pore pressure in the reservoir drops due to depletion. This has two consequences 1) a decrease in pore pressure decreases permeability due to an increase in mean effective stress (Eq. 8), and 2) a decrease in pore pressure will enhance slip flow (including the slip flow parameters in Eq. 33), thus increasing apparent permeability. Therefore the final functioning permeability value involves interplay between effective stress and slip flow effects (Moghadam and Chalaturnyk, 2016).

Eq. 45 can be used to describe the change in water permeability with respect to mean effective stress.

$$k_{abs} = k_w = k_0 \exp(-\alpha\sigma_{eff}) \quad \text{Eq. 45}$$

k_0 can be defined as the water permeability at zero effective stress, and α represents the sensitivity of the sample permeability to changes in mean effective stress (compressibility). The applicability of Eq. 45 depends on the range of mean effective stress covered in the lab experiments, from which α is calculated. The values of α and k_0 can be calculated from Fig. 52 and Fig. 53. Table 11 presents the values of α and k_0 calculated for both intact and failed samples.

Table 11: Parameters for Eq. 45 Calculated from the experimental results.

Sample	Intact Sample		Failed Sample	
	k_0 (nd)	α (MPa ⁻¹)	k_0 (nd)	α (MPa ⁻¹)
Montney 10D	202	0.2	24814	0.07
Montney 17O	9	0.1	-	-
Montney 8H	305	0.06	1014	0.1

If k_{wi} is defined as initial water permeability, and constant in-situ stress is assumed with time, the permeability versus mean effective stress can be written as Eq. 46.

$$k_w = k_{wi} \exp(-\alpha(P_i - P)) \quad \text{Eq. 46}$$

P_i and P are the initial and current reservoir pressures, respectively. k_{wi} is water permeability at the reservoir's initial mean effective stress condition which can be defined according to Eq. 45, setting σ_{eff} equal to the initial mean effective stress. Eq. 46 can be substituted in Eq. 33 in place of absolute (liquid) permeability in order to relate the apparent permeability to mean effective stress.

$$\frac{K_{\text{app}}}{k_{wi}} = \exp(-\alpha(P_i - P)) \left(1 + \frac{b(k_w)}{P} - \frac{a(k_w)}{P^2} \right) \quad \text{Eq. 47}$$

Eq. 47 shows the ratio of apparent permeability to initial water permeability. This ratio is a permeability multiplier related to the mean effective stress and slip effect. Parameters “a” and “b” are functions of water permeability. This work uses the best fit from Fig. 27 and Fig. 29 to relate “a” and “b” to water permeability, as shown in Eq. 48 and Eq. 49.

$$b = \exp(6 - 0.5 \ln(k_w)) \quad \text{Eq. 48}$$

$$a = \exp(1.5 \ln(b) - 3) \quad \text{Eq. 49}$$

k_w in Eq. 48 is the absolute permeability in nano darcy. “a” and “b” in Eq. 48 and Eq. 49 are in MPa^2 and MPa , respectively. Eq. 47 can be used to plot the permeability multiplier against reservoir pressure. Fig. 54 presents the values of the permeability multiplier with respect to reservoir pressure (The pressure axis is reversed). One curve represents a reservoir with an initial water permeability of 5 nd (similar to that of the Montney 170 sample) and another represents a hypothetical reservoir with an initial water permeability of 400 nd. The behaviour of a permeability multiplier with pressure is similar in both curves however, the lower permeability results in a much higher permeability multiplier. Initial mean effective stress is assumed to be 10 MPa. The parameters used to create Fig. 54 have been taken from the laboratory findings on the Montney 170 sample. Fig. 54 also plots the permeability multiplier due only to slip flow (the right hand portion of Eq. 47), omitting the influence of mean effective stress. According to the figure, if the influence of mean effective stress is ignored, the permeability multiplier will be significantly overestimated as reservoir pressure decreases. The value of the permeability multiplier is roughly flat as the pressure drops, and increases as the

pressure reaches very low values. The relatively flat curve at higher pressures indicates that the increase in apparent permeability due to slip flow is largely cancelled out by the increase in mean effective stress. However, the relative sensitivity of the rock to changes in mean effective stress (α) influences the behaviour to an extent. Fig. 55 shows the sensitivity of the permeability multiplier to α for the case with k_{wi} equal to 5 nd in Fig. 54. Higher sensitivity to stress (higher α) could result in further decrease in the permeability multiplier over time, and lower sensitivity (lower α) could increase the permeability multiplier due to a more dominant slip flow effect.

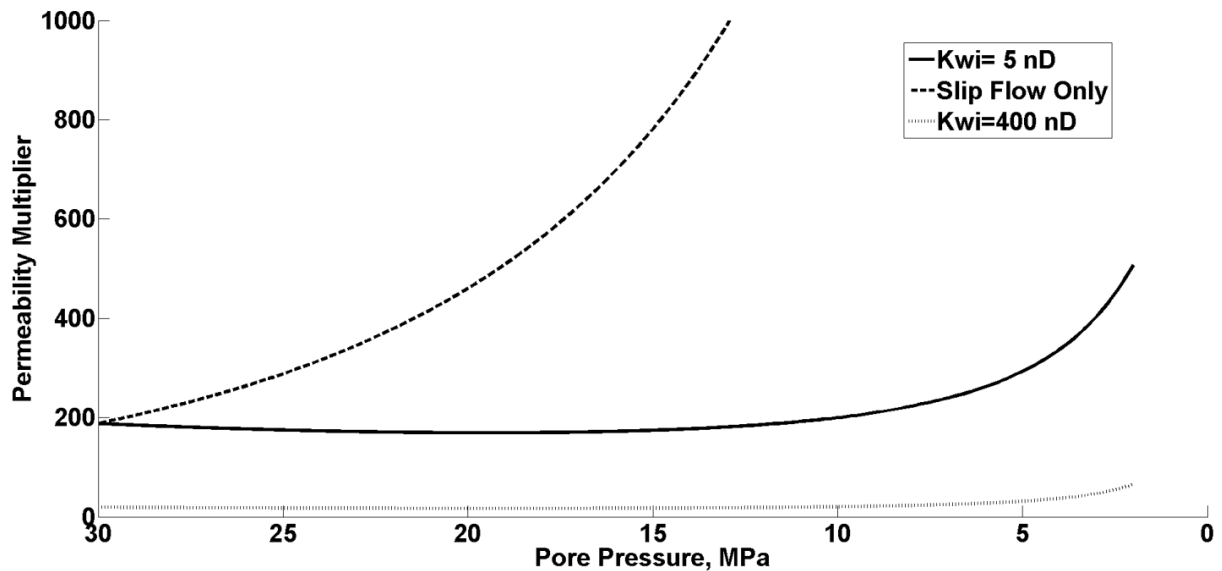


Fig. 54: Permeability multiplier (ratio of apparent permeability to initial water permeability) with respect to reservoir pressure. Dotted curve shows evolution of permeability multiplier considering only slip flow and ignoring influence of effective stress.

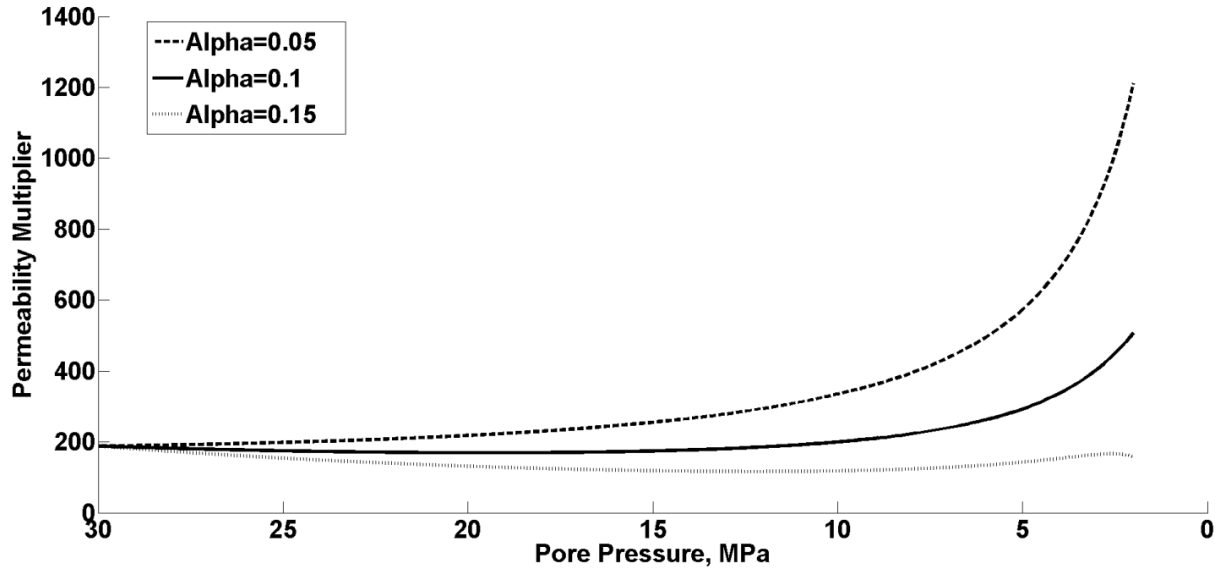


Fig. 55: sensitivity of the permeability multiplier to α for the case with $k_{wi}=5$ nd.

Steady-state permeability tests have been conducted on the Montney 170 sample at two different mean effective stresses. Using the results of this work and Eq. 47, the apparent permeability could be predicted at specific mean effective stresses. Fig. 56 shows the laboratory results and predictions for the apparent permeability of the Montney 170 sample. Predictions for both effective stresses yield R-squared values above 0.95. As mean effective stress increases, apparent permeability decreases. However the reduction in apparent permeability is less than expected due to enhanced slippage. This is indicated by the change in the values of parameters “a” and “b”. The magnitude of “a” increases from 532 to 1308 MPa², and that of “b” increases from 1466 to 3713 MPa as the mean effective stress increases from 10 MPa to 20 MPa. Higher values of “a” and “b” are expected at higher mean effective stresses, according to theory, which ameliorates the permeability reduction effect from the increase in mean effective stress. It must be noted, due to the high dependency of permeability to rate, the results presented in Fig. 56 at each mean pressure are measured at the same rate. If measurements are made at a different rate they do not necessarily follow the theory. It is possible to get a higher permeability at 20 MPa effective stress compared to 10 MPa if the test at 20 MPa is conducted at a higher mass flow rate.

Table 8 presents the experimental values of “a” and “b” for the samples in this work and from the literature. Any parameter that changes the absolute permeability of the rock effectively changes the state of permeability and flow regime (Knudsen number). Mean effective stress and any failure induced in the sample change the absolute permeability, and from the results in Table 8, the change in absolute perm leads to a change in “a” and “b”. As the Montney 10D and 8H fail, “a” and “b” values decline which corresponds to an increase in absolute permeability. Using the database provided here and summarized in Eq. 48 and Eq. 49, one can relate the absolute permeability change to slip flow parameters and calculate the apparent permeability for the new state of the rock.

The methodology proposed here, to incorporate the influence of mean effective stress on apparent permeability, considers the flow regime to be laminar. For rate dependent, pre-laminar flow regime, a similar method can be used along with Eq. 44 to capture the rate dependency of permeability. In this case, the laminar permeability in Eq. 44 is equivalent to the absolute or water permeability in Eq. 45. Therefore, the permeability multiplier becomes:

$$\frac{K_{app}}{k_{wi}} = \exp(-\alpha(P_i - P)) (1 - \exp(-\delta\dot{m})) \left(1 + \frac{b(k_w)}{P} - \frac{a(k_w)}{P^2} \right). \quad \text{Eq. 50}$$

Using Eq. 50, the influence of mean effective stress, pre-laminar rate dependent flow regime, and the mean pressure are incorporated in calculating the apparent permeability. Eq. 50 captures the permeability surface depicted in Fig. 40. The “a” and “b” values in Eq. 50 should be evaluated at the equivalent absolute permeability illustrated in Eq. 51, using Eq. 48 and Eq. 49.

$$k_{abs} = k_w = k_{wi} \exp(-\alpha(P_i - P)) (1 - \exp(-\delta\dot{m})) \quad \text{Eq. 51}$$

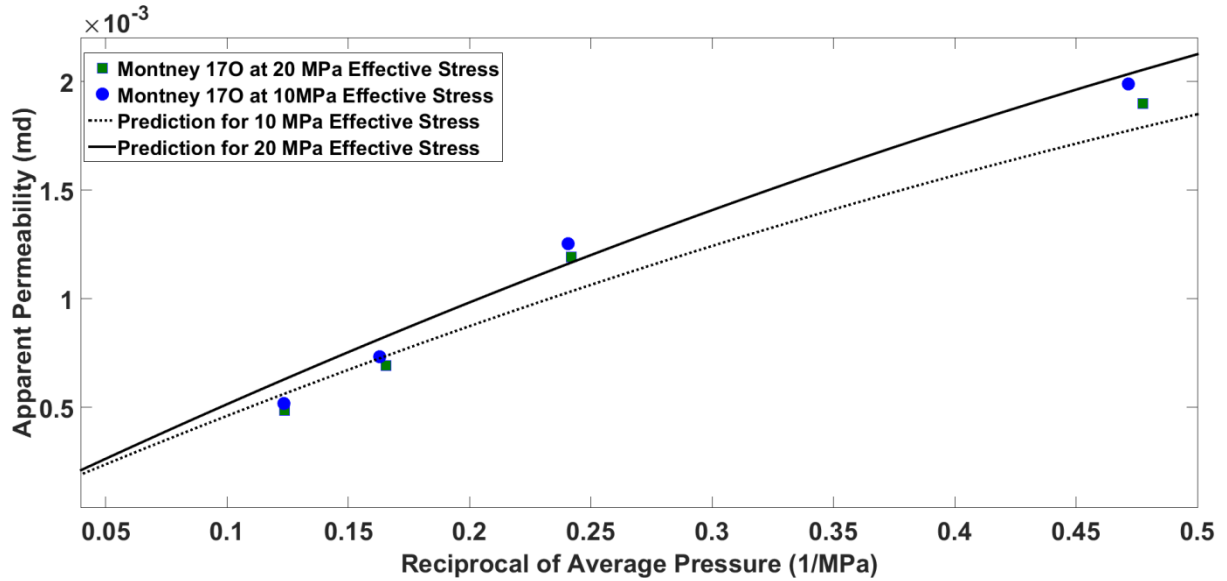


Fig. 56: Experimental results of apparent permeability versus reciprocal of pressure at mean effective stresses of 10 MPa and 20 MPa on the Montney 17O sample. Lines present predictions obtained based on Eq. 47. Note that the data points must be selected from tests at similar mass rate. Generally, in order to analyze the change of permeability with mean pressure (i.e. the slippage effect) all the tests must be conducted at the same mass rate.

Depletion Scenario

At the last stage of the tests, the permeability is measured at relatively high pore pressures, then maintaining the confining stress constant, the pressure is dropped to simulate a depletion scenario. Production from a reservoir is equivalent to reducing the pore pressure while maintaining the same total in-situ stress. These tests are designed to explore the evolution of permeability during the depletion period in a reservoir. The results of the depletion tests on the Montney 10D is illustrated in Fig. 57. Gas permeability is measured at 6 MPa with respect to rate. The pressure is then dropped to 4 MPa while maintaining a constant confining stress (26 MPa). The permeability is measured again at 4 MPa at different rates. Pressure is further dropped to 2 MPa and permeability is measured again. As the pressure drops, apparent permeability is observed to increase due to slippage. This increase in permeability however, is hampered by an increase in mean effective stress. The permeability measurements at 4 MPa and 2 MPa pore pressure, and 20 MPa mean effective stress (original effective stress before depletion) is also plotted in Fig. 57.

The results show that permeability increase due to slippage is slightly hampered by an increase in effective stress. Similar behavior is observed in the depletion tests for the Montney 8H, Montney 17O, and the Clearwater samples presented in Fig. 58, Fig. 59, and Fig. 60. This behavior shows that the effective stress and slippage both control the permeability evolution during depletion of a reservoir. In the case of the present lab results, the slippage effect is more dominant as the permeability increases overall. However, at reservoir pressures the slippage effect is smaller and effective stress might be a more dominant driver of apparent permeability during depletion. This can be clearly observed in Fig. 54. At higher pressures in Fig. 54 the effective stress is relatively dominant and permeability decreases as pressure drops. At lower pressures however, slippage increases permeability as pressure decreases. Laboratory results presented in Fig. 57, Fig. 58, Fig. 59, and Fig. 60 show a similar behavior. It seems that for our samples at pore pressure below 10 MPa, slippage becomes more dominant than the effective stress. Therefore, dropping the pore pressure below 10 MPa enhances the permeability. Using a form of Eq. 47 can predict the behavior observed in the lab results.

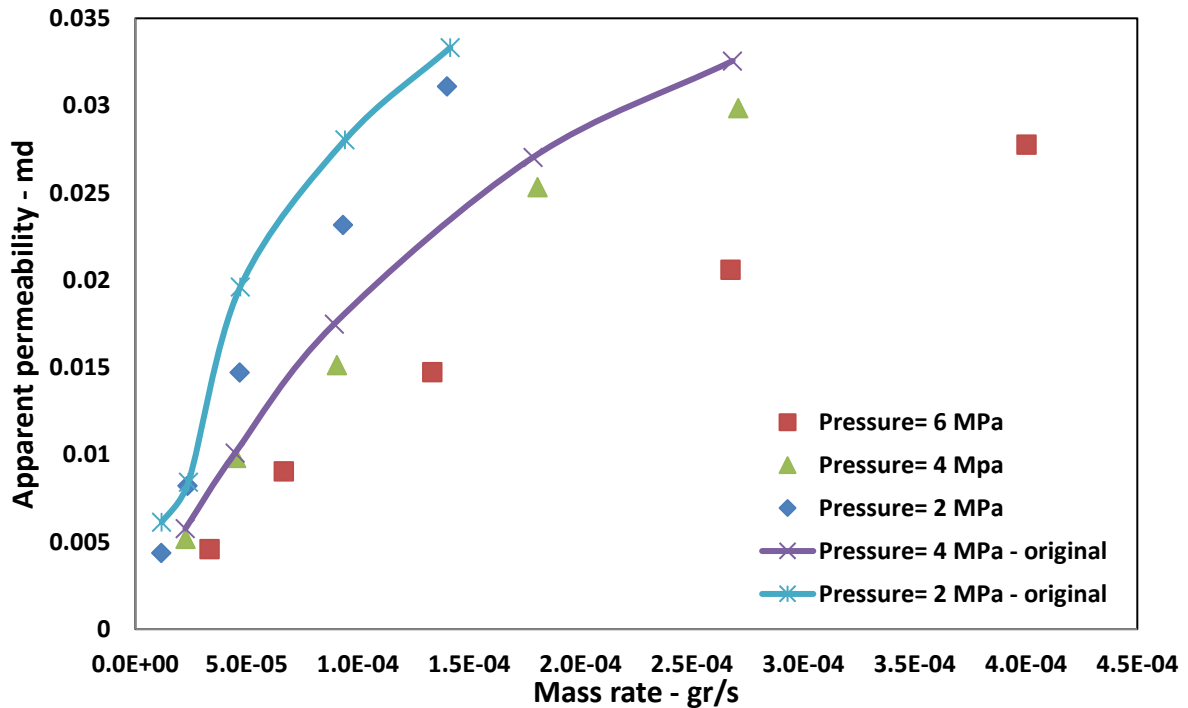


Fig. 57: Depletion scenario for the Montney 10D sample. Total stress is held at 26 MPa. At each stage pressure is reduced while maintaining a constant total stress.

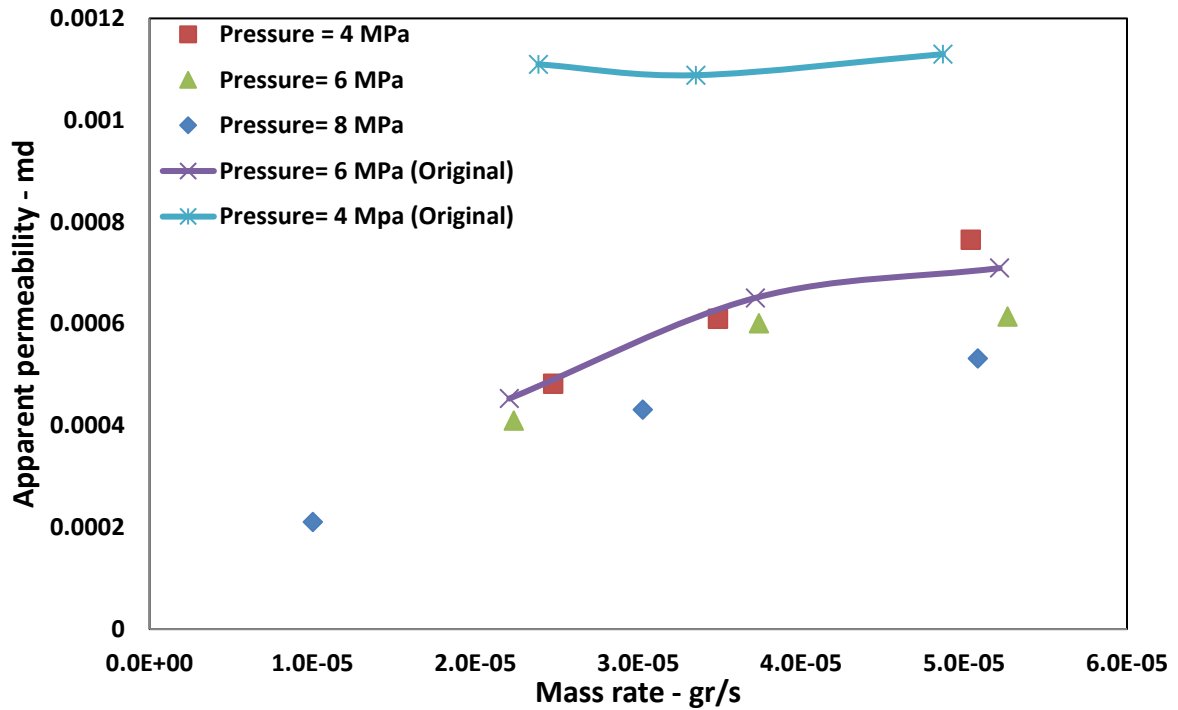


Fig. 58: Depletion scenario for the Montney 8H sample. Total stress is held at 26 MPa. At each stage pressure is reduced while maintaining a constant total stress.

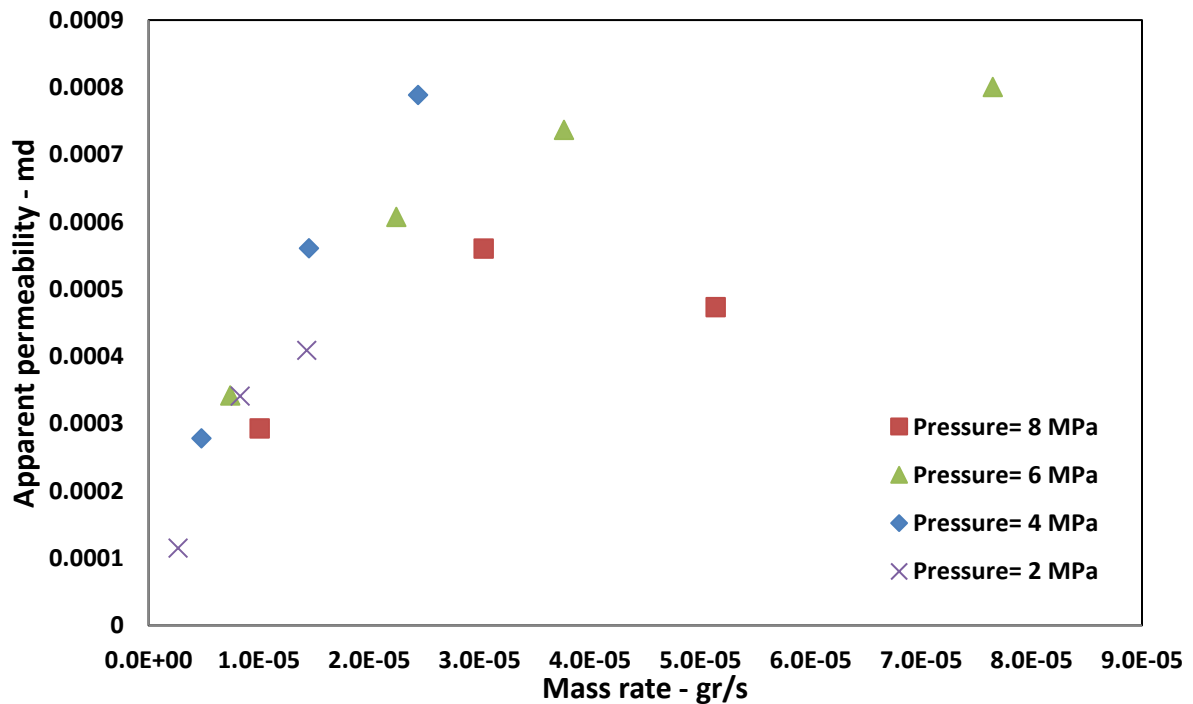


Fig. 59: Depletion scenario for the Montney 170 sample. Total stress is held at 26 MPa. At each stage pressure is reduced while maintaining a constant total stress.

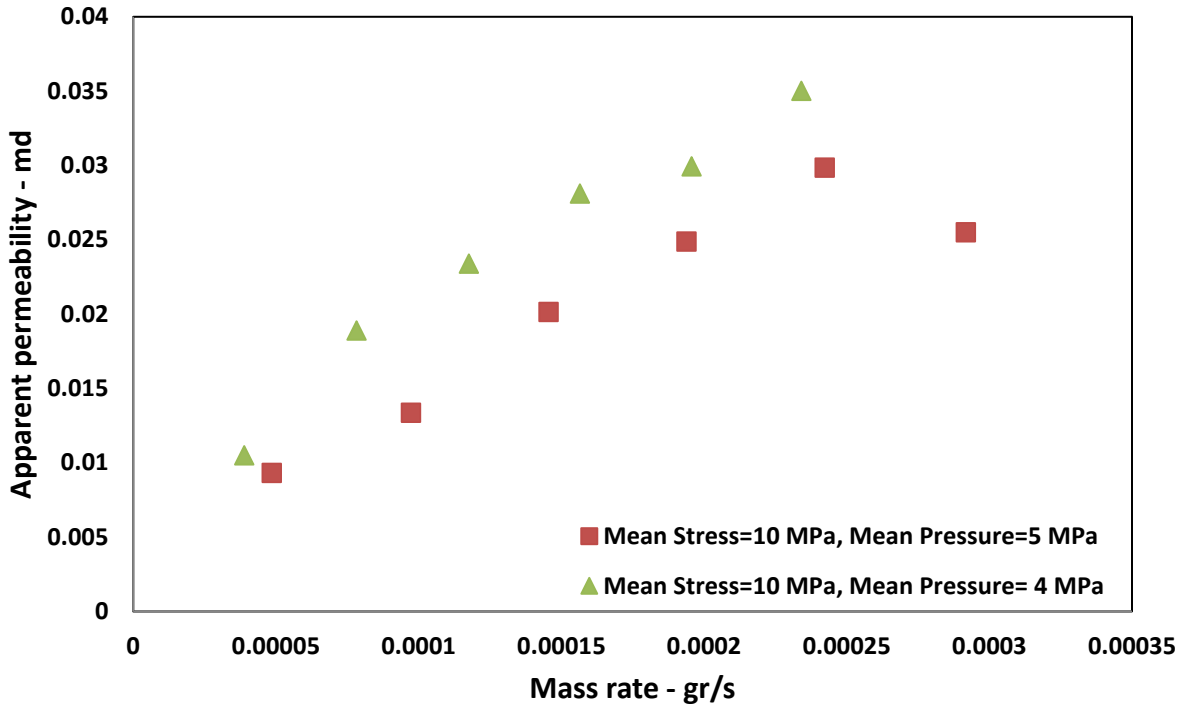


Fig. 60: Depletion scenario for the Clearwater sample. Total stress is held at 10 MPa. At each stage pressure is reduced while maintaining a constant total stress.

Failure

Axial stress on the Clearwater sample is increased to a value 1.5 times the confining stress (8 MPa) and permeability tests are repeated. Fig. 61 shows the permeability values versus mass flow rate. Both sets of tests presented in the Fig. 61 are conducted at 5 MPa mean pressure. One set represents isotropic stress conditions and the other, axial stress is 1.5 times the confining stress. Both results show similar behavior for permeability; it increases with rate but reaches a plateau. The case with the deviatoric stress shows higher permeability which suggests some failure has happened in the sample. This is later on confirmed when the sample is sheared and permeability results follow the deviatoric stress condition in Fig. 61 closely.

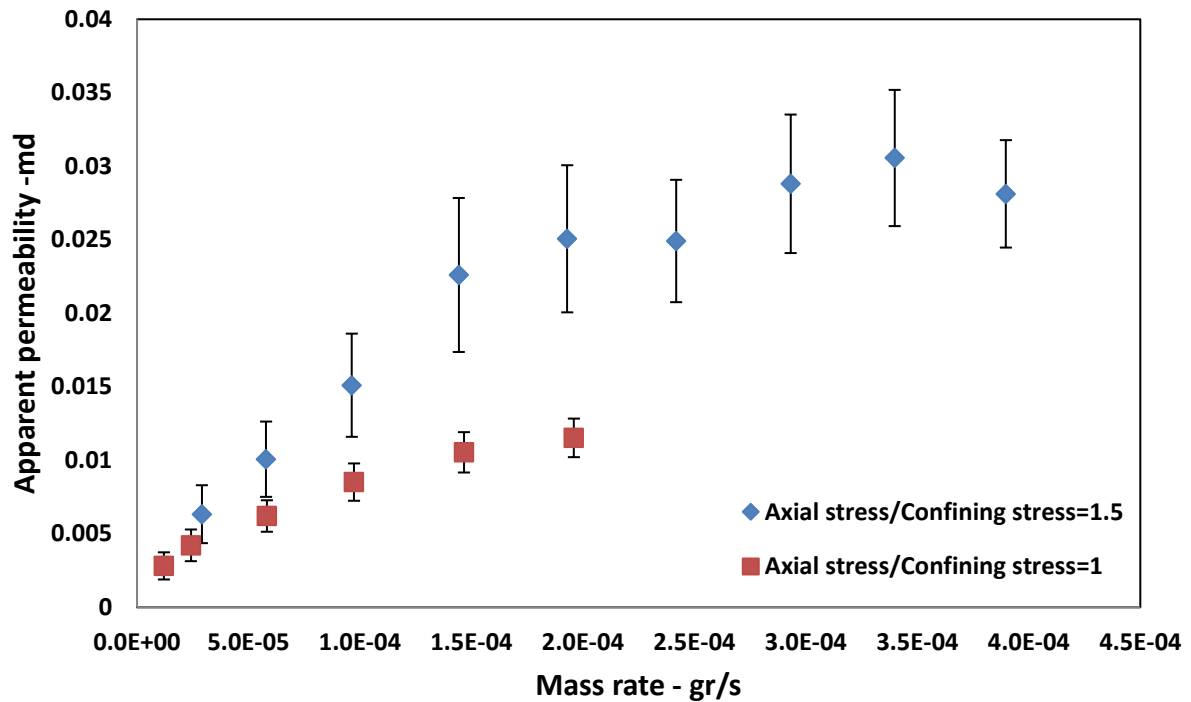


Fig. 61: Gas permeability versus mass flow rate for the Clearwater sample. Both sets of tests presented in the figure are conducted at 5MPa mean pressure. One set represents isotropic stress conditions and the other, axial stress is 1.5 times more than the confining stress. Both results show similar behavior for permeability; it increases with rate but reaches a plateau. The case with the deviatoric stress shows higher permeability which suggests some failure has happened in the sample.

In this work, axial stress is applied on the samples until there is significant flow of water through the sample, as outlined under the methodology section in chapter 5. This process creates micro fractures in the sample. The stress is then reverted back to the isotropic condition, which closes some of the micro fractures. The creation of micro fractures in the rock increases the area to flow and therefore enhances the absolute permeability. Since the area to flow increases, the equivalent pore radius to flow in the Knudsen equation (Eq. 1) rises. This leads to a decrease in the Knudsen value which means a reduction in the gas permeability enhancement. This is illustrated in our lab results by the “a” and “b” values decreasing as the absolute permeability increases (Table 8, Fig. 26, and Fig. 27). Therefore, an increase in absolute permeability though it enhances the apparent permeability overall; it

reduces the permeability enhancement due to flow regime. The increase in absolute permeability could come as a result of a reduction in effective stress or generation of micro fractures. Fig. 62 shows the apparent permeability increase with respect to the absolute permeability at several pore pressures. The results in Fig. 62 are generated using Eq. 33, Eq. 48, and Eq. 49. Fig. 62 indicates that as expected, apparent permeability increases with absolute permeability, though the enhancement due to slippage decreases. This is demonstrated by the apparent permeability values approaching the absolute permeability line (the solid line in Fig. 62) as the permeability increases. The apparent permeability values for pressure of 20 MPa in Fig. 62 shows that even at high pressures the permeability enhancement and therefore the slippage effect is significant and must be taken into account. However, as the absolute permeability increases close to 1 md, the enhancement at high pressures becomes very small. This confirms that at high pressures, in a high permeability porous media, gas permeability reaches the liquid or absolute permeability.

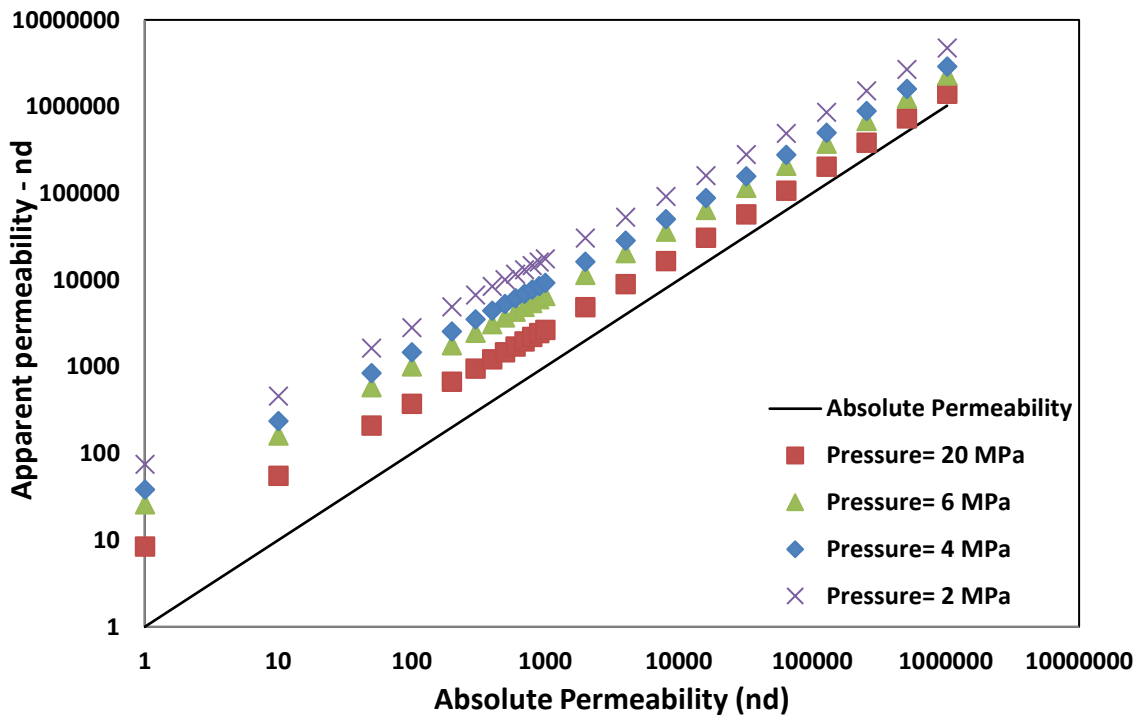


Fig. 62: Apparent permeability increase with respect to the absolute permeability at several pore pressures. The permeability enhancement due to slippage decreases as

absolute permeability increases. This is apparent from the data approaching the solid line at high permeability values.

Fig. 63 shows a summarized version of Fig. 62 that only includes apparent permeability at 8 MPa. Permeability measurements conducted at 8 MPa on the Montney 8H sample before and after failure are also presented. Fig. 63 indicates a good match between theory and experimental results. If the permeability sensitivity of “a” and “b” are neglected, the apparent permeability will be significantly overestimated. This is presented as a dashed line in Fig. 63.

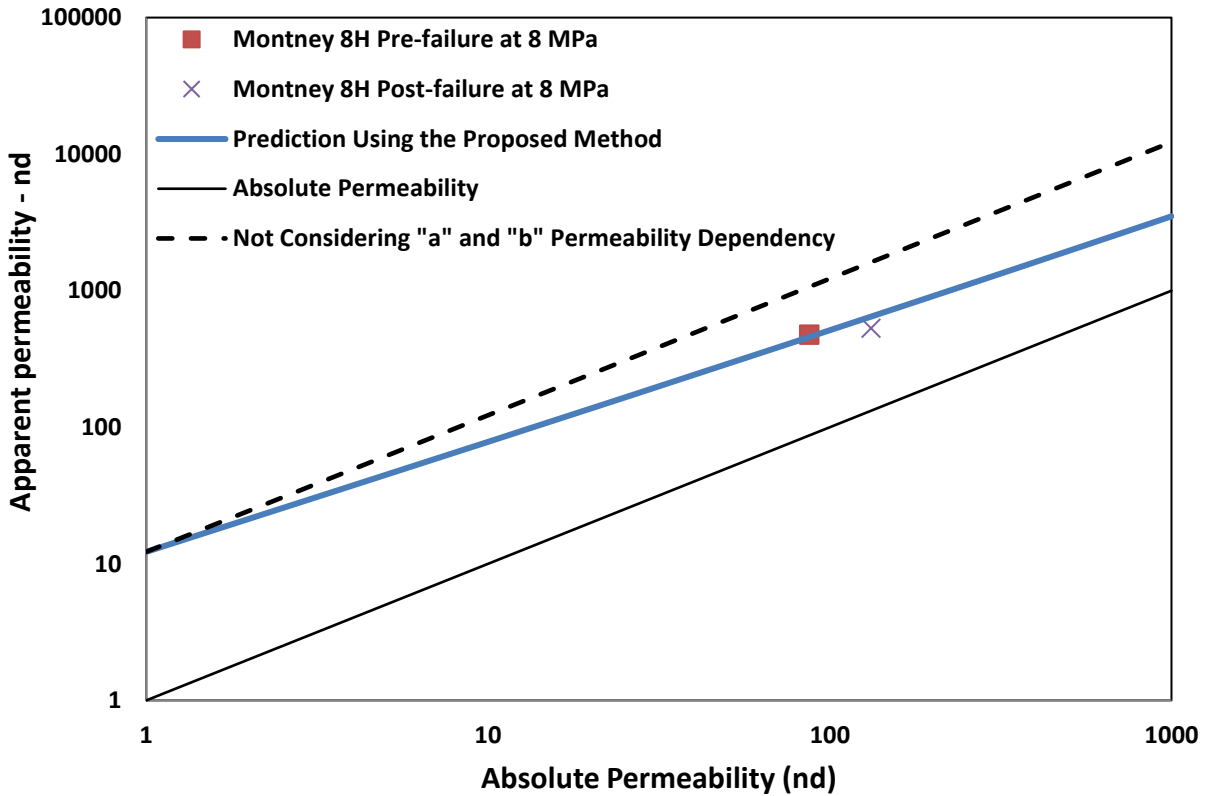


Fig. 63: Apparent permeability increase with respect to the absolute permeability at 8 MPa for the Montney 8H. The dashed line shows the apparent permeability increase if the permeability dependency of “a” and “b” is neglected.

Fig. 64, Fig. 65, and Fig. 66 show examples of measured permeability versus rate, before and after failure, for Montney 10D, 17O and 8H samples. While Montney

10D, and 8H show an increase in gas permeability after the attempt to create micro fractures, Montney 17O shows a similar permeability to the intact sample, within the range of the experimental error. This was expected from analyzing the water permeability values before and after failure. Similar to the intact conditions, apparent permeability of the fractured samples increases with mass flow rate until it reaches a constant value.

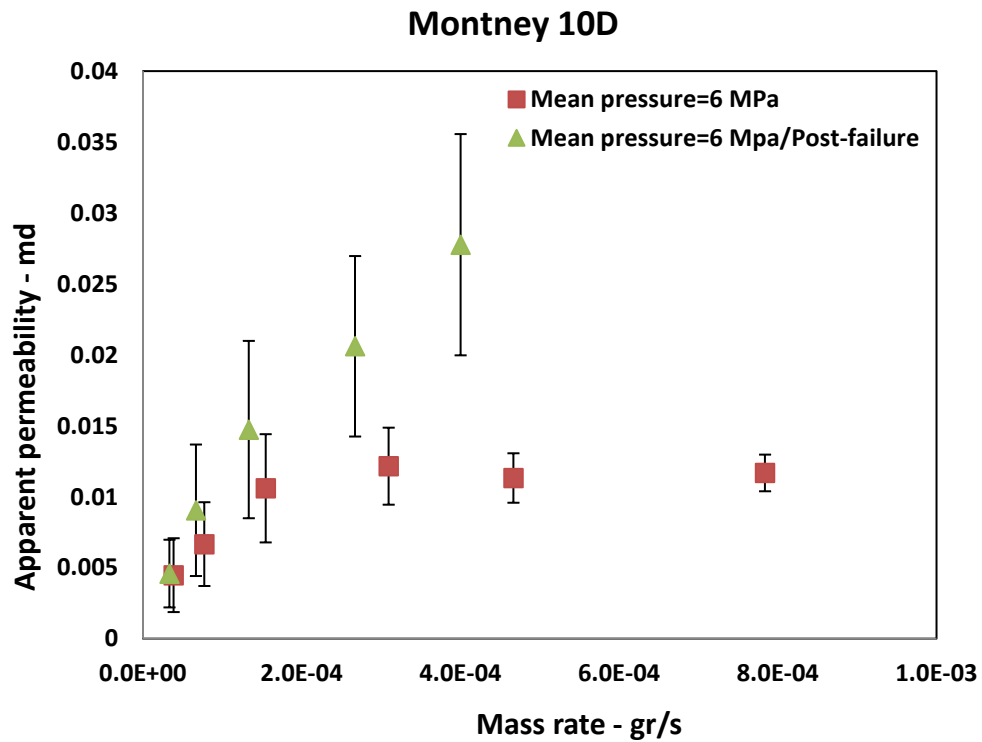


Fig. 64: Measured apparent permeability versus mass rate, before and after failure for the Montney 10D sample.

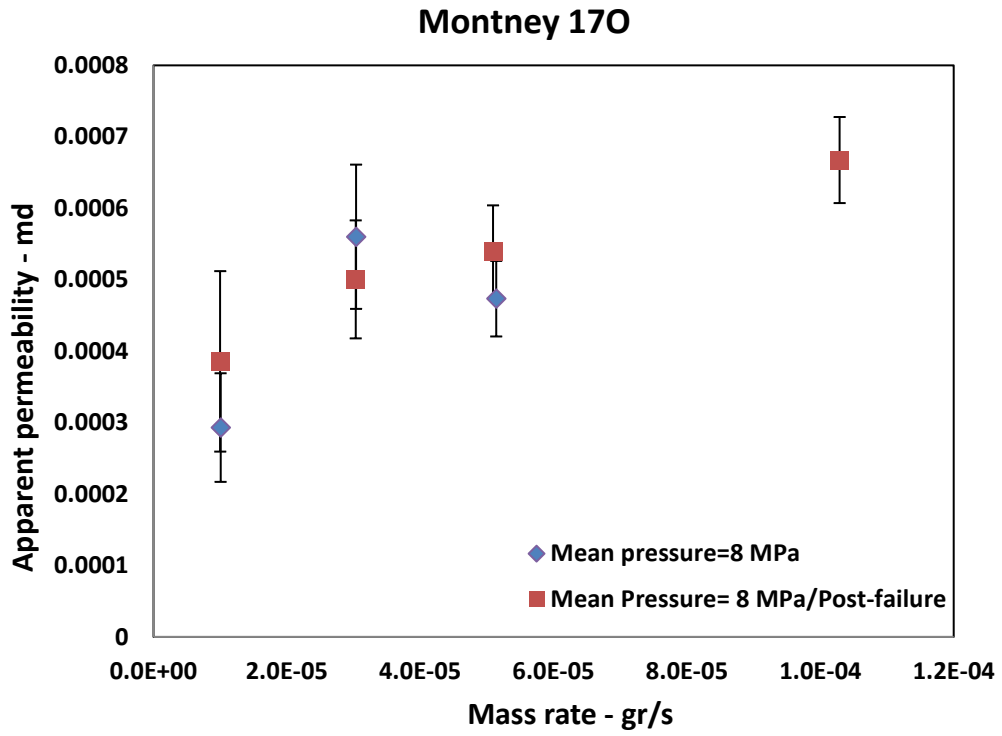


Fig. 65: Measured apparent permeability versus mass rate, before and after failure for the Montney 17O sample.

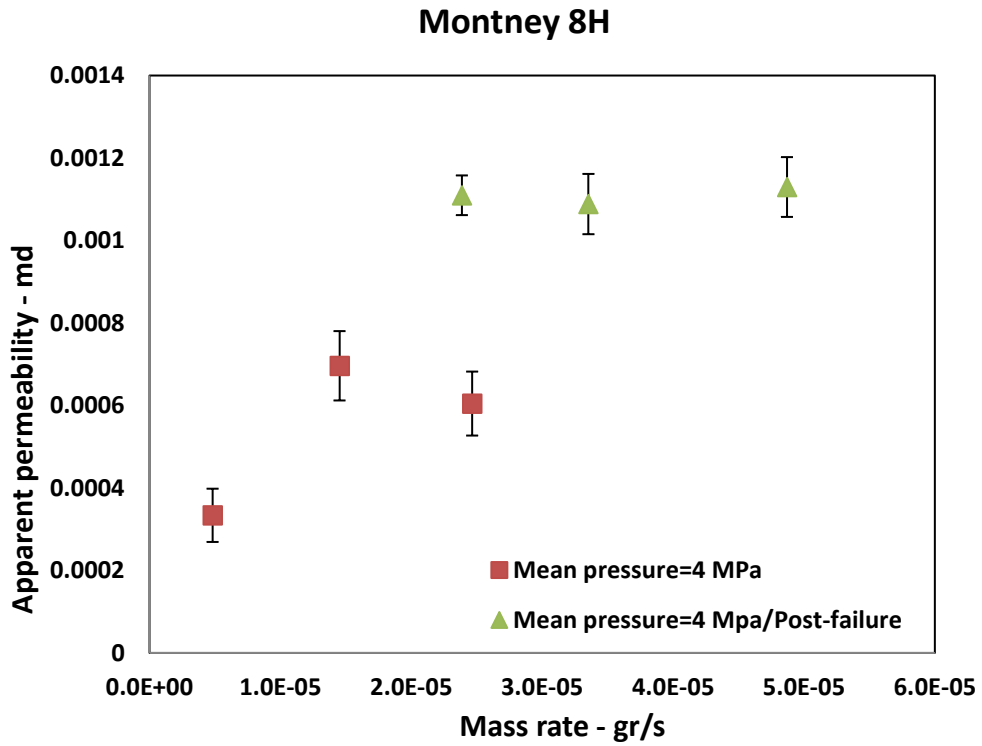


Fig. 66: Measured apparent permeability versus mass rate, before and after failure for the Montney 8H sample. Gas permeability after failure is higher than the intact condition. However, rate dependency of permeability is still observed.

Creep

Creep, or time dependant deformation, has gained attention in shales. The deformations are typically measured with time under a constant deviatoric stress. Creep is considered to be a potential mechanism responsible for loss of conductivity in fractures, and proppant embedment (Morales, 2011; Alramahi and Sundberg, 2012). Sone and Zoback (2014) conducted laboratory tests to measure the magnitude of creep on shale samples from Barnett, Haynesville, Eagle Ford, and Fort St. John. They observed significant creep, up to 30% of the instantaneous deformations, for the Haynesville and Eagle Ford samples. Much less creep was observed for other samples. Overall, the samples with higher clay and organic content, show larger time dependent deformations (Sone and Zoback, 2014).

In order to investigate the influence of creep on permeability, an axial stress of 12 MPa, equal to 1.5 times confining stress (8 MPa) is exerted on the Clearwater sample. The permeability of the sample is then immediately measured at several rates and mean pore pressure of 5 MPa. The sample is held under a constant deviatoric stress for one week. Permeability measurements are then conducted at the same pore pressure and rate conditions after the one week period. Fig. 67 shows the results of the permeability tests immediately after applying the load and after one week. The deformations were not measured during the test. The results do not indicate a change in permeability with time, within the range of experimental error. The Clearwater shale has the highest clay content among our samples. Since the change in permeability with time is insignificant for the Clearwater sample (Fig. 67), this test was not repeated on the Montney samples.

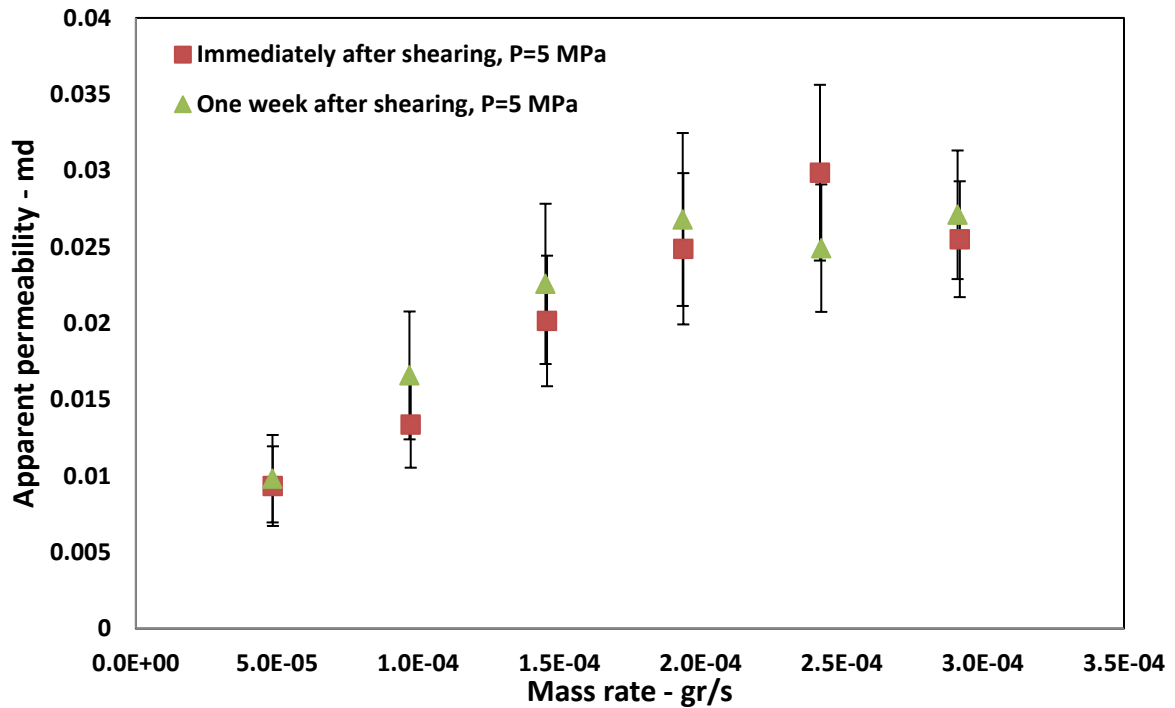


Fig. 67: Permeability results versus rate considering the influence of creep. Apparent permeability for the Clearwater sample is measured once immediately after applying the deviatoric stress, and again after one week. No significant permeability change is observed, within the range of the experimental error.

Influence of Water Saturation

The in-situ permeability of the tight rocks is also influenced by the degree of water saturation. Water saturation in a water-wet pore creates a film on the walls of the pore, effectively reducing the pore radius open to gas flow. The water typically is immobile in this class of materials unless high water saturation is reached (Shaoul et al., 2011). Since water reduces the effective radius to gas flow it is essentially reducing the absolute permeability. There have been a few investigations on the influence of water saturation on gas slippage (Shi et al., 2014; Li and Horne, 2004; Ertekin et al., 1986; Rushing et al., 2003). The slip factors in the model proposed in this work (Eq. 33) or in Klinkenberg's equation (Eq. 7) are a strong function of permeability. As the permeability decreases, the slip factors increase (Fig. 26 and Fig. 27). This can be explained by the fact that Knudsen number increases as permeability decreases which enhances the slippage effect. Presence of water in the

pores reduces the area to flow for gas, reducing the absolute permeability at the same time increasing the slip factors. This behavior has been validated using the Klinkenberg's equation elsewhere (Li and Horne, 2004).

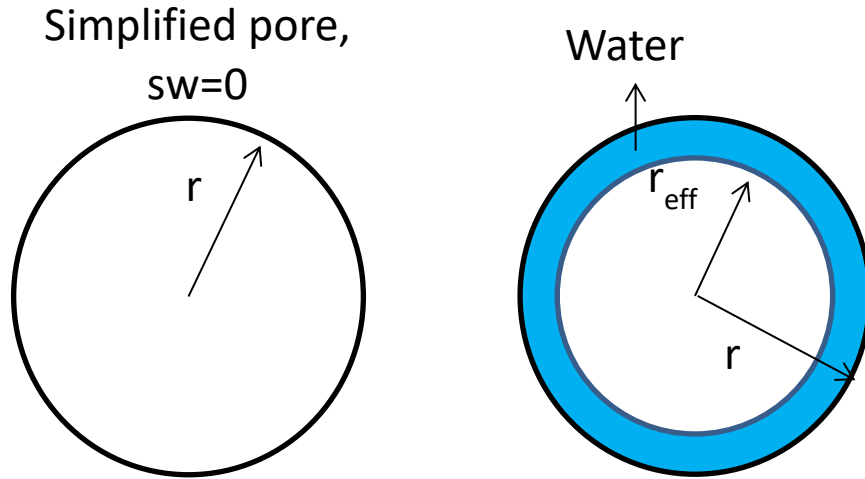


Fig. 68: An illustration of the ideal capillary tube with (on the right) and without (on the left) water saturation. The effective pore radius to flow is smaller in presence of water.

Fig. 68 illustrates an idealistic image of a capillary tube, with and without presence of water. The effective radius to flow is smaller at higher water saturation. The absolute permeability is directly related to effective pore radius. We can use the theoretical relationship proposed by Heid et al. (1950) to relate pore radius to permeability (Eq. 10). Writing Eq. 10 for the total pore radius in the case of zero water saturation and comparing that to the Eq. 10 written for the case of non-zero water saturation we obtain a relationship for the effective absolute permeability in presence of water. The derivation of this relationship (Eq. 52) is outlined in Appendix C.

$$k_{\text{eff}} = k_{\text{abs}}(1 - s_w)^2 \quad \text{Eq. 52}$$

In Eq. 52, k_{eff} is the effective absolute permeability open to gas flow. As k_{eff} is an absolute permeability it is not affected by slippage. k_{abs} in Eq. 52 is the absolute permeability of the media when no water is present. Therefore, the results of the

lab tests on dry samples leads to k_{abs} , in the laminar regime. s_w is the water saturation. Considering k_{eff} to be the effective absolute permeability to gas, the apparent permeability of gas becomes:

$$k_{app} = k_{abs}(1 - s_w)^2 \left(1 + \frac{b}{p} - \frac{a}{p^2} \right). \quad \text{Eq. 53}$$

Eq. 53 can be used to estimate the apparent permeability of gas in presence of water from the dry permeability results. “a” and “b” in Eq. 53 are calculated at the value of k_{eff} using Eq. 48 and Eq. 49.

Verification

In order to validate the proposed relationship in Eq. 53, experiments reported in the literature on preserved (wet) samples are used. Ghanizadeh et al. (2014) conducted lab experiments on Scandinavian Alum shale samples at various pore pressures. Sample Alum#2 in their work was first tested at the as-received condition. The moisture content of the sample was measured to be 1.1%. Subsequently, the sample was dried and gas permeability tests were repeated on the dry sample.

Table 12: Summary of the input parameters for the dried sample Alum#2 in Ghanizadeh et al. (2014) tests.

Pore Pressure	Apparent Permeability	Effective Stress	Moisture content	Porosity
MPa	nd	MPa	Wt%	-
0.7	84	11	1.1	0.089
1.2	68	11		
2.2	56	11		
3.2	45	11		

Table 12 summarizes the permeability results for the dried Alum#2 sample. Using the data in Table 12 as input we can estimate the apparent permeability of the sample under wet conditions. Initially, an estimate of k_{abs} of the dried sample is obtained using Eq. 33, Eq. 48, and Eq. 49. Eq. 53 can then be used to calculate the gas apparent permeability under the wet conditions, with “a” and “b” recalculated at the k_{eff} of the wet sample. The pulse-decay transient technique is used to measure the permeability values. Therefore, the influence of rate is not considered. We

assume that all the tests have been done at a similar rate and therefore, ignored the rate dependency of permeability on the results. The estimated k_{abs} value is at the effective stress of the experiments (11 MPa). In order to estimate apparent permeability at other effective stresses, the k_{abs} value should be converted to the new effective stress value using Eq. 45.

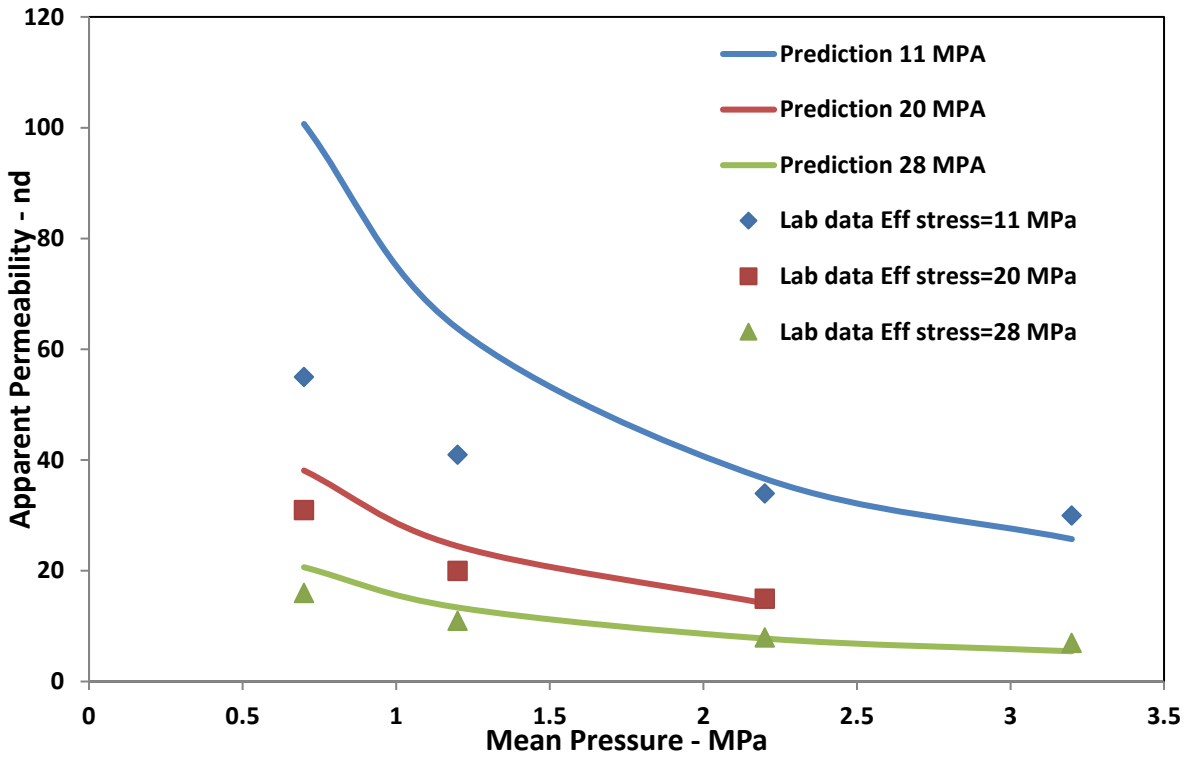


Fig. 69: Prediction of permeability under wet conditions from the dry values. The proposed method shows a good match with the experimental permeability results of the wet sample.

Fig. 69 shows the estimations of apparent permeability made using the proposed method in this work, using only the results of the experiments on the dry sample provided in Table 12. The results of the apparent permeability measurements on the wet sample are also provided in Fig. 69. A good agreement is observed between the predictions and the laboratory values in Fig. 69. Helium is used as the flowing gas in these tests. Based on the previous discussion on gas type, the flow regime of helium at low pressure is most likely diffusion based and difficult to model. Therefore, the match with the lab data at low pressure (1 MPa and lower) is less accurate.

Relative Permeability to Gas

In multiphase flow problems in porous media, each phase flows with a different effective permeability. The effective permeability of each phase depends on the saturation of the phase, the absolute permeability of the rock, and the wettability. The relative permeability of each phase is then defined as the ratio of the effective permeability of the phase and the absolute permeability of the medium. Typically, the relative permeability values for each phase ranges between zero and one. However, in the low permeability medium where slippage effect is dominant, gas permeability is significantly higher than the absolute permeability. The slippage effect still applies in presence of two phases as was demonstrated in the previous section in Eq. 53. Therefore, the gas relative permeability for tight material is most likely above one. We can define gas relative permeability as the ratio of the apparent permeability of gas to the absolute permeability of the medium in the laminar flow regime.

$$k_{rg} = (1 - s_w)^2 \left(1 + \frac{b}{p} - \frac{a}{p^2} \right). \quad \text{Eq. 54}$$

Eq. 54 shows the definition of gas relative permeability including the effect of slippage. Eq. 54 shows that gas relative permeability changes with pressure as well as saturation. This observation has also been made by Li and Horne (2004), Satik and Horne (1998), and Mahiya (1999). Based on the experimental results in this work, we can estimate the relative permeability to methane using Eq. 54. Fig. 70 shows the relative permeability curves at several pressures for the Montney 8H sample. The relative permeability values are greater than one due to the slippage effect but drop significantly as saturation increases. As pressure increases the slippage effect gets smaller and therefore the relative permeability curves are shifted lower.

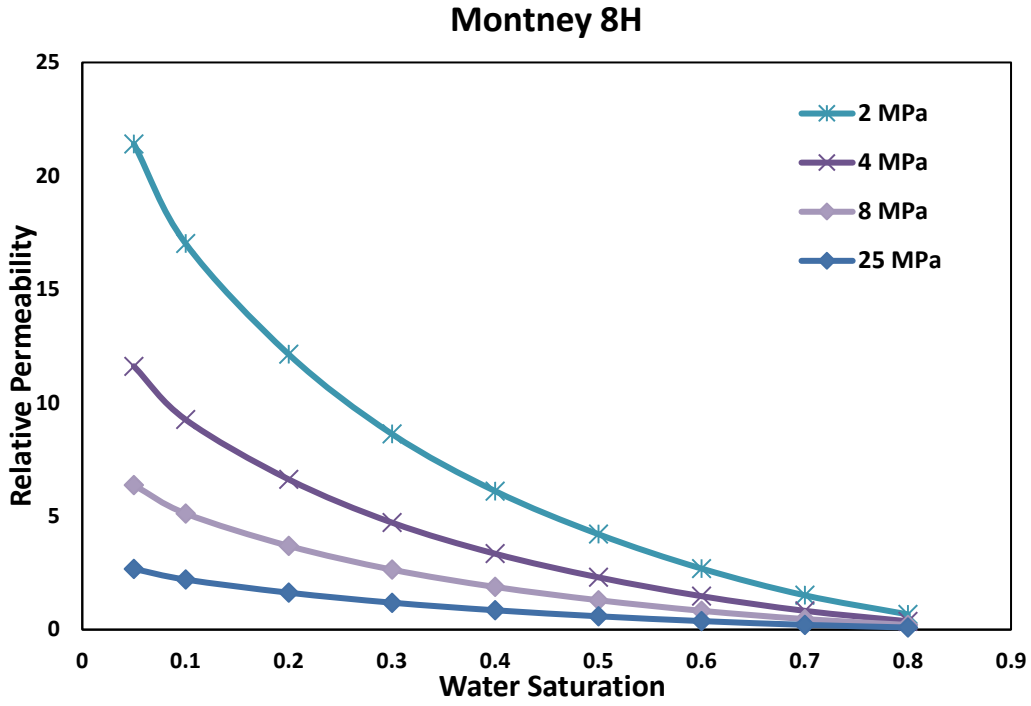


Fig. 70: Gas relative permeability curves for Montney 8H sample at different pressures. The curves are generated using Eq. 54.

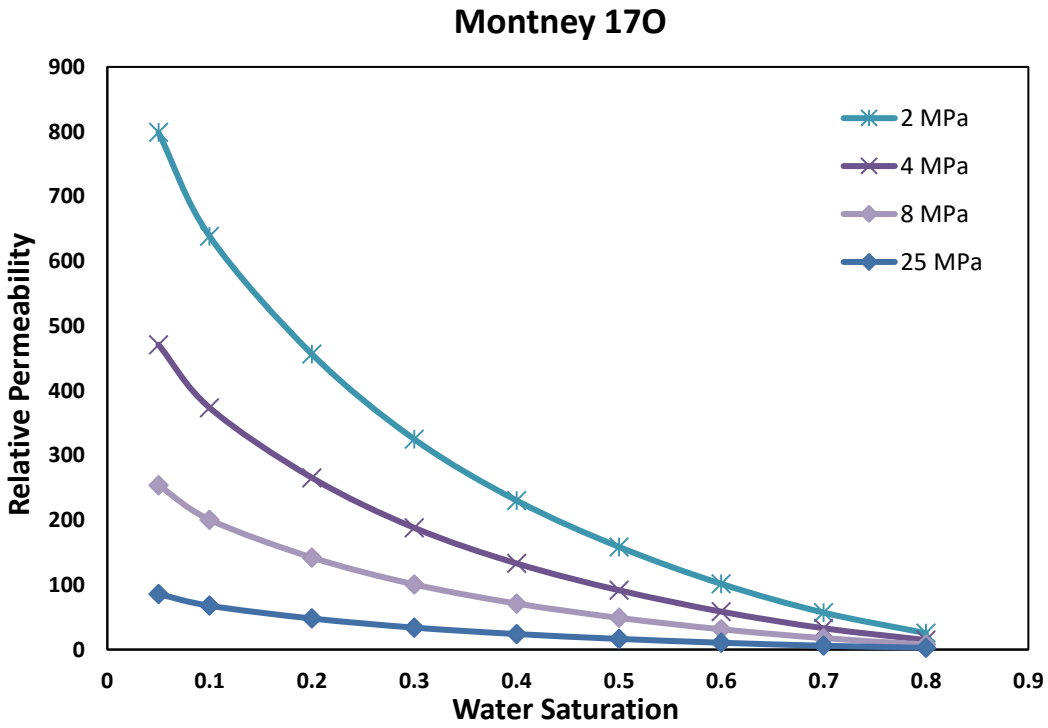


Fig. 71: Gas relative permeability curves for Montney 17O sample at different pressures. The curves are generated using Eq. 54.

Fig. 71 shows a similar plot of relative permeability curves for the Montney 17O sample. While the behavior of the relative permeability versus saturation and pressure remains the same, the relative permeability values are much higher for the Montney 17O sample. The absolute permeability of the Montney 17O sample is 1.5 nd, whereas the Montney 8H has a permeability of 87 nd. The smaller absolute permeability of the Montney 17O sample leads to higher values for the “a” and “b” slip parameters, and therefore significantly higher relative permeability.

The relative permeability in Eq. 54, depicted in Fig. 70 and Fig. 71, is calculated assuming a laminar flow regime. Therefore, the rate dependency of permeability is neglected. It is more likely for the ultra-low permeability rocks such as shales to be in the pre-laminar flow regime. In that case, relative permeability also changes with gas rate, along with pressure and saturation.

$$k_{rg} = (1 - \exp(-\delta\dot{m}))(1 - s_w)^2 \left(1 + \frac{b}{p} - \frac{a}{p^2}\right) \quad \text{Eq. 55}$$

Eq. 55 shows a more general relationship for the relative permeability including the effect of rate dependent permeability. As rate increases the gas relative permeability increases, until the laminar flow regime is reached.

Relative permeability for low permeability rocks is therefore a function of rate, pressure, saturation, and effective stress. Since the relationship is not as straightforward as a classic two phase flow problem, and relative permeability is not between zero and one, it is more useful to use the effective permeability concept rather than the relative permeability.

$$k_{eff} = k_0 \exp(-\alpha\sigma_{eff}) (1 - \exp(-\delta\dot{m}))(1 - s_w)^2 \left(1 + \frac{b}{p} - \frac{a}{p^2}\right) \quad \text{Eq. 56}$$

Eq. 56 shows the most comprehensive relationship to calculate the effective apparent gas permeability. The influence of flow regime, rate, pressure, effective stress and water saturation is included in Eq. 56.

Summary of the Analysis

Following the analysis in this chapter, we have developed and verified a model to capture the influence of slippage on apparent permeability. The rate dependency of permeability is analyzed and an equation is proposed to describe the behavior. The influence of gas type and temperature is discussed, and a methodology to capture the effect of failure and effective stress, is proposed. Finally, the influence of water saturation on gas apparent permeability is studied. Eq. 56 combines the effect of all the parameters on apparent permeability.

The results of the current study lead to calculating gas apparent permeability under in-situ condition, from the lab results. Laboratory gas permeability results are typically conducted on dry specimens. These tests are typically done at various pore pressures. Using Eq. 33, Eq. 48, and Eq. 49 we can estimate k_{abs} for the material at the tests' effective stress and temperature. Ideally, the tests should be repeated at a few rates to ensure the laminar flow regime is reached. Based on the experimental results in this work, at rates above 10^{-4} gr/s, laminar flow regime assumption should stand for most shale rocks. k_{abs} can then be converted to the in-situ effective stress (Eq. 45), water saturation (Eq. 54), and rate (Eq. 44). The updated k_{abs} can then be used along with updated “a” and “b” values (Eq. 48 and Eq. 49) to calculate the apparent permeability of gas at different pressures (Eq. 33). Fig. 72 presents a flow chart outlining the methodology to convert lab results on dry samples to gas permeability under in-situ conditions.

The influence of temperature was not fully characterized in this work. In the lab results, it was observed that temperature reduces the apparent permeability, however more tests and theoretical analysis is required to propose a temperature dependent model. Therefore, for the permeability tests to be a representative of the in-situ conditions, the tests should be done at the in-situ temperature.

The complicated behavior of gas permeability makes it difficult to report a single number as the permeability of a shale sample. New testing standards are required, for all the permeability measurements from different laboratories to be comparable. The most representative gas permeability values in the lab should be conducted at

conditions as close as possible to the in-situ. This is usually not possible in the laboratory environment. Any permeability measurement in the lab should accompany the exact conditions of the tests such as pressure, temperature, effective stress, rate, and the testing technique. Absolute permeability of the sample can be obtained either by directly measuring water permeability, or calculating it from gas permeability measurements. Reporting the absolute permeability values in the laminar flow regime, at a specified temperature and effective stress, can be a suitable measure of the permeability of the medium. A summary of the recommendations for conducting laboratory gas permeability measurements is provided in chapter 7.

Table 13 summarizes the parameters required to fully characterize gas permeability, based on findings of this work. Using these parameters, we can construct the pre-laminar/laminar portion of the permeability surface presented in Fig. 40. Gas permeability experiments in the lab should be designed to produce the parameters summarized in Table 13.

Table 13: Summary of the parameters that should be m required to fully characterize gas permeability.

Parameters	k_{abs}^5	a	b	α	δ	Effective Stress	Temp.	Range of Pressure	s_w	Fluid
Sample	nd	MPa ²	MPa	MPa ⁻¹	s/gr	MPa	°C	MPa		
Clearwater	1000	1.8	8.4	-	10000	20	25	1.5-5	0	Nitrogen
Montney 10D	5	954	10710	0.2	10000	20	25	2.0-6.0	0	Methane
Montney 17O	1.5	1308	3713	0.1	50000	20	25	2.0-8.0	0	Methane
Montney 8H	87	3.5	26.6	0.06	50000	20	25	2.0-8.0	0	Methane

⁵ Absolute permeability reported should be in the laminar flow regime.

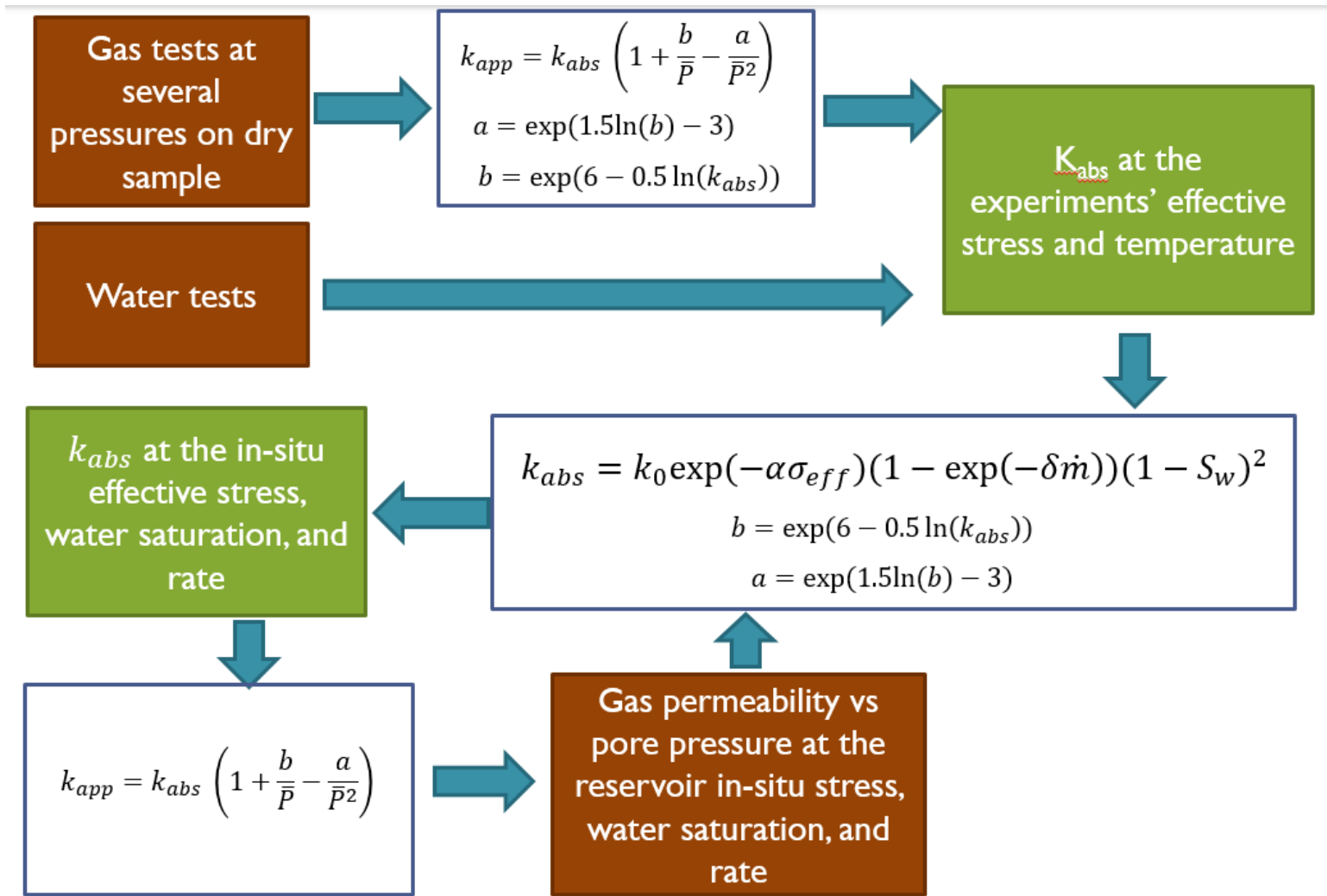


Fig. 72: A flow chart summarizing the method proposed in this work to convert gas permeability measurements in the lab on dry samples, to gas permeability under in-situ conditions.

Potential Sources of Error

This section provides a discussion on various sources of error in the present laboratory experiments and analysis.

Experimental Error

The experimental error introduced by each parameter in Eq. 42 and Eq. 43 are combined to calculate the error in apparent permeability values. This is presented as error bars in the appropriate figures, where it does not affect the clarity. The most significant source of error in the measurements comes from the pressure transducers. Though the transducers are accurate to $\pm 0.1\%$, this can still be significant at high pressures. Other, less significant sources of error stem from the calculation of viscosity and compressibility factor. The experimental errors amount to 5%-30% of the calculated the apparent permeability, depending largely on the testing pressure and rate.

Samples

The samples used in this study are from a non-preserved core. As the rock is cored in a well and transported to the surface, a large release of confining stress occurs. This stress relief typically results in micro-fractures. The Montney samples used in this work are from a depth of 2100-2600 meters. Additionally, as the samples dry over time, the permeability and pore structure could change (Ewy, 2015). Therefore, the magnitude of the permeability values measured on the damaged samples could be a misrepresentation of the reservoir rock's permeability. In this work, the focus is not on the magnitude of permeability for the formations under study, but rather the fundamental physics governing gas flow and how permeability changes under various flow conditions. The tests are conducted at relatively high effective stress (20 MPa). It is assumed that the micro-fractures due to stress relief are mostly closed at the effective stress of the lab tests.

Adsorption

The influence of adsorption and swelling on apparent permeability is ignored in our analysis. Adsorption is a storage mechanism for gas in shale pores similar to coals. The adsorptive capacity of shales however, is much smaller than coals (Gasparik et al., 2015). Shale gas wells are operated at a higher pressure compared to coalbed methane. Therefore, the contribution of adsorbed gas to total production is small in shale reservoirs (Heller and Zoback, 2014). It is postulated that the adsorption layer in shales influences the permeability. Presence of an adsorption layer in the pores could potentially reduce the effective pore radius, impede the flow of gas (Sakhaee-Pour and Bryant, 2012), and possibly change slip flow parameters. Presently, it is a difficult task to differentiate between the influence of slippage and adsorption on apparent permeability. As pressure increases, apparent permeability decreases mainly due to slippage (at a constant mean effective stress). However, part of this reduction could be as a result of an adsorption layer being formed. There are several publications that discuss this phenomenon. These publications generally compare the permeability values of different gases and helium without considering the slippage (Jin et al., 2015). Since helium is a non-adsorptive gas, the difference between helium permeability and other gases is attributed to the effect of adsorption. However, slippage has been observed to enhance permeability to different gases to various degrees in porous rocks (Klinkenberg, 1941). Therefore, the observed difference in permeability could be a result of slippage. Al Ismail et al. (2014) similarly compare permeability values with CO₂ and helium as flowing fluids. The tests are conducted at comparable pore pressures considering the influence of slippage, however the helium molecule is small and it could potentially have access to smaller pores compared to CO₂. This could also enhance the apparent permeability to helium compared to that of CO₂. Additionally, the adsorptive tendency of CO₂ is at least 5 times greater than that of methane (Kang, et al., 2011; Nuttal et al., 2005), therefore the potential influence of adsorption layer on methane permeability will be smaller. Letham (2011) compares the methane permeability to methane permeability with influence of adsorption and finds the error introduced by neglecting adsorption to be small.

Although adsorption has been observed in both clay minerals and organic content (Schettler et al., 1991), majority of the gas adsorbed in shales is in the organic content (Lu et al., 1995). The TOC of the shale samples in this study is below 2%. In this work, it is assumed that the influence of adsorption on permeability is negligible. Further studies are needed to explore the possibility of the influence of adsorption layer on permeability. The experiments should ideally compare argon and methane permeability. Argon has a low adsorptive tendency however, unlike helium, argon's molecular size is still comparable to that of methane. These properties make it suitable to investigate the possibility of permeability change with adsorption. In our results, even if permeability is affected by adsorption it is automatically captured in the values of "a" and "b" slip parameters.

Pore Plugging by Residual Water or Gas

Water permeability is measured on all the samples following the gas tests. Care was taken to ensure all the lines were saturated with water prior to the test and the remaining gas in the sample is assumed to dissolve in water at 5 MPa after 72 hours. However, if free gas still remains in the sample it could potentially reduce water permeability. Additionally, after shearing the sample water permeability is measured. Afterwards, the samples are saturated with gas again. During the saturation process, gas flows through the cores to displace water in the cracks. Any remaining water in the samples could lead to errors in gas permeability tests after shearing.

Effective Stress Coefficient for Permeability

Eq. 9 is used in this study to calculate mean effective stress. Biot's coefficient is introduced instead of χ in Eq. 9 to calculate effective stress in poroelasticity. Biot's coefficient is defined according to the volumetric behavior of the rock. Using Biot's coefficient in Eq. 9, means the effective stress becomes a value at which the rock will have the same bulk volume regardless of the pore pressure and total confining stress. For the case of permeability, effective stress should be a value at which the

permeability of the rock is constant regardless of the pore pressure and total confining stress. Hence, χ in Eq. 9, defined as effective stress coefficient for permeability, is introduced in place of Biot's coefficient. Whether χ is the same value as the Biot's coefficient, is unclear. The value of χ is generally less than or equal to unity for conventional reservoir rocks such as sandstones and carbonates. Kwon et al., (2001) measured the χ values for Wilcox shale and observed that χ is approximately equal to one. Heller et al. (2014) investigated the magnitude of χ on shale samples from Barnett, Eagle Ford, Marcellus, and Montney. They obtained values for χ in the range of 0.15 to 0.85. The measurements by Heller et al. (2014) were made using helium as the flowing fluid. Permeability was measured at high pressures and slip flow effects were neglected in calculating χ . Kwon et al. (2001), on the other hand, used water to measure χ values. The results of the flow regime analysis in chapter 3 (Moghadam and Chalaturnyk, 2016) show that slip flow is dominant in shales even at high pore pressures (Fig. 6). Based on this conclusion, neglecting the slippage effect in analyzing permeability data by Heller et al., (2014) could lead to errors in calculating χ . In chapter 4 a new equation (Eq. 33) is proposed to relate the apparent permeability of gas to the absolute (liquid) permeability (Moghadam and Chalaturnyk, 2014). In Eq. 33, "a" and "b" are slip flow parameters that are a function of permeability. Using the experimental results from this work and the literature, the new model is verified in this chapter and correlations are developed to find "a" and "b". Eq. 48 and Eq. 49 show the correlations used to calculate "a" and "b" values. k_w in Eq. 48 is the absolute permeability in nano darcy. "a" and "b" in Eq. 48 and Eq. 49 are in MPa² and MPa, respectively. The absolute and liquid permeability are assumed to be identical. The permeability measurements by Heller et al., (2014) can be converted to equivalent liquid permeability (k_w) using Eq. 33, Eq. 48, and Eq. 49. The k_w results are then adopted to calculate χ , using Eq. 57.

$$\chi = -\frac{\left(\frac{\partial \ln(k_w)}{\partial P}\right)_\sigma}{\left(\frac{\partial \ln(k_w)}{\partial \sigma}\right)_P} \quad \text{Eq. 57}$$

Fig. 73 shows the slope of logarithm of permeability versus pressure at a constant confining stress (the nominator in Eq. 57) and the slope of logarithm of permeability versus stress at a constant pore pressure (the denominator in Eq. 57) For Marcellus and Montney samples. According to Fig. 73, the two slopes are equal for both samples which leads to a value of one for χ from Eq. 57. Therefore, for the purpose of calculating mean effective stress in this work, the present study takes χ to be equal to unity, relying on the findings by Kwon et al. (2001) and the re-analyzed results of Heller et al., (2014). If the real value of χ differs from unity, it will introduce an error in the analysis of the lab results in the present work.

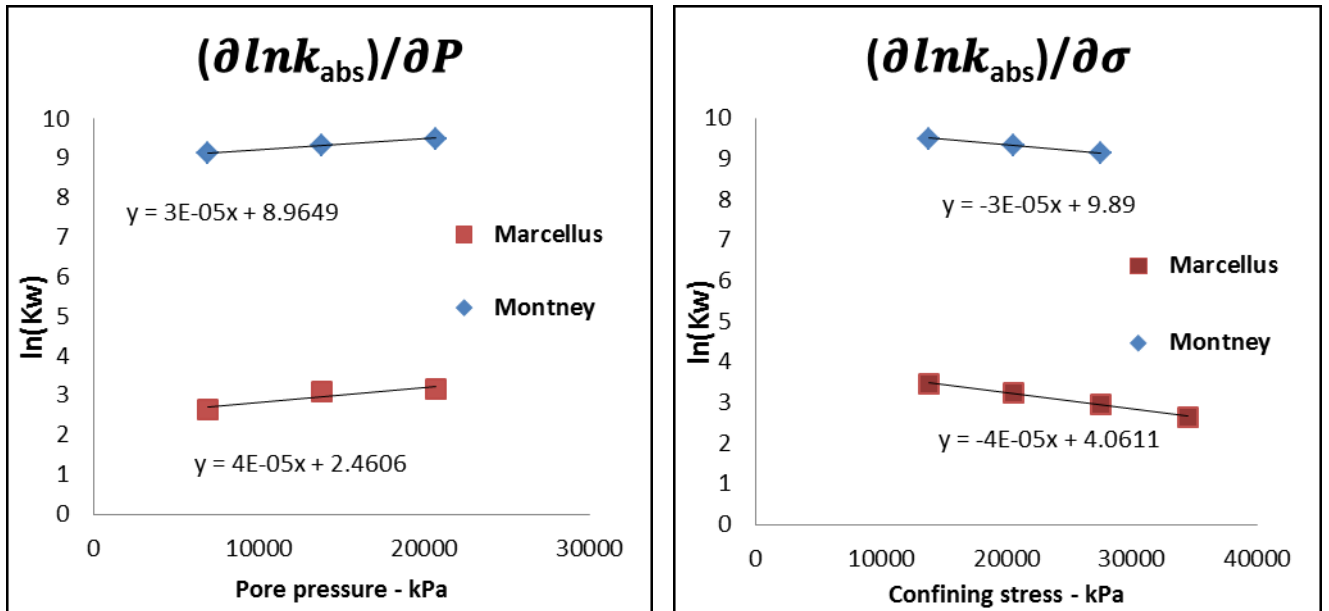


Fig. 73: On the left, the variation of absolute permeability with pore pressure at a constant confining stress is presented. On the right, the variation of absolute permeability with stress at a constant pore pressure is shown. The data presented is for Montney and Marcellus shale samples by Heller et al., (2014), corrected for slippage. The two slopes on the left and right, for Montney and Marcellus shale is equal which leads to $\chi=1$.

Conclusions

Extensive steady-state gas and water permeability tests have been conducted on four shale/siltstone samples. The influence of flow rate, pore pressure, mean effective stress, water saturation, and temperature on apparent permeability of gas is investigated.

The flow model proposed in chapter 4 is verified to predict the apparent permeability of low-permeability porous media. The model parameters are obtained from data in literature, and from the present lab experiments. The model explains the order of magnitude difference between liquid permeability and Klinkenberg-corrected permeability, and matches the lab results with great accuracy. According to the lab results, the model is capable of predicting the apparent permeability within the entire slip flow range and early transition flow regime.

Gas permeability is measured at several rates to study the significance of rate dependent permeability. The results show, while the slippage effect is observed at different mean pore pressures, permeability is also a strong function of gas rate. Permeability is observed to increase with rate until it reaches a plateau at higher rates. This indicates the dominance of pre-laminar flow regime for shales under low velocity flow which is typical of these rocks. A complete picture of permeability and gas flow regimes is developed in this chapter. Based on the experimental results, a discussion is provided on the possible criteria for pre-laminar to laminar flow regime transition. A rate dependent permeability model is then proposed that matches the results with reasonable accuracy.

Water permeability of the samples is also measured before and after failure. The influence of temperature is investigated with a limited number of tests. The results indicate that temperature reduces the apparent permeability. There is no model available at this point that could capture and explain the effect of temperature on the permeability of this class of material. A more comprehensive investigation is required to understand the influence of temperature. A brief discussion on the effect of gas type on the permeability results is provided. Nitrogen and methane show comparable permeability results in our experiments. Helium permeability

measurements are believed to significantly overestimate the permeability of the rock. Helium's small molecular size makes the permeability measurement analysis difficult, due to very high Knudsen numbers.

Further experiments were conducted to study the influence of mean effective stress on the apparent permeability and flow regime. Apparent permeability was observed to be a function of slip flow and mean effective stress. The results show that the interplay between effective stress and flow regime is the deciding factor for apparent permeability. Preliminary results show that slip flow permeability enhancement could be cancelled out by the increase in mean effective stress over the course of production from the reservoir. Ignoring either flow regime or geomechanical effects leads to significant overestimation or underestimation of permeability of up to a few orders of magnitude which will result in considerable errors in long term production forecasts of Shale gas reservoirs. Mean effective stress changes over a long period of time after the start of production and assessing its effect on apparent permeability is paramount in estimating the long term production potential of a given reservoir. This long term behavior was investigated by conducting depletion tests. In addition to the mean effective stress, failure of rock can enhance the absolute permeability, at the same time reducing the slip parameters. The post-failure test results illustrate the relationship between absolute permeability and slippage. The influence of creep was investigated through one test on the Clearwater sample. No meaningful change in permeability was observed, induced by creep.

Based on the findings from the lab tests and the new model, a methodology is proposed to take the effect of water saturation on apparent permeability into account. The new approach is simple, yet reproduces the lab results from the literature with good accuracy. Using the new methodology, gas permeability results on dry samples can be converted to apparent permeability of the wet samples.

Several sources of error in the present experiments have been thoroughly discussed, in this chapter. All the findings in this chapter can be combined, to be able to estimate the in-situ permeability of the tight rocks, from laboratory experiments.

Based on the results presented, new standards and recommendations can be developed in order to produce more accurate and comparable permeability measurements.

Nomenclature

a	=	Secondary slip factor ($M^2L^{-2}T^{-4}$), MPa ²
b	=	Slip factor ($ML^{-1}T^{-2}$), MPa
k_0	=	Permeability to water at zero mean effective stress (L^2), md
k_{abs}	=	Absolute (liquid) permeability (L^2), md
k_{app}	=	Apparent permeability (L^2), md
k_{eff}	=	Effective permeability to gas (L^2), md
$k_{laminar}$	=	Absoluter permeability in the laminar flow regime (L^2), md
k_{rg}	=	Relative permeability to gas, dimensionless
k_w	=	Permeability to water (L^2), md
k_{wi}	=	Permeability to water at initial reservoir mean effective stress (L^2), md
kn	=	Knudsen number, Dimensionless
\dot{m}	=	Mass rate (MT^{-1}), gr/s
P	=	Pressure ($ML^{-1}T^{-2}$), Pa
P_i	=	Initial pressure ($ML^{-1}T^{-2}$), Pa
r_{pores}	=	Radius of pores (L), m
S_w	=	Water saturation, fraction
α	=	Coefficient indicating the sensitivity of permeability to mean effective stress ($ML^{-1}T^{-2}$)-1, Pa-1

- δ = Coefficient indicating the transition between pre-laminar and laminar flow regime ($M^{-1}T$), s/gr
- σ = Total stress ($ML^{-1}T^{-2}$), Pa
- σ_{eff} = Mean effective stress ($ML^{-1}T^{-2}$), Pa
- χ = Effective stress coefficient, Dimensionless

References

- Al Ismail, M.I., Hol, S., Reece, J.S., and Zoback, M., 2014. The effect of CO₂ adsorption on permeability anisotropy in the Eagle Ford shale. Paper URTEC 1921520 presented at the Unconventional Resources Technology Conference, Denver, Colorado, USA, 25-27 August.
- Aramahi B, Sundberg MI. Proppant embedment and conductivity of hydraulic fractures in shales. ARMA Paper 2012-291.
- Barree, R.D., Conway, M.W., 2004. Beyond Beta Factors: A Complete Model for Darcy, Forchheimer, and Trans-Forchheimer Flow in Porous Media. Paper SPE 89325 presented at the SPE Annual Technical Conference and Exhibition, Houston, 26-29 September.
- Basak, P., 1977. Non-darcy flow and its implications to seepage problems. Journal of the Irrigation & Drainage Division 103(4), 459-473.
- Brown, E.T., 1981. Rock Characterization, Testing and Monitoring, ISRM suggested methods. Pergamon Press, Oxford.
- Comiti, J., Sabiri, N.E., Montillet, A., 2000. Experimental characterization of flow regimes in various porous media — III: limit of Darcy's or creeping flow regime

for Newtonian and purely viscous non-Newtonian fluids. *Chemical Engineering Science* 55(15), 3057-3061.

Davies, J.P., and Davies, D.K., 2001. Stress-Dependent Permeability: Characterization and Modelling. *SPE Journal* 6 (2), 224-235.

Dong, M., Li, Z., Li, S., Yao, J., 2012. Permeabilities of Tight Reservoir Cores Determined for Gaseous and Liquid CO₂ and C₂H₆ Using Minimum Backpressure Method. *Journal of natural Gas Science and Engineering* 5, 1-5.

Dou, H., Ma, S., Zou, C., and Yao, S., 2014. Threshold pressure gradient of fluid flow through multi-porous media in low and extra-low permeability reservoirs. *Science China: Earth Sciences* 57(11), 2808-2818.

Ertekin, T., King, G.A., & Schwerer, F.C., 1986. Dynamic Gas Slippage: A Unique Dual-Mechanism Approach to the Flow of Gas in Tight Formations. *SPE Formation Evaluation* 1(01), 43-52.

Ewy, R.T., 2015. Shale/claystone response to air and liquid exposure, and implications for handling, sampling and testing. *International Journal of Rock Mechanics and Mining Sciences* 80, 388-401.

Firouzi, M., Alnoaimi, K., Kovscek, A., Wilcox, J. 2014. Klinkenberg Effect on Predicting and Measuring Helium Permeability in Gas Shales. *International J. of Coal Geology* 123: 62-68. <http://dx.doi.org/10.1016/j.coal.2013.09.006>.

Gasparik, M., Gensterblum, Y., Ghanizadeh, A., Weniger, P., and Krooss, B.M., 2015. High-Pressure/High-Temperature Methane-Sorption Measurements on Carbonaceous Shales by the Manometric Method: Experimental and Data-Evaluation Considerations for Improved Accuracy. *SPE Journal*, preprint, May 2015.

Gavin, L., 2004. Pre-Darcy Flow: A Missing Piece of the Improved Oil Recovery Puzzle? Paper SPE 89433 presented at 2004 SPE/DOE Symposium on Improved Oil Recovery, Tulsa, Oklahoma, 17-21 April.

Ghabezloo, S., Sulem, J., Guedon, S., Martineau, F., 2009. Effective Stress Law for the Permeability of a Limestone. *International Journal of Rock Mechanics and Mining Sciences* 46 (2), 297-306.

Ghanizadeh, A., Gasparik, M., Amann-Hildenbrand, A., Gensterblum, Y., Krooss, B.M., 2014. Experimental study of fluid transport processes in the matrix system of the European organic-rich shales: I. Scandinavian Alum Shale. *Marine and Petroleum Geology* 51, 79-99.

Heid, J.G., McMahon, J.J., Nielsen, R.F., Yuster, S.T., 1950. Study of the Permeability of Rocks to Homogenous Fluids. *API Drilling & Production Practice*, New York 230–246.

Heller, R., and Zoback, M., 2014. Adsorption of methane and carbon dioxide on gas shale and pure mineral samples. *Journal of Unconventional Oil and Gas Resources* 8, 14-24.

Heller, R., Vermynen, J., Zoback, M., 2014. Experimental Investigation of Matrix Permeability of Gas Shales. *AAPG Bulletin* 98 (5), 975-995.

Huang, H., Ayoub, J. A., 2008. Applicability of the Forchheimer Equation for Non-Darcy Flow in Porous Media. *SPE Journal* 13(01), 112-122.

Jackson, R., and Lau, J.S.O., 1990. The effect of specimen size on the mechanical properties of Lac du Bonnet grey granite. *Proceedings of the 1st International Workshop on Scale Effects in Rock Masses*, Leon, Norway. Edited by da Cunha A.P.

Jin, G., Perez, H.G., Agrawal, G., et al., 2015. The impact of gas adsorption and composition on unconventional shale permeability measurement. Paper SPE 172744-MS presented at the SPE Middle East Oil & Gas Show and Conference, Manama, Bahrain, 8-11 March.

Kang, S. M., Fathi, E., Ambrose, R. J., Akkutlu, I. Y., Sigal, R. F., 2011. Carbon Dioxide Storage Capacity of Organic-Rich Shales. *SPE Journal* 16(04), 842-855.

Klinkenberg, L.J 1941. The permeability of porous media to liquids and gases. *API Drilling and Production Practice*, 200-213.

Kutilek, M., 1972. Non-darcian flow of water in soils – laminar region: A review. *Developments in Soil Science* 2, 327-340.

Kwon, O., Kronenberg, A.K., Gangi, A.F., 2001. Permeability of Wilcox Shale and its Effective Pressure Law. *Journal of Geophysical Research* 106 (B9), 19339-19353.

Letham, E.A., 2011. Matrix permeability measurements of gas shales: gas slippage and adsorption as sources of systematic error. BSc (Honours) thesis, University of British Columbia, Vancouver, British Columbia (March 2011).

Li, K., & Horne, R.N., 2004. Experimental Study of Gas Slippage in Two-Phase Flow. *SPE Reservoir Evaluation & Engineering* 7(06), 409-415.

Li, S., Dong, M., Li, Z., 2009. Measurement and Revised Interpretation of Gas Flow Behaviour in Tight Reservoir Cores. *Journal of Petroleum Science and Engineering* 65, 81-88.

Lu, X.C., Li, F.C., and Watson, A.T., 1995. Adsorption measurements in Devonian shales. *Fuel* 74 (4), 599–603.

Macini, P., Mesini, E., Viola, R., 2011. Laboratory measurements of non-Darcy flow coefficients in natural and artificial unconsolidated porous media. *Journal of Petroleum Science and Engineering* 77 (3-4), 365-374.

Martin, C.D., Chandler, N.A., 1994. The Progressive Fracture of Lac du Bonnet Granite. *International Journal of Rock Mechanics and Mining Sciences & Geomechanics Abstracts* 31 (6), 643-659.

Meyer, R., and Krause, F.F., 1998. Experimental evidence for permeability minima at low-velocity gas flow through naturally formed porous media. *Journal of Porous Media* 1(1), 93-106.

- Miller, R.J., and Low, P.F., 1963. Threshold gradient for water flow in clay systems. *Soil Science Society of America Proceedings* 27(6), 605-609.
- Moghadam, A.A., Chalaturnyk, R., 2014. Expansion of the Klinkenberg's slippage equation to low permeability porous media. *International Journal of Coal Geology* 123, 2-9.
- Moghadam, A.A., Chalaturnyk, R., 2015. Laboratory Investigation of Shale Permeability. Paper SPE 175919 presented at the the SPE/CSUR Unconventional Resources Conference held in Calgary, Alberta, Canada, 20–22 October 2015.
- Moghadam, A. A. and Chalaturnyk, R. 2016. Analytical and Experimental Investigations of Gas-Flow Regimes in Shales Considering the Influence of Mean Effective Stress. *SPE Journal* 21(02), 557-572. <http://dx.doi.org/10.2118/178429-PA>.
- Morales RH, Suarez-Rivera R, Edelman E. Experimental evaluation of hydraulic fracture impairment in shale reservoirs. ARMA Paper 2011-380.
- Nicksiar, M., Martin, C.D., 2014. Factors Affecting Crack Initiation in Low Porosity Crystalline Rocks. *Rock Mechanics and Rock Engineering* 47, 1165-1181.
- Nuttall, B.C., Eble, C.F., Drahovzal, J.A., Bustin, R.M., 2005. Analysis of Devonian black shales in Kentucky for potential carbon dioxide sequestration and enhanced natural gas production. Report Kentucky Geological Survey/University of Kentucky (DE-FC26- 2NT41442).
- Sakhaee-Pour, A., Bryant, S., 2012. Gas Permeability of Shale. *SPE Reservoir Evaluation & Engineering* 15(04) 401-409.
- Schettler, P.D., and Parmely, C.R., 1991. Contributions to Total Storage Capacity in Devonian Shales. Paper SPE 23422 presented at 1991 SPE Eastern Regional Meeting, Lexington, Kentucky, 22-25 October.

- Seguin, D., Montillet, A., and Comiti, J., 1998a. Experimental characterisation of flow regimes in various porous media—I: limit of laminar flow regime. *Chemical Engineering Science* 53(21), 3751-3761.
- Seguin, D., Montillet, A., Comiti, J., and Huet, F., 1998b. Experimental characterisation of flow regimes in various porous media—II: Transition to turbulent regime. *Chemical Engineering Science* 53(22), 3897-3909.
- Sinha, S., Braun, E. M., Determan, M. D., Passey, Q. R., Leonardi, S. A., Boros, J. A., ... Kudva, R. A., 2013. Steady-State Permeability Measurements on Intact Shale Samples at Reservoir Conditions - Effect of Stress, Temperature, Pressure, and Type of Gas. Paper SPE 164263 presented at the SPE Middle East Oil and Gas Show and Conference, 10-13 March, Manama, Bahrain.
- Sone, H., and Zoback, M. D., 2014. Time-dependent deformation of shale gas reservoir rocks and its long-term effect on the in-situ state of stress. *International Journal of Rock Mechanics and Mining Science*, 69, 120-132.
- Swartzendruber, D., 1962. Non-darcy flow behavior in liquid-saturated porous media. *Journal of Geophysical Research* 67(13), 5205-5213.
- Tanikawa W., Shimamoto, T., 2009. Comparison of Klinkenberg-Corrected Gas Permeability and Water Permeability in Sedimentary Rocks. *International journal of Rock Mechanics & Mining Sciences* 46, 229-238.
- Venkataraman, P., and Rao, P.R.M., 1998. Darcian, transitional, and turbulent flow through porous media. *Journal of Hydraulic Engineering* 124, 840-846.
- Von Engelhardt, W., and Tunn, W.L.M., 1954. The flow of fluids through sandstones. *Heidelberger Beitrage zur Mineralogie und Petrographie* 2, 12-25.
- Wu, Y.S., Pruess, K., Persoff, P., 1998. Gas flow in porous media with Klinkenberg effects. *Transport in Porous Media* 32, 117–137.

Amann-Hildenbrand, A., Ghanizadeh, A., Krooss, B.M., 2012. Transport Properties of Unconventional Gas Systems. *Marine and Petroleum Geology* 31, 90-99.

Bird, R. B., Stewart, W. E., Lightfoot, E. N., 1960. *Transport Phenomena*. John Wiley and Sons, Inc.

Bustin, A.M.M., Bustin, R.M., Cui, X., 2008. Importance of Fabric on the Production of Gas Shales. Paper SPE 114167 presented at the 2008 SPE Unconventional Reservoirs Conference, Keystone, Colorado, USA, 10-12 February.

Bustin, A.M.M., Bustin, R.M., 2012. Importance of Rock Properties on the Producibility of Gas Shales. *International Journal of Coal Geology*, 103, 132-147.

Darabi, H., Ettehad, A., Javadpour, F., Sepehrnoori, K., 2012. Gas Flow in Ultra-Tight Shale Strata. *Journal of Fluid Mechanics* 710, 641-658.

Dong, M., Li, Z., Li, S., Yao, J., 2012. Permeabilities of Tight Reservoir Cores Determined for Gaseous and Liquid CO₂ and C₂H₆ Using Minimum Backpressure Method. *Journal of natural Gas Science and Engineering* 5, 1-5.

Fathi, E., Tinni, A., Akkutlu, Y., 2012. Correction to Klinkenberg Slip Theory for Gas Flow in Nano-capillaries. *International Journal of Coal geology* 103, 51-59.

Heid, J.G., McMahon, J.J., Nielsen, R.F., Yuster, S.T., 1950. Study of the Permeability of Rocks to Homogenous Fluids. *API Drilling & Production Practice*, New York 230–246.

Jones, F.O., Owens, W.W., 1980. A Laboratory Study of Low Permeability Gas Sands. *Journal of Petroleum Technology* 32, 1631-1640.

Kalantari-Dahaghi, A., Mohaghegh, S.D., 2011. Numerical Simulations and Multiple Realizations for Sensitivity Study of Shale Gas Reservoir. Paper SPE 141058 presented at the 2011 SPE Productions and Operations Symposium, Oklahoma City, Oklahoma, USA, 27-29 March.

Klinkenberg, L.J 1941. The permeability of porous media to liquids and gases. API Drilling and Production Practice, 200-213.

Kundt, A., Warburg, E., 1875. Poggendorfs Ann. Physik 155, 337 and 525.

Li, S., Dong, M., Li, Z., 2009. Measurement and Revised Interpretation of Gas Flow Behaviour in Tight Reservoir Cores. Journal of Petroleum Science and Engineering 65, 81-88.

Loeb, L.B. 1934. The Kinetic Theory of Gases. Second edition, McGraw-Hill Co., Inc.

Mahiya, G.F., 1999. Experimental Measurement of Steam-Water Relative Permeability. MSc Thesis, Stanford University, Stanford, California.

Muskat, M. 1982. The Flow of Homogeneous Fluids through Porous Media. International Human Resources Development Corporation, Boston.

Noman, R. and Kalam, M.Z. 1990. Transition from Laminar to Non-Darcy Flow of Gases in Porous Media. In Advances in Core Evaluation: Accuracy and Precision in Reserves Estimation. edited by P.F. Worthington, 447-482.

Ross, D.J.K., Bustin, R.M., 2008. Characterizing the Shale Gas Resource Potential of Devonian-Mississippian Strata in the Western Canada Sedimentary Basin: Application of an integrated Formation Evaluation. The American Association of Petroleum Geologists Bulletin 92 (No. 1), 87-125.

Rushing, J.A, Newsham, K.E., Lasswell, P.M., Cox, J.C. and Blasingame, T.A. 2004. Klinkenberg-Corrected Permeability Measurements in Tight Gas Sands: Steady-State Versus Unsteady-State Techniques. Paper SPE 89867 presented at the 2004 SPE Annual Technical Conference and Exhibition, Houston, Texas, 26-29 September.

Rushing, J.A., Newsham, K.E., & Van Fraassen, K.C., 2003. Measurement of the Two-Phase Gas Slippage Phenomenon and Its Effect on Gas Relative Permeability

in Tight Gas Sands. Paper SPE 84297 presented at the SPE Annual Technical Conference and Exhibition, 5-8 October, Denver, Colorado.

Satik, C., & Horne, R.N., 1998. Measurement of Steam-Water Relative Permeability. Quarterly report of the Stanford Geothermal Program, January-March.

Shaoul, J.R., van Zelm, L.F., & de Pater, C.J., 2011. Damage Mechanisms in Unconventional-Gas-Well Stimulation--A New Look at an Old Problem. SPE Production & Operations 26(04), 388-400.

Shi, J., Li, X., Li, Q., Wang, F., & Sepehrnoori, K., 2014. Gas permeability model considering rock deformation and slippage in low permeability water-bearing gas reservoirs. Journal of Petroleum Science and Engineering 120, 61-72.

Tanikawa W., Shimamoto, T., 2009. Comparison of Klinkenberg-Corrected Gas Permeability and Water Permeability in Sedimentary Rocks. International journal of Rock Mechanics & Mining Sciences 46, 229-238.

Chapter 7: Conclusions and Recommendations

Theoretical and experimental investigations are conducted on gas permeability in shales and other tight porous media. The scope of this work is geared towards designing more representative permeability tests, developing methods to analyze the tests more accurately, and converting the test results from the lab conditions to the in-situ permeability. These goals have been achieved using a variety of experimental and theoretical methods.

Gas flow regimes are defined, and a theoretical study is conducted to characterize the flow regime in the laboratory and reservoir condition. Flow regime maps are generated for methane and helium indicating the dominant flow regime at a given pressure and permeability. These maps could be useful to assess the gas flow regime under reservoir and laboratory conditions, and to indicate the appropriate flow model. Additionally, the flow regime maps show that under typical shale gas reservoir conditions, slip flow occurs at pressures as high as 30 MPa. Therefore, slippage must be accounted for, even in high-pressure experiments or reservoir flow modelling. Under typical conditions, most shale gas reservoirs lie in the slip flow regime or early transition flow regime. This indicates that for most practical purposes, diffusion may not be a major driving force in gas flow through shale gas reservoirs.

Permeability measurements using helium on the other hand, are under transition, or free-molecule flow regime conditions. This leads to extra enhancement of helium permeability in the lab tests. Permeability measurements using helium must be

corrected for the influence of flow regime regardless of the pressure of the lab tests. Due to the high Knudsen values for helium, more complicated flow models that consider Knudsen diffusion should be used to analyze the lab results.

Klinkenberg's equation has been used for decades to take the slippage effect into account. The equation has proven to be applicable over a wide range of problems. Recently, the inability of Klinkenberg's equation to describe the slippage effect accurately for the low permeability media has been detected and investigated in the literature. By using the findings of Kundt and Warburg, this work proposes a new theoretical equation similar to that of Klinkenberg to describe the slippage effect. The new equation shows a quadratic relationship between apparent permeability and the reciprocal of pressure. The proposed equation accurately predicts the intrinsic permeability from gas flow data. Its accuracy is significantly higher than that of Klinkenberg's equation in low-permeability porous media, while it converges to Klinkenberg's at higher permeabilities.

Extensive steady-state gas and water permeability tests have been conducted on four shale/siltstone samples, using methane or nitrogen. The experiments are designed in order to verify the analytical equation proposed to model gas apparent permeability. Additionally, the influence of flow rate, pore pressure, mean effective stress, and temperature on apparent permeability of gas is investigated.

The flow model proposed in chapter 4 is verified to predict the apparent permeability of low-permeability porous media. The model parameters are obtained from data in literature, and from the present lab experiments. The relationships between the model parameters and permeability are discussed. The model explains the order of magnitude difference between liquid permeability and Klinkenberg-corrected permeability, and matches the lab results with great accuracy. According to the lab results, the proposed model is capable of predicting the apparent permeability within the entire slip flow range and early transition flow regime. It is suggested that the proposed equation be used to analyze unconventional gas reservoirs where permeabilities are commonly less than 1 md.

Gas permeability is measured at several rates to study the significance of rate dependent permeability. The tests are uniquely designed to investigate the influence of rate while keeping the mean pressure constant. The results show, while the slippage effect is observed at different mean pore pressures, permeability is also a strong function of gas rate. Permeability is observed to increase with rate until it reaches a plateau at higher rates. This indicates the dominance of pre-laminar flow regime for shales under low velocity flow which is typical of these rocks. A complete picture of permeability versus pressure and velocity dependent gas flow regimes is developed in this work. Based on the experimental results, a discussion is provided on the possible criteria for pre-laminar to laminar flow regime transition. For the Montney 10D and Clearwater sample, the transition seems to occur at 10^{-4} gr/s, and for Montney 17O and 8H it occurs at 5×10^{-5} gr/s. A rate dependent permeability model is then proposed that matches the results with reasonable accuracy.

Water permeability of the samples is also measured before and after failure. The influence of temperature is investigated with a limited number of tests. The results indicate that temperature reduces the apparent permeability. There is no model available at this point that could capture and explain the effect of temperature on the permeability of this class of material. A more comprehensive investigation is required to understand the influence of temperature. A brief discussion on the effect of gas type on the permeability results is provided. Nitrogen and methane show comparable permeability results in our experiments. Helium permeability measurements are believed to significantly overestimate the permeability of the rock. Helium's small molecular size makes the permeability measurement analysis difficult, due to very high Knudsen numbers.

Experiments were conducted to study the influence of mean effective stress on the apparent permeability and flow regime. Apparent permeability was observed to be a function of slip flow and mean effective stress. The results show that the interplay between effective stress and flow regime is the deciding factor for apparent permeability. Preliminary results show that slip flow permeability enhancement

could be cancelled out by the increase in mean effective stress over the course of production from the reservoir. Ignoring either flow regime or geomechanical effects leads to significant overestimation or underestimation of permeability of up to a few orders of magnitude, which may result in considerable errors in long-term production forecasts of Shale gas reservoirs. Mean effective stress changes over a long period of time after the start of production and assessing its effect on apparent permeability is paramount in estimating the long term production potential of a given reservoir. This long-term behavior was investigated by conducting depletion tests. In addition to the mean effective stress, failure of rock can enhance the absolute permeability, at the same time reducing the slip parameters. The post-failure test results illustrate the relationship between absolute permeability and slippage. The influence of creep was investigated through one test on the Clearwater sample. No meaningful change in permeability due to creep was observed.

Based on the findings from the lab tests and the new model, a methodology is proposed to take the effect of water saturation on apparent permeability into account. The new approach is simple, yet reproduces the lab results from the literature with good accuracy. Using the new methodology, gas permeability results on dry samples can be converted to apparent permeability of the wet samples. A discussion is provided on the magnitude of the gas relative permeability. Gas relative permeability in shales is likely higher than 1, and dependent on pressure and rate. Based on the theory developed in this work, a new equation is proposed to calculate the gas effective or relative permeability.

All the findings in this chapter can be combined, to be able to estimate the in-situ permeability of the tight rocks, from laboratory experiments. Based on the results presented, new standards and recommendations can be developed in order to produce more accurate and comparable permeability measurements. Table 14 summarizes the recommendations, based on the results of this work, for conducting gas permeability measurements.

Understanding the fundamentals of flow regime behaviour is the first step of studying flow in shales. Flow regime is a function of fluid type, pressure, and pore size. If it is assumed that pore size is directly related to permeability, then in a specific reservoir, pressure and permeability are the main parameters that dictate flow regime. Any parameter that influences pore radius potentially influences the flow regime and apparent permeability. A change in pore radius translates to a change in absolute permeability (Eq. 10) and at the same time a change in parameters “a” and “b” (Fig. 26 and Fig. 27). Apparent permeability then can be calculated using Eq. 33 considering the change in pore radius. This work flow has been applied to the effect of mean effective stress, rate, and water saturation in this work. It could also be extended to quantify the influence of other factors on apparent permeability. Other factors such as adsorption/desorption, fractures, and creep also influence the pore radius. Using the methodology presented here, the change in pore radius due to any of the aforementioned effects can be directly related to the apparent permeability.

Permeability of a certain gas flowing through a rock depends on mean pressure, flow rate, and mean effective stress. Therefore, in conducting laboratory investigations these parameters along with temperature should be controlled and taken into account in data analysis. Additionally, dependence of permeability on rate introduces a new source of uncertainty to transient methods of permeability measurements. There are implications for rate dependence of permeability in shales. Creating a larger pressure gradient can increase the apparent gas permeability and possibly the liquid permeability in shales. In addition, the permeability at the fracture faces (where pressure gradient is large) is potentially higher than inside the matrix. This could cause a delayed production response as it takes some time for the rate to increase and enhance the permeability with it, inside the matrix. Numerical simulations are required to analyze the full effect of this phenomenon in reservoir scale.

Table 14: Summary of the recommendations to measure gas permeability in the lab.

Parameter	Recommendation
Gas type	Methane, or nitrogen produce more representative results. Helium can be used when only qualitative permeability measurements are needed.
Temperature	Temperature of the tests should be close to the in-situ temperature, as there is no method to take the effect of temperature into account.
Saturation	Due to the difficulty of obtaining preserved samples, dry samples could be used for the permeability tests. The results can then be converted to the wet condition using the methodology proposed in this work.
Effective stress	The effective stress of the tests should be as close as possible to the in-situ condition. If this is not possible, tests should be repeated at different effective stresses to obtain the relationship between permeability and effective stress. A method is proposed in this work to take the effect of stress into account.
Pressure	The pressure of the test should be as close as possible to the in-situ pressure. Where this is not possible, pressures higher than 2 MPa should be used. The model proposed in chapter 4 can be used to estimate the absolute permeability from gas permeability results.
Rate	The mass flow rate should be higher than 10^{-4} gr/s to ensure laminar flow regime. The model proposed in this work can be used to estimate permeability in the pre-laminar flow regime.
Testing technique	Steady-state tests are recommended. A comprehensive study is require to ensure pulse-decay method yields the same value to the steady-state at similar conditions. In addition, the influence of the rate dependency of permeability on the pulse-decay results should be studied.

Future Work

This work proposes a work flow to convert measured permeability values from laboratory to the in-situ condition, in terms of gas pressure, effective stress, and gas rate. However, the influence of temperature on apparent permeability is not fully quantified. Based on the limited test results in this study, temperature has been observed to decrease the apparent permeability. Further theoretical and experimental investigations are required to be able to convert permeability values measured under room temperature to the permeability at reservoir temperature.

In the present work, rate dependency of permeability is studied in the lab scale. The large scale ramification of rate dependent permeability is still unknown. Short term and long term production from tight reservoirs can be influenced by rate dependent permeability. Additionally, cap rock integrity calculations in SAGD process and other thermal recovery methods can be affected considering an increase in permeability with rate. Large scale numerical simulations, incorporating the proposed permeability models in this work, are required to investigate the implications of rate dependency of permeability in field scale.

The laboratory tests in this work have been conducted on three siltstone samples, and one caprock shale (Clearwater shale). These samples do not contain significant amount of clays (less than 15%) and organic content (less than 2%). The applicability of the proposed models and parameters in this work should be investigated for shale rocks with high TOC and clay content.

References

Aguilera, R., 2002. Incorporating capillary pressure, pore throat aperture radii, height above free water table and Winland r_{35} values on Pickett plots. AAPG Bulletin 86, 605–624.

Al Ismail, M.I., Hol, S., Reece, J.S., and Zoback, M., 2014. The effect of CO₂ adsorption on permeability anisotropy in the Eagle Ford shale. Paper URTEC 1921520 presented at the Unconventional Resources Technology Conference, Denver, Colorado, USA, 25-27 August.

Aramahi B, Sundberg MI. Proppant embedment and conductivity of hydraulic fractures in shales. ARMA Paper 2012-291.

Amann-Hildenbrand, A., Ghanizadeh, A., Krooss, B.M., 2012. Transport Properties of Unconventional Gas Systems. Marine and Petroleum Geology 31, 90-99.

Baihly, J.D., Malpani, R., Altman, R., Lindsay, G., and Clayton, R., 2015. Shale Gas Production Decline Trend Comparison Over Time and Basins—Revisited. Paper SPE 135555 presented at the SPE Unconventional Resources Technology Conference, San Antonio, Texas, USA, 20-22 July.

Barree, R.D., Conway, M.W., 2004. Beyond Beta Factors: A Complete Model for Darcy, Forchheimer, and Trans-Forchheimer Flow in Porous Media. Paper SPE 89325 presented at the SPE Annual Technical Conference and Exhibition, Houston, 26-29 September.

Basak, P., 1977. Non-darcy flow and its implications to seepage problems. Journal of the Irrigation & Drainage Division 103(4), 459-473.

BC Ministry of Energy and Mines, 2012. Summary of shale gas activities in Northeast British Columbia 2011. Geoscience and Strategic Initiatives Branch, Oil and Gas Division. Oil and Gas report 2012-1, 19 p.

Belhaj, H.A., Agha, K.R., Nouri, A.M., Butt, S.D. and Islam, M.R., 2003. Numerical and Experimental Modeling of Non-Darcy Flow in Porous Media. Paper SPE 81037 presented at the SPE Latin American and Caribbean Petroleum Engineering Conference, Port-of-Spain, Trinidad and Tobago, 27-30 April.

Bernabe, Y., 1987. The Effective Pressure Law for Permeability During Pore Pressure and Confining Pressure Cycling of Several Crystalline Rocks. *Journal of Geophysical Research* 92, 649-657.

Berryman, J.G., 1992. Effective Stress for Transport Properties of Inhomogeneous Porous Rock. *Journal of Geophysical Research* 97, 17409-17424.

Beskok, A., Karniadakis, G.E., 1999. A model for flows in channels, pipes, and ducts at micro and nano scales. *Nanoscale and Microscale Thermophysical Engineering* 3, 43-77.

Bird, R. B., Stewart, W. E., Lightfoot, E. N., 1960. *Transport Phenomena*. John Wiley and Sons, Inc.

Brace, W.F., Walsh, J.B., and Frangos, W.T., 1968. Permeability of granite under high pressure. *Journal of Geophysical Research* 73, 2225-2236.

Brown, E.T., 1981. *Rock Characterization, Testing and Monitoring, ISRM suggested methods*. Pergamon Press, Oxford.

Bustin, A.M.M., Bustin, R.M., 2012. Importance of Rock Properties on the Producibility of Gas Shales. *International Journal of Coal Geology*, 103, 132-147.

Bustin, A.M.M., Bustin, R.M., Cui, X., 2008. Importance of Fabric on the Production of Gas Shales. Paper SPE 114167 presented at the 2008 SPE Unconventional Reservoirs Conference, Keystone, Colorado, USA, 10-12 February.

Bustin, R.M., Bustin, A.M.M., Cui, A., Ross, D., and Pathi, V.M., 2008. Impact of shale properties on pore structure and storage characteristics. Paper SPE 119892-

MS presented at the SPE Shale Gas Production Conference, Fort Worth, Texas, USA.

Chalmers, G.R.L., Ross, D.J.K., Bustin, R.M., 2012. Geological controls on matrix permeability of Devonian Gas Shales in the Horn River and Liard basins, northeastern British Columbia, Canada. *International Journal of Coal Geology* 103, 120-131.

Cipolla, C. L., Lolon, E. P., Erdle, J. C., Rubin, B., 2010. Reservoir Modeling in Shale-Gas Reservoirs. *SPE Reservoir Evaluation & Engineering* 13 (04), 638-653.

Civan, F., 2010. Effective correlation of apparent gas permeability in tight porous media. *Transport in Porous Media* 82, 375–384.

Clarkson, C.R., Jensen, J.L., Pedersen, P.K., Freeman, M., 2012. Innovative Methods for Flow Unit and Pore Structure Analysis in a Tight Siltstone and Shale Gas Reservoir. *AAPG Bulletin* 96(2), 355-374.

Comiti, J., Sabiri, N.E., Montillet, A., 2000. Experimental characterization of flow regimes in various porous media — III: limit of Darcy's or creeping flow regime for Newtonian and purely viscous non-Newtonian fluids. *Chemical*

Craft, B.C, Hawkins, M., Terry, R.E. 1991. *Applied Petroleum Reservoir Engineering*. Second edition, Prentice Hall, Inc.

Cui, A., Wust, R., Nassichuk, B., Glover, K., Brezovski, R., Twemlow, C., 2013. A Nearly Complete Characterization of Permeability to Hydrocarbon Gas and Liquid for Unconventional Reservoirs: A Challenge to Conventional Thinking. Paper SPE 168730 presented at the 2013 SPE Unconventional Resources Technology Conference, Denver, USA.

Cui, X., Bustin, A.M., and Bustin, R., 2009. Measurements of Gas Permeability and Diffusivity of Low-permeability Reservoir Rocks: Different Approaches and Their Applications. *Geofluids* 9, 208-223.

- Darabi, H., Ettehad, A., Javadpour, F., Sepehrnoori, K., 2012. Gas Flow in Ultra-Tight Shale Strata. *Journal of Fluid Mechanics* 710, 641-658.
- Davies, J.P., and Davies, D.K., 2001. Stress-Dependent Permeability: Characterization and Modelling. *SPE Journal* 6 (2), 224-235.
- Dong, M., Li, Z., Li, S., Yao, J., 2012. Permeabilities of Tight Reservoir Cores Determined for Gaseous and Liquid CO₂ and C₂H₆ Using Minimum Backpressure Method. *Journal of natural Gas Science and Engineering* 5, 1-5.
- Dou, H., Ma, S., Zou, C., and Yao, S., 2014. Threshold pressure gradient of fluid flow through multi-porous media in low and extra-low permeability reservoirs. *Science China: Earth Sciences* 57(11), 2808-2818.
- Dunn, L., Schmidt, G., Hammermaster, K., Brown, M., Bernard, R., Wen, E., Befus, R., Gardiner, S., 2012. The Duvernay Formation (Devonian): sedimentology and reservoir characterization of a shale gas/liquids play in Alberta, Canada. Canadian Society of Petroleum Geologists, Annual Convention, Calgary.
- Ertekin, T., King, G.A., & Schwerer, F.C., 1986. Dynamic Gas Slippage: A Unique Dual-Mechanism Approach to the Flow of Gas in Tight Formations. *SPE Formation Evaluation* 1(01), 43-52.
- Ewy, R.T., 2015. Shale/claystone response to air and liquid exposure, and implications for handling, sampling and testing. *International Journal of Rock Mechanics and Mining Sciences* 80, 388-401.
- Ezeudembah, A.S. and Dranchuk, P.M., 1982. Flow Mechanism of Forchheimer's Cubic Equation in High-Velocity Radial Gas Flow Through Porous Media. Paper SPE 10979 presented at the SPE Annual Technical Conference and Exhibition, NewOrleans, 26-29 September.
- Fathi, E., Tinni, A., Akkutlu, Y., 2012. Correction to Klinkenberg Slip Theory for Gas Flow in Nano-capillaries. *International Journal of Coal geology* 103, 51-59.

Firouzi, M., Alnoaimi, K., Kovscek, A., Wilcox, J. 2014. Klinkenberg Effect on Predicting and Measuring Helium Permeability in Gas Shales. *International J. of Coal Geology* 123: 62-68. <http://dx.doi.org/10.1016/j.coal.2013.09.006>.

Florence, F.A., Rushing, J.A., Newsham, K.E., Blasingame, T.A., 2007. Improved permeability prediction relations for low permeability sands. Paper SPE 107954 presented at the 2007 SPE Rocky Mountain Oil and Gas Technology Symposium, Denver, Apr 16–18.

Forchheimer, P. 1901. Wasserbewegung durch Boden. *Zeitz ver Deutch Ing.*, 45, 1781-1788.

Freeman, C.M., Moridis, G.J., Blasingame, T.A., 2011. A Numerical Study of Microscale Flow Behavior in Tight Gas and Shale Gas Reservoir Systems. *Transport in Porous Media* 90(1) 253-268.

Friedel, T., Voigt, H.D., 2006. Investigation of non-Darcy flow in tight-gas reservoirs with fractured wells. *Journal of Petroleum Science and Engineering* 54(3-4), 112-128.

Gad-el-Hak, M., 1999. The Fluid Mechanics of Microdevices-The Freeman Scholar Lecture. *Journal of Fluids Engineering* 121, 5-33.

Gasparik, M., Gensterblum, Y., Ghanizadeh, A., Weniger, P., and Krooss, B.M., 2015. High-Pressure/High-Temperature Methane-Sorption Measurements on Carbonaceous Shales by the Manometric Method: Experimental and Data-Evaluation Considerations for Improved Accuracy. *SPE Journal*, preprint, May 2015.

Gavin, L., 2004. Pre-Darcy Flow: A Missing Piece of the Improved Oil Recovery Puzzle? Paper SPE 89433 presented at 2004 SPE/DOE Symposium on Improved Oil Recovery, Tulsa, Oklahoma, 17-21 April.

Ghabezloo, S., Sulem, J., Guedon, S., Martineau, F., 2009. Effective Stress Law for the Permeability of a Limestone. *International Journal of Rock Mechanics and Mining Sciences* 46 (2), 297-306.

Ghanizadeh, A., Amann-Hildenbrand, A., Gasparik, M., Gensterblum, Y., Krooss, B.M., Littke, R., 2013. Experimental study of fluid transport processes in the matrix system of the European organic-rich shales: II. Posidonia Shale (Lower Toarcian, northern Germany). *International Journal of Coal Geology* 123, 20-33.

Ghanizadeh, A., Bhowmik, S., Haeri-Ardakani, O., Sanei, H., Clarkson, C.R., 2015. A Comparison of Shale Permeability Coefficients Derived Using Multiple Non-steady-state Measurement Techniques: Examples from the Duvernay Formation, Alberta (Canada). *Fuel* 140, 371-387.

Ghanizadeh, A., Gasparik, M., Amann-Hildenbrand, A., Gensterblum, Y., Krooss, B.M., 2014. Experimental study of fluid transport processes in the matrix system of the European organic-rich shales: I. Scandinavian Alum Shale. *Marine and Petroleum Geology* 51, 79-99.

Halpern, A.M., Glendening, E.D., 1996. Estimating Molecular Collision Diameter Using Computational Methods. *Journal of Molecular Structure* 365, 9-12.

Heid, J.G., McMahon, J.J., Nielsen, R.F., Yuster, S.T., 1950. Study of the Permeability of Rocks to Homogenous Fluids. *API Drilling & Production Practice*, New York 230–246.

Heller, R., and Zoback, M., 2014. Adsorption of methane and carbon dioxide on gas shale and pure mineral samples. *Journal of Unconventional Oil and Gas Resources* 8, 14-24.

Heller, R., Vermilyen, J., Zoback, M., 2014. Experimental Investigation of Matrix Permeability of Gas Shales. *AAPG Bulletin* 98 (5), 975-995.

Heller, R., Zoback, M., 2013. Laboratory Measurements of Matrix Permeability and Slippage Enhanced Permeability in Gas Shales. Paper SPE 168856-MS

presented at Unconventional Resources Technology Conference, Denver, Colorado, USA, August 12-14.

Huang, H., Ayoub, J. A., 2008. Applicability of the Forchheimer Equation for Non-Darcy Flow in Porous Media. SPE Journal 13(01), 112-122.

International Energy Agency, 2013. World's Energy Outlook 2013. November 213.

Jackson, R., and Lau, J.S.O., 1990. The effect of specimen size on the mechanical properties of Lac du Bonnet grey granite. Proceedings of the 1st International Workshop on Scale Effects in Rock Masses, Leon, Norway. Edited by da Cunha A.P.

Javadpour, F., 2009. Nanopores and Apparent Permeability of Gas Flow in Mudrocks (Shales and Siltstone). Journal of Canadian Petroleum Technology 48, 16-21.

Javadpour, F., Fisher, D., Unsworth, M., 2007. Nanoscale Gas Flow in Shale Gas Sediments. Journal of Canadian Petroleum Technology 46.

Jin, G., Perez, H.G., Agrawal, G., et al., 2015. The impact of gas adsorption and composition on unconventional shale permeability measurement. Paper SPE 172744-MS presented at the SPE Middle East Oil & Gas Show and Conference, Manama, Bahrain, 8-11 March.

Jones, F.O., Owens, W.W., 1980. A Laboratory Study of Low Permeability Gas Sands. Journal of Petroleum Technology 32, 1631-1640.

Kalantari-Dahaghi, A., Mohaghegh, S.D., 2011. Numerical Simulations and Multiple Realizations for Sensitivity Study of Shale Gas Reservoir. Paper SPE 141058 presented at the 2011 SPE Productions and Operations Symposium, Oklahoma City, Oklahoma, USA, 27-29 March.

Kang, S. M., Fathi, E., Ambrose, R. J., Akkutlu, I. Y., Sigal, R. F., 2011. Carbon Dioxide Storage Capacity of Organic-Rich Shales. SPE Journal 16(04), 842-855.

Karniadakis, G., Beskok, A., Aluru, N., 2005. *Microflows and Nanoflows: Fundamentals and Simulation*, Vol. 29. New York: Interdisciplinary Applied Mathematics, Springer.

Kestin, J., and Leidenfrost, W., 1959. An Absolute Determination of Viscosity of Eleven Gases over a Range of Pressures. *Physica* 25 (7-12), 1033-1062.

Klinkenberg, L.J 1941. The permeability of porous media to liquids and gases. *API Drilling and Production Practice*, 200-213.

Kolodzie, J.S., 1980. Analysis of pore throat size and use of the Waxman–Smits equation to determine OOIP in Spindle field, Colorado. Paper SPE 9382-MS presented at SPE 55th Annual Technical Conference and Exhibition, Dallas, Sep 21–24.

Kundt, A., Warburg, E., 1875. *Poggendorfs Ann. Physik* 155, 337 and 525.

Kutilek, M., 1972. Non-darcian flow of water in soils – laminar region: A review. *Developments in Soil Science* 2, 327-340.

Kwon, O., Kronenberg, A.K., Gangi, A.F., 2001. Permeability of Wilcox Shale and its Effective Pressure Law. *Journal of Geophysical Research* 106 (B9), 19339-19353.

Lai, B., Miskimins, J. L., Wu, Y.-S., 2012. Non-Darcy Porous-Media Flow According to the Barree and Conway Model: Laboratory and Numerical-Modeling Studies. *SPE Journal* 17(01), 70-79.

Lee, A. L., Gonzalez, M. H., Eakin, B. E., 1966. The Viscosity of Natural Gases. *Journal of Petroleum Technology* 18(08), 997-1000.

Letham, E.A., 2011. Matrix permeability measurements of gas shales: gas slippage and adsorption as sources of systematic error. BSc (Honours) thesis, University of British Columbia, Vancouver, British Columbia (March 2011).

Li, D., 2002. Analytical Study of the Wafer Non-Darcy Flow Experiments. Paper SPE 76778 presented at the SPE Western Regional/AAPG Pacific Section Joint Meeting, Anchorage, Alaska, 20-22 May.

Li, K., & Horne, R.N., 2004. Experimental Study of Gas Slippage in Two-Phase Flow. *SPE Reservoir Evaluation & Engineering* 7(06), 409-415.

Li, S., Dong, M., Li, Z., 2009. Measurement and Revised Interpretation of Gas Flow Behaviour in Tight Reservoir Cores. *Journal of Petroleum Science and Engineering* 65, 81-88.

Loeb, L.B. 1934. *The Kinetic Theory of Gases*. Second edition, McGraw-Hill Co., Inc.

Lu, X.C., Li, F.C., and Watson, A.T., 1995. Adsorption measurements in Devonian shales. *Fuel* 74 (4), 599–603.

Macini, P., Mesini, E., Viola, R., 2011. Laboratory measurements of non-Darcy flow coefficients in natural and artificial unconsolidated porous media. *Journal of Petroleum Science and Engineering* 77 (3-4), 365-374.

Mahiya, G.F., 1999. Experimental Measurement of Steam-Water Relative Permeability. MSc Thesis, Stanford University, Stanford, California.

Mao, Z., Sinnott, S.B., 2001. Separation of organic molecular mixtures in carbon nanotubes and bundles: Molecular dynamic simulations. *Journal of Physical Chemistry* 105, 6916-6924.

Martin, C.D., Chandler, N.A., 1994. The Progressive Fracture of Lac du Bonnet Granite. *International Journal of Rock Mechanics and Mining Sciences & Geomechanics Abstracts* 31 (6), 643-659.

Meyer, R., and Krause, F.F., 1998. Experimental evidence for permeability minima at low-velocity gas flow through naturally formed porous media. *Journal of Porous Media* 1(1), 93-106.

Miller, R.J., and Low, P.F., 1963. Threshold gradient for water flow in clay systems. *Soil Science Society of America Proceedings* 27(6), 605-609.

Moghadam, A.A., Chalaturnyk, R., 2014. Expansion of the Klinkenberg's slippage equation to low permeability porous media. *International Journal of Coal Geology* 123, 2-9.

Moghadam, A.A., Chalaturnyk, R., 2015. Laboratory Investigation of Shale Permeability. Paper SPE 175919 presented at the the SPE/CSUR Unconventional Resources Conference held in Calgary, Alberta, Canada, 20–22 October 2015.

Moghadam, A. A. and Chalaturnyk, R. 2016. Analytical and Experimental Investigations of Gas-Flow Regimes in Shales Considering the Influence of Mean Effective Stress. *SPE Journal* 21(02), 557-572. <http://dx.doi.org/10.2118/178429-PA>.

Morales RH, Suarez-Rivera R, Edelman E. Experimental evaluation of hydraulic fracture impairment in shale reservoirs. ARMA Paper 2011-380.

Mullen, J., 2010. Petrophysical Characterization of the Eagle Ford Shale in South Texas. Paper SPE 138145-MS presented at Canadian Unconventional Resources and International Petroleum Conference, Calgary, Alberta, Canada, 19-21 October.

Muskat, M. 1982. *The Flow of Homogeneous Fluids through Porous Media*. International Human Resources Development Corporation, Boston.

National Energy Board, 2013. *Canada's Energy Future 2013*. November 2013.

Nicksiar, M., Martin, C.D., 2014. Factors Affecting Crack Initiation in Low Porosity Crystalline Rocks. *Rock Mechanics and Rock Engineering* 47, 1165-1181.

Noman, R. and Kalam, M.Z. 1990. Transition from Laminar to Non-Darcy Flow of Gases in Porous Media. In *Advances in Core Evaluation: Accuracy and Precision in Reserves Estimation*. Edited by P.F. Worthington, 447-482.

Nuttall, B.C., Eble, C.F., Drahovzal, J.A., Bustin, R.M., 2005. Analysis of Devonian black shales in Kentucky for potential carbon dioxide sequestration and enhanced natural gas production. Report Kentucky Geological Survey/University of Kentucky (DE-FC26- 2NT41442).

Peng, D.Y., and Robinson, D.B., 1976. A New Two-Constant Equation of State. *Industrial and Engineering Chemistry: Fundamentals* 15, 59-64.

Pittman, E.D., 1992. Relationship of porosity and permeability to various parameters derived from mercury injection-capillary pressure curves for sandstone. *AAPG Bulletin*. 76, 191-198.

Rahmanian, M., Aguilera, R., & Kantzas, A., 2013. A New Unified Diffusion--Viscous-Flow Model Based on Pore-Level Studies of Tight Gas Formations. *SPE Journal* 18(01), 38-49.

Reyes, L., Osisanya, S.O., 2002. Empirical Correlation of Effective Stress Dependant Shale Rock Properties. *Journal of Canadian Petroleum Technology* 41(12).

Rivard, C., Lavoie, D., Lefebvre, R., Sejourne, S., Lamontagne, C., Duchesne, M., 2014. An overview of Canadian shale gas production and environmental concerns. *International Journal of Coal Geology* 126, 64-76.

Ross, D.J.K., Bustin, R.M., 2008. Characterizing the Shale Gas Resource Potential of Devonian-Mississippian Strata in the Western Canada Sedimentary Basin: Application of an integrated Formation Evaluation. *The American Association of Petroleum Geologists Bulletin* 92(No. 1), 87-125.

Roy, S., Raju, R., Chuang, H.F., Cruden, B.A., Meyyappan, M., 2003. Modeling gas flow through microchannels and nanopores. *Journal of Applied Physics* 93, 4870–4879.

Rushing, J.A, Newsham, K.E., Lasswell, P.M., Cox, J.C. and Blasingame, T.A. 2004. Klinkenberg-Corrected Permeability Measurements in Tight Gas Sands:

Steady-State Versus Unsteady-State Techniques. Paper SPE 89867 presented at the 2004 SPE Annual Technical Conference and Exhibition, Houston, Texas, 26-29 September.

Rushing, J.A., Newsham, K.E., & Van Fraassen, K.C., 2003. Measurement of the Two-Phase Gas Slippage Phenomenon and Its Effect on Gas Relative Permeability in Tight Gas Sands. Paper SPE 84297 presented at the SPE Annual Technical Conference and Exhibition, 5-8 October, Denver, Colorado.

Ruth, D., Ma, H., 1992. On the derivation of the Forchheimer equation by means of the averaging theorem. *Transport in Porous Media* 7(3), 255-264.

Sakhaee-Pour, A., Bryant, S., 2012. Gas Permeability of Shale. *SPE Reservoir Evaluation & Engineering* 15(04) 401-409.

Sampath, K., Keighin, C.W., 1982. Factors Affecting Gas Slippage in Tight Sandstones of Cretaceous Age in the Uinta Basin. *Journal of Petroleum Technology* 34, 2715-2720.

Satik, C., & Horne, R.N., 1998. Measurement of Steam-Water Relative Permeability. Quarterly report of the Stanford Geothermal Program, January-March.

Schettler, P.D., and Parmely, C.R., 1991. Contributions to Total Storage Capacity in Devonian Shales. Paper SPE 23422 presented at 1991 SPE Eastern Regional Meeting, Lexington, Kentucky, 22-25 October.

Seguin, D., Montillet, A., and Comiti, J., 1998a. Experimental characterisation of flow regimes in various porous media—I: limit of laminar flow regime. *Chemical Engineering Science* 53(21), 3751-3761.

Seguin, D., Montillet, A., Comiti, J., and Huet, F., 1998b. Experimental characterisation of flow regimes in various porous media—II: Transition to turbulent regime. *Chemical Engineering Science* 53(22), 3897-3909.

Shaoul, J.R., van Zelm, L.F., & de Pater, C.J., 2011. Damage Mechanisms in Unconventional-Gas-Well Stimulation--A New Look at an Old Problem. *SPE Production & Operations* 26(04), 388-400.

Shi, J., Li, X., Li, Q., Wang, F., & Sepehrnoori, K., 2014. Gas permeability model considering rock deformation and slippage in low permeability water-bearing gas reservoirs. *Journal of Petroleum Science and Engineering* 120, 61-72.

Sigal, R.F. and Qin, B. 2008. Examination of the Importance of Self Diffusion in the Transportation of Gas in Shale Gas Reservoirs. *Petrophysics* 49 (3).

Singh, H., Javadpour, F., Ettehadtavakkol, and A., Darabi, H., 2014. Nonempirical apparent permeability of shale. *SPE Reservoir Evaluation & Engineering* 17(03), 414-424.

Sinha, S., Braun, E. M., Determan, M. D., Passey, Q. R., Leonardi, S. A., Boros, J. A., ... Kudva, R. A., 2013. Steady-State Permeability Measurements on Intact Shale Samples at Reservoir Conditions - Effect of Stress, Temperature, Pressure, and Type of Gas. Paper SPE 164263 presented at the SPE Middle East Oil and Gas Show and Conference, 10-13 March, Manama, Bahrain.

Sinha, S., Braun, E. M., Passey, Q. R., Leonardi, S. A., Wood, A. C., Zirkle, T., Kudva, R. A. 2012. Advances in Measurement Standards and Flow Properties Measurements for Tight Rocks such as Shales. Paper SPE 152257 presented at the 2012 SPE/EAGE European Unconventional Resources Conference and Exhibition, Vienna, Austria, 20-22 March.

Soeder, D., 2013. Groundwater protection during shale gas development. Abstract, *Americana, Salon international des technologies environnementales*, 19-21 mars 2013, Montreal, Quebec, Canada.

Sone, H., and Zoback, M. D., 2014. Time-dependent deformation of shale gas reservoir rocks and its long-term effect on the in-situ state of stress. *International Journal of Rock Mechanics and Mining Science*, 69, 120-132.

- Swami, V., Settari, A., 2012. A pore scale gas flow model for shale gas reservoir. Paper SPE 155756-MS presented at 2012 SPE Americas Unconventional Resources Conference, Pittsburgh, Pennsylvania, USA, 5-7 June.
- Swartzendruber, D., 1962. Non-darcy flow behavior in liquid-saturated porous media. *Journal of Geophysical Research* 67(13), 5205-5213.
- Tanikawa W., Shimamoto, T., 2009. Comparison of Klinkenberg-Corrected Gas Permeability and Water Permeability in Sedimentary Rocks. *International journal of Rock Mechanics & Mining Sciences* 46, 229-238.
- Terzaghi, K., 1925. Principles of Soil Mechanics. *Engineering News Record* 95, 987-996.
- U.S. Energy Information and Administration, 2013. Annual Energy Outlook 2013 with projections to 2040. April 2013.
- Venkataraman, P., and Rao, P.R.M., 1998. Darcian, transitional, and turbulent flow through porous media. *Journal of Hydraulic Engineering* 124, 840-846.
- Von Engelhardt, W., and Tunn, W.L.M., 1954. The flow of fluids through sandstones. *Heidelberger Beitrage zur Mineralogie und Petrographie* 2, 12-25.
- Warpinski, N.R., and Teufel, L.W., 1992. Determination of the Effective-Stress Law for Permeability and Deformation in Low-Permeability Rocks. *SPE Formation Evaluation* 7, 123-131.
- Whitaker, S., 1986. Flow in porous media I: A theoretical derivation of Darcy's law. *Transport in Porous Media* 1, 3-35.
- Wu, Y.S., Pruess, K., Persoff, P., 1998. Gas flow in porous media with Klinkenberg effects. *Transport in Porous Media* 32, 117-137.
- Zeng, Z., Grigg, R., 2006. A criterion for non-Darcy flow in porous media. *Transport in Porous Media* 63(01), 57-69.

Ziarani, A.S., Aguilera, R., 2012. Knudsen's permeability correction for tight porous media. *Transport in Porous Media* 91(1), 239-260.

Zoback, M.D., and Bayerlee, J.D., 1975. Permeability and Effective Stress. *AAPG Bulletin* 59, 154-158.

Appendix A: Derivation of Eq. 17

Consider a horizontal cylindrical tube with radius R and length L . Let “ x ” and “ r ” be the coordinates in the horizontal and radial direction, respectively. Assuming steady state, laminar flow of a Newtonian fluid we can write the force balance on a shell with inner and outer radius of “ r ” and “ $r + dr$ ” and length “ dx ”. Fig. 74 shows the geometry of the problem. Forces due to fluid pressure are applied at the ends and drag forces are applied on the inside and outside surfaces of the shell. Eq. 58 shows the force balance equation on the shell in Fig. 74.

$$P_x(2\pi r dr) - P_{x+dx}(2\pi r dr) + (2\pi r dx)\tau_r - (2\pi r dx)\tau_{r+dr} = 0 \quad \text{Eq. 58}$$

Dividing Eq. 58 by $2\pi r dx$ we reach Eq. 59.

$$\frac{\partial}{\partial r}(r\tau) = -\left(\frac{\partial P}{\partial x}\right)r \quad \text{Eq. 59}$$

Integrating Eq. 59 with respect to r , we obtain Eq. 60.

$$\tau = -\left(\frac{\partial P}{\partial x}\right)\frac{r}{2} + \frac{A}{r} \quad \text{Eq. 60}$$

Newton’s law of viscosity states:

$$\tau_{rx} = -\mu \frac{\partial v_r}{\partial r}. \quad \text{Eq. 61}$$

Replacing Eq. 61 into Eq. 60 and integrating with respect to r will yield Eq. 17.

$$v_r = \frac{1}{4\mu} \frac{dP}{dx} r^2 + A \ln(r) + B \quad \text{Eq. 17}$$

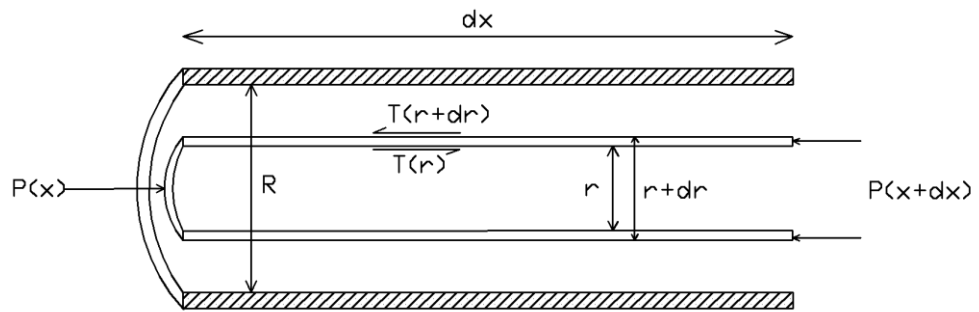


Fig. 74: An element of flow with the applicable forces in a capillary tube.

Appendix B: Experimental Results

Table 15: Results of the gas permeability measurements in this work.

Sample	Fluid	Temp. (°C)	P _{up} (kPa)	P _{down} (kPa)	P _{mean} (kPa)	P _{eff} (kPa)	Rate (gr/s)	K (md)
Clearwater	Nitrogen	25	1633	1586	1609	3530	3.075E-06	1.665E-03
Clearwater	Nitrogen	25	1634	1577	1606	3534	9.235E-06	4.125E-03
Clearwater	Nitrogen	25	1645	1569	1607	3530	1.394E-05	4.697E-03
Clearwater	Nitrogen	25	1667	1572	1619	3520	3.139E-05	8.387E-03
Clearwater	Nitrogen	25	1671	1566	1619	3521	4.407E-05	1.058E-02
Clearwater	Nitrogen	25	1670	1555	1612	3527	5.033E-05	1.109E-02
Clearwater	Nitrogen	25	2136	2087	2111	3543	5.028E-06	2.004E-03
Clearwater	Nitrogen	25	2124	2076	2100	3552	1.200E-05	4.889E-03
Clearwater	Nitrogen	25	2128	2064	2096	3568	2.004E-05	6.182E-03
Clearwater	Nitrogen	25	2153	2064	2109	3555	4.056E-05	8.874E-03
Clearwater	Nitrogen	25	2170	2060	2115	3548	8.176E-05	1.442E-02
Clearwater	Nitrogen	25	2151	2060	2106	3558	6.078E-05	1.301E-02
Clearwater	Nitrogen	25	2191	2060	2126	3538	1.032E-04	1.518E-02
Clearwater	Nitrogen	25	2196	2061	2129	3535	1.241E-04	1.771E-02
Clearwater	Nitrogen	25	5131	5095	5113	3544	1.208E-05	2.815E-03
Clearwater	Nitrogen	25	5133	5086	5110	3547	2.417E-05	4.216E-03
Clearwater	Nitrogen	25	5155	5078	5116	3540	5.826E-05	6.209E-03

Sample	Fluid	Temp. (°C)	P _{up} (kPa)	P _{down} (kPa)	P _{mean} (kPa)	P _{eff} (kPa)	Rate (gr/s)	K (md)
Clearwater	Nitrogen	25	5167	5072	5120	3537	9.732E-05	8.516E-03
Clearwater	Nitrogen	25	5190	5075	5133	3534	1.466E-04	1.054E-02
Clearwater	Nitrogen	25	5202	5061	5132	3525	1.960E-04	1.152E-02
Clearwater	Nitrogen	25	5231	5040	5136	3521	6.689E-04	2.894E-02
Axial Stress=12 Mpa								
Clearwater	Nitrogen	25	5149	5111	5130	4621	2.910E-05	6.335E-03
Clearwater	Nitrogen	25	5121	5073	5097	4649	5.788E-05	1.007E-02
Clearwater	Nitrogen	25	5115	5061	5088	4663	9.634E-05	1.511E-02
Clearwater	Nitrogen	25	5108	5055	5082	4665	1.443E-04	2.261E-02
Clearwater	Nitrogen	25	5122	5058	5090	4661	1.930E-04	2.507E-02
Clearwater	Nitrogen	25	5135	5054	5094	4659	2.418E-04	2.492E-02
Clearwater	Nitrogen	25	5188	5104	5146	4607	2.932E-04	2.881E-02
Clearwater	Nitrogen	25	5155	5062	5109	4646	3.398E-04	3.056E-02
Clearwater	Nitrogen	25	5173	5058	5115	4641	3.897E-04	2.812E-02
Post-Failure								
Clearwater	Nitrogen	25	5154	5111	5132	4618	4.854E-05	9.332E-03
Clearwater	Nitrogen	25	5168	5108	5138	4611	9.734E-05	1.337E-02
Clearwater	Nitrogen	25	5154	5094	5124	4623	1.456E-04	2.015E-02
Clearwater	Nitrogen	25	5147	5082	5115	4634	1.939E-04	2.488E-02

Sample	Fluid	Temp. (°C)	P _{up} (kPa)	P _{down} (kPa)	P _{mean} (kPa)	P _{eff} (kPa)	Rate (gr/s)	K (md)
Clearwater	Nitrogen	25	5145	5078	5112	4635	2.423E-04	2.986E-02
Clearwater	Nitrogen	25	5164	5069	5117	4630	2.918E-04	2.551E-02
Creep (after 1 week)								
Clearwater	Nitrogen	25	5142	5101	5121	4631	4.842E-05	9.820E-03
Clearwater	Nitrogen	25	5146	5098	5122	4635	9.693E-05	1.658E-02
Clearwater	Nitrogen	25	5136	5083	5110	4644	1.451E-04	2.258E-02
Clearwater	Nitrogen	25	5142	5082	5112	4641	1.937E-04	2.680E-02
Clearwater	Nitrogen	25	5155	5074	5115	4642	2.428E-04	2.492E-02
Clearwater	Nitrogen	25	5151	5062	5106	4655	2.911E-04	2.711E-02
Depletion								
Clearwater	Nitrogen	25	4136	4099	4117	5644	3.896E-05	1.050E-02
Clearwater	Nitrogen	25	4157	4115	4136	5625	7.830E-05	1.889E-02
Clearwater	Nitrogen	25	4162	4111	4136	5626	1.176E-04	2.339E-02
Clearwater	Nitrogen	25	4157	4100	4128	5636	1.566E-04	2.812E-02
Clearwater	Nitrogen	25	4156	4089	4122	5641	1.957E-04	2.994E-02
Clearwater	Nitrogen	25	4144	4076	4110	5655	2.342E-04	3.503E-02
Montney 10D	Methane	25	2093	2074	2083	20013	2.330E-05	1.139E-02
Montney 10D	Methane	25	2095	2072	2084	20013	4.666E-05	1.840E-02

Sample	Fluid	Temp. (°C)	P _{up} (kPa)	P _{down} (kPa)	P _{mean} (kPa)	P _{eff} (kPa)	Rate (gr/s)	K (md)
Montney 10D	Methane	25	2105	2075	2090	20006	7.032E-05	2.138E-02
Montney 10D	Methane	25	2105	2071	2088	20008	9.377E-05	2.472E-02
Montney 10D	Methane	25	2099	2057	2078	20019	1.168E-04	2.548E-02
Montney 10D	Methane	25	2098	2050	2074	20030	1.402E-04	2.677E-02
Montney 10D	Methane	25	2104	2051	2078	20028	1.640E-04	2.815E-02
Montney 10D	Methane	25	2108	2045	2076	20028	2.112E-04	3.074E-02
Montney 10D	Methane	25	2099	2032	2066	20036	2.337E-04	3.248E-02
Montney 10D	Methane	25	2100	2083	2092	20013	1.169E-05	6.201E-03
Montney 10D	Methane	25	4097	4080	4089	20013	2.379E-05	6.305E-03
Montney 10D	Methane	25	4104	4080	4092	20013	4.767E-05	8.752E-03
Montney 10D	Methane	25	4117	4081	4099	20013	9.562E-05	1.185E-02
Montney 10D	Methane	25	4125	4068	4096	20013	1.916E-04	1.517E-02
Montney 10D	Methane	25	4136	4060	4098	20013	2.882E-04	1.707E-02
Montney 10D	Methane	25	4159	4050	4104	20013	4.830E-04	1.965E-02
Montney 10D	Methane	25	6439	6415	6427	19744	3.864E-05	4.477E-03
Montney 10D	Methane	25	6446	6414	6430	19741	7.736E-05	6.665E-03
Montney 10D	Methane	25	6442	6402	6422	19751	1.546E-04	1.060E-02
Montney 10D	Methane	25	6450	6380	6415	19759	3.096E-04	1.216E-02
Montney 10D	Methane	25	6484	6370	6427	19746	4.669E-04	1.132E-02
Montney 10D	Methane	25	6532	6347	6440	19734	7.839E-04	1.168E-02
Montney 10D	Nitrogen	25	4108	4081	4095	20478	1.944E-05	6.282E-03

Sample	Fluid	Temp. (°C)	P _{up} (kPa)	P _{down} (kPa)	P _{mean} (kPa)	P _{eff} (kPa)	Rate (gr/s)	K (md)
Montney 10D	Nitrogen	25	4098	4066	4082	20489	3.879E-05	1.055E-02
Montney 10D	Nitrogen	25	4112	4067	4089	20482	7.784E-05	1.527E-02
Montney 10D	Nitrogen	25	4130	4056	4093	20480	1.564E-04	1.853E-02
Montney 10D	Nitrogen	25	4139	4041	4090	20482	2.350E-04	2.127E-02
Montney 10D	Nitrogen	25	4173	4035	4104	20467	3.950E-04	2.514E-02
Montney 10D	Nitrogen	25	4369	4001	4185	20387	1.241E-03	2.906E-02
Montney 10D	Nitrogen	25	5896	5873	5884	19723	2.788E-05	7.654E-03
Montney 10D	Nitrogen	25	5898	5869	5883	19724	5.578E-05	1.184E-02
Montney 10D	Nitrogen	25	5915	5873	5894	19712	1.119E-04	1.653E-02
Montney 10D	Nitrogen	25	5921	5858	5890	19717	2.240E-04	2.223E-02
Montney 10D	Nitrogen	25	5924	5840	5882	19725	3.362E-04	2.516E-02
Montney 10D	Nitrogen	25	5952	5830	5891	19717	5.628E-04	2.905E-02
Montney 10D	Nitrogen	45	5916	5879	5897	19805	2.599E-05	4.954E-03
Montney 10D	Nitrogen	45	5936	5884	5910	19792	5.217E-05	7.083E-03
Montney 10D	Nitrogen	45	5959	5876	5918	19784	1.047E-04	8.845E-03
Montney 10D	Nitrogen	45	5984	5850	5917	19785	2.104E-04	1.093E-02
Montney 10D	Nitrogen	45	6025	5837	5931	19772	3.177E-04	1.184E-02
Montney 10D	Nitrogen	45	6132	5828	5980	19724	5.390E-04	1.229E-02
Post-Failure								
Montney 10D	Methane	25	2134	2117	2126	19963	1.187E-05	6.129E-03

Sample	Fluid	Temp. (°C)	P _{up} (kPa)	P _{down} (kPa)	P _{mean} (kPa)	P _{eff} (kPa)	Rate (gr/s)	K (md)
Montney 10D	Methane	25	2141	2115	2128	19963	2.381E-05	8.418E-03
Montney 10D	Methane	25	2119	2097	2108	19982	4.713E-05	1.961E-02
Montney 10D	Methane	25	2118	2087	2102	19992	9.422E-05	2.804E-02
Montney 10D	Methane	25	2119	2081	2100	19998	1.415E-04	3.332E-02
Montney 10D	Methane	25	4157	4139	4148	20413	2.252E-05	5.766E-03
Montney 10D	Methane	25	4136	4115	4126	20437	4.481E-05	1.009E-02
Montney 10D	Methane	25	4124	4100	4112	20451	8.936E-05	1.749E-02
Montney 10D	Methane	25	4123	4091	4107	20453	1.787E-04	2.704E-02
Montney 10D	Methane	25	4127	4088	4107	20451	2.683E-04	3.256E-02
Montney 10D	Methane	25	5574	5551	5562	20240	3.341E-05	4.589E-03
Montney 10D	Methane	25	5566	5542	5554	20228	6.673E-05	9.049E-03
Montney 10D	Methane	25	5563	5534	5549	20228	1.334E-04	1.474E-02
Montney 10D	Methane	25	5574	5532	5553	20223	2.673E-04	2.061E-02
Montney 10D	Methane	25	5565	5518	5542	20215	4.003E-04	2.777E-02
Depletion								
Montney 10D	Methane	25	4178	4157	4167	21613	2.263E-05	5.180E-03
Montney 10D	Methane	25	4176	4154	4165	21613	4.524E-05	9.827E-03
Montney 10D	Methane	25	4180	4152	4166	21613	9.056E-05	1.513E-02
Montney 10D	Methane	25	4171	4137	4154	21625	1.807E-04	2.532E-02
Montney 10D	Methane	25	4166	4123	4144	21634	2.708E-04	2.987E-02

Sample	Fluid	Temp. (°C)	P _{up} (kPa)	P _{down} (kPa)	P _{mean} (kPa)	P _{eff} (kPa)	Rate (gr/s)	K (md)
Montney 10D	Methane	25	2101	2077	2089	23691	1.169E-05	4.381E-03
Montney 10D	Methane	25	2114	2088	2101	23676	2.352E-05	8.230E-03
Montney 10D	Methane	25	2105	2076	2091	23686	4.684E-05	1.471E-02
Montney 10D	Methane	25	2098	2061	2079	23697	9.335E-05	2.317E-02
Montney 10D	Methane	25	2097	2055	2076	23703	1.400E-04	3.111E-02
Montney 17O	Methane	25	2169	2082	2125	19976	2.415E-06	2.538E-04
Montney 17O	Methane	25	2157	2032	2095	20008	1.201E-05	8.886E-04
Montney 17O	Methane	25	2230	2091	2160	19942	2.483E-05	1.603E-03
Montney 17O	Methane	25	2548	2034	2291	19811	5.673E-05	9.332E-04
Montney 17O	Methane	25	4178	4107	4143	19959	4.853E-06	3.040E-04
Montney 17O	Methane	25	4182	4086	4134	19967	1.457E-05	6.804E-04
Montney 17O	Methane	25	4208	4093	4150	19955	2.443E-05	9.514E-04
Montney 17O	Methane	25	4328	4052	4190	19911	5.026E-05	8.080E-04
Montney 17O	Methane	25	4603	3999	4301	19800	9.622E-05	6.870E-04
Montney 17O	Methane	25	6073	5997	6035	20067	7.288E-06	2.844E-04
Montney 17O	Methane	25	6102	5977	6039	20062	2.197E-05	5.231E-04
Montney 17O	Methane	25	6112	5970	6041	20060	3.667E-05	7.668E-04
Montney 17O	Methane	25	6296	5955	6126	19975	7.556E-05	6.491E-04
Montney 17O	Methane	25	6712	5939	6325	19777	1.369E-04	5.030E-04
Montney 17O	Methane	25	8059	8003	8031	20071	1.000E-05	3.857E-04

Sample	Fluid	Temp. (°C)	P _{up} (kPa)	P _{down} (kPa)	P _{mean} (kPa)	P _{eff} (kPa)	Rate (gr/s)	K (md)
Montney 17O	Methane	25	8142	8012	8077	20024	3.032E-05	5.005E-04
Montney 17O	Methane	25	8202	8000	8101	20000	5.091E-05	5.389E-04
Montney 17O	Methane	25	8288	7959	8124	19977	1.029E-04	6.675E-04
Montney 17O	Nitrogen	25	6150	6020	6085	20017	5.815E-06	2.757E-04
Montney 17O	Nitrogen	25	6233	5998	6115	19987	1.768E-05	4.619E-04
Montney 17O	Nitrogen	25	6251	5947	6099	20002	2.955E-05	5.970E-04
Montney 17O	Nitrogen	25	6619	5975	6297	19804	6.258E-05	5.813E-04
Montney 17O	Methane	25	2152	2089	2121	9980	2.397E-06	3.461E-04
Montney 17O	Methane	25	4185	4125	4155	9945	4.860E-06	3.657E-04
Montney 17O	Methane	25	6166	6100	6133	9969	6.681E-06	3.255E-04
Montney 17O	Methane	25	8128	8077	8102	9999	1.009E-05	4.175E-04
Post-Failure Depletion								
Montney 17O	Methane	25	8111	8037	8074	20026	1.006E-05	2.930E-04
Montney 17O	Methane	25	8164	8047	8105	19995	3.037E-05	5.601E-04
Montney 17O	Methane	25	8287	8056	8172	19928	5.139E-05	4.734E-04
Montney 17O	Methane	25	6183	6119	6151	21950	7.413E-06	3.419E-04
Montney 17O	Methane	25	6244	6137	6190	21911	2.246E-05	6.075E-04
Montney 17O	Methane	25	6279	6131	6205	21896	3.764E-05	7.368E-04
Montney 17O	Methane	25	6380	6105	6242	21859	7.649E-05	8.007E-04
Montney 17O	Methane	25	4127	4048	4088	24014	4.788E-06	2.783E-04

Sample	Fluid	Temp. (°C)	P _{up} (kPa)	P _{down} (kPa)	P _{mean} (kPa)	P _{eff} (kPa)	Rate (gr/s)	K (md)
Montney 17O	Methane	25	4172	4055	4114	23987	1.452E-05	5.609E-04
Montney 17O	Methane	25	4209	4070	4139	23967	2.442E-05	7.888E-04
Montney 17O	Methane	25	2228	2032	2130	25971	2.671E-06	1.148E-04
Montney 17O	Methane	25	2305	2107	2206	25894	8.290E-06	3.411E-04
Montney 17O	Methane	25	2390	2110	2250	25851	1.432E-05	4.092E-04
Montney 8H	Methane	25	2256	2169	2212	19889	2.512E-06	2.105E-04
Montney 8H	Methane	25	2292	2156	2224	19877	7.655E-06	4.083E-04
Montney 8H	Methane	25	2359	2134	2247	19855	1.313E-05	4.181E-04
Montney 8H	Methane	25	4148	4094	4121	19980	4.818E-06	3.337E-04
Montney 8H	Methane	25	4167	4089	4128	19974	1.452E-05	6.963E-04
Montney 8H	Methane	25	4245	4094	4170	19932	2.465E-05	6.047E-04
Montney 8H	Methane	25	6132	6078	6105	19997	3.680E-06	1.656E-04
Montney 8H	Methane	25	6135	6058	6096	20006	7.362E-06	2.337E-04
Montney 8H	Methane	25	6170	6060	6115	19988	2.221E-05	4.910E-04
Montney 8H	Methane	25	6222	6085	6153	19949	3.733E-05	6.608E-04
Montney 8H	Methane	25	8081	8011	8046	20056	5.016E-06	1.282E-04
Montney 8H	Methane	25	8095	8019	8057	20044	1.005E-05	2.367E-04
Montney 8H	Methane	25	8168	8054	8111	19990	3.042E-05	4.746E-04
Montney 8H	Methane	25	8169	8013	8091	20017	5.070E-05	5.782E-04
Montney 8H	Methane	45	8994	8848	8921	19885	5.213E-06	6.617E-05

Sample	Fluid	Temp. (°C)	P _{up} (kPa)	P _{down} (kPa)	P _{mean} (kPa)	P _{eff} (kPa)	Rate (gr/s)	K (md)
Montney 8H	Methane	45	9015	8857	8936	19866	1.045E-05	1.214E-04
Montney 8H	Methane	45	9112	8867	8989	19813	3.169E-05	2.367E-04
Post-Failure								
Montney 8H	Methane	25	4114	4033	4073	20028	2.387E-05	1.110E-03
Montney 8H	Methane	25	4129	4012	4071	20031	3.353E-05	1.088E-03
Montney 8H	Methane	25	4198	4036	4117	19984	4.870E-05	1.130E-03
Montney 8H	Methane	25	6139	6019	6079	20022	2.208E-05	4.529E-04
Montney 8H	Methane	25	6205	6066	6136	19966	3.720E-05	6.508E-04
Montney 8H	Methane	25	6218	6038	6128	19977	5.218E-05	7.093E-04
Montney 8H	Methane	25	8087	8001	8044	20056	1.003E-05	2.101E-04
Montney 8H	Methane	25	8138	8013	8076	20025	3.028E-05	4.309E-04
Montney 8H	Methane	25	8199	8029	8114	19986	5.084E-05	5.317E-04
Depletion								
Montney 8H	Methane	25	6216	6084	6150	21950	2.236E-05	4.094E-04
Montney 8H	Methane	25	6239	6088	6164	21937	3.740E-05	6.005E-04
Montney 8H	Methane	25	6276	6068	6172	21928	5.267E-05	6.141E-04
Montney 8H	Methane	25	4272	4082	4177	23923	2.478E-05	4.818E-04
Montney 8H	Methane	25	4296	4086	4191	23915	3.489E-05	6.099E-04
Montney 8H	Methane	25	4346	4105	4226	23875	5.042E-05	7.648E-04

Appendix C: Derivation of Eq. 52

Fig. 68 illustrates an idealistic image of a capillary tube, with and without presence of water. Heid et al., (1950) proposed an analytical equation to relate the average pore radius to porosity and permeability of the rock (Eq. 10). Based on Eq. 10 we can write the following relationship between effective permeability and porosity, and pore radius open to gas.

$$r_{eff} = 88.5 \sqrt{\frac{k_{eff}}{\phi_{eff}}} \quad \text{Eq. 62}$$

$$\phi_{eff} = (1 - s_w)\phi_t \quad \text{Eq. 63}$$

A similar relationship can be written for total pore radius and permeability.

$$r_t = 88.5 \sqrt{\frac{k_t}{\phi_t}} \quad \text{Eq. 64}$$

Considering the area of the pore open to flow, water saturation can be defined as the ratio of the area filled with water to the total area of the pore (see Fig. 68). Similarly, the gas saturation is the ratio of the area of the pore open to gas to the total area.

$$s_g = 1 - s_w = \frac{r_{eff}^2}{r_t^2} \quad \text{Eq. 65}$$

Replacing Eq. 62, Eq. 63, and Eq. 64 for effective and total pore radius in Eq. 65, leads to Eq. 52.